Surface longwave cloud radiative effect derived from space lidar observations : application in the Arctic

Assia Arouf

SORBONNE UNIVERSITÉ SCIENCES

ÉCOLE DOCTORALE 129

Surface longwave cloud radiative effect derived from space lidar observations: application in the Arctic

---

presented by ASSIA AROUF

Doctoral thesis in PHYSICS OF THE ATMOSPHERE

Will be presented the 21^{th} April, 2023 with a jury composed by :

Mss.	CÉLINE CORNET	Professeure, Lille University/LOA, FR	Rapporteuse
Mr.	DAVID M. WINKER	Senior Scientist, NASA LaRC, USA	Rapporteur
Mss.	LAURENCE PICON	Professeure, Sorbonne University/LMD, FR	Présidente
Mr.	TRISTAN S. L'ECUYER	Professeur, Wisconsin University, USA	Examinateur
Mr.	VINCENT NOEL	Chargé de Recherche, CNRS/LA, FR	Examinateur
Mss.	HÉLÈNE CHEPFER	Professeure, Sorbonne University/LMD, FR	Directrice

PhD prepared at Laboratoire de Météorologie Dynamique
Institut Pierre-Simon Laplace
École polytechnique

Acknowledgments

First of all, I would like to express my gratitude to my supervisor *Hélène Chepfer*, professor at Sorbonne University. Thank you for allowing me to carry out my PhD and Master internships within your team. I would also like to thank you for your guidance, advice, and many explanations and help in each of my steps throughout these last four years.

I would like to thank all of my team: *Patrick Raberanto*, *Rodrigo Guzman*, *Artem Feofilo*, and *Olivier Chomette* for their technical support and all our long scientific discussions; *Jean Lac*, *Erik Hojgard-Olsen*, and *Zacharie Titus* for being there and discussions; and particularly I would like to thank *Marine Benzola* for her advice and reading my thesis manuscript and *Thibault Vaillant de Guélis* for sharing with me all his knowledge, codes and this thesis LaTeX-template.

My acknowledgments go to *Airbus* for contributing to the funding of my PhD grant as well as *Ed 129*.

I also wish to thank the reviewers of my thesis: *Céline Cornet* and *David M. Winker* and all members of the jury of my defense: *Tristan S. L'Ecuyer*, *Vincent Noel*. I would like to thank *Laurence Picon* for being the president of my jury.

I am grateful to *Stéphane Jacquemoud* and *Laurence Picon*, for the follow-up they provided and the advice they gave me during my master's degree.

My thanks also go to all of my co-authors for sharing with me their science and their datasets. I would like to thank my "comité de suivi de thèse": *Alexis Bern* and *Jean-Christophe Raut* for their follow-up during my thesis.

I am grateful to all the people I had interact with during my thesis, for their good mood and their attentive listening, for all the drinks and lunches we shared, my colleagues and friends: *Milena* ♡, *Naveen*, *Jean*, *Alessandro*, *Antoine*, *Clement*, *Sakina*, *Mélania*, *Jonnathan*, *Doug*, *Felipe*, *Stavros*, and all many other young researchers of the lab *TDJMCPB*. I want to thank also some permanents of the lab: *Cécile*, *Jolio*, *Jordi*, *Michel Capderou*, *Riwal*, *Albert*... I thank also all administration members.

Out of work, I would like to thank the closest persons in my life for always being there for me and supporting me through life: *Kevin* ♡, *Meriem* ♡, *Youcef* ♡, *Tina* ♡, *Amine*, *Racim*, *Marie*, *Matthieu*, *Chanez*, *Sissi*, *Souhila*, *Marwa*, *Lydia* and the teams *Les Kabyles contre "ElBourage"*, *LaFamaX* and *Le Crew*.

And last but not least, my lovely family. First, I would like to thank my *parents* ♡ for all their love and help. My *sisters* ♡, for their advice and for showing me the way. My many *nieces* ♡ and *nephews* ♡, for being cute and lovely. Je vous remercie tous d'avoir été là pour moi, ***Sahit***.

À mes petits Neveux et Nièces,
pour leurs Bêtises et Bisous.

À mes Parents et mes Sœurs,
pour leur Soutien et Amour.

"In the sweetness of friendship, let there be laughter and sharing of pleasures, for in the dew of little things, the heart finds its morning and is refreshed"

F.R.I.E.N.D.S

Contents

Introduction

Clouds are large reservoirs of condensed water suspended in the atmosphere, constantly changing in time and space. Composed of billions of tiny particles, they travel from place to place. Clouds have long been a mystery to men. They dominate the water cycle by transporting tons of water masses from oceans to continents where they pour down as rain, hail, and snow. In addition to their invaluable effect on the water cycle, they play a complex and vital role in Earth's energy budgets through their effect on solar and thermal energy exchange (Ramanathan et al., 1989).

The climate system (Earth and atmosphere) is complex and involves energy exchange between the atmosphere, hydrosphere, biosphere, and soil. At the **T**op **O**f the **A**tmosphere (TOA), on a global scale over a year, Earth receives and loses almost the same amount of energy (*e.g.* Dines, 1917; London, 1957; Hartmann et al., 1986; Ramanathan, 1987; Trenberth et al., 2009; Wild et al., 2015). Earth receives mostly all its energy from the Sun in form of electromagnetic radiation, centered in the *visible* domain. Part of this energy is directly reflected back to space by the surface and the atmosphere. The remaining part goes into heating Earth. Earth emits electromagnetic radiation, centered in the *thermal* domain. Each modification in the climate system alters the energy balance.

Clouds play an important role in these energy budgets at both the TOA and surface (*e.g.* Ramanathan et al., 1989) since they cover approximately $70\,\%$ of Earth's surface (*e.g.* Stubenrauch et al., 2013; Guzman et al., 2017; L'Ecuyer et al., 2019). They absorb, emit, and reflect a large part of the radiation passing through the atmosphere. Their effect on the outgoing radiation at the TOA is well-retrieved thanks to satellite observations (*e.g.* Wielicki et al., 1996; Vaillant de Guélis et al., 2017a; Loeb et al., 2018, 2022). However, their effect on the global radiation received at Earth's surface on a long time scale is less well established (*e.g.* Kato et al., 2011, 2018; L'Ecuyer et al., 2008, 2015, 2019; Wild et al., 2013, 2019). The only way to get direct measurements of the radiation received at Earth's surface is through ground stations. However, these measurements are few and mostly located over land in the northern hemisphere (Ohmura et al., 1998), therefore, do not cover the entire surface of the globe, unlike satellites. To retrieve surface fluxes at a global scale, satellite observations are combined with radiative transfer computations since surface measurements, from a satellite perspective, are not direct. Hence, surface radiations reaching the satellite instruments are affected by the atmosphere. Earth's surface

energy budget is a key determinant of weather, climate, water and energy cycles within the climate system. The importance of the surface energy budget has been determined for a long time and has been investigated by pioneers in the climate field such as Budyko (1961), Hartmann et al. (1986) and Ramanathan (1987). However, global surface fluxes are still affected by considerable uncertainties, despite their importance (*e.g.* Wild et al., 2017).

Human-induced activities since the pre-industrial era alter the climate system's energy equilibrium by increasing the trapping part of the outgoing thermal radiation (*e.g.* IPCC, 2021). Indeed, increasing concentrations of greenhouse gases, with their long lifetime in the atmosphere, increase the amount of the outgoing thermal radiation absorbed and reemitted at lower temperatures, resulting in less outgoing thermal radiation and disequilibrium in the TOA energy budget. To restore equilibrium, the global surface temperature is increasing such that the outgoing thermal radiation at the TOA counterbalances the incoming solar radiation, which the latter is relatively stable from year to year. As a result, Earth's surface temperature is increasing at a rate never observed before (*e.g.* Stocker et al., 2013; Wendisch et al., 2017; von Schuckmann et al., 2020; IPCC, 2021). A visible and direct effect of human-induced global warming is the Arctic's fast warming (Holland and Bitz, 2003; Serreze and Barry, 2011; Wendisch et al., 2017). Internal and external mechanisms of the Arctic affect and enhance the rapid Arctic warming, resulting in strikingly sea ice loss (*e.g.* Stroeve et al., 2012, 2014; Döscher et al., 2014; Boisvert and Stroeve, 2015; Serreze and Stroeve, 2015; Notz and Stroeve, 2018) and Greenland ice-sheet melt (*e.g.* van den Broeke et al., 2009; van Tricht et al., 2016; Hofer et al., 2017). With this global surface temperature increase, many climate components are affected and are changing, including clouds.

Cloud formation, composition, and distribution depend on the surrounding conditions such as the amount of humidity, temperature profiles, and aerosols in the atmosphere. One of the biggest challenges in climate science is to predict how clouds will change in response to a warming world and how they will affect global warming (IPCC, 2021). Because clouds highly impact Earth's energy budgets, small changes in cloud properties may alter the climate. Nevertheless, clouds' response to/influence on global warming remains one of the largest uncertainty of climate prediction (Stocker et al., 2013; Sherwood et al., 2020; IPCC, 2021). Climate models predict that, in a warming world, cloud altitude will increase, low-level clouds will get fewer, and cloud composition will change to more numerous and smaller liquid droplets (IPCC, 2021). These changing cloud properties have a direct effect on the energy budgets at both the TOA (*e.g.* Zelinka and Hartmann, 2010; Zelinka et al., 2012a; Vaillant de Guélis et al., 2018) and the surface (*e.g.* Kay and Gettelman, 2009; Kay and L'Ecuyer, 2013; Huang et al., 2019). Hence, clouds may amplify or partially offset the initial warming.

Clouds, because of their direct effect on the surface energy budget, have an influence on the sea ice and Greenland ice sheet melt. Indeed, clouds reflect part of the incoming solar radiation preventing it from reaching the surface, hence, cooling the surface. In the meantime, clouds absorb and reemit toward Earth's surface thermal radiation, hence, warming the surface. Clouds have both cooling and warming effects at the surface. The latter is the core of interest in this thesis as during polar nighttime, the cloud warming effect dominates over the cloud cooling effect. Thus, clouds may enhance Arctic sea ice loss and Greenland ice sheet melt. Moreover, the cloud warming effect at a global long-time scale is not well retrieved as it depends highly on cloud vertical structure. In this thesis, we investigate surface cloud warming and develop a new retrieval from high-resolution spaceborne cloud observations which document cloud vertical structure. We retrieve at a global scale the surface cloud warming and evaluate it against other independent retrievals. We focus further on the polar region, a region highly sensitive to global warming and where clouds may have significant impacts on modulating future Arctic trajectory (Kay et al., 2016). Some of the questions we asked during this thesis are:

1. *Can we retrieve the surface cloud warming from spaceborne lidar observations over more than a decade?*
2. *How accurately can we retrieve the surface cloud warming from space?*
3. *How the surface cloud warming varies in response to Arctic sea ice cover variability during Fall?*

This thesis is divided into four major parts. A detailed overview of the motivation and scientific context is given in chapter 1. Chapter 2 presents in detail the observations and tools used in this thesis. Then two chapters of results are presented in a form of two papers. The first paper answers the two first questions asked above. It consists in retrieving the surface cloud warming from **C**loud–**A**erosol **L**idar and **I**nfrared **P**athfinder **S**atellite **O**bservations (CALIPSO) spaceborne lidar observations collected over 16 years and in an evaluation of the retrieval (see chapter 3). The second paper answers the third question. It consists in quantifying the effect of sea ice cover variability on surface cloud warming over the Arctic during an interesting period of the year where clouds may delay sea ice freeze-up (see chapter 4).

Chapter 1

Scientific context

Contents

1.1 Earth's energy budgets

Weather, climate, and life on Earth are influenced by the amount and distribution of incoming and outgoing radiation (Sect. 1.1.1). Indeed, the radiation budget of Earth is a key determinant of the present climate and its evolution. The fundamental importance of Earth's energy budget date back to the beginning of the twentieth century (Dines, 1917; London, 1957). Energy transfers within the atmosphere and between the atmosphere and Earth's surface determine Earth's energy budget at the surface (Sect. 1.1.2).

1.1.1 Earth's energy budget at the top of the atmosphere

Earth's energy budget at the **T**op **O**f the **A**tmosphere (TOA) describes incoming and outgoing energy flow within the climate system. The Earth's energy balance at the TOA is a fundamental determinant of our planet's climatic conditions (*e.g.* Hartmann et al., 1984; Wild et al., 2015). In a stable climate (in balance), incoming solar radiative fluxes are counterbalanced by outgoing radiative fluxes in an annual global average (*e.g.* Poitou, 2013; Wild et al., 2015; Trenberth et al., 2009). A perturbation within these radiative fluxes will break the radiative equilibrium at the TOA.

Earth receives (almost) all its energy from the Sun. The Sun emits energy through electromagnetic radiation in the **S**hort**W**ave (SW) centered around the *visible* domain. Almost a third of this incoming energy is directly reflected and backscattered to space by clouds, aerosols, and the surface (primarily by bright surfaces such as ice and snow). The two-thirds left are absorbed by the atmosphere and Earth's surface which are radiatively heated. Earth (ground plus atmosphere) then emits energy in the **L**ong**W**ave (LW), centered in the *thermal* domain, back to space. The radiative net flux of Earth at the TOA (S_E) is given by equation 1.1 which represents the TOA energy equation:

$$S_E = [F^{\downarrow}_{SW}(E) \times (1 - r_E)] - OLR. \tag{1.1}$$

where E denotes Earth (ground plus atmosphere), $F^{\downarrow}_{SW}(E)$ is the solar flux reaching the Earth at the TOA, and r_E is the Earth albedo. $[F^{\downarrow}_{SW}(E) \times (1 - r_E)]$ denotes the solar flux reaching the Earth at TOA and that is absorbed by the climate system (ground plus atmosphere). OLR denotes the TOA Outgoing Longwave Radiation.

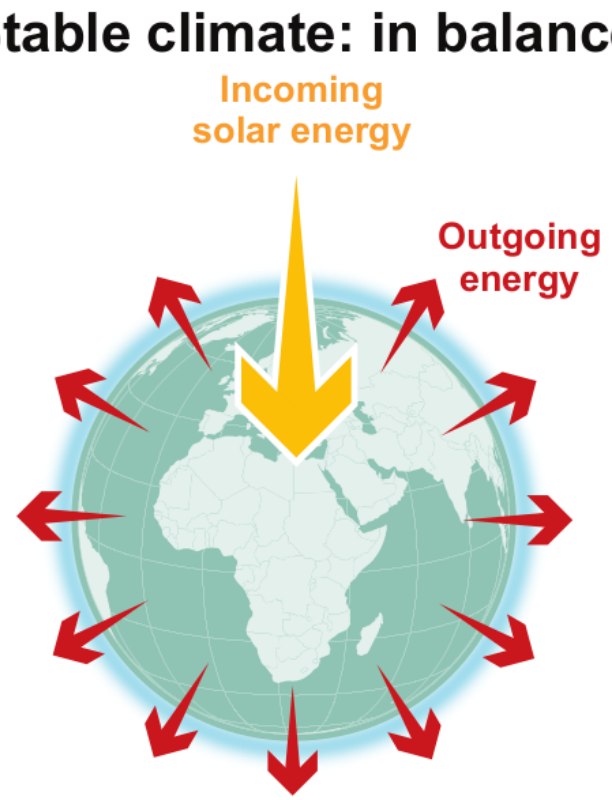

Figure 1.1 : Earth's energy budget in stable climate, part 1 (see also 1.5): FAQ 7.1, Fig. 1 p1816 from IPCC (2021).

1.1.2 Earth's energy budget at the surface

While the Earth's radiative budget at the TOA is accurately measured from satellites, the corresponding fluxes at the Earth's surface are not equally well established, as they cannot be directly measured from space (Wild et al., 2019). The energy budget at the surface is essential for understanding Earth's weather and climate (Wild et al., 2017) and has applications in many sectors such as renewable energy, agriculture, and water management. Establishing the surface energy budget has been a key research topic over many years (*e.g.* Budyko, 1961; Hartmann et al., 1986; Ramanathan, 1987; Ohmura et al., 1998; Trenberth et al., 2009; Wild et al., 2013). Yet, the energy budget at the surface is still affected by considerable uncertainties, despite its importance. Ground stations have limited spatial coverage and satellite observations don't provide direct observations of the surface. Indeed, the surface signals reaching the satellite sensors are perturbed through the atmosphere (Wild et al., 2017). Recently, progress has been made to better constrain the surface energy budget by combining surface observations, satellite retrievals, and models (Trenberth et al., 2009; Trenberth and Fasullo, 2012; Wild et al., 2013, 2015, 2019)

At the surface, part of the transmitted solar radiation through the atmosphere is

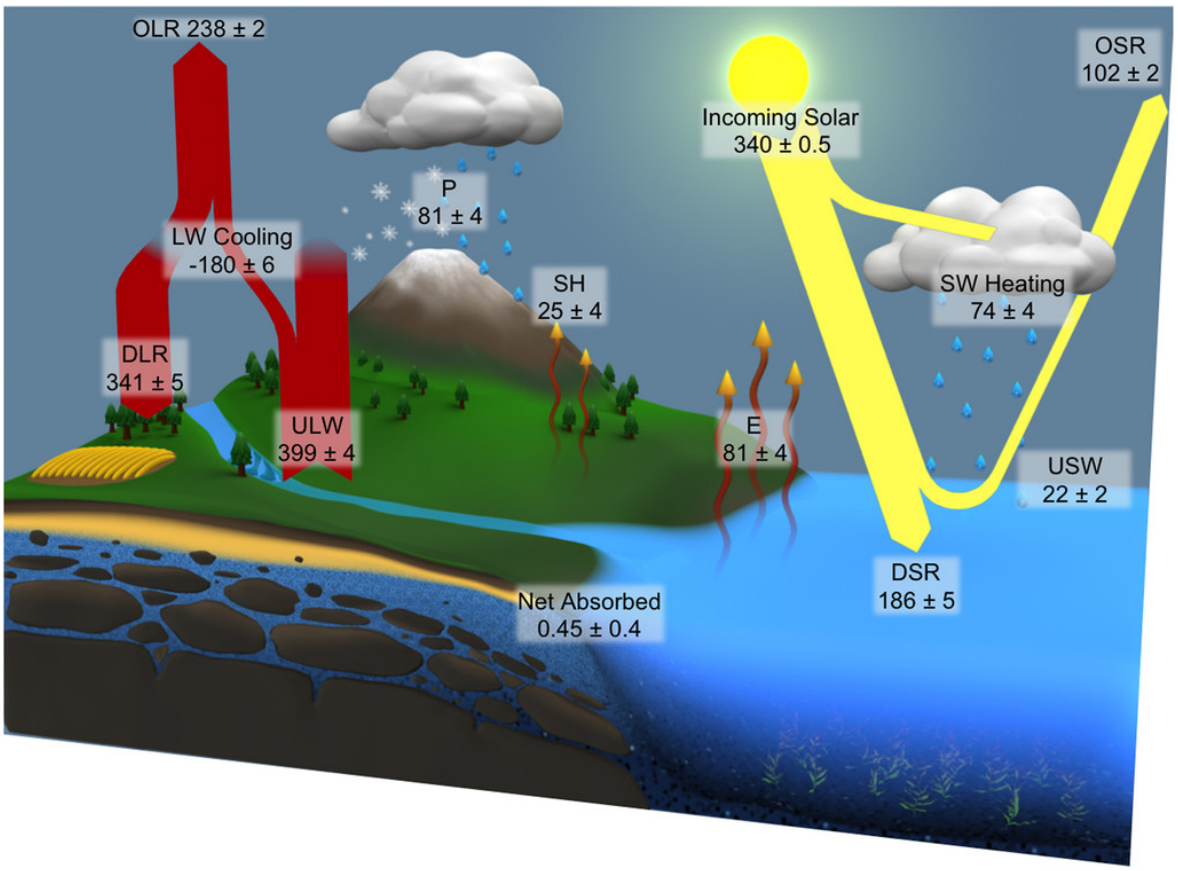

Figure 1.2 : The observed annual mean global energy budget of Earth over the period $2000 - 2009$ (fluxes in Wm^{-2}): Fig. 4 from L'Ecuyer et al. (2015).

absorbed by Earth's surface which warms up (Trenberth et al., 2009). Radiative solar energy is transformed into sensible heat, latent energy (involving different water states), and LW thermal radiation (Trenberth et al., 2009). At the surface, Earth's energy budget is described by upwelling and downwelling *radiative* and *non-radiative* fluxes. The net flux of energy absorbed by the Earth's surface must equal the rate at which the surface stores energy S_s. Equation 1.2 represents the basic surface energy equation and is taken from Liou (2002):

$$S_s = [F^{\downarrow}_{SW}(0) \times (1 - r_s)] - [\varepsilon_s \sigma T_s^4 - \varepsilon_s F^{\downarrow}_{LW}(0)] - [E + SH]. \tag{1.2}$$

where $[F^{\downarrow}_{SW}(0) \times (1 - r_s)]$ is the solar fluxes reaching the surface and that are absorbed by the surface. $F^{\downarrow}_{SW}(0)$ is the solar flux reaching the surface, which depends highly on the zenithal angle and cloud optical depth, r_s is the surface albedo. $[\varepsilon_s \sigma T_s^4 - \varepsilon_s F^{\downarrow}_{LW}(0)]$ is the budget of net LW fluxes at the surface, which is the difference between the upwelling flux emitted by Earth's surface and the downwelling flux emitted by the atmosphere and absorbed by Earth's surface. ε_s is the surface emissivity, which is equal to surface absorptance (Eq. A.6). σ is the Stefan-Boltzmann constant, T_s is the surface temperature, and $F^{\downarrow}_{LW}(0)$ is the downward LW flux emitted from the atmosphere toward the surface. These first two terms on

the right-hand side of Eq. 1.2 represent the net radiative fluxes at the surface of solar (SW) and infrared (LW) domains respectively. $[E + SH]$ represents the *non-radiative* fluxes at the surface. It consists of latent heat flux from the surface E and sensible heat flux from the surface SH.

For instance, L'Ecuyer et al. (2015, Fig. 1.2) combined satellite observations from both active and passive remote sensing with climate models to establish Earth's surface energy budget. They found that the downwelling SW and LW radiations that reach the surface, in global annual mean, are near $186\,\mathrm{Wm^{-2}}$ and $341\,\mathrm{Wm^{-2}}$ respectively. These values differ by $1\,\mathrm{Wm^{-2}}$ from those of Wild et al. (2013). These downwelling radiative fluxes are partly balanced by upwelling LW radiative fluxes ($399\,\mathrm{Wm^{-2}}$). This leaves $106\,\mathrm{Wm^{-2}}$ for the non-radiative surface energy budget component, same as in Wild et al. (2013). Latent (E) and sensible (SH) turbulent heat fluxes are close to $81\,\mathrm{Wm^{-2}}$ and $25\,\mathrm{Wm^{-2}}$ respectively with a residual heat flux that goes into the oceans of $0.45\,\mathrm{Wm^{-2}}$.

Thanks to Earth's surface energy being almost balanced at global annual mean, achieved by all the components of the climate system including clouds, the global annual mean surface temperature is close to $15\,^{\circ}\mathrm{C}$.

1.2 Clouds and radiation

Clouds are very complex components of our climate system because of their large variability in time and space and their dependence on the surrounding conditions. The cloud processes have various length scales, from microphysical scales to hundreds of kilometers (Sect. 1.2.1). They play a key role in climate and weather processes through their radiative impacts (Sect. 1.2.2) and hydrological impacts over a wide range of spatial and temporal scales. Indeed, clouds radiatively impact global surface temperature (Sect. 1.2.3). The text in sections 1.2.2 is based primarily on Lenoble (1993) and Liou (2002) handbooks.

1.2.1 Clouds formation and distribution

Cloud formation, amount, and properties depend upon the surrounding conditions and are influenced by both large-scale dynamics and local processes. Clouds are composed of small droplets and/or ice crystals of different sizes, ranging from a few microns to over $100\,\mu\mathrm{m}$, which form when water vapor condenses or deposits around cloud condensation nuclei (CCNs, Hudson, 1993). The CCNs are tiny particles called aerosols and can be dust, salt, smoke, sulfate, organics... Clouds form in environments where water vapor is in supersaturation (Thomson, 1871). The supersaturation generally occurs when a parcel of moist air cools (*e.g.* rising up) or

by getting wetter (*e.g.* adding convection). Therefore, global cloud distribution is highly driven by large-scale atmospheric circulation. Clouds are numerous in the *warm-pool*[1] and along the **I**nter**T**ropical **C**onvergence **Z**one (ITCZ) that corresponds to the ascending branch of the Hadley cell (Hadley, 1735). In these two regions, convection is strong, adding the ascending air motions, resulting in deep convective clouds that can extend from the boundary layer ($\sim 2\,\mathrm{km}$) to the tropopause ($\sim 16\,\mathrm{km}$). Clouds are numerous also over oceans on either side of the $60°$N/S latitudinal bands. These regions correspond to the storm tracks regions (*e.g.* Trenberth, 1991).

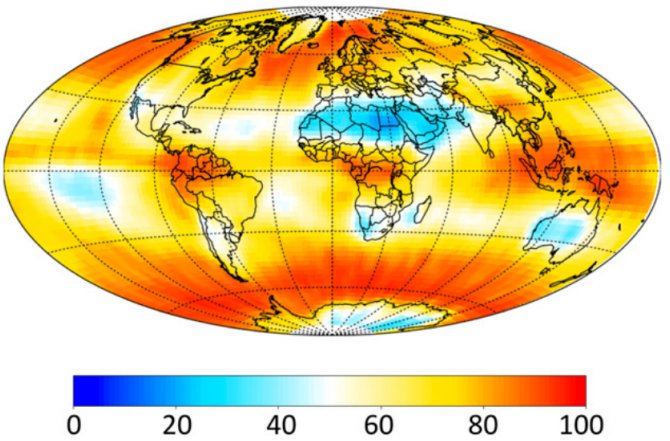

Figure 1.3 : Maps of cloud fraction using CloudSat and CALIPSO observations over $2007-2010$. Global means is $70.8\,\%$. Fig. 4 from L'Ecuyer et al. (2019).

Clouds cover roughly two-thirds of the Earth's surface (Stubenrauch et al., 2013; Guzman et al., 2017). For instance, L'Ecuyer et al. (2019), combining spaceborne lidar and radar observations over $2007-2010$ period, found that clouds cover $71\,\%$ of Earth's surface (Fig. 1.3). Clouds are characterized by their coverage, altitude, optical and geometrical depths, and microphysical properties. These cloud properties may change in the context of global warming. Clouds are sometimes classified according to their altitude as high-level (*e.g.* Cirrus), mid-level (*e.g.* Altocumulus), and low-level (*e.g.* Stratocumulus) clouds. Cumulonimbus clouds can extend vertically from the boundary layer to the tropopause and Cumulus clouds cover most of the tropics. Low-level clouds are generally composed of liquid water droplets, which are spherical, and high-level clouds are usually composed of ice crystals, which have various geometrical shapes that can be randomly distributed or oriented in a particular direction.

[1]Region in the tropics where the sea surface temperature is the warmest

1.2.2 Cloud-Radiation interaction

When an electromagnetic wave crosses a cloud, it can be subject to *scattering* or/and *absorption* from the cloud particles. If we consider clouds are uniformly distributed in plane-parallel infinite layers and vary vertically only, the attenuation of the radiative energy is described by the *extinction coefficient* $\sigma_{\lambda,e}$ $[m^{-1}]$:

$$\sigma_{\lambda,e} = \sigma_{\lambda,a} + \sigma_{\lambda,s} \tag{1.3}$$

where $\sigma_{\lambda,a}$ and $\sigma_{\lambda,s}$ are the absorption and scattering coefficients of the cloud.

The *optical thickness* δ_λ of the cloud layer between two levels $z1$ and $z2$ is a quantity without dimension and can be retrieved by the following equation:

$$\delta_\lambda = \int_{z1}^{z2} \sigma_{\lambda,a}(z)dz + \int_{z1}^{z2} \sigma_{\lambda,s}(z)dz \tag{1.4}$$

The corresponding *transmittance* (τ_λ) of this layer can be retrieved by:

$$\tau_\lambda = e^{(-\delta_\lambda/\mu)} \tag{1.5}$$

where $\mu = cos(\theta)$ is the cosine of the angle (θ) between the direction of radiation and the vertical.

The *refractive index*[2] m of atmospheric particles and molecules is composed of a real m_r and an imaginary m_i part. For a spherical cloud particle, *scattering* and *absorption* depend on the imaginary part of the *refractive index* m_i and the *size parameter* x (Eq. A.5). *Absorption* by cloud particles is proportional to the m_i. In the solar *visible* spectrum, m_i is small, so absorption of solar radiation by cloud particles may be neglected. On the contrary, in the *infrared*, m_i is quite large so the absorption of infrared radiation by cloud particles is large.

Another way to express the absorption and scattering of radiation by cloud particles is through the *single-scattering albedo*, which is defined as the ratio of the scattering coefficient to the extinction coefficient at a given wavelength and is given by the following equation:

$$\tilde{\omega}_\lambda = \frac{\sigma_{\lambda,s}}{\sigma_{\lambda,e}} \tag{1.6}$$

In the *infrared* domain, *scattering* by clouds is small ($\tilde{\omega} \approx 0$). In the *visible* domain, the *absorption* of radiation by clouds is small and negligible but *scattering* by clouds is large ($\tilde{\omega} \approx 1$).

[2] An optical parameter, dimensionless number, associated with the velocity change of electromagnetic waves in a medium with respect to a vacuum (Liou, 2002).

1.2.3 Cloud radiative effect at the surface

Clouds play an important role in the Earth's energy budget at the TOA as they affect the outgoing fluxes. They reflect part of the incoming solar radiation back to space and cool Earth's system (atmosphere plus surface). On the other hand, clouds absorb part of the outgoing thermal radiation and reemit it at colder temperatures. Therefore, they reduce the outgoing thermal radiation and contribute to warming Earth's system. Their effects at the TOA have been characterized by several previous studies which found that clouds *cool* the Earth system (atmosphere and surface) (*e.g.* Stephens, 2005; Trenberth et al., 2009; Trenberth and Fasullo, 2012; Henderson et al., 2013; Wild et al., 2015; L'Ecuyer et al., 2015; Loeb et al., 2012, 2018; Wild et al., 2019). However, the corresponding effect of clouds on Earth's surface energy at a global scale is less well established. In this thesis, I am interested in the *surface* cloud radiative fluxes.

Radiative transfer through the atmosphere in both the SW and LW domains can be modified by clouds. Therefore, clouds play an important role in regulating Earth's surface energy budget (*e.g.* Kato et al., 2011; L'Ecuyer et al., 2015; Wild et al., 2019) as stated above. To quantify the effect of clouds on Earth's surface energy budget, a classical approach is to define the surface **C**loud **R**adiative **E**ffect (CRE). To do so, the magnitudes of the radiative fluxes both under "all-sky" (including clouds) and "clear-sky" (excluding clouds) conditions need to be known (*e.g.* Ramanathan, 1987; Wild et al., 2019). At the surface, the **C**loud **R**adiative **E**ffect (CRE) equations are:

$$CRE = F^{net}_{All-sky} - F^{net}_{Clear-sky} \tag{1.7}$$

where the net fluxes are: $F^{net} = F^{\downarrow} - F^{\uparrow}$. Equation 1.7 can be written:

$$CRE = (F^{\downarrow}_{All-sky} - F^{\uparrow}_{All-sky}) - (F^{\downarrow}_{Clear-sky} - F^{\uparrow}_{Clear-sky}) \tag{1.8}$$

A *positive* CRE indicates that clouds *warm* the surface as the surface net fluxes in presence of clouds are higher than the surface net fluxes without clouds. On the opposite, a *negative* CRE indicates that the surface loose radiation in presence of clouds, so in this case clouds *cool* the surface.

The CRE is generally decomposed into its contributions in the SW (SW CRE), centered on solar radiation, and LW (LW CRE), centered on terrestrial radiation. In the SW, clouds generally have a cooling effect at the surface because they reflect back to space part of the incident solar radiation and stopping it from reaching Earth's surface (*solar albedo effect*). Surface SW CRE depend mostly on cloud coverage, cloud optical depth, and cloud phase (ice particles Vs water droplets that have different effects on scattering SW radiation). In the LW, as opposed to the SW, clouds have a warming effect because they absorb part of the radiation emitted by Earth's surface and reemit it toward the surface, thus amplifying the downward fluxes toward

the surface (*greenhouse effect*). Surface LW CRE depends mostly on cloud coverage, cloud optical depth, and cloud altitude/temperature (vertical cloud distribution) as LW fluxes depend upon the cloud temperature (Eq. A.7 *i.e.* low clouds at warmer temperature emit more LW radiation than colder high clouds).

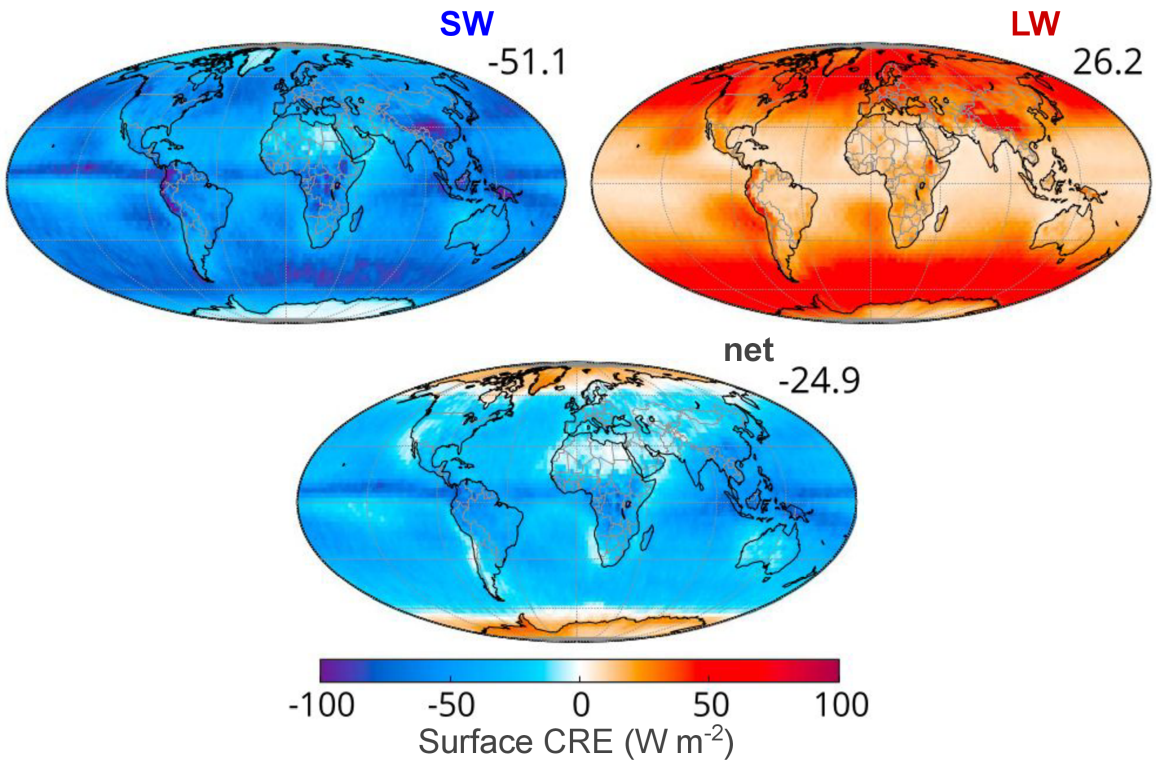

Figure 1.4 : Maps of annual mean SW, LW, and net cloud radiative effects (CRE) at the surface (Wm^{-2}). Flux are from 2BFLX $2007 - 2010$ (see section 2.3.2). Adapted from fig. 6 from Matus and L'Ecuyer (2017).

The many orbiting satellites around Earth made retrieval of global cloud properties and TOA radiative fluxes possible. Therefore, retrieval of the surface CRE at global scale has become possible with indirect methods through radiative transfer computations and satellite observations. For instance, Kiehl and Trenberth (1997), then updated by Trenberth et al. (2009), determined the surface CRE from space-borne radiometers observations collected by **E**arth **R**adiation **B**udget **E**xperiment (ERBE) (Ramanathan et al., 1989), and by **C**louds and **E**arth's **R**adiant **E**nergy **S**ystems (CERES) (Wielicki et al., 1996). Kato et al. (2013) quantified also the surface CRE using CERES and **MOD**erate-resolution **I**maging **S**pectroradiometer (MODIS) observations. Kato et al. (2010, 2011) and L'Ecuyer et al. (2008, 2019) combined observations from radiometer and a new generation of satellites (that provide the cloud vertical distribution) to retrieve the surface LW and SW CREs on global scale over ~ 5 years. Wild et al. (2019) combined space observations and ground base observations as well as climate model and found that clouds on global annual average *cool* Earth's surface by $-26\,\mathrm{Wm}^{-2}$.

Clouds have a net *cooling* effect at Earth's surface on an annual global average (Fig. 1.4, Matus and L'Ecuyer, 2017). They *cool* the surface in the *SW* domain by $-51\,\mathrm{Wm}^{-2}$ and *warm* the surface in the *LW* domain by $+\,26\,\mathrm{Wm}^{-2}$, according to Matus and L'Ecuyer (2017), resulting in a *cooling net* radiative effect of $-25\,\mathrm{Wm}^{-2}$. Nevertheless, in some specific regions such as polar regions, clouds have a net *warming* effect on an annual average (Fig. 1.4 *LW*). For instance, over polar night regions, the surface SW CRE vanishes away as it depends on the radiation emitted by the Sun. At this time of year, the surface *net* CRE is equal to the surface LW CRE and clouds *warm* the surface. Moreover, the SW $F^{\uparrow}_{All-sky}$ and SW $F^{\uparrow}_{Clear-sky}$ are quite large over polar regions since icy surfaces have large albedo that reflects much of the incoming solar radiation. Thus, this results in a small surface SW CRE . Taken together, clouds *warm* the surface over polar regions on an annual average. This warming effect may have significant impacts on melting icy surfaces and delaying sea ice freeze-up during Fall.

For the reasons stated above, we are interested in this thesis in the LW CRE at the surface as clouds may influence sea ice melting (see Sect. 1.4.2). Surface LW fluxes depend on cloud vertical distribution, which can be documented from some spaceborne instruments that are reliable everywhere, and are used in this thesis.

1.3 Global warming

Earth's energy budget at the TOA is currently imbalanced because of human-induced activities (Sect. 1.3.1). Clouds respond to human-induced climate warming in complex ways that induce large uncertainties in climate projections (Sect. 1.3.2).

1.3.1 Today's Earth energy budget

Human-induced activities have increased greenhouse gas emissions into the atmosphere, especially over the past 50 years due to increased industrialization and public transportation. Greenhouse gases, with their long lifetime in the atmosphere, affect the flow of outgoing radiative fluxes at the TOA. Adding more greenhouse gases to the atmosphere traps part of the outgoing thermal radiations that would otherwise escape the Earth system and warm up Earth's surface (*e.g.* IPCC, 2021). Thanks to the satellite observing systems in operation since 2000, the incoming and outgoing radiative fluxes of the climate system at the TOA are well known (*e.g.* Wielicki et al., 1996; Loeb et al., 2009, 2012, 2018, 2022). Since 1970, there has been a persistent imbalance in the energy flows at the TOA that has led to excess energy being absorbed by the climate system, primarily by the ocean (*e.g.* von Schuckmann et al., 2020; IPCC, 2021, fig. 1.5)

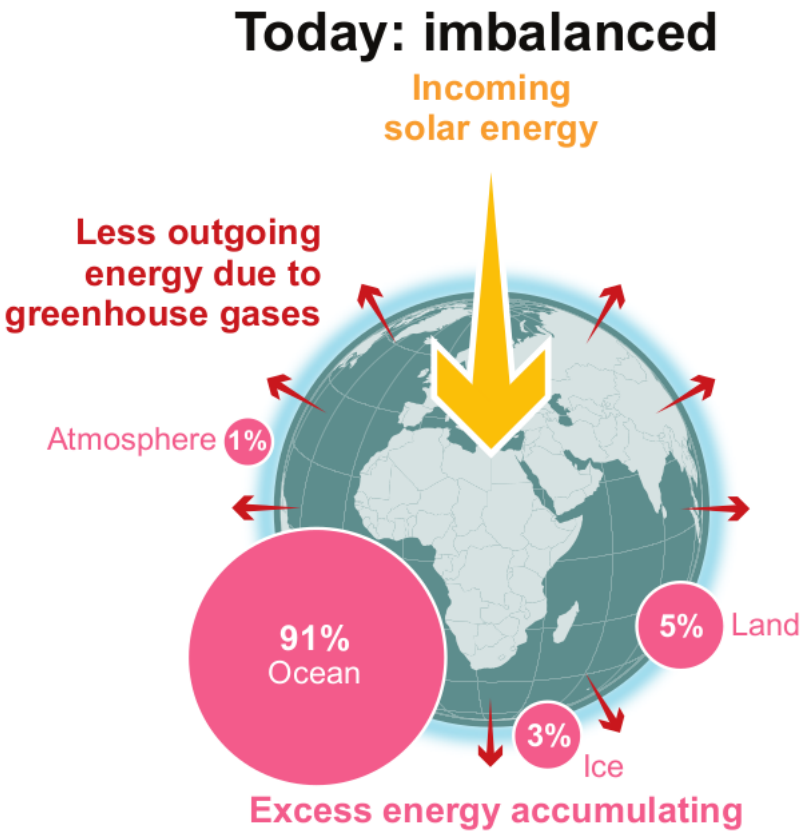

Figure 1.5 : The Earth's energy budget in a changing climate, part 2 (see also 1.1): FAQ 7.1, Fig. 1 p1816 from IPCC (2021).

As a result, the Earth's surface temperature is increasing at an alarming rate (*e.g.* IPCC, 2021). Ground station observations all over the globe show a visible increase in surface temperature. Since 1850, Earth has warmed by about $1.1\,^{\circ}\mathrm{C}$ (Masson-Delmotte et al., 2021). Global warming has caused major climate changes, such as heatwaves, ocean level rise, flooding, ice melt, a decrease in Earth's albedo, and an increase in Earth's surface temperature (Briffa et al., 2009; Duffy and Tebaldi, 2012). The Paris Agreement, signed in 2015, aims to reduce global greenhouse emissions to restrain global warming to $2\,^{\circ}\mathrm{C}$ after the pre-industrial era. However, projections of future warming by climate models for a doubling of atmospheric CO_2 indicate an increase of surface temperature between $1.5\,^{\circ}\mathrm{C}$ and $4.5\,^{\circ}\mathrm{C}$, with high uncertainty (*e.g.* National Research Council, 1979; Stocker et al., 2013). This uncertainty is largely due to clouds.

1.3.2 Cloud feedbacks

An initial perturbation of the climate system, such as human-induced global warming, changes cloud characteristics and affects Earth's energy budget. Clouds respond to warming in complex ways, as they depend highly on the surrounding

humidity and temperature profiles. They affect both LW and SW fluxes at both the TOA and surface, which in turn have a direct effect on global warming and humidity and temperature profiles. Therefore, projections of the Earth's future climate, for a given CO_2 emission scenario, are largely affected by uncertainties induced by clouds (*e.g.* Sherwood et al., 2020; IPCC, 2021). Thus, the prediction of cloud changes in a warming world and their influence on global warming has been one of the biggest challenges in climate science.

One way to quantify the impact of the perturbation on the surface temperature is through feedback. Feedback determines whether an initial perturbation to a system is amplified or damped by internal mechanisms of the system. It is generally determined by linking surface temperature change to a perturbation of the TOA radiative fluxes induced by changes in a climate component (*e.g.* water vapor, aerosols, clouds). Cloud feedbacks are the most uncertain of the radiative feedbacks (Zelinka et al., 2012a,b, 2016; Goosse et al., 2018; Sherwood et al., 2020; IPCC, 2021) since they depend on several factors that can be changed by the initial perturbation such as humidity and temperature profiles.

At the TOA

Climate models predict that human-induced global warming is expected to alter the cloud altitude (higher clouds that will trap more of the outgoing LW fluxes) and the amount of clouds (fewer low-level clouds that will reflect less SW fluxes to space), which will amplify global warming and increase global surface temperature (IPCC, 2021). On the other hand, they predict that cloud composition will change, with cloud droplets becoming more numerous and smaller, damping some of the initial warming by reflecting more SW fluxes back to space. In the tropics for instance, Lindzen and Choi (2022) suggested that anvil cirrus clouds would shrink in a warming world, leaving more LW radiation escaping the Earth system, resulting in a cooling LW effect. This phenomenon is referred to as the *iris effect*. The most recent report of IPCC states that clouds are expected to amplify future warming with high confidence. The last report of IPCC (IPCC, 2021) reduced the uncertainty of cloud feedbacks by $50\,\%$ compared to the previous IPCC report in 2013 (Stocker et al., 2013). Nevertheless, clouds remain the largest uncertainty of climate feedbacks.

At the surface

As the climate warms, we observe an increase in the specific humidity in the lower troposphere. If the humidity increase in the lower troposphere is associated with an increase in low-level clouds, these clouds would reflect more SW fluxes back to space and cool the surface, resulting in damping warming as the SW effect dominates over the LW effect. If the low-level cloud cover remains constant in response

to a warming world, the increase of humidity in the lower troposphere will increase downwelling LW radiation toward the surface, resulting in amplifying warming (Boucher et al., 2013; Sherwood et al., 2020). In some specific regions (*e.g.* Arctic), the increase of humidity in the lower atmosphere would increase low-level clouds that may reflect more of the SW radiation back to space, at the same time, trap more of the LW radiation and reemit it toward the surface resulting in amplifying warming and is detailed more in section 1.4.2.

1.4 Arctic's climate

Human-induced global warming has increased Arctic surface temperature (Sect. 1.4.1) and changed the Arctic energy budget (Sect. 1.4.2).

1.4.1 Arctic warming

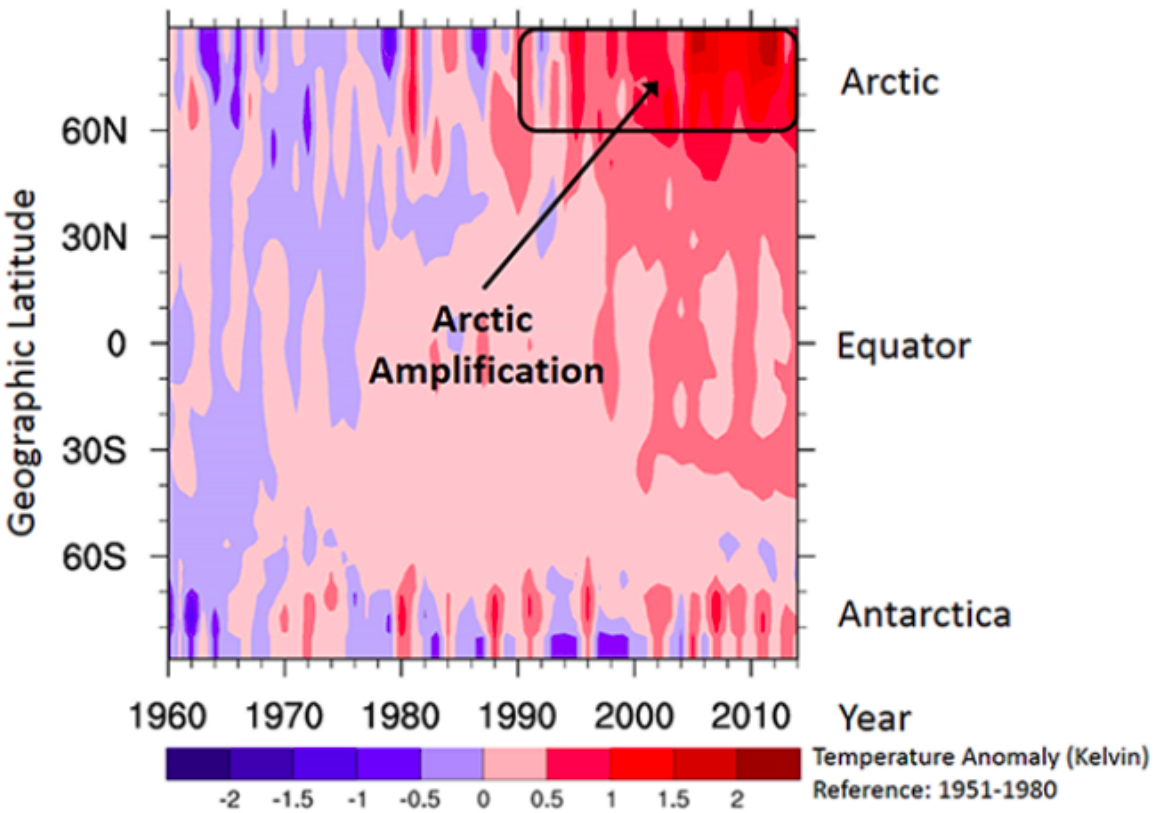

Figure 1.6 : Zonal mean temperature variations over 1951 – 1980. The increase in red areas in more recent years indicates global warming. The area inside the black box shows the *Arctic amplification*, particularly within the past 25 years. The data are provided by the NASA Goddard Institute for Space Studies. : Fig. 1 from Wendisch et al. (2017).

The Arctic is experiencing the fastest and most evident warming on Earth (Serreze and Barry, 2011). As the climate warms in response to human-induced activities, Arctic sea ice melts. Indeed, more open water extent is observed, reducing the amount of reflected sunlight and increasing SW absorption by the ocean and leading to greater warming (an amplifying feedback, IPCC, 2021). As a consequence, Arctic sea ice melts even more leading to more open water and more SW radiation being absorbed. This phenomenon is referred to as *Arctic amplification* (Holland and Bitz, 2003). Hence, over the past decades (more than 40 years), the Arctic region has warmed more than twice the global average (Fig. 1.6, Wendisch et al., 2017).

Figure 1.6 shows the zonal average of surface temperature evolution since 1960 and highlights the fast warming in the Arctic. As a result, Arctic sea ice is experiencing a decline at a rate never observed before (Stroeve et al., 2012, 2014). Notably, Arctic sea ice decline is more pronounced during late Summer and early Fall (Stroeve et al., 2012; Döscher et al., 2014), resulting in larger Summer melt and longer melt season (Stroeve et al., 2014; Boisvert and Stroeve, 2015; Notz and Stroeve, 2018; Serreze and Stroeve, 2015),

1.4.2 Arctic energy budget at the surface

In polar regions, interactions between the atmosphere, ocean, sea ice, and the surface play an important role in the surface energy budget and thus in shaping the polar climate (*e.g.* Kay and Gettelman, 2009; Kay and L'Ecuyer, 2013; van Tricht et al., 2016; Goosse et al., 2018). Specifically, both *radiative* and *non-radiative* interactions between these components are major controllers of the Arctic's climate. Arctic cloud complexity and radiative effects have been explored for many years (*e.g.* Curry et al., 1996; Intrieri et al., 2002; Kay and Gettelman, 2009). However, knowledge of the interaction processes between clouds, ocean, and sea ice remains poorly understood because cloud formation and evolution are influenced by dynamic interaction with the fully coupled climate system (Kay et al., 2016) over a wide range of time and space scales. Hence, the need for accurate long-time cloud observations.

Clouds play a crucial role in the Polar climate due to their interaction with both SW and LW radiation and their role in the hydrological cycle, which both have direct effects on sea ice loss and growth. Clouds have both positive (amplifying the initial perturbation) and negative (dampening the initial perturbation) feedbacks in polar regions. For instance, one example of global and polar cloud feedback is the *cloud optical depth feedback*. As the climate warms up, the amount of liquid and mixed-phase clouds increases. Cloud particles get smaller (cloud water droplets are smaller than cloud ice particles) and therefore reflect more solar radiation back to space, resulting in *negative feedback*. This will have an effect on the SW fluxes but not on the LW fluxes. Another polar cloud feedback is *cloud sea-ice feedback*. When sea

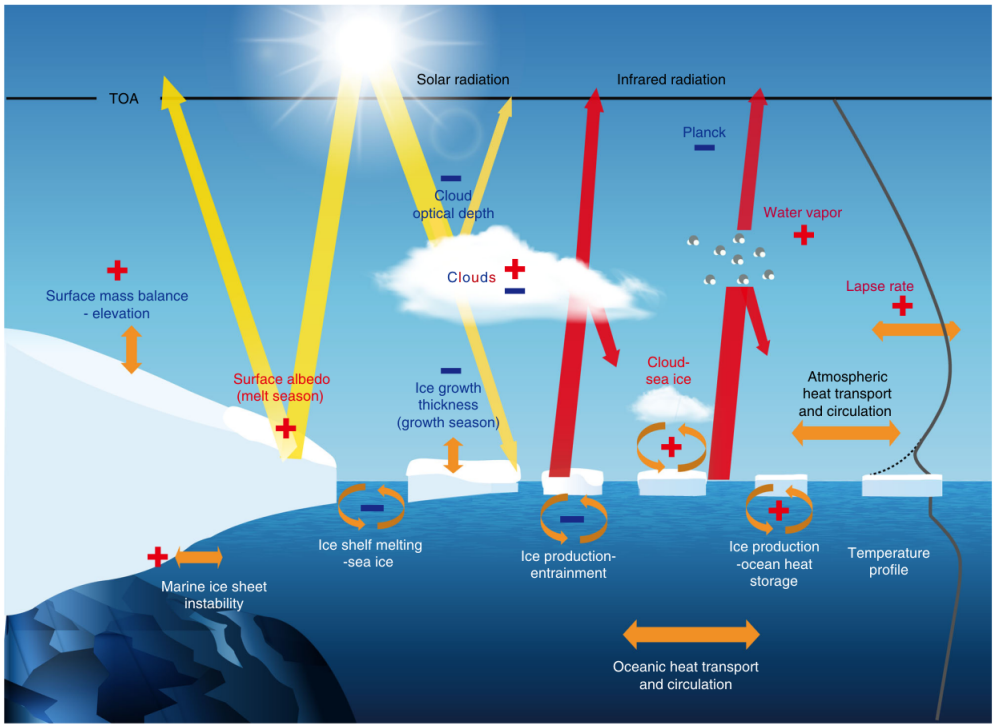

Figure 1.7 : A schematic of some important *radiative* and *non-radiative* feedbacks in polar regions involving the atmosphere, the ocean, sea ice and ice sheets. SW (in yellow) and LW (in red) radiation exchanges are the radiative processes in which we are interested in this thesis. A red plus sign means that the *feedback is positive* (amplifying the initial perturbation), and a negative blue sign corresponds to a *negative feedback* (damping the initial perturbation). Both signs are present for cloud feedbacks as both positive and negative feedbacks are occurring simultaneously and the net effect is not known. Fig. 1 from Goosse et al. (2018).

ice melts, leaving more open water exposure, surface turbulent fluxes increase humidity in the boundary layer and can increase low-level clouds (Kay and Gettelman, 2009; Goosse et al., 2018). During Arctic Summer, any increase in low-level clouds may increase Earth's albedo and reflect more solar radiation back to space (sea ice bright surface being replaced by cloud bright surface), this would have a *negative feedback*. During Arctic night, the SW fluxes which depend on solar radiation vanish, leaving the LW fluxes only. At this time of year, any increase in low-level clouds may increase downwelling LW radiation toward the surface, increase surface temperature, and amplify sea ice loss, this would have a *positive feedback*. Observations show that the increase in low-level clouds in response to sea ice loss occurs during non-summer seasons (*e.g.* Kay and Gettelman, 2009; Morrison et al., 2018; Huang et al., 2019), thus, generates a *positive feedback*. Although, the increase of downwelling LW radiation due to increasing the occurrence of low-level clouds remains unclear given the lack of reliable cloud radiative effect retrieval in polar regions on a long-time scale. Indeed, sea ice moves with ocean currents (Kay and L'Ecuyer, 2013) and clouds are constantly changing (Liou, 2002), hence, the difficulty to quantify the co-variability between these two components and the need of observations with high

spatiotemporal resolution.

Chapter 2

Tools

Contents

2.1 Observation of Earth's components from space

Observations of Earth's components from space are performed by remote sensing which encompasses all techniques of detecting and characterizing an object/area by measuring the emitted or reflected radiation. The characteristics of this object/area are carried from the observed object/area to the observer by waves, generally electromagnetic waves. *Passive remote sensing* (Sect. 2.1.1) deals with the observation of a target that emits or reflects electromagnetic radiation external to the instrument (*e.g.* solar radiation or earth radiation). *Active remote sensing* (Sect. 2.1.2), deals with cases where the electromagnetic radiation to be measured is emitted by the instrument itself. Satellites flying on the *A-Train* constellation (Sect. 2.1.3) carry both active and passive remote sensing instruments. This chapter describes instruments, their measurements, and datasets that have been used in this thesis.

2.1.1 Passive remote sensing

Passive instruments are commonly used to measure infrared radiation emitted by the Earth, and/or solar radiation reflected from the Earth's surface, atmosphere, clouds, and aerosols. Depending on the studied object, the instruments measure in well-defined wavelength ranges. The text in this section is based primarily on Lenoble (1993) and Liou (2002) textbooks.

The *visible* spectrum (0.4–$0.8\,\mu\mathrm{m}$) is the wavelength range where the Sun emits most of its radiation. Molecules and clouds do not absorb much radiation in this spectral band and can be negligible. In this spectrum, most of the radiation can travel through the atmosphere. However, part of the radiation in this spectrum can be scattered by atmospheric gases (Rayleigh scattering), see figure 2.1. Spaceborne instruments, therefore, measure solar radiation reflected from clouds and surfaces in this spectral band.

The *infrared* spectrum (5–$100\,\mu\mathrm{m}$) is the wavelength range where most of the solar energy absorbed by Earth is re-emitted. At these wavelengths, scattering is negligible most of the time. The atmosphere is relatively opaque at these wavelengths because the majority of the radiation is absorbed by atmospheric water vapor, H_2O, and some other gases such as CO_2 and N_2O at specific wavelengths. The 8–$12\,\mu\mathrm{m}$ region (Fig. 2.1), known as the thermal infrared atmospheric window, allows the signal emitted from the Earth's surface to travel through the atmosphere to space, in absence of clouds and aerosols. Therefore, the atmospheric window's wavelengths are commonly used to observe Earth's surface and clouds since atmospheric gases absorb little radiation in this spectral band.

In the *microwave* spectrum (1 mm–1 m), the atmosphere and clouds do not interact with the radiation, except at specific wavelengths explained below. Therefore, this spectrum is used to observe surface characteristics such as vegetation, soil moisture, or sea ice and snow. In the microwave spectrum, spaceborne instruments observe Earth's surface emissivity (see Eq. A.6). The emissivity of the surface depends on the moisture content of the soil (over land), on the salinity, sea ice, and surface roughness (over ocean). Thereby, spaceborne instruments observe the sea ice extent and its evolution in this spectral band. However, large cloud particles and precipitation particles (∼0.5–3 mm) start to interact with radiation at wavelengths around 1–10 mm. Therefore, some spaceborne instruments, with both passive and active remote sensing techniques, operate at these wavelengths to observe clouds and precipitations.

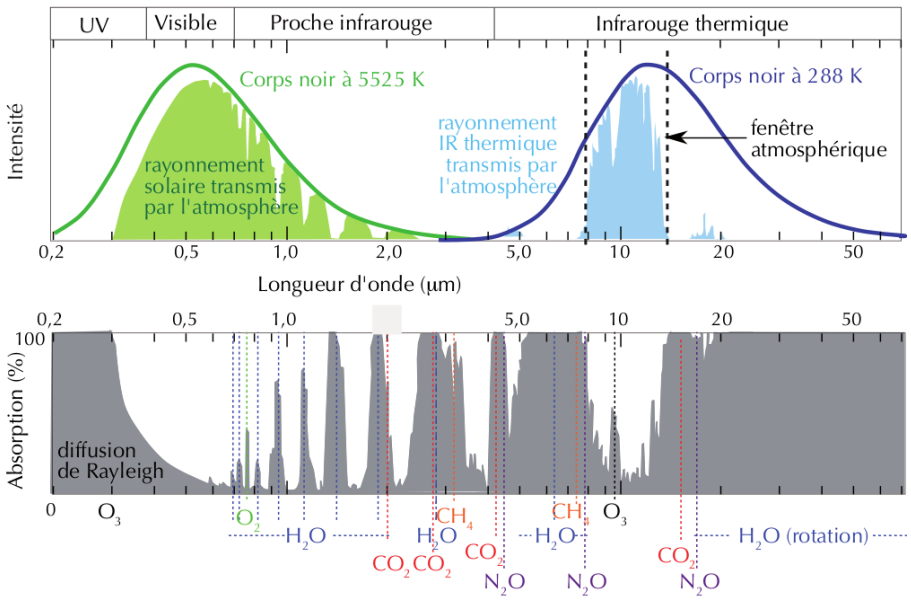

Figure 2.1 : Spectra of emission and absorption by the atmosphere of solar and terrestrial radiation, in absence of clouds and aerosols. Fig. 1 from Poitou (2013).

Passive instruments on board satellites can have large horizontal coverage due to their generally large field of view and/or to horizontal scanning mechanisms along the satellite track (*e.g.* up to 200 km for the instrument presented in Sect. 2.4.1). Most global cloud climatologies are based on passive instruments. However, these instruments do not directly document the vertical distribution of clouds. The retrieval of cloud altitude is based on indirect methods, *e.g.* based on measurement of brightness temperature and can be biased (*e.g.* Liu et al., 2010; Stubenrauch et al., 2013). Therefore, the retrieval of cloud altitude is not very reliable from passive instruments (e.g. Holz et al., 2008; Shea et al., 2017), introducing biases on the surface **L**ong**W**ave (LW) **C**loud **R**adiative **E**ffect (CRE) estimates, which depends highly on cloud vertical distribution as shown in section 1.2.3.

2.1.2 Active remote sensing

Active remote sensing is based on the measurement of electromagnetic waves emitted by the instrument itself. Indeed, active sensors produce their own electromagnetic waves, unlike passive instruments. They generate very short pulses of high-power energy and measure the backscattering signal (*i.e.* if the transmitter and detector are collocated which is the case for most spaceborne instruments). Active instruments directly measure the round-trip time of photons between the transmitter and the receiver and deduce the distance between the instruments and the objects that interact with the electromagnetic wave (*e.g.* Liou, 2002; Sherwood et al., 2004; Kato et al., 2011; Mace and Wrenn, 2013; Di Michele et al., 2013; Stubenrauch et al., 2013) as given by the following equation:

$$d = \frac{c \times \Delta t}{2} \tag{2.1}$$

where c $[\approx 3.00 \times 10^8\,\mathrm{m\,s^{-1}}]$ is the velocity of light, Δt is the round-trip time $[s]$. A pixel in active remote sensing from a spaceborne perspective is a volume at a given latitude, longitude, and *altitude* (the vertical thickness of a layer).

The wavelength of the electromagnetic wave emitted by the instrument is chosen according to at least two criteria: i) a wavelength that will interact with the object to be studied and therefore is less than/equal to the size of the object; ii) that the object to be studied is alone/dominant to interact with the electromagnetic wave at the chosen wavelength. *Ultraviolet* and *visible* (0.4–$0.8\,\mu\mathrm{m}$) sensors interact with particles of all sizes but may be rapidly attenuated and only sense the upper portions of optically dense layers. They interact with aerosol and cloud particles and might sens the entire atmospheric column in optically thin layers. Sensors operating in the *microwave* spectrum ($1\,\mathrm{mm}$–$1\,\mathrm{m}$) are not sensitive to aerosol particles but are sensitive to a wide range of cloud and precipitation particles and experiences much less attenuation than *ultraviolet* and *visible* sensors.

A widely used instrument in active remote sensing to observe clouds and aerosols is the **Li**ght **D**etection **A**nd **R**anging (Lidar). Lidar detects light from a laser beam that is backscattered by molecules and particles (clouds and aerosols) toward a telescope. Lidars are frequently used to observe aerosols and thin clouds but the lidar signal may be completely attenuated by clouds with visible optical thicknesses greater than 3 to 5 (Chepfer et al., 2014). Space lidars operate at typical wavelengths of $355\,\mathrm{nm}$, $532\,\mathrm{nm}$, and $1064\,\mathrm{nm}$.

In the wavelengths at $10\,\mu\mathrm{m}$–$3\,\mathrm{mm}$, large cloud particles, such as liquid water and ice droplets, and precipitation particles begin to interact with the radiation. **Ra**diation **D**etection **A**nd **R**anging (Radar) typically uses these wavelengths to observe precipitations and clouds.

Therefore, the combination of spaceborne lidar and spaceborne radar is essential to have a good representation of the global vertical distribution of clouds (Henderson et al., 2013).

2.1.3 A-Train constellation

Several Earth observation satellites follow each other closely along the same (or very similar) orbit (Stephens et al., 2002). These satellites carry passive and active instruments that operate at different wavelengths. This allows observing almost simultaneously the same atmospheric scene with passive instruments combined with active instruments. The measurements collected by the instruments of these satellites are used synergistically to advance our understanding of clouds, aerosols, atmospheric chemistry, and other elements of Earth system science to better understand climate and climate change.

The *A-Train* satellites are in a polar orbit, at $98.2°$ of inclination with respect to the equatorial plane, sun-synchronous[1] at $705\,\mathrm{km}$ of altitude, crossing the equator in an upward direction at about $13\,\mathrm{h}\ 30\,\mathrm{min}$ local solar time, hence the name of the afternoon constellation and the name *A-Train*. Satellites in this constellation follow each other within seconds or a few minutes. Figure 2.2 shows the *A-Train* constellation and the time spacing between each satellite according to their configuration in June 2011. The *A-Train* satellites circle the Earth in $99\,\mathrm{min}$ and are in a controlled orbit where the ground tracks repeat every 16 days. Therefore, they sample the entire globe in ∼one day for passive instruments which have a wide field of view. The active instruments, which have a more restricted field of view, have some areas that are not sampled due to the controlled orbit.

Aqua was the first satellite on this orbit, launched in 2002. This satellite carries passive remote sensing instruments. **C**loud–**A**erosol **L**idar and **I**nfrared **P**athfinder **S**atellite **O**bservations (CALIPSO) and CloudSat join the constellation in 2006 with new generation instruments: lidar and radar respectively, that provide vertical profiles of the Earth's atmosphere. In this thesis, I will use the observations of these three satellites, mainly those of CALIPSO.

In February 2018, CloudSat exited the *A-Train*, due to a loss of one of its reaction wheels. In September 2018, CALIPSO joined CloudSat in the orbit called *C-Train*, at about $680\,\mathrm{km}$, to continue observing simultaneously the same scenes. The local solar time of crossing the equator for these two satellites changed from $\sim 13\,\mathrm{h}\ 30\,\mathrm{min}$ to $\sim 14\,\mathrm{h}\ 30\,\mathrm{min}$. The evolution of the orbital parameters of these satellites is available on Ixion (Capderou, 2012).

[1] Slightly retrograde quasi-polar Earth orbit whose altitude and inclination are chosen so that a satellite in this orbit passes over the Earth's surface at the same local solar time.

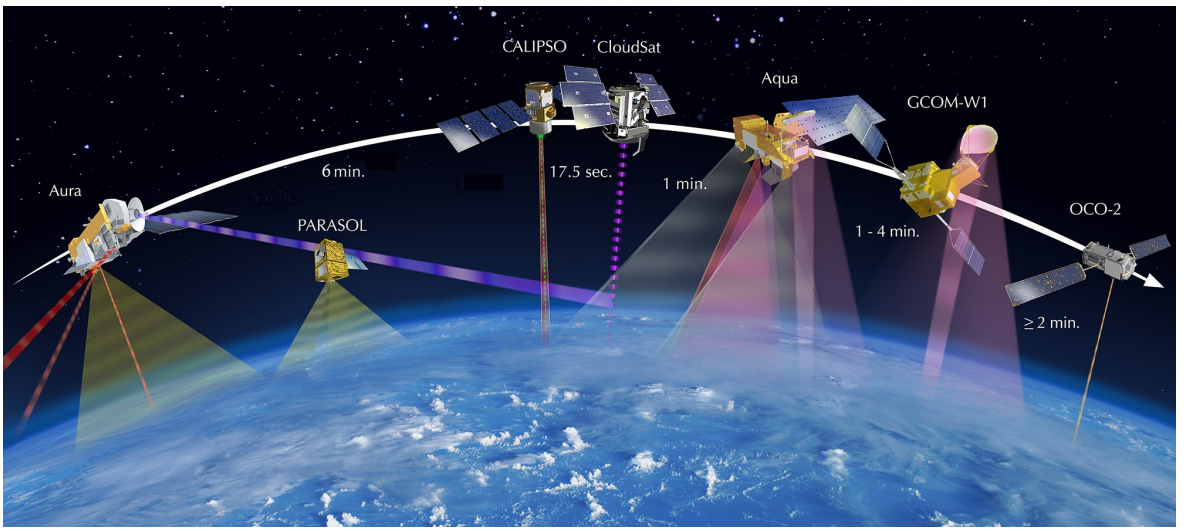

Figure 2.2 : Illustration of the *A-Train* constellation according to their configuration in June 2011. Source : ATrain.nasa.gov.

2.2 Observation of clouds by the Lidar CALIOP/ CALIPSO

CALIPSO (Winker et al., 2004; Winker et al., 2010) is a joint mission of the United States (NASA) and France (Centre National d'Études Spatiales/CNES). The satellite was launched in June 2006 and has been in orbit for over 16 years. The satellite carries three instruments which are illustrated on figure 2.3 (Winker et al., 2010): **C**loud–**A**erosol **LI**dar with **O**rthogonal **P**olarization (CALIOP), **I**maging **I**nfra**R**ed Imager (IIR)[2], and **W**ide-**F**ield **C**amera (WFC)[3]. In my thesis, I use observations collected by the lidar CALIOP.

2.2.1 Lidar onboard CALIPSO: CALIOP

The CALIOP lidar is a polarized elastic[4] backscattering lidar. CALIOP has a two-wavelength laser transmitter, $532\,\mathrm{nm}$ and $1064\,\mathrm{nm}$, a three-channel receiver. The $1064\,\mathrm{nm}$ wavelength does not correspond to any atmospheric gas absorption line but the $532\,\mathrm{nm}$ wavelength does correspond to a weak O3 absorption line which is corrected during Level 1 data processing. Therefore, the lidar signal is subject to both scattering and absorption by atmospheric molecules and particles. In this thesis, only the observations at $532\,\mathrm{nm}$ are used.

[2]Nadir-viewing three-channel infrared radiometer: $8.7\,\mu\mathrm{m}$, $10.5\,\mu\mathrm{m}$, and $12.0\,\mu\mathrm{m}$; with a swath of $64\,\mathrm{km}$ centered on the CALIOP footprint

[3]Nadir-viewing single-channel visible imager ($620-670\,\mathrm{nm}$) with a swath of $61\,\mathrm{km}$ centered on the CALIOP footprint

[4]signal backscattered by atmospheric molecules and particles without changing wavelength.

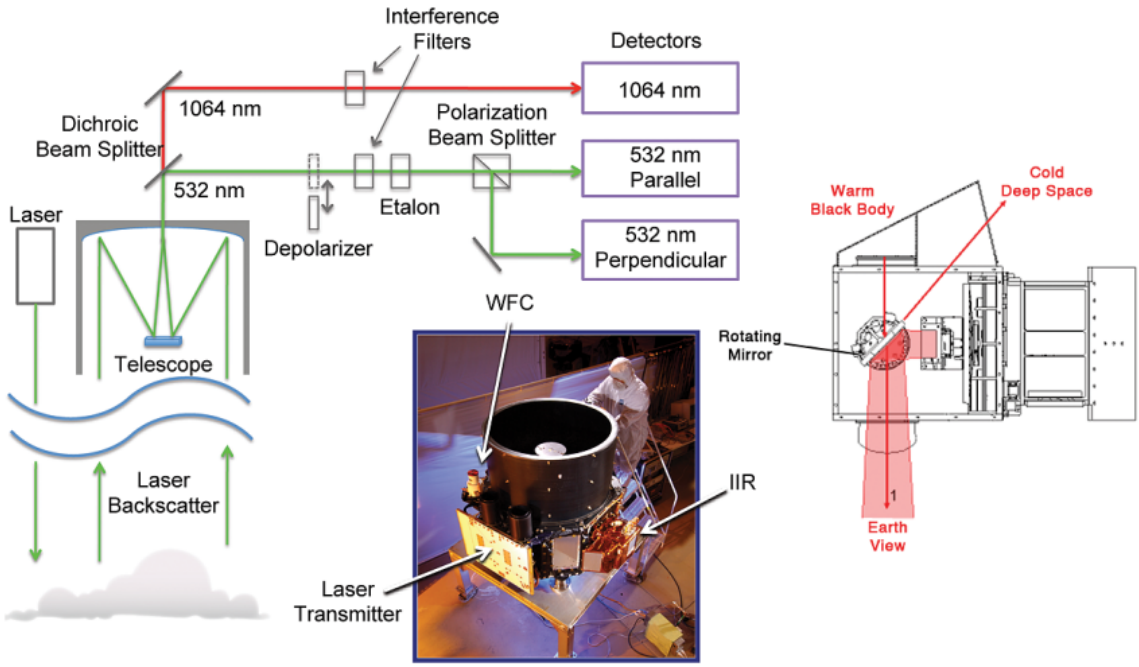

Figure 2.3 : Illustration of the payload onboard CALIPSO. CALIOP has a laser transmitter with two wavelengths (532 nm, 1064 nm) and a receiver with three channels. Source: Fig.1 from Winker et al. (2010).

The CALIOP's laser is a pulsed laser that emits a linearly polarized signal with a near nadir-viewing (at 3° off-nadir). The laser changed slightly in its direction on November 28, 2007, it was moved from 0.3° to 3° off-nadir. This change allows avoiding the specular reflection[5] of horizontal ice crystals which produce retrieval anomalies (Hu et al., 2009).

The laser pulse repetition rate of 20.16 Hz translates into a horizontal sampling resolution of 330 m along the orbit track. The telescope of 1 m diameter and field of view of 130 μrad corresponds to a ground footprint of about 90 m diameter. The vertical resolution of the signal, related to the sampling frequency of the analog signal of 10 MHz, is 15 m. The horizontal and vertical resolutions are degraded by averaging onboard the satellite before being transmitted to Earth. The signal at 532 nm is thus reduced to a vertical resolution of 30 m every 330 m along the orbit track, between 0 and 8.2 km of altitude, and of 60 m every 1 km along the orbit track, between 8.2 and 20 km of altitude. The resolution is coarser above 8.2 km because the atmosphere contains fewer particles and therefore the backscatter signal is weaker. This orbital averaging improves the signal-to-noise ratio. Data below 8.2 km are at full resolution along orbit track (90 m cross track, 330 m along orbit track) which allows observing better the spatial variability of aerosol and clouds which tend to be larger within the atmospheric boundary layer (Winker et al., 2010).

[5]The incident ray gives a single reflected beam, on contrary to the diffuse reflection where the incident ray is redistributed in a great number of directions.

The telescope collects photons at $532\,\mathrm{nm}$ and allows retrieving the **AT**tenuated **B**ackscatter (ATB) at each level of the atmosphere. The $532\,\mathrm{nm}$ ATB is separated into parallel and perpendicular returns by a beamsplitter and then collected in two independent channels. The first channel measures the polarized component which is parallel to the plane of the transmitted signal's polarization. The second channel measures the polarized component which is perpendicular to the plane of the transmitted signal's polarization. The total ATB at $532\,\mathrm{nm}$ is the sum of the two. The ATB profile is the sum of the particle and molecular contributions in $km^{-1}sr^{-1}$ and is given by the following equation:

$$\mathrm{ATB}(z) = [\beta_{mol}(z) + \beta_{part}(z)]\tau^2(z) \tag{2.2}$$

where $\beta_{mol}(z)$ and β_{part} represent the molecular and particle backscatter coefficients respectively [$km^{-1}sr^{-1}$], z the altitude [km] and τ^2 the round trip transmittance [$no\ unit$] from the satellite to the altitude z. ATB profiles are available in the CALIOP L1 data (Winker et al., 2010), an example of an ATB profile is shown in Fig. 2.4 (Guzman et al., 2017).

The nighttime lidar data are of better quality than the daytime lidar data. During the day, CALIPSO's telescope receives backscattered photons emitted by the laser as well as photons from the Sun that are reflected or scattered toward the telescope by the Earth. This can be more pronounced over icy surfaces, which have a high albedo, than oceans. This adds noise to the daytime signal and deteriorates the signal-to-noise ratio. In April 2009, CALIOP switched from its primary to its backup laser as the primary laser began to be subject to low-energy impulses in March 2009, due to a slow pressure leak in the laser's canister. Since September 2016, CALIPSO's backup laser has been experiencing low-energy laser shots due to decreased pressure inside the laser canister too. These low-energy shots primarily occur over the **S**outh **A**tlantic **A**nomaly (SAA) region (Noel et al., 2014). More details are available at: *CALIPSO Low Laser Energy Technical Advisory for Data Users*. A study analyzing the effect of the low-energy laser shots on CALIPSO's observations and cloud properties derived from CALIPSO's observations is currently being conducted by Vincent Noel, Hélène Chepfer, David Winker, and myself. Therefore, data collected before 2008 (laser tilt) and after 2020 (laser low-energy shots) are excluded from my thesis manuscript. Moreover, CALIPSO's observations are limited to a geographical range of $82°$N–$82°$S leaving a part of the polar regions not sounded ($82°$ to $90°$N/S). All CALIPSO's instruments, performances, and history can be found at: *www.eoportal.org/satellite-missions/CALIPSO*

2.2.2 CALIPSO–GOCCP–OPAQ product

GCM-**O**riented **C**ALIPSO **C**loud **P**roduct (GOCCP) has been developed at **L**aboratoire de **M**étéorologie **D**ynamique (LMD) to evaluate clouds representation in climate models (Chepfer et al., 2010). This product uses the ATB profiles from CALIOP–L1 data at $532\,\mathrm{nm}$.

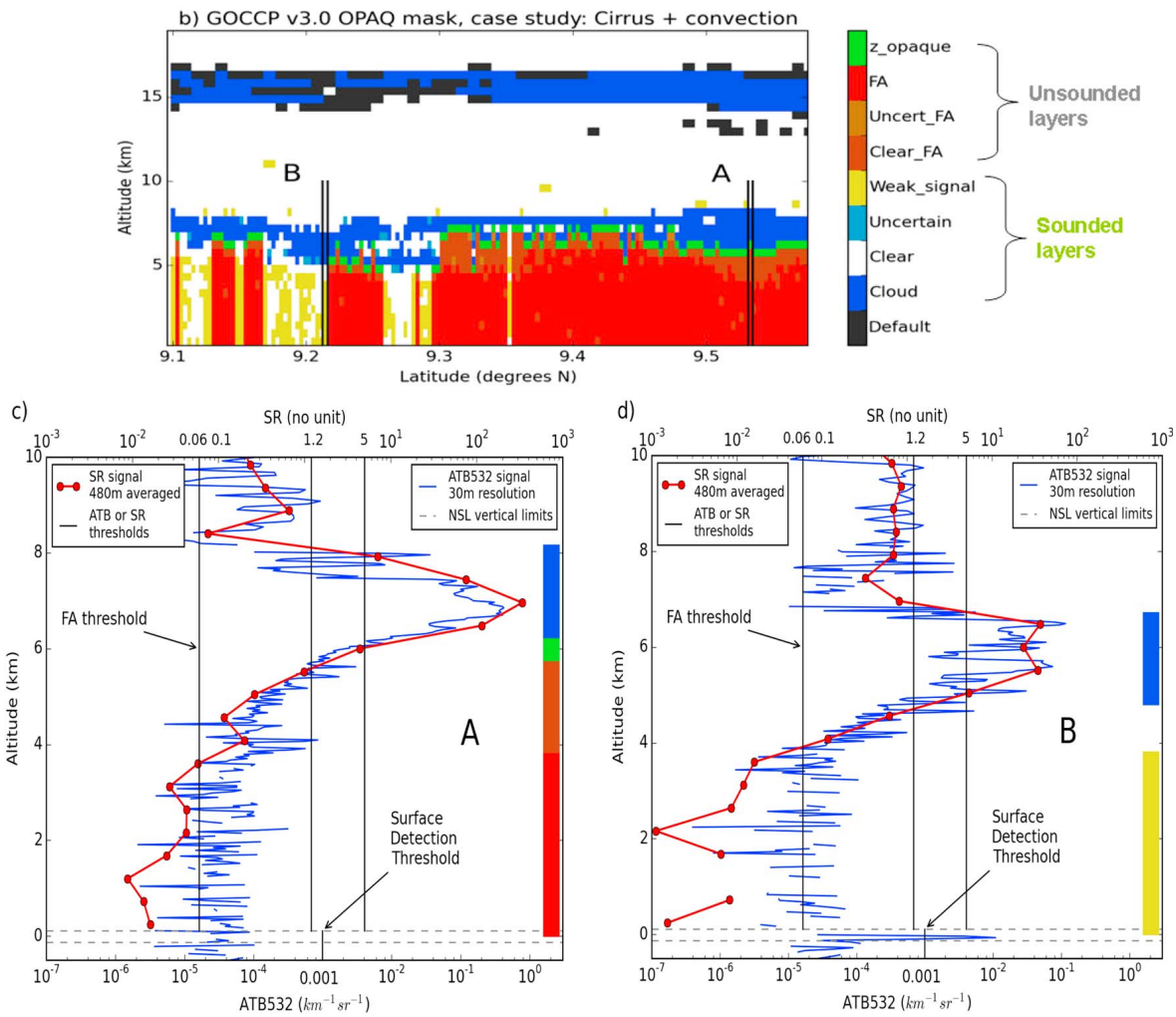

Figure 2.4 : first line) GOCCP v3.0 instant–OPAQ mask; second line) $ATB_{30m}(z)$ in blu and $SR_{480m}(z)$ in red. Profile A represents an Opaque cloud and profile B represents a Thin cloud. Source : Fig. 3 from Guzman et al. (2017).

To detect clouds, the GOCCP algorithm calculates the **S**cattering **R**atio (SR) at each level of the atmosphere which is the ratio between the measured ATB and the ATB_{mol} that would be measured in the presence of molecules only, *i.e.* in absence of clouds and aerosols. In the GOCCP algorithm, $ATB(z)$ profiles are vertically averaged to a vertical resolution of $480\,\mathrm{m}$ ($\mathrm{ATB}_{480m}(z)$) between 0 and $19.2\,\mathrm{km}$, this

averaging improves the signal-to-noise ratio while keeping the full horizontal resolution. This vertical resolution coincides with the resolution of the lidar simulator **C**FMIP **O**bservation **S**imulator **P**ackage (COSP)[6].

The signal that would be measured in the presence of molecules only (ATB_{mol}) is obtained from the **M**olecular **D**ensity (MD) profile, which is derived from temperature and pressure profiles from the **G**oddard **E**arth **O**bserving **S**ystem version **5** **D**ata **A**ssimilation **S**ystem (GEOS5-DAS) reanalyses[7]. The MD profiles are also available in the CALIPSO–L1 data. The $\text{MD}(z)$ profiles are also averaged and interpolated to a vertical resolution of $480\,\text{m}$ ($\text{MD}_{480m}(z)$) between 0 and $19.2\,\text{km}$. The $\text{MD}_{480m}(z)$ profiles are converted to $\text{ATB}_{480m,mol}(z)$ by analyzing and averaging the $\text{MD}_{480m}(z)$ and $\text{ATB}_{480m}(z)$ in the cloud-free portions of the stratosphere, 22–$25\,\text{km}$ and 20–$25\,\text{km}$ during nighttime and daytime respectively, and 28.5–$35\,\text{km}$ in the Southern Hemisphere ($60°$ S–$90°$ S) during winter (Chepfer et al., 2010).

Cloud detection, for each profile at each level of $480\,\text{m}$, is based on i) the value of SR and ii) the value of $\Delta\text{ATB}_{480m}(z)$:

$$\text{SR}(z) = \frac{\text{ATB}_{480m}(z)}{\text{ATB}_{480m,mol}(z)} \tag{2.3}$$

$$\Delta\text{ATB}_{480m}(z) = \text{ATB}_{480m}(z) - \text{ATB}_{480m,mol}(z) \tag{2.4}$$

Each $480\,\text{m}$ vertical level is therefore classified as:

GOCCP diagnostic	**Conditions on SR(z) and ΔATB$_{480m}(z)$**
"Cloud"	$SR(z) > 5$ and $\Delta\text{ATB}_{480m}(z) > 2,5 \times 10^{-3}\ km^{-1}\ sr^{-1}$
"Uncertain"	$1,2 < \text{SR}(z) < 5$
"Clear"	$0,01 < \text{SR}(z) < 1,2$
"Completely attenuated"	$SR(z) < 0,01$

Table 2.1: Classification of each $480\,\text{m}$ vertical level of the atmosphere from CALIOP profiles at $532\,\text{nm}$ using the GOCCP algorithm.

A *"Cloud"* is thus detected for an $\text{SR}(z) > 5$ and $\Delta\text{ATB}_{480m}(z) > 2,5 \times 10^{-3}\ km^{-1}\ sr^{-1}$. The top of the cloud corresponds to the first level where this condition is respected and the base of the cloud corresponds to the last level where this condition is respected. In this case, cloud phase restitution is possible and has been implemented in the GOCCP algorithm by Cesana and Chepfer (2013) but is not used in this thesis as in the infrared, cloud phase (*i.e.* liquid spherical Vs icy non-spherical

[6] A tool for simulating a spaceborne lidar in a **G**eneral **C**irculation **M**odel (GCM) to test the realism of cloud representations in climate models

[7] Reanalyses consist in the assimilation of data from multiple observations by a numerical forecasting model in order to produce consistent data over the entire computing grid.

droplets), that affect scattering which is negligible in the infrared, does not change much the LW radiative fluxes.

The category "*Uncertain*" may contain aerosols or optically thin clouds.

For the category "*Completely attenuated*", the backscattered signal contains only noise due to the attenuation of the signal by optically opaque clouds. The signal is completely attenuated typically by clouds with visible optical thickness > 3 to 5 depending on the cloud microphysical properties (Chepfer et al., 2014). The surface echo is generally not detected in this case and confirms the complete attenuation of the signal (Guzman et al., 2017). If the surface echo is not detected, then all the layers below the lowest detected cloud are classified as "*Completely attenuated*". The level below the lowest detected cloud is called the atmospheric *Full Opacity Altitude* Z_{Opaque} (referred to as Z_{FA} in the rest of this thesis and in Arouf et al. (2022b)) and was implemented in CALIPSO–GOCCP–OPAQ algorithm by Guzman et al. (2017). Figure 2.4c shows ATB profiles at full vertical resolution in blue and the SR signal at $480\,\mathrm{m}$ vertical resolution of GOCCP in red. The ATB signal of the A profile shows no surface echo inside the **N**ear–**S**urface **L**ayer (NSL) delimited by the dotted grey lines around $0\,\mathrm{km}$ **asl!** (**asl!**), which validates its classification as an Opaque cloud. On the contrary, for the B profile in figure 2.4d, a clear surface echo is observed in the NSL layer. This profile is, therefore, classified as a Thin cloud.

The lidar profiles are then classified into three types: *Clear-Sky* profile when no cloud is detected within the entire profile, *Thin* profile when one or several cloud layers and a surface echo are detected within the entire profile, and an *Opaque* profile when one or several cloud layers are detected within the entire profile but no surface echo is detected. All other profile cases that are not in these three profile classifications are classified as *Uncertain*, *e.g.* surface echo not detected and no fully attenuated altitude detected.

In the presence of a thin cloud, its infrared emissivity (ε_{Thin}) can be retrieved from CALIOP observations and has been implemented in the GOCCP algorithm by Vaillant de Guélis et al. (2017a). The apparent two-way *transmittance* through the cloud (τ^2_{app}) can be retrieved from the ratio of the mean scattering ratio ($\tilde{SR}$) of the clear-sky portions above and below the cloud (Garnier et al., 2015):

$$\tau^2_{app} = \frac{\tilde{SR}_{below}}{\tilde{SR}_{above}} \tag{2.5}$$

From this equation, we can retrieve the apparent optical depth (δ_{app}, from Eq. 1.5). One can thereby retrieve the visible optical depth $\delta_{VIS} = \delta_{app}/\eta$, where η is the multiple-scattering factor[8]. Dividing δ_{app} by η is the required correction to account

[8]Coefficient to account for multiple scattering effects. In single-scattering, $\eta = 1$. In CALIOP V4 algorithm, $\eta = f(T)$ (Garnier et al., 2015).

for multiple-scattered photons within the lidar receiver field of view. Indeed, photons emitted by a laser with a wavelength in the *visible* domain have large probabilities to be scattered by cloud particles at small forward angles before being backscattered by lower cloud particles. When the diameter of the lidar footprint is relatively large, the detector is more subject to detecting multiple-scattered photons. More details are given in Garnier et al. (2015) and the references therein. If we neglect scattering in the LW, we can approximate δ_{IR} to be half δ_{VIS} (Garnier et al., 2015). Assuming that scattering by cloud particles is negligible in the LW, we can retrieve ε_{Thin} from equations A.4, 1.5, A.6:

$$\varepsilon_{Thin} = 1 - e^{-\delta^{LW}_{Thin}} \tag{2.6}$$

More details are available in the paper Vaillant de Guélis et al. (2017a) and in the thesis Vaillant de Guélis (2017).

2.2.3 Cloud properties from CALIPSO–GOCCP–OPAQ

From the classification of lidar profiles, three fundamental cloud properties are obtained along CALIPSO's orbit at full $333\,\mathrm{m}$ horizontal resolution:

- Altitude of the opaque cloud temperature ($Z_{T_{Opaque}}$): the average between the Altitude of the highest cloud layer (Z_{Top}) and the Altitude of lidar beam where it is fully attenuated (Z_{FA}), is calculated for each profile classified as *Opaque*.
- Altitude of the thin cloud temperature ($Z_{T_{Thin}}$): the average between Z_{Top} and the Altitude of the lowest cloud layer (Z_{Base}) is calculated for each profile classified as *Thin*.
- Emissivity of thin clouds (ε_{Thin}): derived for each profile classified as *Thin* (Eq. 2.6).

Figure 2.5 (Arouf et al., 2022b) shows the altitudes of interest of an opaque cloud and a thin cloud as seen from a downlooking space lidar beam and from an uplooking ground lidar beam. The figure illustrates the fundamental cloud properties along CALIPSO's orbit. A thin cloud (fig. 2.5a) is characterized by three altitudes: Z_{Top}, Z_{Base}, and $Z_{T_{Thin}}$. In an optically thin cloud, these three altitudes are the same when observed from a spaceborne lidar or a ground-based lidar as the laser beam penetrates through the entire cloud. All the thin cloud layers, that contribute to surface LW CRE, are sounded by the spaceborne lidar.

An opaque cloud (fig. 2.5b) is characterized by three altitudes. When the lidar is ground-based, we measure Z_{Base}, the altitude at which the ground-based lidar beam is fully attenuated (Z_{FA-G}; G for **G**round) and $Z_{T_{Opaque}-G}$, which is the average of the two. The cloud layers above Z_{FA-G} do not contribute to the surface LW fluxes

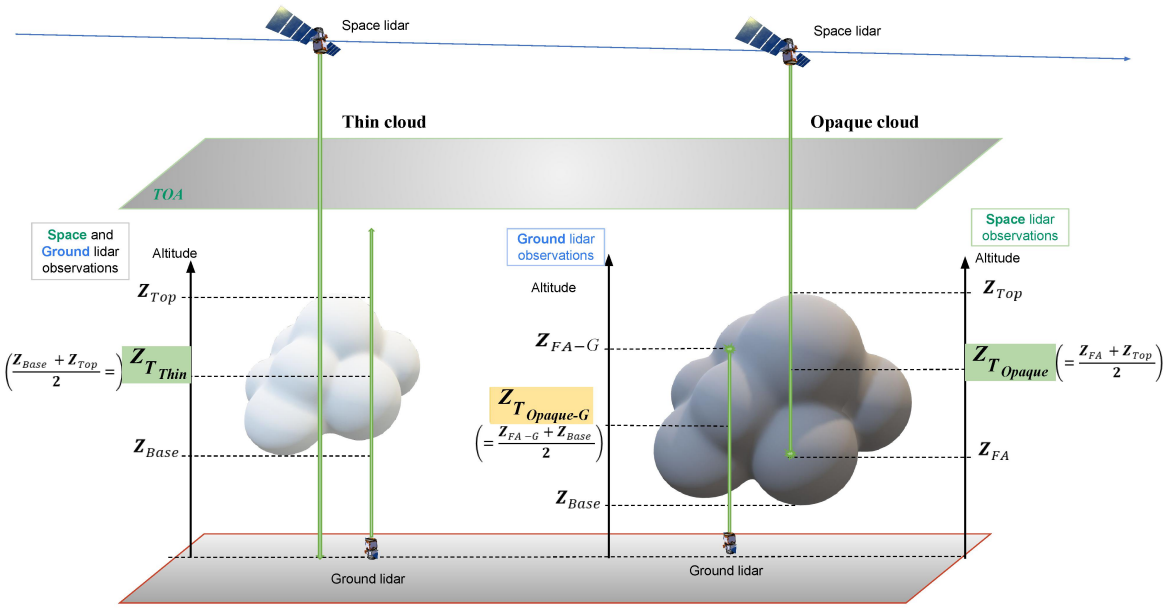

Figure 2.5 : Schematic of cloud altitudes seen from space lidar and from a ground-based lidar in an atmospheric column containing thin cloud only (a) and opaque cloud only (b). The altitudes used to retrieve the surface LW CRE from CALIPSO–GOCCP are reported in green. Fig. 1 from Arouf et al. (2022b).

(Vaillant de Guélis et al., 2017a). For the spaceborne lidar, we measure Z_{Top}, Z_{FA} and the average of the two ($Z_{T_{Opaque}}$). The cloud layers between Z_{FA} and Z_{Base}, which are not visible from a spaceborne lidar, have a contribution to the surface LW fluxes emitted by the cloud. Stated differently, the bottom part of the cloud under Z_{FA}, which is not sounded by a spaceborne lidar, does contribute to the surface LW CRE. This limit will be detailed in chapter 3.

Cloud detection is performed for each profile at each altitude as shown in figure 2.4. To have a gridded product at a global scale, we accumulate the number of profiles for each level in each grid box at a given temporal and spatial resolution (*e.g.* in this thesis, we use gridded products of resolution $1°\times1° -daily$ and $2°\times2° -monthly$). Five gridded cloud properties are used in this thesis. Figure 2.6 (Arouf et al., 2022b) presents the gridded maps of these cloud properties at a $2°\times2° -monthly$ resolution. These five cloud properties are obtained as follows:

- Cover of opaque clouds (C_{Opaque}) : number of *Opaque* profiles divided by the number of *total* profiles in a $2°\times2°$ latitude-longitude grid box for a given month.
- Cover of thin clouds (C_{Thin}) : number of *Thin* profiles divided by the number of *total* profiles in a $2°\times2°$ latitude-longitude grid box for a given month.
- Gridded $Z_{T_{Opaque}}$ is the average value of $Z_{T_{Opaque}}$ for all *Opaque* profiles in a $2°\times2°$ latitude-longitude grid box for a given month.

- Gridded $Z_{T_{Thin}}$ is the average value of $Z_{T_{Thin}}$ for all *Thin* profiles in a $2°\times2°$ latitude-longitude grid box for a given month.
- Gridded ε_{Thin} is the average value of ε_{Thin} for all *Thin* profiles in a $2°\times2°$ latitude-longitude grid box for a given month.

Figure 2.6 (Arouf et al., 2022b) illustrates these five cloud properties averaged over the 2008–2020 period of the monthly $2°\times2°$ gridded CALIPSO–GOCCP–V3.1.2 product. Clouds cover roughly two-thirds of the Earth ($67\,\%$). At a global scale, opaque clouds are dominant ($42\,\%$; fig. 2.6a) over thin clouds ($25\,\%$; fig. 2.6b) in version 3.1.2 of CALIPSO-GOCCP. These numbers are different from CALIPSO–GOCCP–V3.1.1 ($35\,\%$ and $36\,\%$, respectively). CALIPSO–GOCCP–V3.1.1 (Guzman et al., 2017) was only applied to nighttime data, as noise in CALIPSO's signal is lower at night than during the day, the threshold used to detect the surface echo, which influences the identification of opaque clouds, was lower. CALIPSO–GOCCP–V3.1.2 is applied to both night and daytime observations. Opaque cloud distribution is highly driven by large-scale atmospheric circulation, they are numerous in deep convective regions such as the ITCZ, the *warm-pool*, and storm track regions where opaque cloud cover reaches $\sim60\,\%$. Opaque clouds are also numerous in the tropical subsidence region on the west coast of continents, a region known as *stratocumulus region*. In contrast to opaque clouds, thin cloud distribution is more homogeneous at a global scale. Thin cloud cover is a uniform $\sim20-30\,\%$ across the globe except over icy polar regions where it reaches $\sim40\,\%$. Over Greenland and Antarctica ice sheets, the dry cold air favors the formation of thin clouds rather than opaque clouds. In addition, the icy surface beneath the clouds is easier to detect by lidar than the oceans and may allow an echo from the surface to be detected, increasing thin cloud cover.

As expected, the mean altitudes of opaque and thin clouds ($Z_{T_{Opaque}}$, $Z_{T_{Thin}}$, Fig. 2.6c, d) are highly driven by the large scale atmospheric circulation. The cloud altitudes reach maxima ($>9\,\mathrm{km}$) in the deep convective region such as over the *warm-pool*, tropical continents and the ITCZ, while minima ($<3\,\mathrm{km}$) are observed in subsidence tropical regions such as stratocumulus regions. Thin cloud emissivity (Fig. 2.6e) is larger along the ITCZ, over continental regions, and around the Antarctic Peninsula.

To have a consistent time series from year to year, it is recommended to use data collected by CALIOP with a constant looking angle and stable laser power over time.

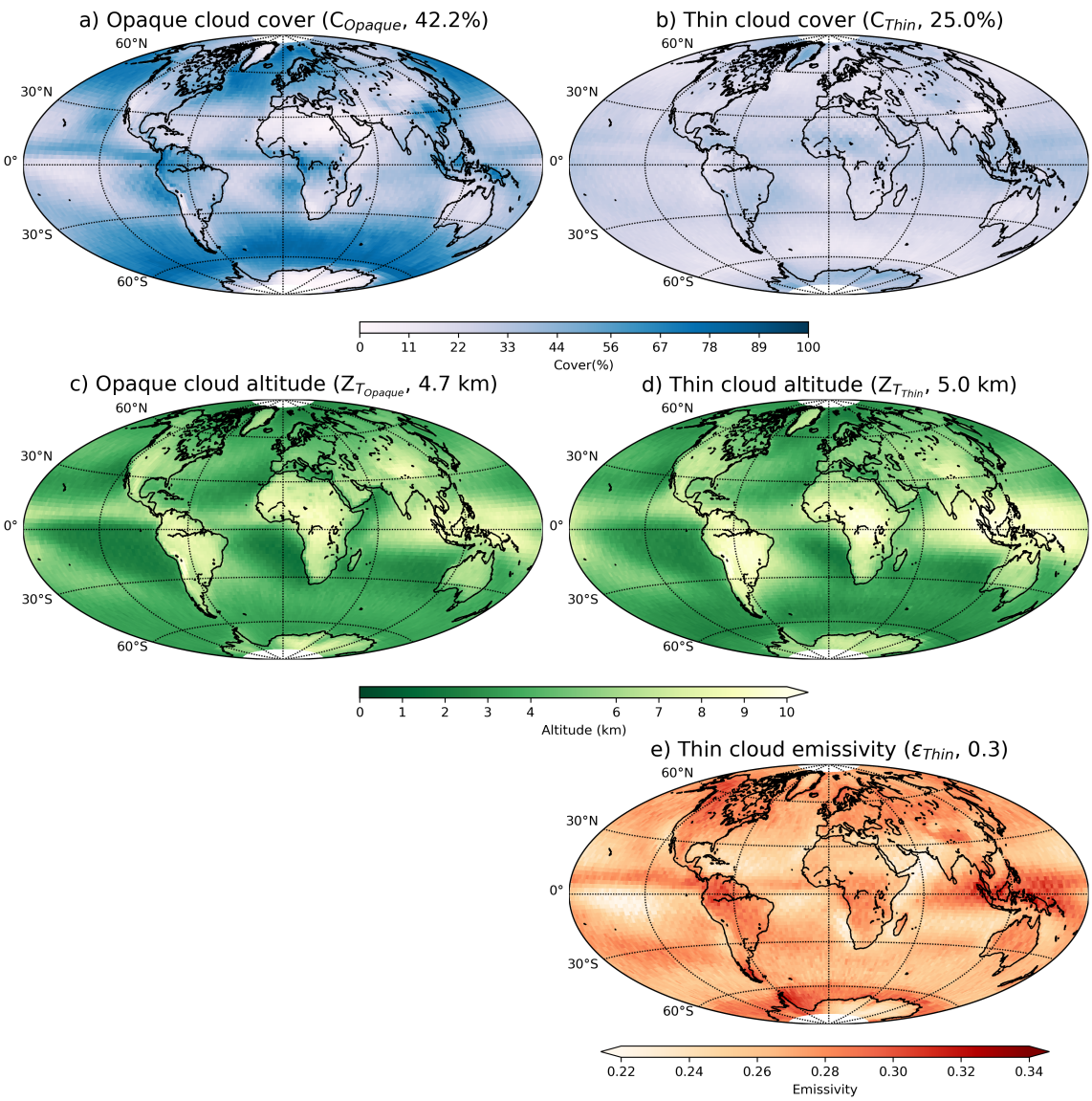

Figure 2.6 : Maps of (a) opaque cloud cover C_{Opaque}, (b) thin cloud cover C_{Thin}, (c) opaque cloud altitude $Z_{T_{Opaque}}$, (d) thin cloud altitude $Z_{T_{Thin}}$, and (e) thin cloud emissivity ε_{Thin}. Global averages are shown in parentheses. Built from CALIPSO–GOCCP–V3.1.2 (Guzman et al., 2017) over $2008 - 2020$ for daytime and nighttime. Fig. 2 from Arouf et al. (2022b).

2.3 Observation of clouds by the Radar CPR/ CloudSat

CloudSat (Stephens et al., 2002) is a joint mission of the United States (NASA, U.S. Air Force) and Canada (Canadian Space Agency). The satellite was launched on April 2006, with CALIPSO. CloudSat, with CALIPSO, study clouds to better characterize the role they play in regulating Earth's climate. Combined together they provide for the first time the global direct vertical structure of clouds. CloudSat carries a **C**loud **P**rofiling **R**adar (CPR) (Sect. 2.3.1). Various cloud properties have been derived from CloudSat observations allowing the retrieval of the corresponding cloud radiative fluxes (Sect. 2.3.2).

2.3.1 Cloud Profiling Radar: CPR

The CPR is a pulsed radar, with a pulse width of $3.3\,\mu\mathrm{sec}$, that emits at a nadir viewing angle ($0.16°$ off-nadir). The CPR operating frequency is $94\,\mathrm{GHz}$ (a wavelength of $3.2\,\mathrm{mm}$). The signal at this wavelength is less attenuated by clouds than lidar and can penetrate through the entire cloud down to the surface, unlike CALIOP lidar. The antenna of $1.85\,\mathrm{m}$ diameter, which measures the power backscattered by clouds, corresponds to a ground footprint of $1.4\,\mathrm{km}$ cross-track and $1.8\,\mathrm{km}$ along-track. The vertical resolution of the data is $500\,\mathrm{m}$, coarser than that of CALIPSO which is $30\,\mathrm{m}$ in the lower layers of the atmosphere ($< 8.2\,\mathrm{km}$).

The general design of CloudSat's CPR is quite simple and benefits from the heritage of many cloud radars already in service on ground-based stations and airborne stations. The chosen frequency of $94\,\mathrm{GHz}$ for the CPR offers the best compromise, allowing to obtain performances within the limits of the satellite resources. This frequency allows observing clouds, multilayered cloud systems but also precipitations, however, some optically thin clouds like cirrus are not detected by this radar. Moreover, the powerful CPR pulse generates a surface clutter echo which tends to partially mask the cloud signal below $1\,\mathrm{km}$ (Arouf et al., 2022b; Marchand et al., 2008).

CloudSat experienced a battery problem in September 2011 and temporarily left the A–train. In mid-July 2012, CloudSat returned to the A–train, but limited its observations to daylight scenes only, when solar radiation powers the satellite's solar panels. Standard CloudSat products and data are distributed by CloudSat Data Processing Center. In my thesis, I will use the surface radiative products, derived from CloudSat, CALIPSO, and MODIS observations, that are defined in the following section.

2.3.2 2B–FLXHR–LIDAR product

The CloudSat $2B-FLXHR-LIDAR\ P1-R04$ product (level-**2** **FL**u**X**es and **H**eating **R**ates release 04–LIDAR (2BFLX)) combines measurements from CloudSat, CALIPSO, and MODIS to generate estimates of LW and SW fluxes and heating rates throughout the atmosphere (L'Ecuyer et al., 2008; Henderson et al., 2013). The product 2BFLX is based on a plane-parallel broadband two-stream, doubling–adding radiative transfer model (Henderson et al., 2013). The algorithm uses vertical profiles deduced from cloud water content, precipitation, and particle size retrieved from satellite observations. It also uses temperature, humidity, pressure, and ozone profiles taken from the **E**uropean **C**entre for **M**edium-**R**ange **W**eather **F**orecasts (ECMWF) reanalyses as input to the radiative transfer model.

A detailed description of the approach used to retrieve the surface fluxes and the associated uncertainties is provided in Matus and L'Ecuyer (2017) and Henderson et al. (2013). The surface LW and SW CRE products are provided for each CloudSat orbit at the $1.8\,\mathrm{km}$ instantaneous footprint scale. The corresponding gridded products, at $2°\times2°$ -$monthly$ and $2.5°\times2.5°$ -$monthly$ resolutions, are provided by Tristan L'Ecuyer (L'Ecuyer et al., 2019). The dataset covers the period from August 2006 to April 2011 before CloudSat experienced its battery anomaly that limited nighttime operations.

Surface fluxes derived from a combination of radar and lidar observations, that provide a detailed cloud vertical structure, in 2BFLX are less sensitive than those derived primarily from passive observations to uncertainties due to undetected multilayer clouds and uncertainties in cloud base height (L'Ecuyer et al., 2019; Hang et al., 2019). However, the 2BFLX product is sensitive to errors due to uncertainties in the radiative transfer simulations and biases introduced by the limited spatial and temporal characteristics of CloudSat and CALIPSO. Sensitivity studies suggest that the uncertainties in $2.5°\times2.5°$ -$monthly$ mean surface LW fluxes derived from 2BFLX are $\pm11\,\mathrm{Wm^{-2}}$, mainly due to errors in the specification of the lower tropospheric temperature and humidity (Haynes et al., 2013) and uncertainty in the cloud base height (Henderson et al., 2013). Uncertainties in SW fluxes are smaller than that of LW fluxes, and are mainly due to cloud microphysical properties (Henderson et al., 2013, uncertainties of $\pm5.5\,\mathrm{Wm^{-2}}$).

2.4 Observation of radiation from CERES and MODIS radiometers

Aqua is an international Earth science satellite mission. The Aqua satellite was launched in May 2002, the first satellite on the A-Train, and carried six different

Earth-observing instruments, which are all passive remote sensing instruments. Aqua collects information on water in the Earth/atmosphere system and the water cycle, hence the name Aqua, and many other observations of the climate system. Of the six instruments on board this satellite, two will be of particular interest in this thesis: **C**louds and **E**arth's **R**adiant **E**nergy **S**ystems (CERES) (Sect. 2.4.1) and **MOD**erate-resolution **I**maging **S**pectroradiometer (MODIS) (Sect. 2.4.2). The two same instruments are also on board the Terra satellite, which passes over the equator in the morning, while Aqua passes over the equator in the afternoon. This configuration allows observing the entire surface of the Earth every one to two days. Terra was launched on December 1999. Similar instruments are also on board some geostationary satellites (GEO) which provide a better temporal resolution (Doelling et al., 2013). The GEO instruments are calibrated against tho polar orbiting instruments to maintain temporal consistency.

2.4.1 Broadband radiometer: CERES

CERES (Loeb et al., 2005) is a broadband radiometer that has been retrieving outgoing fluxes at the TOA for over two decades. It aims to obtain radiative fluxes from the top to the bottom of the atmosphere. It measures both solar radiation and radiation emitted from the Earth in three spectral bands: $0.3-5\,\mu\mathrm{m}$ (SW), $0.3-200\,\mu\mathrm{m}$ (total), and $8-12\,\mu\mathrm{m}$ (atmospheric window) (Loeb et al., 2001). The Thermal radiation, $5-200\,\mu\mathrm{m}$, is deduced from the difference between the first two spectral bands. Each CERES instrument is a scanning radiometer with a narrow field of view, whose nadir footprint is $20\,\mathrm{km}$ (for Terra and Aqua), and provides ∼daily global coverage by scanning from limb-to-limb perpendicular to the orbit-track, resulting in a swath of $200\,\mathrm{km}$ cross-track.

CERES observations are generally combined with observations from imagers, either polar (*i.e.* MODIS) or geostationary, which document the scene observed by CERES. The imagers are used to infer cloud, aerosol, and surface characteristics (Minnis et al., 2011; Sun-Mack et al., 2018). Geostationary observations are used to infer cloud fluxes and properties between the observation times of CERES and polar imagers (e.g. MODIS) in order to improve the diurnal cycle representation (Doelling et al., 2013). The geostationary observations are tied with those of CERES and polar imagers to ensure uniform fluxes and cloud properties across the different satellite datasets (Minnis et al., 2011; Rutan et al., 2015; Kato et al., 2018).

2.4.2 Moderate Resolution Imaging Spectroradiometer: MODIS

MODIS instrument provides measurements of radiances at 36 wavelengths, including infrared and visible bands, ranging from 0.4 to $14.4\,\mu\mathrm{m}$. The spectral regions covered are visible (VIS), Near Infrared (NIR), Shortwave/Midwave Infrared (SWIR/MWIR) and Longwave Infrared (LWIR). Two spectral bands are imaged at a resolution of $250\,\mathrm{m}$ at nadir, five bands at $500\,\mathrm{m}$ and the remaining 29 bands at $1\,\mathrm{km}$. MODIS provides ∼daily global coverage by scanning from $\pm 55°$ perpendicular to the orbit-track, resulting in a swath of $2330\,\mathrm{km}$ cross-track and $10\,\mathrm{km}$ along-track at nadir.

Cloud detection is based on the contrast (*i.e.*, cloud compared to background surface) in a given area/pixel (*e.g.* King et al., 2003; Frey et al., 2008). For instance, in the IR, MODIS measures brightness temperatures[9] and usually clouds are colder than the surface. In the VIS, clouds are more reflective than the surface in most cases. However, over icy surfaces, the distinction between cloud and surface is less straightforward since their brightness temperatures can be close and both the cloud and the icy surface have large reflectivity of sunlight. Therefore, MODIS has more bias in cloud detection in the polar regions (Stubenrauch et al., 2013; Kay and Gettelman, 2009), especially during the polar night when the VIS channels are not used. Cloud detection by MODIS is more reliable over oceans than over icy surfaces and lands because the contrast between clouds and the ocean background surfaces is more obvious. MODIS is also more sensitive to the first cloud layer from the TOA. Therefore, the detection of multilayered clouds (*e.g.* low cloud below a high thin cirrus cloud) is limited.

2.4.3 CERES-CCCM product

The CERES-CCCM (Kato et al., 2011, 2019) product is derived from the combination of passive spaceborne instruments (that provide a large field of view) with active spaceborne instruments, that document the vertical structure of the atmosphere along orbit-track of the A-Train constellation. It combines observations of fluxes from CERES radiometer at TOA with observations of the atmospheric vertical structure from CloudSat ($1.4\,\mathrm{km}$ cross-track, $1.8\,\mathrm{km}$ along-track.), CALIPSO ($90\,\mathrm{m}$ cross-track, $330\,\mathrm{m}$ along orbit-track), and observations from MODIS (pixels of $500\,\mathrm{m}$ to $1\,\mathrm{km}$) to document CERES **S**ingle **S**canner **F**ootprint (SSF) scenes of about $20\,\mathrm{km}$ in diameter. An illustration of the surface footprints of the four instruments is shown in figure 2.7 (Kato et al., 2011).

[9]Corresponds to the temperature at which a black body has the same spectral luminance as a grey body.

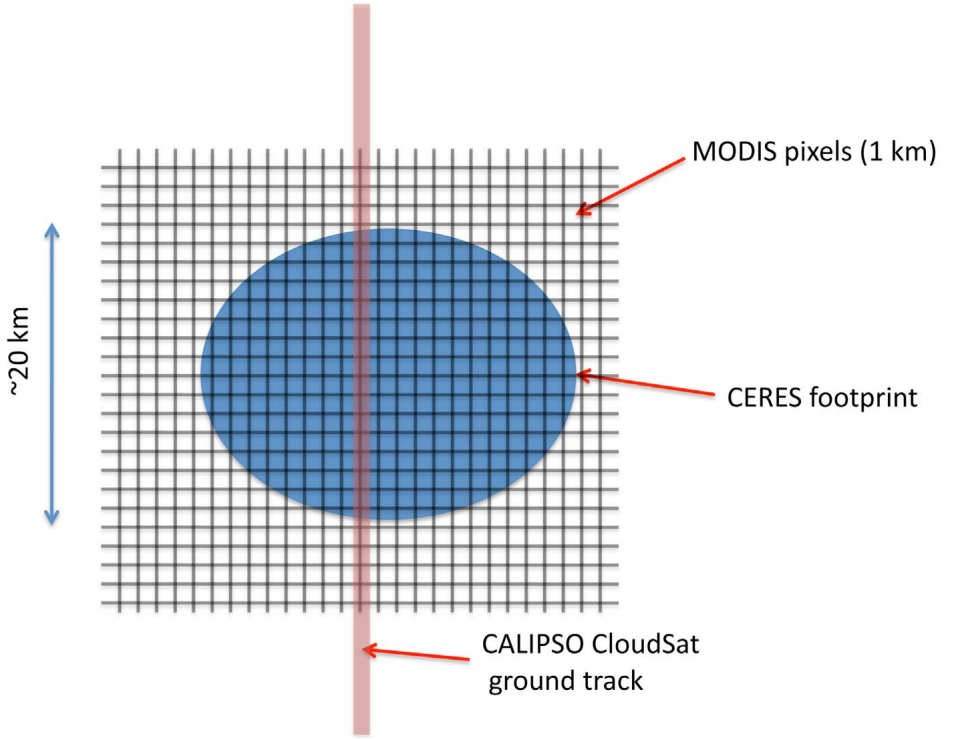

Figure 2.7 : Schematic of a CERES **S**ingle **S**canner **F**ootprint (SSF) containing the CALIPSO and CloudSat ground track as well as MODIS 1 km meshgrid. Fig. 1 from Kato et al. (2011).

This product is part of **C**ALIPSO, **C**loudSat, **C**ERES, and **M**ODIS Merged Product (CCCM) (or C3M; Kato et al., 2010) and extends from July 2006 through April 2011 before the anomaly of CloudSat's battery. It uses radiative transfer calculations to retrieve the surface LW fluxes in all-sky and clear-sky conditions at SSF resolution. Thereby, it retrieves the surface LW CRE at SSF footprint. In this thesis, I use the RelB1 version. More details are given in Kato et al. (2011), for merging the cloud properties, and in (Ham et al., 2017; Kato et al., 2019), for the approach to retrieve the radiative fluxes.

2.4.4 CERES-EBAF product

CERES–**E**nergy **B**alanced and **F**illed (EBAF)–Surface Edition 4.1 product (Kato et al., 2013, 2018) is a *monthly*-$1^\circ \times 1^\circ$ gridded dataset extending from 2000 to present day, providing averages of surface clear-sky and all-sky upward and downward SW and LW fluxes. This product is based on *hourly*-CERES–Synoptic product (SYN1deg-Day) (Rutan et al., 2015) which converts CERES TOA radiance measurements into instantaneous SW and LW surface fluxes using radiative transfer model calculations. Cloud properties are derived from MODIS and GEOs radiometers, which enhance temporal interpolation between the overpass of the polar-orbiting instruments (Doelling et al., 2013). Temperature and humidity profiles are from **G**oddard **E**arth **O**bserving **S**ystem (GEOS) (Rienecker et al., 2008). The CERES-SYN hourly

fluxes are then adjusted and temporally interpolated, in the CERES-EBAF product. A detailed description of the approach used to retrieve this product is provided in Kato et al. (2018).

Note that only MODIS-derived cloud properties are used for surface irradiance computation over polar regions between $60°$ to poles because GEO data are only available between $60°$ S et $60°$ N. As CERES–EBAF product is based on passive instruments only, it is less reliable over ice surfaces and continents than over oceans. It is also less reliable in the presence of multi-layered clouds where the lower cloud may be obscured by the overlying cloud (p. ex. Liu et al., 2010; Stubenrauch et al., 2013).

2.5 Other observations

2.5.1 Observation from ground stations

Since the surface CRE retrieval from spaceborne observations is not direct, we will also use surface LW CRE derived from ground measurements collected directly by ground stations. For this aim, we selected three sites located in different regions. At these three ground sites, measurements of the surface flux in all-sky conditions are made using two pyrgeometers [10] Kipp and Zonen CM22, which measures in the spectral range of $4.5 - 40\,\mu\mathrm{m}$.

Summit, station over Greenland

The first site is located over the Greenland ice sheet in the Arctic. Here, surface CRE may influence Greenland ice sheet melt (van Tricht et al., 2016; Hofer et al., 2017; Shupe et al., 2013). *Summit* station (Shupe et al., 2013; Gallagher et al., 2018) is located at the top of the Greenland ice cap ($72.6°$ N–$38.5°$ W) with an altitude of $3250\,\mathrm{m}$ above **m**ean **s**ea **l**evel (m.s.l.). *Summit* is unique because it is the only location where we have enough observations to make a robust assessment of surface LW CRE over Greenland (Lacour et al., 2018) as it is well maintained over time. Here, the clear-sky flux is calculated using a radiative transfer algorithm with measurements of temperature and moisture profiles, while the all-sky flux is measured directly using a pair of broadband pyrgeometers (Shupe and Intrieri, 2004; Intrieri et al., 2002).

[10] Infrared precision radiometer, designed for unidirectional operation, it measures the incoming and outgoing infrared fluxes and thus allows to estimate the net fluxes in the LW.

SIRTA, station over France

The second site is located in the mid-latitudes regions over land. This site (Haeffelin et al., 2005; Chiriaco et al., 2018) is located in France ($48.7°$ N–$2.2°$ E) at an elevation of $156\,\mathrm{m}$ above m.s.l.. The data are part of the **B**aseline **S**urface **R**adiation **N**etwork (BSRN) (Ohmura et al., 1998; Driemel et al., 2018). Over this station, the clear-sky flux is derived from a parameterization made from the measurements of surface humidity, the integrated moisture content on the atmospheric column, and the air temperature at $2\,\mathrm{m}$.Details are given in Dupont and Haeffelin (2008). The all-sky fluxes are measured directly using a pair of upward- and downward-looking pyrgeometers.

KWA, station over the tropics

The third site is located in the tropical belt, in the northern Pacific Ocean ($8.72°$ N–$167.73°$ E) with an elevation of $10\,\mathrm{m}$. In the tropics, clouds influence global climate and heat transport (Loeb et al., 2016). Here, the surface LW CRE is small, because much of the downwelling LW radiation reaching the surface originates from fluxes emitted by the moist atmospheric layers near the surface (Prata, 1996). This station of **Kwa**jalein (KWA) (Roesch et al., 2011), is also part of the BSRN.

2.5.2 Observation of sea ice: NSIDC

The Arctic is experiencing the most rapid and obvious climate change on our planet (Serreze and Barry, 2011) resulting in an increase in surface temperature and a decrease in sea ice surface (Meier et al., 2014). We use the **N**ational **S**now and **I**ce **D**ata **C**enter (NSIDC) data to study the impact of sea ice on clouds and on the surface LW CRE. Sea ice observations, at a *daily* 25 km horizontal resolution, are from passive microwave imagers. They are provided by the NSIDC's Near Real-Time SSM/I EASE-Grid Daily Global Sea Ice Concentration and Snow Extent data product (Nolin et al., 1998). Each CALIPSO-L1 footprint along each orbit receives a *daily* sea ice concentration value, which is assigned from the imager's sea ice concentration value at the latitude/longitude closest to that CALIPSO-L1 footprint. Values of the sea ice concentration are implemented in the GOCCP products at instantaneous and gridded monthly and daily scales. We use sea ice concentration observations at a *daily* $1° \times 1°$ gridded and on a local instantaneous scale in the GOCCP products. These data have uncertainties ranging from $\pm 5\%$ in winter to $\pm 15\%$ in summer (Agnew and Howell, 2003). We also use sea ice extent at a monthly resolution between 1979 and 2021 from the NSIDC center and available at doi.org/10.7265/N5K072F8 (Fetterer et al., 2017).

2.6 Radiative transfer code: GAME

We use the radiative transfer code **G**lobal **A**tmospheric **M**ode**l** (GAME) (Dubuisson et al., 2004) to simulate infrared fluxes at the Earth's surface in the presence and absence of clouds.

This radiative transfer code computes the radiative fluxes at 50 levels of the atmosphere with a vertical resolution of $1\,\mathrm{km}$ between $0\,\mathrm{km}$–$25\,\mathrm{km}$ of altitude, of $2.5\,\mathrm{km}$ between $25\,\mathrm{km}$–$50\,\mathrm{km}$ of altitude, and a coarser resolution of $5\,\mathrm{km}$ between $50\,\mathrm{km}$–$120\,\mathrm{km}$ of altitude. It simulates the upward and downward fluxes at each level of the atmosphere in the solar and infrared spectra. The code has a fixed spectral resolution of $10\,\mathrm{cm}^{-1}$ that is a relatively coarse resolution for a radiative transfer code, which can be for instance $0.01\,\mathrm{cm}^{-1}$ for other radiative transfer codes that need to solve ~ 1000 **R**adiative **T**ransfer **E**quation (RTE) over a spectral interval of $10\,\mathrm{cm}^{-1}$ (Dubuisson et al., 2004), therefore, GAME is a simplified radiative transfer code used for satellite data applications.

In GAME, the **DiS**crete **O**rdinates **R**adiative **T**ransfer (DISORT) method (Stamnes et al., 1988; Nakajima and Tanaka, 1988) is used to solve the RTE. This method takes into account the scattering processes and the interactions between scattering and absorption. The RTE is solved at each spectral band ($10\,\mathrm{cm}^{-1}$), assuming an atmosphere stratified into plane-parallel layers and bounded at the base and top. Molecules and clouds are uniformly distributed in each layer and each layer is considered plane-parallel infinite.

In this thesis, the fluxes are spectrally integrated between 5 and $200\,\mu\mathrm{m}$ (2000-$200\,\mathrm{cm}^{-1}$), consistent with CERES measurements. Atmospheric gases with relatively stable atmospheric concentrations in time on the global scale are fixed in GAME (*e.g.* CO2, CH4...). On the other hand, gases with variable concentrations, including water vapor and ozone, are taken as inputs in GAME. This radiative transfer code has been used and described in the thesis of Vaillant de Guélis (2017) to simulate LW fluxes at the TOA.

To simulate the radiative fluxes with GAME, we specify various surface temperatures and atmospheric profiles of humidity and temperature, pressure, and ozone. Surface temperatures are from **ERA**–**I**nterim (ERA-I) reanalyses (Dee et al., 2011). The atmospheric profiles of humidity and temperature are based on ERA-I reanalyses between $0-45\,\mathrm{km}$ of altitude and based on **A**ir **F**orce **R**esearch **L**aboratory (AFRL) (McClatchey et al., 1972) between $45-120\,\mathrm{km}$ of altitude. Standard ozone and pressure profiles are based on AFRL between $0-120\,\mathrm{km}$ of altitude.

ERA-I reanalyses are provided by **E**uropean **C**entre for **M**edium-**R**ange **W**eather **F**orecasts (ECMWF). The ERA-I product used in this thesis has a spatial resolution of $0.75°\times0.75°$ and a temporal resolution of one *month* and provides data between

$0-45\,\mathrm{km}$ of altitude. We also use sub-daily (6–*hourly*) temporal resolutions of temperature/humidity profiles from ERA-I for a sensitivity study. AFRL provides average profiles of some atmospheric variables as a function of season and latitude band.

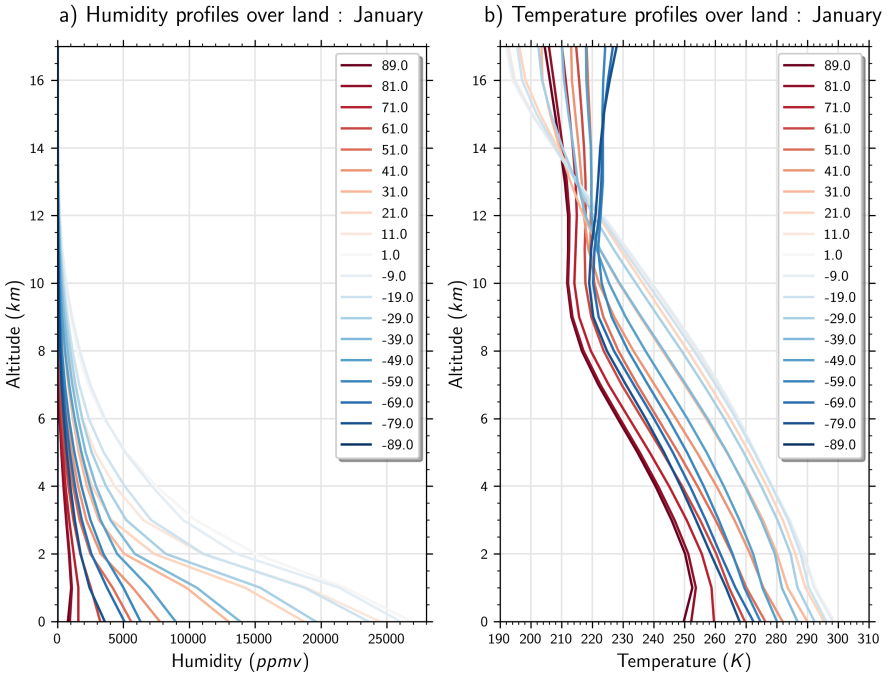

Figure 2.8 : Example of ERA–I atmospheric profiles taken over continents in January and averaged over latitude bands of $10°$.

Examples of averaged humidity and temperature profiles over the continents for each $10°$ in latitude band for January, from ERA-I are shown in figure 2.8. We observe a large latitudinal variability in the humidity within the first $2\,\mathrm{km}$ of the atmosphere, with an increase in the humidity from the polar regions ($\sim$2000 ppmv) to the tropics where large values reach $\sim$20 000 ppmv.The temperature profiles in the first $2\,\mathrm{km}$ of the atmosphere is larger in the tropics ($\sim$290 K) than the polar regions ($\sim$260 K). In the polar region, sometimes we can observe a temperature inversion in the boundary layer (*e.g.* latitudes $81°$ N to $89°$ N).

The radiative transfer simulations are performed over oceans and continents for each month, each $2°$ latitude band, and each $100\,\mathrm{m}$ surface elevation. We perform clear-sky simulations using the atmospheric profiles and surface temperature defined before. We perform all-sky simulations using the same atmospheric profiles and surface temperature plus clouds by choosing: the type of particle (spherical or non-spherical), the effective size index of the particles, the optical thickness of the cloud, the altitude and the vertical extent of the cloud. In the LW, the cloud phase (*i.e.* liquid or ice particle) has a small impact on the radiative fluxes because the scattering, which is impacted by the shape of the diffusers (spherical liquid droplet or non-spherical ice crystal) is a second order term in the infrared.

2.7 Data used in this thesis

Table 2.2 summarizes instruments and datasets used in this thesis with their corresponding temporal and spatial resolutions as well as their time period extension.

Instruments	Resolutions	Period
CALIOP/CALIPSO (Winker et al., 2010)	90 m cross-track; 330 m along orbit-track; 30 m vertical resolution between $0-8.2$ km	06/2006 to present
CPR/CloudSat (Stephens et al., 2002)	1.4 km cross-track; 1.8 km along orbit-track; 500 m vertical resolution	04/2006 to present
CERES/Aqua (Wielicki et al., 1996)	20 km SSF; 200 km swath cross orbit-track	04/2002 to present
MODIS/Aqua (King et al., 2003; Frey et al., 2008)	250 m–1 km pixel; 2330 km swath cross orbit-track	04/2002 to present
Passive microwave imagers/SSM/I	25 km×25 km horizontal resolution	11/1978 to present
Derived products	**Resolutions**	**Period used**
GOCCP/CALIOP Cloud properties (Chepfer et al., 2010; Guzman et al., 2017; Vaillant de Guélis et al., 2017a)	**Instant**: 90 m cross-track; 330 m along orbit-track; 480 m vertical resolution between $0-19.2$ km **Gridded**: *daily*–$1° \times 1°$; *monthly*–$2° \times 2°$	$2008-2020$
2BFLX/CALIOP-CPR-MODIS Surface LW and SW fluxes (L'Ecuyer et al., 2008, 2019)	**Instant**: 5 km surface resolution **Gridded**: *monthly*–$2° \times 2°$; *monthly*–$2.5° \times 2.5°$	$2007-2011$
CCCM/CERES-CALIOP-CPR-MODIS Surface LW fluxes (Kato et al., 2010, 2011)	**Instant**: 20 km surface resolution	$2008-2010$
CERES-EBAF/CERES-MODIS from *Aqua+Terra+GEO* ***Surface LW fluxes*** (Kato et al., 2013, 2018)	**Gridded**: *monthly*–$1° \times 1°$	$2008-2020$
NSDIC/SSM/I Sea ice concentration (Nolin et al., 1998)	**Gridded**: *daily*–$1° \times 1°$	$2008-2020$
Ground stations	**Resolutions**	**Period used**
Summit/Greenland Surface LW fluxes (Shupe et al., 2013)	30 min around CALIPSO overpass	$2011-2015$
SIRTA/France Surface LW fluxes (Haeffelin et al., 2005)	30 min around CALIPSO overpass	$2008-2015$
KWA/Tropics Surface LW fluxes (Roesch et al., 2011)	30 min around CALIPSO overpass	$2008-2015$
Reanalyses	**Resolutions**	**Period used**
ERA-Interim Humidity and temperature profiles (Dee et al., 2011)	*monthly*–$0.75° \times 0.75°$ 6*–hourly*–$0.75° \times 0.75°$	$1989-2017$

Table 2.2: Datasets used in this thesis with their characteristics

Chapter 3

Publication I: *The surface longwave cloud radiative effect derived from space lidar observations*

Paper published July 1st, 2022 in *Atmospheric Measurement Techniques*.

How to cite: **Arouf, A.**, Chepfer, H., Vaillant de Guélis, T., Chiriaco, M., Shupe, M. D., Guzman, R., Feofilov, A., Raberanto, P., L'Ecuyer, T. S., Kato, S., and Gallagher, M. R. (2022). "The surface longwave cloud radiative effect derived from space lidar observations". In: *Atmospheric Measurement Techniques* 15, p. 3893–3923. DOI : 10.5194/amt-15-3893-2022

Introduction of Publication I

Cloud vertical distribution is more sensitive to climate warming than the horizontal distribution (Chepfer et al., 2014). Studies showed that to detect cloud changes due to anthropogenic forcing, observation time-extend needs to be longer than 30 years. Natural variability is always present, in short and long time series. It is however easier to make non-natural forcings emerge from the natural variability (*i.e.* El-Niño, **N**orth **A**tlantic **O**scillation (NAO), volcanic eruptions ...) when the time series are longer. As the surface **L**ong**W**ave (LW) **C**loud **R**adiative **E**ffect (CRE) is highly sensitive to cloud vertical distribution, we need observations that document cloud vertical distribution to observe a response of the surface LW CRE to external forcing.

Spaceborne radiometers have been observing clouds at a global scale for more than two decades (*e.g.* Loeb et al., 2018; Stubenrauch et al., 2013). However, radiometers are limited in documenting the vertical distribution of clouds and they are highly sensitive to the surface type. Indeed, cloud top height retrieved from radiometers is based on models and a number of assumptions, and clouds are detected better over oceans than over bright surfaces (Kay and Gettelman, 2009). Therefore, they are limited in observing cloud changes due to natural or non-natural forcing.

Spaceborne lidar and radar can measure cloud vertical distribution and are poorly sensitive to surface type, unlike passive instruments. They can observe cloud vertical distribution over all types of surfaces including deserts and snow-covered surfaces. **C**loud–**A**erosol **L**idar and **I**nfrared **P**athfinder **S**atellite **O**bservations (CALIPSO) have been vertically sampling the atmosphere since 2006 over all types of surfaces. CALIPSO time record ($\sim$ 16 years) may not be long enough to document cloud change due to anthropogenic forcing. Combining CALIPSO observations with the upcoming lidar satellite missions, such as EarthCARE (Illingworth et al., 2014) and **A**tmosphere **O**bserving **S**ystem (AOS) (aos.gsfc.nasa.gov) would help to document better cloud response to anthropogenic forcing. However, the reconciliation between these three lidars is hard given the time lag between the missions and the differences in wavelength and orbit inclination. Nevertheless, cloud change due to natural variability, such as cloud response to El Niño (Vaillant de Guélis et al., 2017b) or to sea ice variability (Morrison et al., 2018), CALIPSO's record can be sufficiently appropriate. Therefore, to document surface LW CRE change due to natural variability, in this thesis sea ice change, CALIPSO time record is suitable enough to quantify the surface LW CRE change due to sea ice cover change (Chap. 4).

Chapter 3 describes the retrieval of the surface LWCRE–LIDAR Edition 1 product over 13 years ($2008 - 2020$) and its evaluations against independent retrievals. The algorithm is based on theoretical parameterizations derived from radiative transfer simulations (Dubuisson et al., 2004) that involve different humidity and temperature profiles from ERA-Interim reanalysis (Dee et al., 2011) and different

cloud configurations. Then the algorithm relies on five cloud properties derived from CALIPSO–GOCCP product. The surface LW CRE is retrieved at a $2^\circ \times 2^\circ$ gridded scale and on the local instantaneous scale (90 m cross track, 330 m along orbit track) with each lidar profile containing either a value of surface LW Opaque CRE or a value of surface LW Thin CRE or zero (for clear sky profiles). Comparisons to the 2BFLX product (which is retrieved from combined observations of MODIS, CloudSat, and CALIPSO) at *monthly*–$2^\circ \times 2^\circ$, showed a good statistical evaluation. Quantitatively, uncertainties reaching $\sim 13\,\mathrm{W\ m^{-2}}$ can be induced by the lower tropospheric temperature and humidity representations and cloud base height. Comparison to CERES–CCCM product (which is retrieved from combined observations of CERES, MODIS, CloudSat, and CALIPSO) and to 2BFLX product at footprint scales ($20\,\mathrm{km}$ and $5\,\mathrm{km}$ respectively), showed a good statistical evaluation (correlations of 0.84 and 0.71, RMSE of $11.9\,\mathrm{W\ m^{-2}}$ and $17.0\,\mathrm{W\ m^{-2}}$, respectively). Comparison to ground stations showed that the surface LWCRE–LIDAR is biased somehow low but has a good seasonal cycle representation. Comparison to CERES–EBAF product (which is based on passive instruments only; Appendix B) shows that the LWCRE–LIDAR and 2BFLX are more accurate over polar icy surfaces than CERES–EBAF, especially in retrieving the seasonal cycle of the surface LW CRE (in comparison to ground stations which are the reference).

The uncertainties of this new LWCRE–LIDAR are found in other space-derived products (*e.g.* Henderson et al., 2013), but the added value of this new retrieval is the long 13 years time series that it provides ($2008-2020$). Moreover, LWCRE–LIDAR is accurate over polar regions since it is derived from CALIPSO, unlike CERES–EBAF.

Atmos. Meas. Tech., 15, 3893–3923, 2022
https://doi.org/10.5194/amt-15-3893-2022

Atmospheric Measurement Techniques
Open Access
EGU

The surface longwave cloud radiative effect derived from space lidar observations

Assia Arouf[1], Hélène Chepfer[1], Thibault Vaillant de Guélis[2,3], Marjolaine Chiriaco[4], Matthew D. Shupe[5,6], Rodrigo Guzman[1], Artem Feofilov[1], Patrick Raberanto[7], Tristan S. L'Ecuyer[8], Seiji Kato[3], and Michael R. Gallagher[5,6]

[1]LMD/IPSL, Sorbonne Université, École Polytechnique, Institut Polytechnique de Paris, ENS, PSL Université, CNRS, Palaiseau, France
[2]Science Systems and Applications, Inc., Hampton, Virginia, USA
[3]NASA Langley Research Center, Hampton, Virginia, USA
[4]LATMOS/IPSL, UVSQ, Université Paris-Saclay, Sorbonne Université, CNRS, 78280, Guyancourt, France
[5]Cooperative Institute for Research in Environmental Sciences, University of Colorado, Boulder, Colorado, USA
[6]NOAA Physical Sciences Laboratory, Boulder, Colorado, USA
[7]LMD/IPSL, CNRS, Sorbonne Université, École Polytechnique, Institut Polytechnique de Paris, ENS, PSL Université, Palaiseau, France
[8]Department of Atmospheric and Oceanic Sciences, University of Wisconsin-Madison, Madison, USA

Correspondence: Assia Arouf (assia.arouf@lmd.ipsl.fr)

Received: 20 November 2021 – Discussion started: 23 December 2021
Revised: 5 April 2022 – Accepted: 30 May 2022 – Published: 1 July 2022

Abstract. Clouds warm the surface in the longwave (LW), and this warming effect can be quantified through the surface LW cloud radiative effect (CRE). The global surface LW CRE has been estimated over more than 2 decades using space-based radiometers (2000–2021) and over the 5-year period ending in 2011 using the combination of radar, lidar and space-based radiometers. Previous work comparing these two types of retrievals has shown that the radiometer-based cloud amount has some bias over icy surfaces. Here we propose new estimates of the global surface LW CRE from space-based lidar observations over the 2008–2020 time period. We show from 1D atmospheric column radiative transfer calculations that surface LW CRE linearly decreases with increasing cloud altitude. These computations allow us to establish simple parameterizations between surface LW CRE and five cloud properties that are well observed by the Cloud-Aerosol Lidar and Infrared Pathfinder Satellite Observations (CALIPSO) space-based lidar: opaque cloud cover and altitude and thin cloud cover, altitude, and emissivity. We evaluate this new surface LWCRE–LIDAR product by comparing it to existing satellite-derived products globally on instantaneous collocated data at footprint scale and on global averages as well as to ground-based observations at specific locations. This evaluation shows good correlations between this new product and other datasets. Our estimate appears to be an improvement over others as it appropriately captures the annual variability of the surface LW CRE over bright polar surfaces and it provides a dataset more than 13 years long.

1 Introduction

Small changes in the surface irradiance may lead to large climatological responses (Chylek et al., 2007; Kwok and Untersteiner, 2011). Therefore, quantifying irradiance at the Earth's surface is a useful step to better understand the climate system. Clouds exert a very important effect on the energy balance at the surface of the Earth through their effects on shortwave (SW) and longwave (LW) radiation. They radiatively warm the surface in the LW domain because they absorb upward LW radiation that would otherwise escape the Earth system and re-emit it back towards the surface. They cool the surface in the SW domain because they reflect solar radiation back to space that would otherwise partly be

absorbed by the surface. These effects are usually quantified using the surface cloud radiative effect (CRE), defined as the change in the SW and LW radiation reaching the surface induced by the presence of clouds. Globally, clouds radiatively cool the Earth's surface by $20\,W\,m^{-2}$ according to Kato et al. (2018) and by $25\,W\,m^{-2}$ according to L'Ecuyer et al. (2019), where the (negative) surface SW CRE cooling is 2 times larger in magnitude than the (positive) surface LW CRE warming. Nevertheless, in some specific regions, like at high latitudes or over the tropical ocean below persistent stratocumulus clouds, the surface LW CRE warming can be larger than the surface SW CRE cooling, so that the clouds exert a net radiative warming of the surface.

As an example, SW effects vanish in the winter-hemisphere polar regions, leading to positive net CRE as LW effects dominate (Henderson et al., 2013). While climate warming in the Arctic is already visible with the sea ice melting (Stroeve et al., 2012), previous works showed that clouds may exert some control on future Arctic climate trajectories (Kay et al., 2012), because they play a primary role in regulating the surface energy balance (Ramanathan et al., 1989; Curry et al., 1996; Shupe and Intrieri, 2004), which influences the surface melting (van den Broeke et al., 2009). Specifically, over Greenland, van Tricht et al. (2016) showed that clouds increase the radiative fluxes into the surface and could therefore modulate the Greenland ice sheet mass balance (van Tricht et al., 2016; Hofer et al., 2017), which is a large contributor to global sea-level rise (Shepherd et al., 2012; IPCC, 2022). At the southern high latitudes, clouds likely exert an important role in the surface energy budget of Antarctica (Shepherd et al., 2012; Kopp et al., 2016), but their radiative impact in this region remains largely unexplored (Scott et al., 2017) in spite of the fact that Antarctica contains the largest reservoir of ice on Earth. King et al. (2015) showed large errors in Antarctic surface energy budget and surface melting rates in models and underlined the importance of improving observations of cloud radiative properties in this region.

Acquaotta and Fratianni (2014) underlined the current urgent need to develop long-term reliable and high-quality climatic time series in order to better understand, detect, predict and react to global climate variability and change. Given the importance of the surface LW CRE and the need for multiyear time series, it is necessary to get reliable estimates of the surface LW CRE over multiple years everywhere around the globe, including over continents and ice-covered regions. The main motivation for the current work is to derive a 13-year time series of the global surface LW CRE that can be used to better understand the cloud property that has driven the evolution of the surface LW CRE during the last decade (Vaillant de Guélis et al., 2017b; Norris et al., 2016). This is a necessary step towards understanding how clouds might interact with the surface in the future as the climate warms (Lindzen and Choi, 2021). A possible way to observe cloud variability is to combine space radar and space lidar observations (Henderson et al., 2013), because passive sensors often struggle to distinguish clouds from the surface over continents and ice-covered regions. The launch of Cloud-Aerosol Lidar and Infrared Pathfinder Satellite Observations (CALIPSO; Winker et al., 2010) and CloudSat Profiling Radar (CPR; Stephens et al., 2008) in 2006 provided the first opportunity to incorporate information about the global vertical cloud distribution (Henderson et al., 2013) over all surface types and is an important parameter for surface LW CRE estimates from space. As CloudSat experienced a battery anomaly that limited future observations to daytime scenes only in 2011, CALIPSO's global observations collected since 2006 are the main tool for providing information on the cloud vertical distribution over more than a decade. Therefore, we retrieve the surface LW CRE from space lidar alone over 13 years.

Section 2 presents the satellite and ground-based data used in this study. In Sect. 3, we present the method followed to retrieve the surface LW CRE from radiative transfer computations. In Sect. 4, we present the radiative-transfer-based statistical regressions tying the surface LW CRE to cloud altitude and emissivity. In Sect. 5, we present the new surface LW CRE retrieved from the analytical relationships and CALIPSO space-based lidar observations (cloud cover, cloud altitude, and cloud opacity). In Sect. 6, we evaluate this new surface LW CRE product against ground-based observations. In Sect. 7, we evaluate it at footprint scale and at $2° \times 2°$ gridded scale against existing independent surface LW CRE satellite-derived products. In Sect. 8, we discuss the limit of the new surface LW CRE product. Section 9 summarizes the main results and perspectives of this work.

2 Data

This section describes the CALIPSO cloud observations used to retrieve the surface LW CRE and the independent space-based and ground-based datasets used to evaluate it.

2.1 Cloud observations from CALIPSO–GOCCP–OPAQ

We use cloud properties from the GCM Oriented CALIPSO Cloud Product (GOCCP v3.1.2; Chepfer et al., 2010; Cesana et al., 2012; Guzman et al., 2017) over the period 2008–2020. We do not use data collected between 2006 and 2007 because the laser tilted off nadir in November 2007, which introduced some change in the CALIPSO signal. In this product (hereafter, CALIPSO–GOCCP), lidar profiles are classified into three types: clear-sky profile when no cloud is detected, thin cloud profile when one or several cloud layers and a surface echo are detected, and opaque cloud profile when one or several cloud layers are detected but no surface echo is detected. Surface echo is not detected typically when the profile contains a cloud with visible optical depth > 3–5 depend-

ing on the cloud microphysical properties. The cloud base height corresponds to the lowest cloud layer detected. From this classification, five fundamental cloud properties for CRE studies are derived.

- C_{Opaque}: the opaque cloud cover, i.e., the number of opaque cloud profiles divided by the total number of profiles within a $2^\circ \times 2^\circ$ latitude–longitude grid box.
- $Z_{T_{\text{Opaque}}}$: the altitude of opaque cloud, i.e., the average between the altitude of the highest cloud layer in the profile (Z_{Top}) and the altitude of the layer where the lidar beam is fully attenuated (Z_{FA}), is computed for each profile; a schematic illustrating these altitudes is presented in Fig. 1. Then the gridded $Z_{T_{\text{Opaque}}}$ is the average value of all the $Z_{T_{\text{Opaque}}}$ profiles within a grid box.
- C_{Thin}: the thin cloud cover, i.e., the number of thin cloud profiles divided by the total number of profiles within a grid box.
- $Z_{T_{\text{Thin}}}$: the altitude of thin cloud, i.e., the average between the altitude of the highest cloud layer in the profile (Z_{Top}) and the altitude of the lowest cloud layer (Z_{Base}), is computed for each profile; a schematic illustrating these altitudes is presented in Fig. 1. Then, the gridded $Z_{T_{\text{Thin}}}$ is the average value of all the $Z_{T_{\text{Thin}}}$ profiles within a grid box.
- $\varepsilon_{\text{Thin}}$: the thin cloud emissivity, derived from the space lidar retrieval of the thin cloud visible optical depth $\tau_{\text{Thin}}^{\text{VIS}}$ from which we estimate the thin cloud LW optical depth $\tau_{\text{Thin}}^{\text{LW}}$, which is approximately half of $\tau_{\text{Thin}}^{\text{VIS}}$ (Garnier et al., 2015). The relationship $\varepsilon_{\text{Thin}} = 1 - e^{-\tau_{\text{Thin}}^{\text{LW}}}$ (e.g., Vaillant de Guélis et al., 2017a) is computed for each profile and then averaged over all the values within a grid box.

Figure 1 presents the altitudes of interest of an opaque cloud and a thin cloud seen from a downward space-based lidar beam and from an upward ground-based lidar beam. A thin cloud (Fig. 1a) is characterized by three altitudes: Z_{Top}, Z_{Base} and $Z_{T_{\text{Thin}}}$, which is the average value of the previous two. For an ideal case, these three altitudes are the same when observed from a space-based lidar or a ground-based lidar.

An opaque cloud (Fig. 1b) is characterized by three altitudes. When the lidar is based on the ground, we measure the altitude of the lowest cloud layer (Z_{Base}), the altitude where the lidar beam is fully attenuated ($Z_{\text{FA-G}}$), and $Z_{T_{\text{Opaque-G}}}$, which is the average of the two. When the lidar is onboard a satellite, we measure the highest cloud layer (Z_{Top}), the altitude where the lidar beam is fully attenuated (Z_{FA}), and the average of the two ($Z_{T_{\text{Opaque}}}$).

Figure 2 illustrates the mean $2^\circ \times 2^\circ$ latitude–longitude gridded values of these five variables over the period 2008–2020. At global scale, opaque clouds are more numerous (42 %; Fig. 2a) than thin clouds (25 %; Fig. 2b) in CALIPSO–GOCCP v3.1.2. Note that these numbers are different from CALIPSO–GOCCP v3.1.1 (35 % and 36 %, respectively), where the threshold used to detect surface echo, which influences the identification of opaque clouds, was lower because CALIPSO–GOCCP v3.1.1 (Guzman et al., 2017) was applied only to nighttime data since noise is lower during nighttime than daytime. CALIPSO–GOCCP v3.1.2 is applied to nighttime and daytime observations. As expected, the multiyear, annual mean opaque and thin cloud altitudes (Fig. 2c, d) reach maxima (> 9 km) in the presence of deep convective clouds over the warm pool and over tropical continents and minima (< 3 km) in subsidence regions such as over stratocumulus along the western coast of continents. The thin cloud emissivity (Fig. 2e) is larger along the intertropical convergence zone (ITCZ), in the continental regions, and around the Antarctic Peninsula.

2.2 Surface LW CRE from satellites

In this subsection, we describe the already existing global surface LW CRE datasets derived from satellite measurements, against which we will evaluate our new satellite retrieval.

2.2.1 CERES–CCCM

This product combines Clouds Earth's Radiant Energy System (CERES) radiometer observations of top of the atmosphere (TOA) LW fluxes with observations from CloudSat, CALIPSO and MODIS as well as radiative transfer calculations to retrieve the surface LW fluxes in all-sky and clear-sky scenes at a resolution of the CERES Single Scanner Footprint (SSF, 20 km diameter). This product contains the surface LW CRE at the CERES SSF footprint and is part of the CALIPSO, CloudSat, CERES, and MODIS Merged Product (CCCM or C3M: Kato et al., 2010). This product stops in 2011 because of the CloudSat battery anomaly. This product (version RelB1) contains the CERES footprints that include the ground track of CALIPSO and CloudSat. TOA LW fluxes are derived from CERES radiance observations using the Edition 2 Aqua angular distribution model (Loeb et al., 2005, 2007). Surface LW fluxes are computed using cloud properties derived from CALIPSO, CloudSat, and MODIS. CALIOP (Cloud-Aerosol LIdar with Orthogonal Polarization)-derived cloud products are extracted from version 3 of CALIPSO VFM, 0.5 kmALay, and 0.5 kmCLay, and 0.5 kmCPro, products (Vaughan et al., 2018), and R-04 CloudSat CLDCLASS (Sassen and Wang, 2008) and CWC-RO (Austin et al., 2009) products. MODIS cloud properties are derived by the CERES MODIS cloud algorithm described in Minnis et al. (2010). Cloud boundaries derived from CALIOP at a 1 / 3 km resolution and cloud boundaries derived from CPR CloudSat are merged to form cloud vertical profiles by the method described in Kato et al. (2011). These cloud profiles are further merged into CERES foot-

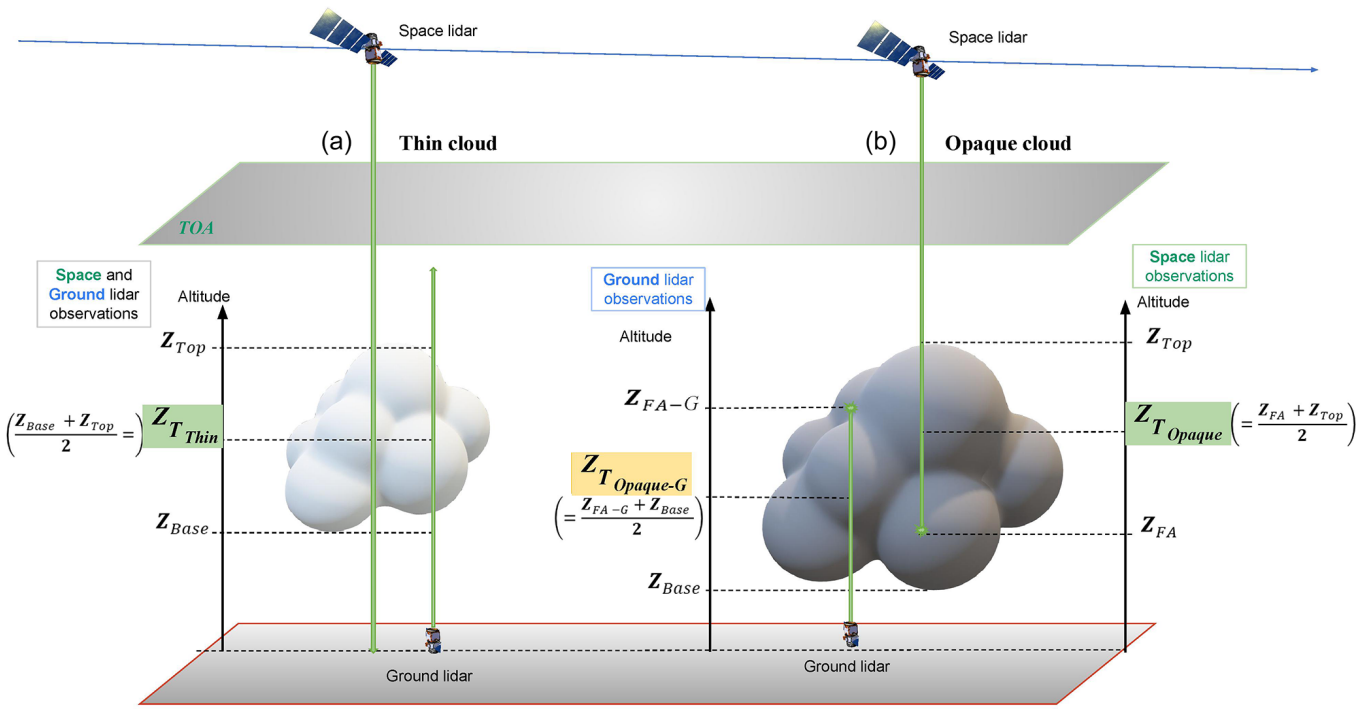

Figure 1. Schematic of cloud altitudes seen from space lidar and from a ground-based lidar in an atmospheric column containing thin cloud only **(a)** and opaque cloud only **(b)**. The altitudes used to retrieve the surface LW CRE from CALIPSO–GOCCP are reported in green.

prints, the sizes of which are approximately 20 km. Temperature and humidity profiles used in flux computations are from the Goddard Earth Observing System Data Assimilation System reanalysis (GEOS, Rienecker et al., 2008). GEOS-4 is used from July 2006 through October 2007, and GEOS-5.2 is used from November 2007. Further description of the RelB1 CERES-CCCM product is given in Ham et al. (2017) and Kato et al. (2019).

2.2.2 2B-FLXHR-LIDAR

The CloudSat 2B–FLXHR–LIDAR P1_R04 (hereafter, 2BFLX) product combines measurements from CloudSat, CALIPSO, and MODIS to generate estimates of longwave and shortwave fluxes and heating rates throughout the atmosphere (L'Ecuyer et al., 2008; Henderson et al., 2013). The algorithm uses inferred vertical profiles of cloud and precipitation water contents and particle size and temperature and humidity profiles from ECMWF analyses as input to a broadband radiative transfer model. A detailed description of the approach used to reconstruct the atmospheric columns and prescribe surface characteristics as well as a thorough uncertainty assessment is provided in Henderson et al. (2013) and Matus and L'Ecuyer (2017). The surface LW CRE product used here is provided for each CloudSat orbit at the instantaneous footprint scale of 1.8 km and gridded for the comparisons that follow. The dataset currently covers the period August 2006 through April 2011 before CloudSat experienced a battery anomaly that limited operations to daylight conditions.

The surface fluxes derived from a combination of radar and lidar observations in 2BFLX are less susceptible to uncertainties due to undetected multi-layered clouds and uncertainties in cloud base height than those derived primarily from passive observations (L'Ecuyer et al., 2019; Hang et al., 2019). However, both 2BFLX as well as the LWCRE–LIDAR product are sensitive to retrieval errors and biases introduced by the limited spatial and temporal characteristics of CloudSat and CALIPSO. Sensitivity studies suggest that uncertainties in monthly-mean surface longwave irradiances at 2.5° resolution derived from 2BFLX are $\sim 11\ \mathrm{W\,m^{-2}}$, owing primarily to errors in specifying lower tropospheric temperature and humidity and uncertainty in cloud base height (Henderson et al., 2013).

2.3 Surface LW CRE from ground-based sites

As the retrieval of the surface CRE from space observations is not direct, we will evaluate the surface LW CRE retrieved from space against that derived from surface radiation measurements collected directly at ground-based sites. For this purpose, we selected three sites located in different regions.

The first site is located in the Arctic, where constraining radiative transfer is challenging with the limited cloud, available atmospheric temperature and humidity profile observations (Kay et al., 2015) and where the surface CRE may influence the Greenland ice-cap melt (van Trich et al., 2016;

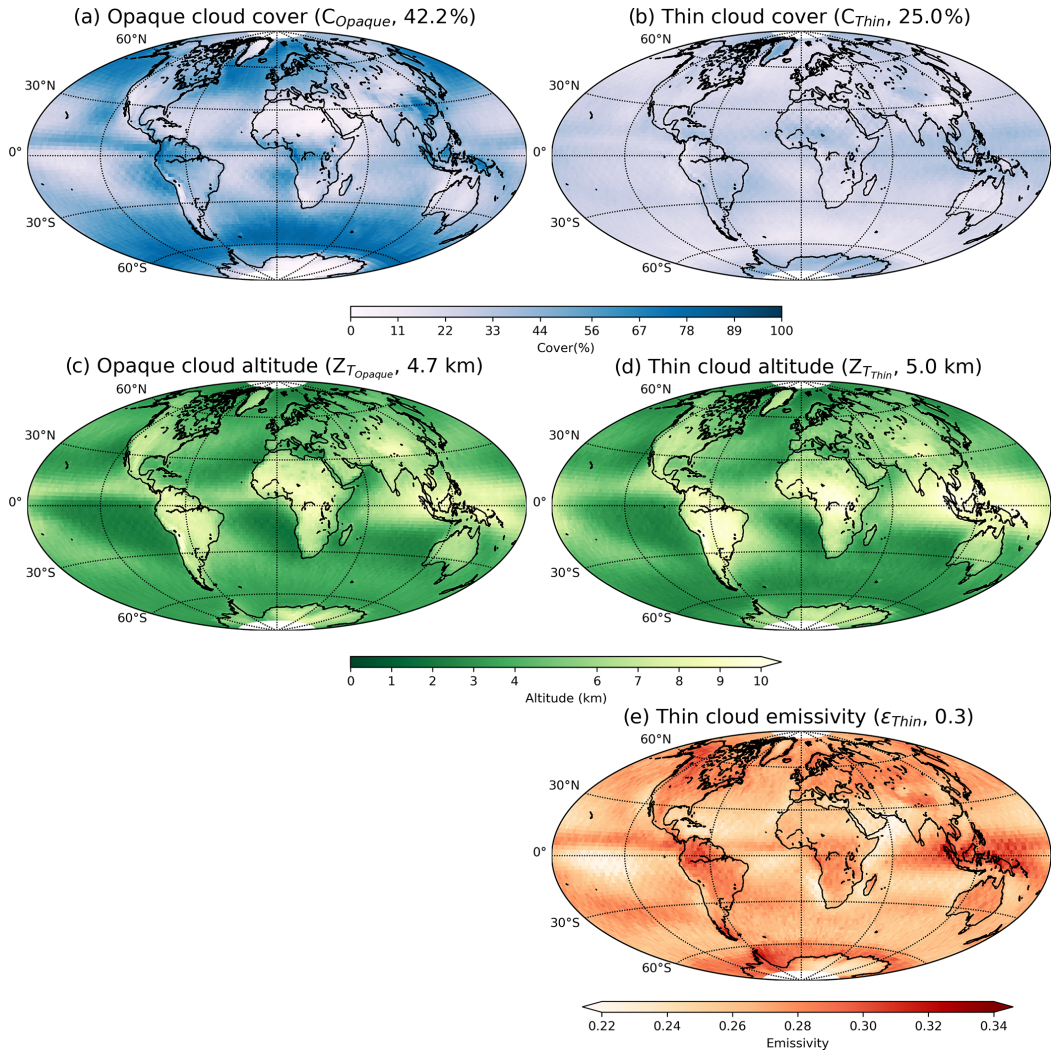

Figure 2. Maps of **(a)** opaque cloud cover C_{Opaque}, **(b)** thin cloud cover C_{Thin}, **(c)** opaque cloud altitude $Z_{T_{\text{Opaque}}}$, **(d)** thin cloud altitude $Z_{T_{\text{Thin}}}$ and **(e)** thin cloud emissivity $\varepsilon_{\text{Thin}}$. Global means are reported in parentheses. Build from CALIPSO–GOCCP v3.1.2 over 2008–2020.

Hofer et al., 2017; Shupe et al., 2013). This Summit station (Shupe et al., 2013; Gallagher et al., 2018) is located at the top of the Greenland ice cap (72.6° N–38.5° W) with an elevation of 3250 m. Summit is unique because it is the only place where we have enough observations to make a robust assessment of the surface CRE over Greenland (Lacour et al., 2018). Here, the clear-sky flux is computed using a radiative transfer algorithm with measurements of temperature and humidity profiles (e.g., REFs), while the all-sky flux is measured directly using a pair of upward- and downward-looking broadband pyrgeometers (e.g., Shupe and Intrieri, 2004; Intrieri et al., 2002).

The second site is located at continental mid-latitudes. This Site Instrumental de Recherche par Télédétection Atmosphérique (SIRTA, Haeffelin et al., 2005; Chiriaco et al., 2018) is located in France (48.7° N–2.2° E) with an elevation of 156 m. The data are part of the Baseline Surface Radiation Network (BSRN; Ohmura et al., 1998; Driemel et al., 2018). At SIRTA, the clear-sky flux is a parameterization made from the surface humidity, the integrated moisture content over the atmospheric column and the air temperature at 2 m. The details are given in Dupont and Haeffelin (2008), and this product has also been used in Rojas et al. (2021). The resulting clear-sky uncertainty is approximately $\pm 5\,\mathrm{W\,m^{-2}}$.

The third site is located in the tropical belt, where clouds influence the global climate and heat transport (Loeb et al., 2016) and where extensive deep convective clouds reach the cold tropical tropopause. Here, the surface LW CRE is small, since much of the surface downward LW radiation originates from emission by the moist near-surface layers of the atmosphere (Prata, 1996). This Kwajalein station (KWA, Roesch et al., 2011), which is also part of the BSRN, is located in the northern Pacific Ocean (8.72° N–167.73° E) with an elevation of 10 m.

Over the three ground-based sites, the radiative flux measurements at the surface are carried out using two Kipp and

Zonen CM22 pyrgeometers, which measure in the spectral range of 4.5–40 µm.

3 Method

3.1 Approach

Vaillant de Guélis et al. (2017a, b) retrieved the TOA LW CRE from the five CALIPSO–GOCCP cloud properties presented in Fig. 2: the opaque cloud cover, the opaque cloud altitude, the thin cloud cover, the thin cloud altitude, and thin cloud emissivity. In adapting their approach to the surface instead of the TOA, we developed a method to retrieve the surface LW CRE from the same five CALIPSO–GOCCP cloud properties. The method we have developed is based on simple parameterization. This will allow us to, in future work, more easily decompose the temporal variations of the surface LW CRE into several components in order to identify which cloud variables have driven the variations of the surface LW CRE during the last 13 years. The following physical differences exist between the surface and the TOA.

3.1.1 Moisture

Moisture within the boundary layer influences the surface LW CRE more than the TOA LW CRE. To take moisture effects into account, we add the surface elevation in the framework of Vaillant de Guélis et al. (2017), and we consider different humidity and temperature profiles at a monthly resolution and for every 2° latitude, differentiating oceans from continents. Compared to the fluxes themselves, small water vapor variability does not affect CRE much, as the equivalent clear-sky contribution is removed from CRE. The surface LW CRE dependence on temperature and humidity profiles is shown in Sect. 4.1, 4.2, and 4.3. The impact on the results of using monthly-mean humidity and temperature profiles will be discussed in Sect. 8.

3.1.2 Cloud heights used for the surface LW CRE estimate

In thin cloud situations, the surface LW CRE is influenced by radiation emitted downwards by all cloud layers between the cloud base (Z_{Base}) and the cloud top (Z_{Top}). Therefore, the surface LW CRE depends on the vertical distribution of condensed water between Z_{Base} and Z_{Top}, which are measured by the lidar. Therefore, we use the average of both ($Z_{T_{\mathrm{Thin}}}$) to estimate the surface LW CRE from lidar observations.

In opaque cloud situations, the surface LW CRE is influenced by radiation emitted by all cloud layers between cloud base (Z_{Base}) and the altitude Z_{Emisv1}, defined as the altitude where the emissivity between Z_{Base} and Z_{Emisv1} is close to 1. Cloud layers at altitudes higher than Z_{Emisv1} do not contribute to the surface LW CRE. Therefore, the surface LW CRE depends on the vertical distribution of condensed water between Z_{Base} and Z_{Emisv1}.

In those specific cases where the vertical distribution of condensed water is such that Z_{Base} equals Z_{Emisv1}, meaning that the Z_{Base} layer (480 m thick) contains enough condensed water to alone make the emissivity close to 1, then the surface LW CRE is driven only by Z_{Base}. In that specific case, the lidar Z_{FA} should be used to compute the surface LW CRE, and the larger the difference between Z_{FA} and the actual Z_{Base}, the more the space-based lidar surface LW CRE will be underestimated.

In all other opaque cloud situations, where Z_{Base} is lower than Z_{Emisv1}, all cloud layers between Z_{Base} and Z_{Emisv1} contribute to the surface LW CRE, and the relative weight of each layer depends on the detailed vertical distribution of condensed water between Z_{Base} and Z_{Emisv1}. In that case, the lidar measures Z_{Top} and Z_{FA}, and we use the average $Z_{T_{\mathrm{Opaque}}}$, which is the average of Z_{Top} and Z_{FA} to estimate the surface LW CRE from lidar observations.

To retrieve the surface LW CRE, we could use Z_{Base} from CloudSat, but this would limit our time series to 2011 only instead of 2021, and CloudSat is not always optimal for detecting cloud base, in particular if it is a liquid-water cloud. We chose to use what we have access to with CALIPSO: a first option consists in using Z_{FA}, the lowest opaque cloud altitude observable by space lidar ($Z_{\mathrm{FA}} < 3$ km above the surface most of the time, Guzman et al., 2017), which is close to the actual cloud base height except in deep convective towers and some frontal mid-latitude clouds. A second option is to use $Z_{T_{\mathrm{Opaque}}}$, which might represent the altitude of emission of the cloud in some cases. This second option will overestimate the mean altitude of the deep convective towers, where the downward space-based lidar beam attenuates quickly without seeing much of the cloud bottom. The bias will be larger when the cloud base temperature is far from that of Z_{FA}. Moreover, this bias will depend on the opacity of the part of the cloud laying under Z_{FA} that is not observable by space lidar.

Hereafter, we describe the method with $Z_{T_{\mathrm{Opaque}}}$. Afterwards, we show the results for both option 1 (Z_{FA}) and option 2 ($Z_{T_{\mathrm{Opaque}}}$).

The impact of the results on using these cloud heights will be discussed in Sects. 7 and 8.

3.2 Definition of the radiative quantities

In order to get simple notation and because we are only interested in the CRE at the surface in the LW domain in this study, the surface LW CRE will simply be denoted "CRE" in the following equations.

To infer "CRE", the net LW radiative fluxes over all types of scenes ($F^{\mathrm{net}}_{\mathrm{Allsky}}$) may be compared with corresponding fluxes where the influence of clouds has been removed ($F^{\mathrm{net}}_{\mathrm{Cloudy-freesky}}$). Then, we define the surface LW CRE as fol-

lows:

$$\mathrm{CRE} = F^{\mathrm{net}}_{\mathrm{Allsky}} - F^{\mathrm{net}}_{\mathrm{Cloudy-freesky}}. \quad (1)$$

Using downwelling (↓) and upwelling (↑) fluxes, the surface LW CRE is expressed as follows:

$$\mathrm{CRE} = \left(F^{\downarrow}_{\mathrm{Allsky}} - F^{\uparrow}_{\mathrm{Allsky}}\right) - \left(F^{\downarrow}_{\mathrm{Cloudy-freesky}} - F^{\uparrow}_{\mathrm{Cloudy-freesky}}\right). \quad (2)$$

Rearranging the terms on the right-hand side of this equation, we get

$$\mathrm{CRE} = \left(F^{\downarrow}_{\mathrm{Allsky}} - F^{\downarrow}_{\mathrm{Cloudy-freesky}}\right) - \left(F^{\uparrow}_{\mathrm{Allsky}} - F^{\uparrow}_{\mathrm{Cloudy-freesky}}\right), \quad (3)$$

which can also be expressed as

$$\mathrm{CRE} = \mathrm{CRE}^{\downarrow} - \mathrm{CRE}^{\uparrow}, \quad (4)$$

where $\mathrm{CRE}^{\downarrow}$ represents the surface CRE on the LW downward fluxes and $\mathrm{CRE}^{\uparrow}$ the surface CRE on the LW upward fluxes. $\mathrm{CRE}^{\uparrow}$ does not exceed $1\,\mathrm{W\,m^{-2}}$ in the annual global average (Allan, 2011) and in the radiative transfer computations. Therefore, the error in the surface properties plays a minor role.

Nevertheless, in the LW domain, clouds can warm the surface, changing the surface temperature, which is then related to the upwelling LW radiation. This is a subtle but important issue and is dependent to some degree on the surface type (i.e., land surface will warm more than ocean). If "CRE" is determined in a hypothetical way, one could assume that the surface temperature is the same. However, this does not capture the full impact of the clouds. To understand the full impact of the clouds, one would need to consider the adjustments of all other parameters, most importantly the surface temperature. In this study we assume that the surface temperature is the same under clouds and clear skies, consistent with the definition used in previous satellite-derived products (e.g., Kato et al., 2018; L'Ecuyer et al., 2019).

3.3 Radiative transfer simulations

We use a radiative transfer code to compute the surface LW CRE due to an opaque cloud ($\mathrm{CRE_{Opaque}}$) or an optically thin cloud ($\mathrm{CRE_{Thin}}$) in an atmospheric column fully overcast by that cloud. In these 1D atmospheric columns, molecules and clouds are evenly distributed within each layer, and each layer is considered infinite and homogeneous. For a single column fully overcast by an opaque cloud, we derived a parameterization between $\mathrm{CRE_{Opaque}}$ and the opaque cloud altitude $Z_{T_{\mathrm{Opaque}}}$ (see Sect. 2.1). For the single column fully overcast by a thin cloud, we derived a parameterization between $\mathrm{CRE_{Thin}}$, the thin cloud altitude $Z_{T_{\mathrm{Thin}}}$ (see Sect. 2.1) and the thin cloud emissivity $\varepsilon_{\mathrm{Thin}}$, as in Vaillant de Guélis et al. (2017).

The radiative transfer simulations are performed with GAME (Dubuisson et al., 2004). This radiative transfer code computes LW fluxes at 50 different levels with a vertical resolution of 1 km in the first 25 levels. The fluxes are spectrally integrated between 5 and 200 µm, consistent with CERES measurements. We prescribe various surface temperatures and the atmospheric profiles of humidity, temperature, ozone and pressure based on ERA-Interim reanalysis (Dee et al., 2011) over oceans and lands for each month and 2° latitude. Humidity and temperature profiles over land for January are presented in Fig. A2 in Appendix A. Figure A3 presents the seasonal and latitudinal behavior of the first layer of the humidity and temperature profiles (from the surface to 1 km above the surface) over ocean and over land. We perform all-sky fluxes through radiative transfer computations for numerous combinations of cloud opacity and vertical distribution. We prescribe the vertical extent of each cloud, the effective size of cloud particles and the infrared optical thickness. For a column fully overcast by an opaque cloud, the cloud is represented by a 1 km-thick cloud layer with an emissivity close to 1 at $Z_{\mathrm{FA-G}}$ (Z_{Top}) above optically uniform cloud layers for different vertical extents with a vertically integrated emissivity equal to 0.8. For a column fully overcast by a thin cloud, the cloud is represented by optically uniform cloud layers with vertically integrated emissivities equal to 0.1, 0.3, 0.5 or 0.7. The cloud top altitude varies according to latitude and can reach 17 km in tropical regions and only 11 km in polar regions. For instance, the cloud top altitude at a latitude of 39° N takes 11 different values ranging between 2 and 13 km, and for each cloud top value, the cloud base altitude takes all possible values between 1 km above the surface and the cloud top altitude minus 1 km. Clear-sky fluxes are defined by recalculating fluxes after removing clouds with the same humidity and temperature profiles.

3.4 Retrieval of the surface LW cloud radiative effect from CALIPSO observations and radiative transfer simulations

The surface LW CRE is retrieved from parameterizations derived from radiative transfer simulations that involve five observed CALIPSO–GOCCP cloud properties. Two surface LW CRE datasets are built from the CALIPSO–GOCCP product using this theoretical relationship over the 2008–2020 period, an orbit dataset at the CALIOP footprint resolution of instantaneous cloud property observations and a $2° \times 2°$ gridded dataset of mean cloud properties. For the orbit dataset, each lidar profile contains either an opaque or thin cloud or no cloud, and the surface LW CRE for this last category is zero. For the gridded product, at each grid point, the opaque surface LW CRE is computed from the gridded $Z_{T_{\mathrm{Opaque}}}$ and weighted by the gridded opaque cloud cover C_{Opaque} in the same way as Vaillant-de-Guélis et al. (2017).

The thin surface LW CRE is computed from the gridded $Z_{T_{\text{Thin}}}$ and gridded $\varepsilon_{\text{Thin}}$ and then weighted by the gridded thin cloud cover C_{Thin}. The total gridded surface LW CRE is the sum of the two.

$$\text{CRE} = \text{CRE}_{\text{Opaque}} + \text{CRE}_{\text{Thin}} \quad (5)$$

In the retrievals, we tested both Z_{FA} and $Z_{T_{\text{Opaque}}}$ for estimating the mean altitude of opaque clouds (as discussed in Sect. 3.1).

The new product name is "LWCRE–LIDAR–Ed1" for "LW Cloud Radiative Effect derived from space Lidar observations Edition 1", and the acronyms are LWCRE–LIDAR and $\text{CRE}_{\text{LIDAR}}$ in this study. This new monthly gridded product is available for the 2008–2020 time period at https://doi.org/10.14768/70d5f4b5-e740-4d4c-b1ec-f6459f7e5563 (Arouf et al., 2022), and Table C1 summarizes the data included in the dataset.

4 Modeled CRE sensitivity to cloud properties

This section establishes parameterizations of the surface LW CRE against cloud altitude and emissivity over a single cloudy column using radiative transfer computations (Sect. 4.1). Then it analyzes the sensitivity of the surface LW CRE to the humidity and temperature profiles (Sect. 4.2) and to the surface elevation (Sect. 4.3).

4.1 Sensitivity of the CRE to cloud altitude

Figure 3 shows the results of numerous simulations for the opaque cloud column (Fig. 3a) and the thin cloud column (Fig. 3b) for a specific atmospheric state over oceans in January at a latitude of 39° N. $\text{CRE}_{\text{Opaque}}$ decreases approximately linearly with opaque cloud altitude at a rate of $6.0\,\text{W}\,\text{m}^{-2}\,\text{km}^{-1}$ in this atmospheric state. This figure shows that the surface LW cloud radiative effect depends mostly on the mean altitude of the cloud and only weakly on the detailed vertical cloud distribution and the cloud bottom altitude. CRE_{Thin} also decreases linearly with thin cloud altitude, and the rate of decrease depends linearly on the cloud emissivity. The linearity of these relationships is consistent with Ramanathan (1977) and Vaillant de Guélis et al. (2017, 2018). It is an empirical relation derived from radiative transfer calculations that has been verified in the observation at the TOA in Vaillant de Guélis et al. (2017a, 2018). Corti and Peter (2009) also derived an empirical relationship (power laws) from radiative transfer computation. Our linear relationship can be seen as an approximation of the Corti and Peter (2009) power law.

Based on a regression, we obtain the following linear relationships between the surface LW CRE and cloud altitude and emissivity:

$$\text{CRE}_{\text{Opaque}} = C_{\text{Opaque}} \times \left[a\,(\text{RH}, T) \times Z_{T_{\text{Opaque}}} + b\,(\text{RH}, T)\right], \quad (6)$$

$$\text{CRE}_{\text{Thin}} = C_{\text{Thin}} \times (\varepsilon_{\text{Thin}} + 0.06) \times \left[a\,(\text{RH}, T) \times Z_{T_{\text{Thin}}} + b\,(\text{RH}, T)\right], \quad (7)$$

where $a(\text{RH},T)\,\text{W}\,\text{m}^{-2}\,\text{km}^{-1}$ and $b(\text{RH},T)\,\text{W}\,\text{m}^{-2}$ are constants whose values depend on the humidity and temperature profiles as discussed hereafter. For the specific case presented in Fig. 3, $a = -6.0\,\text{W}\,\text{m}^{-2}\,\text{km}^{-1}$ and $b = +88.0\,\text{W}\,\text{m}^{-2}$.

4.2 Sensitivity of the CRE to humidity and temperature profiles

The temperature and humidity profiles in the first layers of the atmosphere largely vary according to seasons and location as presented in Fig. A3 in Appendix A. Since these are variables that influence the surface LW CRE, their variations must be taken into account in order to retrieve the global surface LW CRE.

As an example, Fig. 4a presents the opaque surface LW CRE for a standard humidity profile and Fig. 4b presents the opaque surface LW CRE for an enhanced humidity profile (shown in Fig. A4). A 10 % change in humidity in the first few kilometers of the tropical atmosphere leads to a surface LW CRE change of $7.7\,\text{W}\,\text{m}^{-2}$ for a cloud at 1 km and by $5\,\text{W}\,\text{m}^{-2}$ for a cloud at 4 km. To capture some variability of humidity and temperature, we have established similar relationships as in Fig. 3 for each month and latitude (every 2°) over land and ocean. As an example, Fig. A1 shows the simulations for cloud columns for an atmospheric state over land in January at a latitude of 39° N (same as Fig. 3 but over land instead of ocean). At this latitude, the amount of humidity is lower over land than ocean, and therefore the LW $F^{\text{net}}_{\text{Cloudy}-\text{freesky}}$ over land is lower and the surface LW CRE would be larger than over the ocean. The surface LW CRE is greater than that over ocean and decreases at a rate ($a(\text{RH},T)\,\text{W}\,\text{m}^{-2}\,\text{km}^{-1}$) of $6.5\,\text{W}\,\text{m}^{-2}\,\text{km}^{-1}$ instead of $6.0\,\text{W}\,\text{m}^{-2}\,\text{km}^{-1}$ over ocean. Figure 5 presents the latitudinal and seasonal behavior of the linear regression coefficients ($a(\text{RH},T)\,\text{W}\,\text{m}^{-2}\,\text{km}^{-1}$ and $b(\text{RH},T)\,\text{W}\,\text{m}^{-2}$). The shape of these coefficients' spatiotemporal variation is influenced by the shape of the seasonal cycle of humidity and temperature in the first layers of the atmosphere (Fig. A3). For instance, the behavior of the intercept ($b(\text{RH},T)\,\text{W}\,\text{m}^{-2}$) over ocean and land (Fig. 5b and d, respectively) is driven by the shape of the humidity amount where the largest humidity amount (in tropical regions) causes the smallest intercept coefficients. The seasonal cycle of the surface LW CRE is more pronounced over land than over ocean because the seasonal cycles of humidity and temperature are more pronounced over land than over ocean due to the heat capacity of the surface (Chepfer et al., 2019).

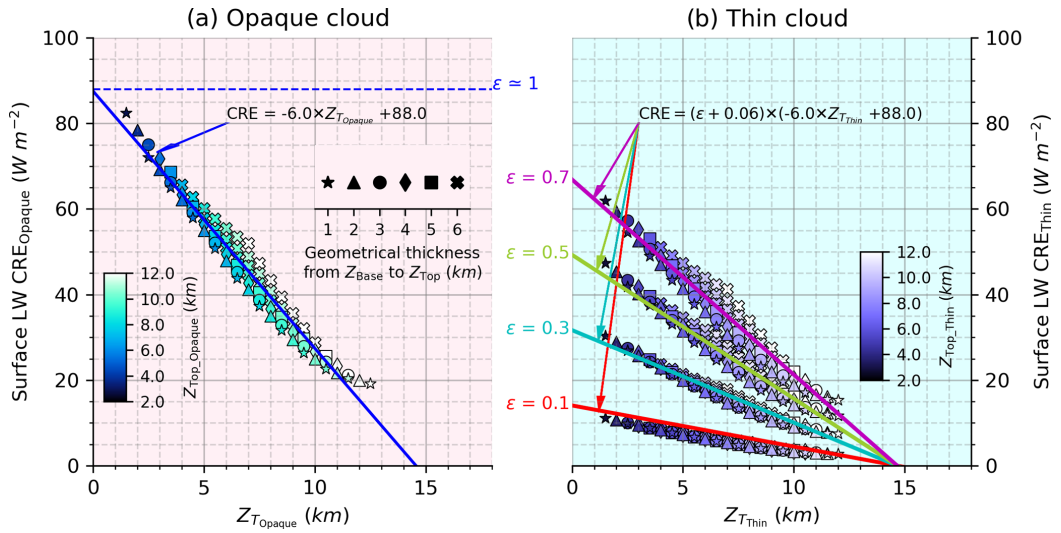

Figure 3. Linear relationships derived from 1D radiative transfer computations between the surface LW CRE and the cloud altitude for a single overcast column containing **(a)** an opaque cloud above a thin cloud, both moving in altitude, and **(b)** a thin cloud of emissivity 0.1 (red), 0.3 (cyan), 0.5 (green) and 0.7 (pink). These linear relationships (solid lines) are derived from direct radiative transfer computations (dots). Each dot represents the result of one radiative transfer computation. The color of dots represents the cloud top altitude (2 km, dark, to 13 km, bright) and the shape of dots the geometrical thickness from the cloud base to cloud top (1 km, a star, to 6 km and above, a cross). The atmospheric state is taken from ERA-Interim reanalysis for January at a latitude of 39° N over the ocean. As an example, in plot **(a)** the slope is $-6.0\,\mathrm{W\,m^{-2}\,km^{-1}}$, and the intercept is $88.0\,\mathrm{W\,m^{-2}}$.

4.3 Sensitivity of the CRE to surface elevation

In order to take the surface elevation in the simulation into account, we consider the surface temperature to be the temperature of the atmospheric layer located at the same altitude as the surface elevation with respect to sea level, and we discard all layers located between sea level and the altitude of surface elevation. We then performed numerous radiative transfer simulations corresponding to different clouds, as described in Sect. 3.2.

The results presented in Fig. 6 show the sensitivity of the surface LW CRE to the surface elevation over continents in January at 39° N. As the surface elevation increases, the atmosphere is drier, so $F^{\mathrm{net}}_{\mathrm{Cloudy-freesky}}$ decreases and the surface LW CRE increases. The same cloud with the same cloud properties (i.e., same altitude and emissivity) will warm a surface with a high elevation more than a low elevation. For instance, an opaque cloud at an altitude of 5.5 km m.s.l. (mean sea level) will warm a surface at sea level by $\sim 58\,\mathrm{W\,m^{-2}}$ and a surface with an elevation of 4 km m.s.l. by $\sim 102\,\mathrm{W\,m^{-2}}$. These results are consistent with Wang et al. (2019), who found that the surface LW CRE increases over the Summit station in Greenland due to the dry atmosphere at high elevations. We performed radiative transfer simulations for different surface elevations at all latitudes and months (not shown) and used these to retrieve the surface LW CRE from space-based lidar observations over land. Thus, the regression coefficients over land also depend on surface elevation, with a 100 m resolution (a(RH,T,SE) $\mathrm{W\,m^{-2}\,km^{-1}}$, b(RH,T,SE) $\mathrm{W\,m^{-2}}$).

5 New surface LW cloud radiative effect derived form CALIPSO–GOCCP: LWCRE–LIDAR

5.1 Orbit product

Figure 7 (first panel) show the CALIPSO–GOCCP cloud vertical mask (Guzman et al., 2017) for two different parts of an orbit, both in the tropical region. The blue areas over green areas represent the opaque clouds. The blue areas over white areas represent thin clouds. The second line represents the instantaneous surface LWCRE–LIDAR derived from CALIPSO–GOCCP instantaneous cloud properties (opaque cloud altitude, thin cloud altitude and emissivity; $\mathrm{CRE_{LIDAR}}$), as described in Sect. 3.3. As expected, the surface LWCRE–LIDAR is larger for opaque clouds (Fig. 7a, $\sim 22\,\mathrm{W\,m^{-2}}$) than for thin clouds (Fig. 7b, $\sim 5\,\mathrm{W\,m^{-2}}$) for almost the same atmosphere.

5.2 Gridded product

Figure 8a shows the map of the surface LWCRE–LIDAR derived from the CALIPSO–GOCCP product over the 2008–2020 time period.

In annual global means, clouds radiatively warm the surface in the LW domain by $27.0\,\mathrm{W\,m^{-2}}$. $\mathrm{CRE_{LIDAR}}$ is maximal in the Southern Ocean ($\sim$50–65 $\mathrm{W\,m^{-2}}$), where the

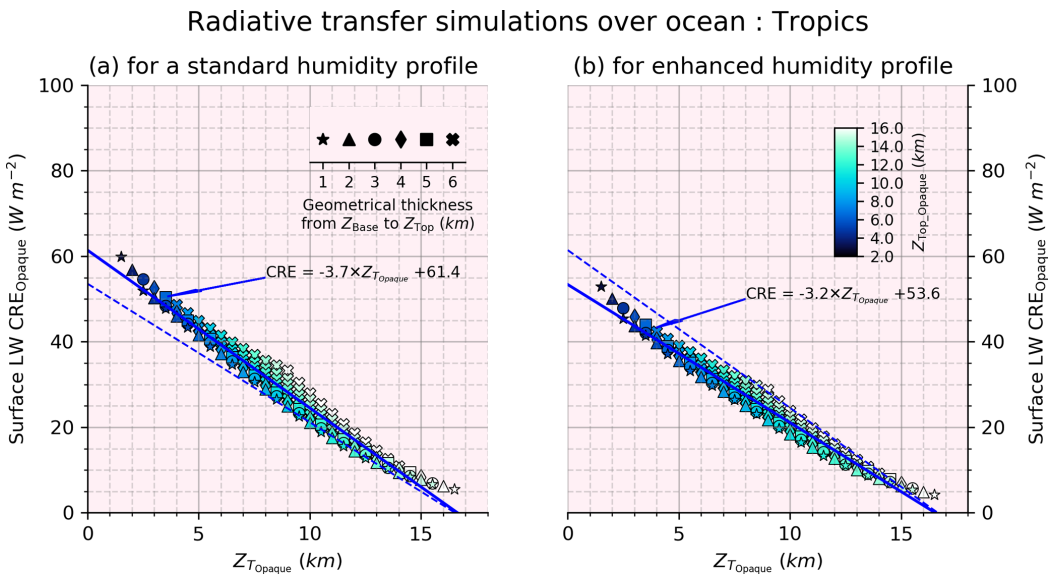

Figure 4. Same as Fig. 3a for **(a)** a standard humidity profile and **(b)** an enhanced humidity profile, both in the tropics: [30° S–30° N].

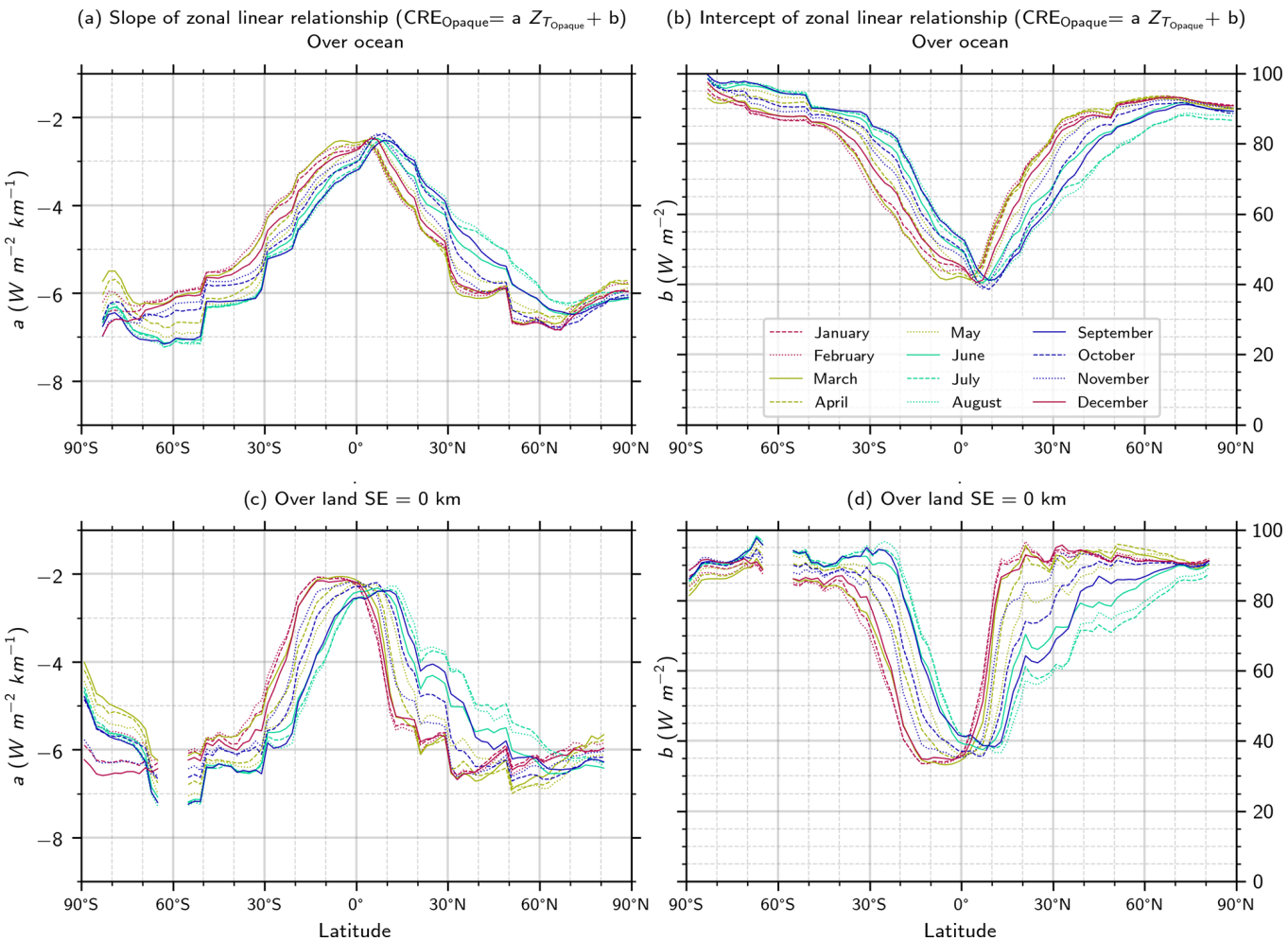

Figure 5. Coefficients of the linear relationships derived from 1D radiative transfer computations between the surface LW CRE and the cloud altitude for all latitudes and seasons: **(a)** the slope of the relationships over ocean, **(b)** the intercept of the relationships over ocean, **(c)** the slope of the relationships over land and **(d)** the intercept of the relationships over land.

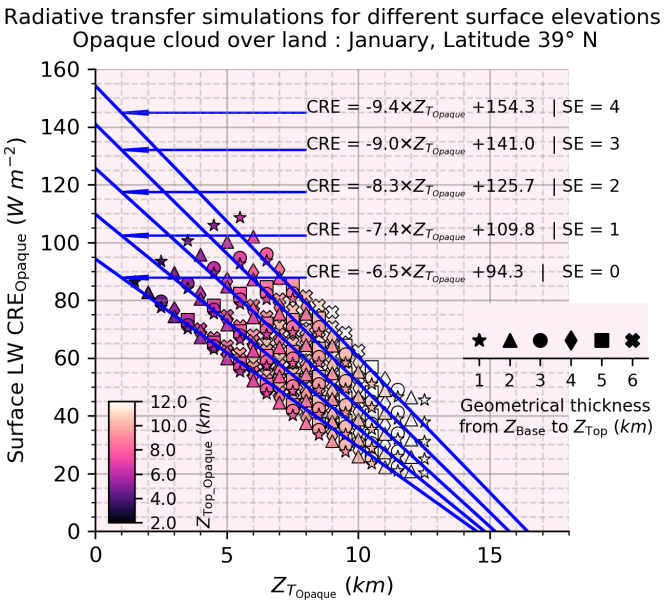

Figure 6. Sensitivity of the surface LW opaque CRE to the surface elevation (SE): same as Fig. 3a but over land and for different values of SE: SE = 0 (sea level), SE = 1 km, SE = 2 km, SE = 3 km, and SE = 4 km for January at a latitude of 39° N.

warm opaque low clouds are numerous, as already stated by L'Ecuyer et al. (2019) and Henderson et al. (2013). There are also particularly high values in the North Atlantic ($>\sim 55\,W\,m^{-2}$) observed between Svalbard and Greenland. In the tropics, clouds typically radiatively warm the surface in the LW domain by only $\sim 15\,W\,m^{-2}$. The moist tropical oceanic atmosphere enhances the downward clear-sky fluxes, which decreases the surface LW CRE over these oceans. The maximum tropical CRE_{LIDAR} (~ 30 to $\sim 40\,W\,m^{-2}$) is produced by warm opaque low oceanic stratocumulus clouds along the western coast of the continents.

Over continents, the weakest CRE_{LIDAR} ($<\sim 5\,W\,m^{-2}$) occurs over the Wadi Abadi basin in the Egyptian desert (25° N, 33° E), a cloud-free region most of the time (80 %). The largest CRE_{LIDAR} (~ 60–$65\,W\,m^{-2}$) occurs over the Tibet Autonomous Region (29° N, 97° E), where the opaque cloud cover is high (58 %) and the mean surface elevation is high (~ 4.42 km) over 2.5 million km^2. Here, the high amount of moisture is uplifted towards southern Tibet, amplified by Rayleigh distillation as the vapor moves over the Himalayan mountains (He et al., 2015), which enhances the formation of opaque clouds.

CALIPSO space-based lidar differentiates well opaque clouds from thin clouds. Therefore, we can decompose the CRE_{LIDAR} into contributions due to opaque clouds (CRE_{Opaque}: Fig. 8b) and thin clouds (CRE_{Thin}: Fig. 8c). This decomposition shows that 85 % ($23.0\,W\,m^{-2}$) of the overall annual global mean CRE_{LIDAR} ($27.0\,W\,m^{-2}$) is produced by opaque clouds. Their effect is maximal (~ 50–$55\,W\,m^{-2}$) over the extra-tropical oceans (60° S and 60° N), where low warm opaque clouds are numerous. Thin clouds contribute only 15 % ($4.0\,W\,m^{-2}$) to the global CRE_{LIDAR}, and their effect is maximal ($\sim 13\,W\,m^{-2}$) over the dry continental polar regions of the Greenland and Antarctic ice sheets, where the thin cloud cover is large (~ 40 %).

6 Evaluation of the new surface LW cloud radiative effect against ground-based stations

6.1 Method

Comparisons between ground-based measurements and the satellite-derived products (CRE_{LIDAR}, CRE_{2BFLX}) provide a direct evaluation of the satellite retrievals but are limited by the difference in the spatial resolution of the satellite-derived product ($2° \times 2°$) and the ground station observations (a few meters). For the satellite retrievals, we extract the monthly $2° \times 2°$ grid box centered at each ground site. For the ground-based observations, we extract the hourly observation at CALIPSO satellite overpass time above each ground site (two observations per day) and average over each month. We consider all days of each month, even if CALIPSO has no sampling over the site, because there are only a few days where CALIPSO observations are not available (e.g., 18 d in 2008). Moreover, in this study, we are interested in an accurate representation of the surface LW CRE interannual variability, which might have significant impacts on climate-relevant processes, and not only in an accurate representation of the anomalies observed in, e.g., Rutan et al. (2015). That CALIPSO is missing some sampling over the ground-based site will likely not significantly affect the interannual variability (i.e., months of maxima/minima of the surface LW CRE). The locations of the three ground-based sites are reported on the maps (stars in Fig. 14).

6.2 Time series

Over the Summit station Greenland site, on average compared to ground-based observations, LWCRE–LIDAR underestimates the surface LW CRE by $8.5\,W\,m^{-2}$, while 2BFLX underestimates it by $16.4\,W\,m^{-2}$ (Fig. 9a). Averages over the 2008–2010 and 2011–2015 periods (Fig. 10) show that these biases calculated for a short period are similar to the longer periods. Over the 2008–2011 time period, CRE_{LIDAR} is close to CRE_{2BFLX}, and both show consistent summer maxima and winter minima, with CRE_{2BFLX} slightly smaller than CRE_{LIDAR} ($0.8\,W\,m^{-2}$). Over the 2011–2015 time period, CRE_{LIDAR} and the ground station data show similar annual cycles, and CRE_{LIDAR} remains smaller than the Greenland site ($13.0\,W\,m^{-2}$). In winter, the bias in CRE_{LIDAR} can go up to $\sim 15\,W\,m^{-2}$ compared to the Greenland site and is partly due to CALIPSO–GOCCP missing thin cloud below 2 km above ground level in winter, as shown in Lacour et al. (2017). While this comparison suggests that LWCRE–LIDAR could be biased somewhat low compared

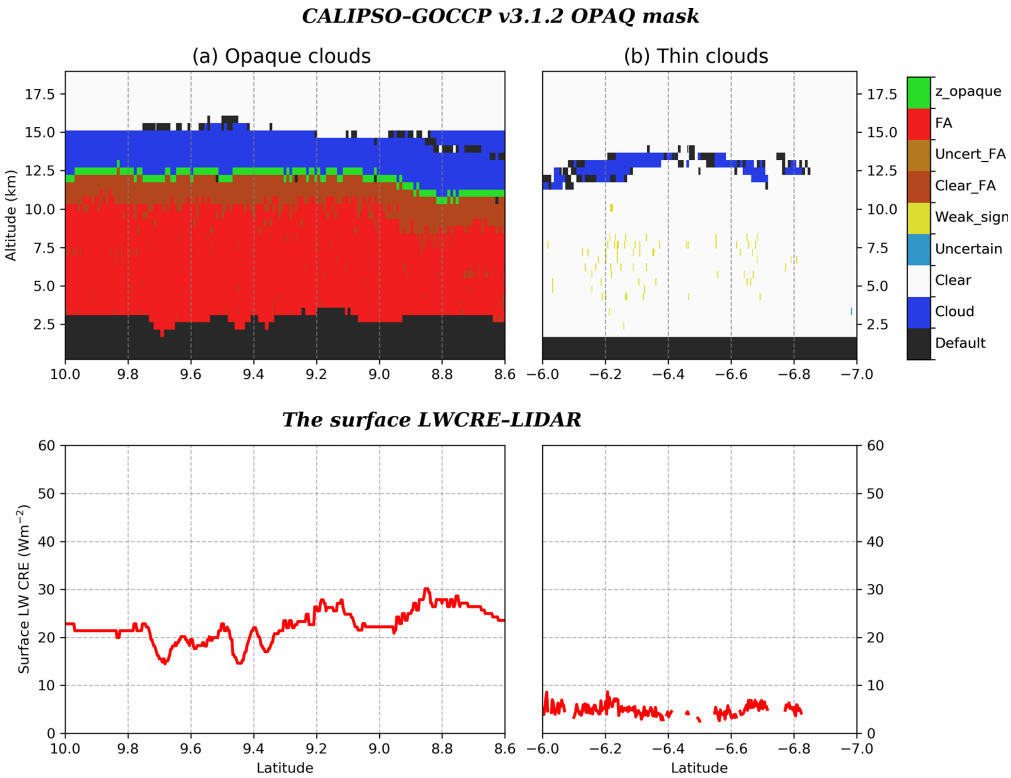

Figure 7. Pieces of the CALIPSO orbit passing over Africa on 11 August 2010 at 23:02:38 LST. Opaque clouds (left column) and thin clouds (right column). Top line: vertical feature mask from the CALIPSO–GOCCP–OPAQ product (Guzman et al., 20017); the black areas below 4 km correspond to land. Bottom line: the surface LWCRE–LIDAR.

to the ground station perspective over Greenland, it is also clear that this approach captures the annual variability with a correlation coefficient between the CRE_{LIDAR} and ground base site of 0.69 and a RMSE of 15.9 W m^{-2}. The retrieval using Z_{FA} instead of $Z_{T_{Opaque}}$ seems to compare to the Greenland ground-based observations more favorably (correlation coefficient of 0.70 and RMSE of 15.0 W m^{-2}) with a smaller bias (−11.6 W m^{-2} vs. −13.6 W m^{-2}, Table 1).

Over the mid-latitude continental site (Fig. 9b) on average, LWCRE–LIDAR underestimates the surface LW CRE by 5.7 W m^{-2} compared to ground-based observations with a correlation coefficient of 0.73 and RMSE of 11.0 W m^{-2}, while 2BFLX underestimates it by 9.4 W m^{-2} with a correlation coefficient of 0.67 and RMSE of 15.5 W m^{-2}.

Over the tropical ocean site (Fig. 9c) on average, LWCRE–LIDAR underestimates the surface LW CRE by 2.3 W m^{-2} compared to ground-based observations, and 2BFLX underestimates it by 4.1 W m^{-2}. This same behavior is found on the map of differences between CRE_{LIDAR} and CRE_{2BFLX} (Fig. 14a) along the tropical Pacific and tropical Atlantic oceans, where 2BFLX underestimates the surface LW CRE compared to LWCRE–LIDAR.

6.3 Seasonal cycle

Figure 10 presents the comparison of seasonal cycles between the satellite retrievals and the ground-based observations.

Over the Greenland site (Fig. 10a, d), LWCRE–LIDAR and 2BFLX find the same seasonal cycle of the surface LW CRE with maxima in July that correspond to the maximum opaque cloud cover, same as the ground-based seasonal cycle.

Over the mid-latitude continental site (Fig. 10b, e), the surface LW CRE seasonal cycles of LWCRE–LIDAR and 2BFLX are close to each other, and the two satellite-derived products show similar seasonal cycles to the ground station.

Over the tropical ocean site (Fig. 10c, f), the surface LW CRE seasonal cycle is relatively flat.

6.4 Diurnal cycle

The time sampling is limited for LWCRE–LIDAR and 2BFLX as they observe each location only two times per day at about 01:30 and 13:30 local solar time (LST), and they do not implement diurnal variation correction in their algorithm. Nevertheless, diurnal variations of the cloud fraction profiles documented by the CATS/ISS lidar (Noel et al., 2018; Chepfer et al., 2019) indicate that the average of the cloud profiles

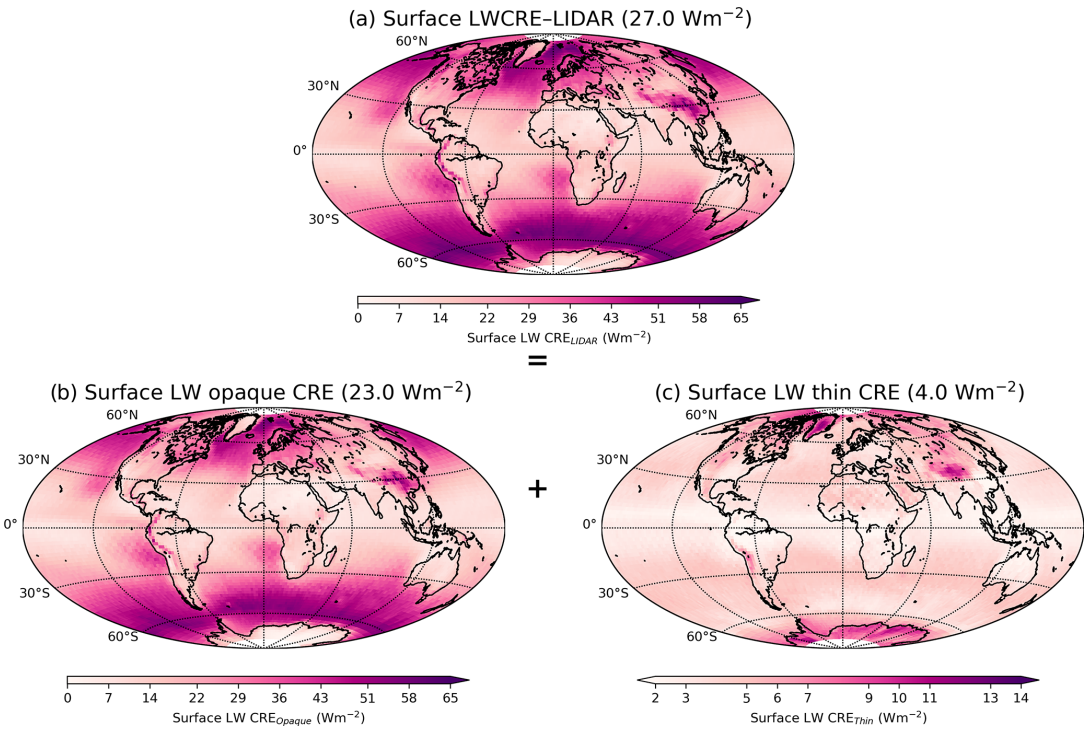

Figure 8. Maps of the surface LW CRE: **(a)** all clouds, **(b)** opaque clouds, and **(c)** thin clouds. This surface LW CRE is built from the CALIPSO–GOCCP v3.1.2 dataset (Fig. 2) and radiative transfer computations (Figs. 4–7, A1). The surface LW CRE is averaged over 2008–2020. Note that the color scale is different in panel **(c)**.

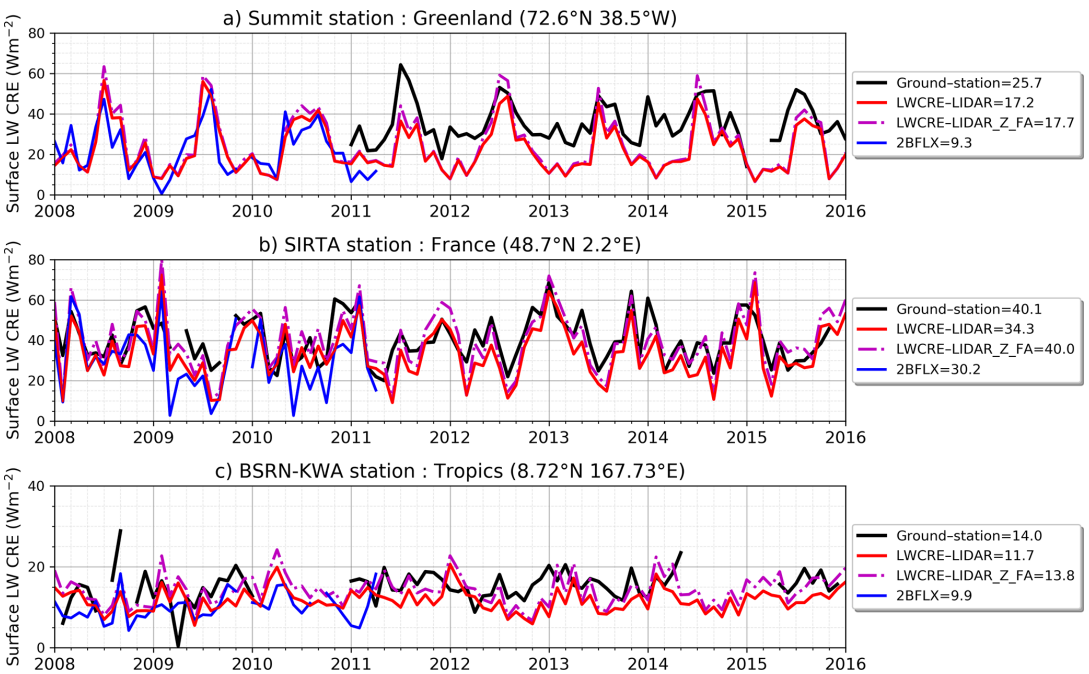

Figure 9. Comparisons between the surface LW CRE derived from ground station measurements and from satellites in three locations: **(a)** polar region at the Greenland Summit site, **(b)** mid-latitudes at the SIRTA site, and **(c)** tropics at the KWA site. Mean values reported in the legend are computed only over the time period when all products are available, e.g., only four months (Jan–Feb–Mar–Apr, 2011) for Greenland Summit mean values. The locations of the three sites are reported in Fig. 14. Note that the y-axis scale is different in each subplot.

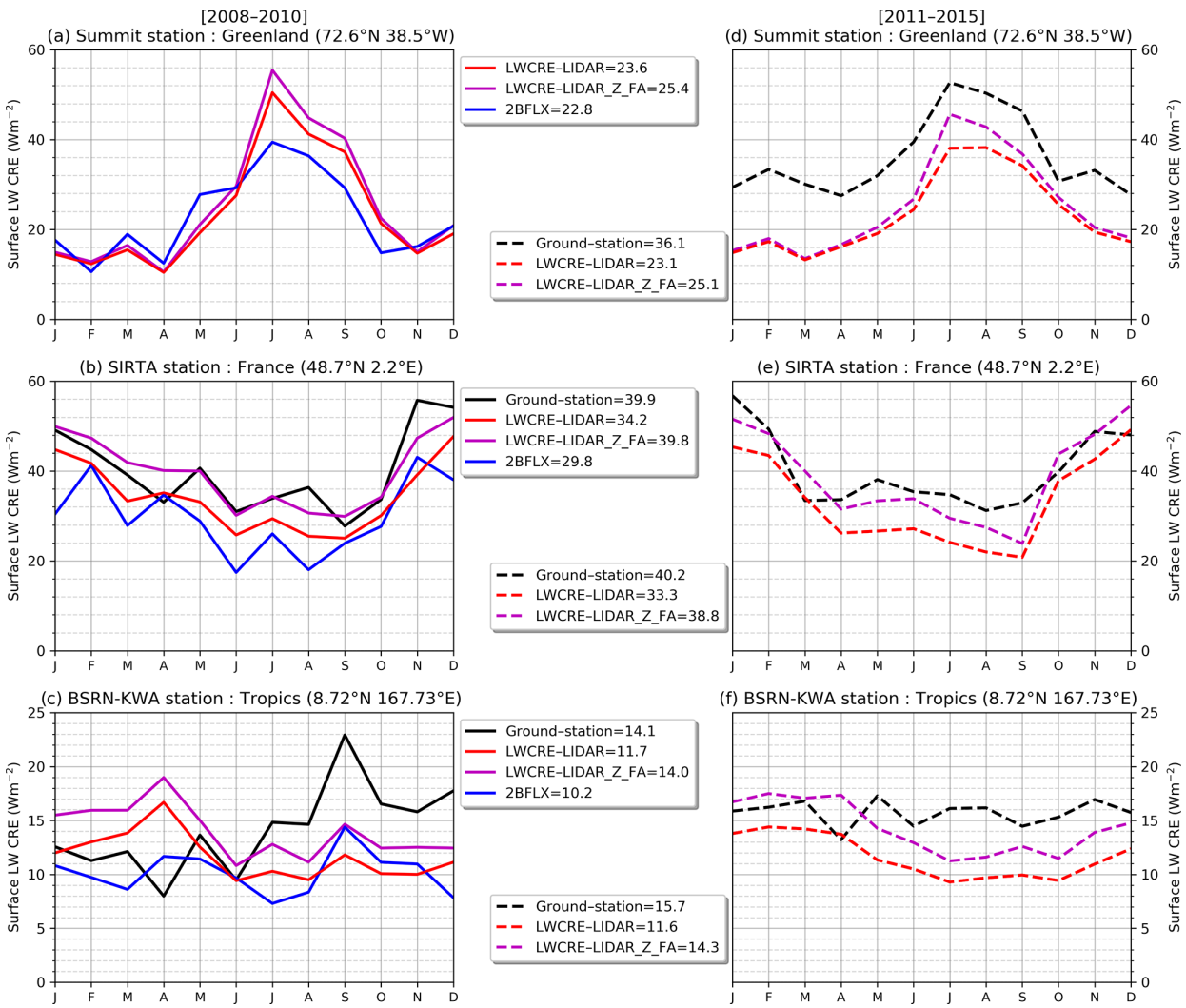

Figure 10. Same as Fig. 9 but in mean seasonal cycles. Panels **(a)**, **(b)**, and **(c)** correspond to 2008–2010 and panels **(d)**, **(e)**, and **(f)** correspond to 2011–2015. Note that the y-axis scale is different in each subplot.

Table 1. Bias, root-mean-squared error (RMSE) and correlation coefficient between satellite products and ground-based observations.

		2008/01-2011/04 periode			2008-2015 periode	
		LWCRE–LIDAR	LWCRE–LIDAR_Z_FA	2BFLX	LWCRE–LIDAR	LWCRE–LIDAR_Z_FA
Greenland	Bias	-8.5	-7.9	-16.4	-13.6	-11.6
	RMSE	9.0	8.4	16.9	15.9	15.0
	Correlation	0.91	0.95	0.45	0.69	0.70
SIRTA	Bias	-5.7	-0.1	-9.9	-6.6	-0.8
	RMSE	11.0	10.4	15.5	10.8	9.5
	Correlation	0.73	0.73	0.67	0.77	0.77
KWA	Bias	-2.3	-0.3	-4.1	-3.4	-0.9
	RMSE	6.1	5.6	6.9	5.7	4.9
	Correlation	0.03	0.15	0.23	0.08	0.21

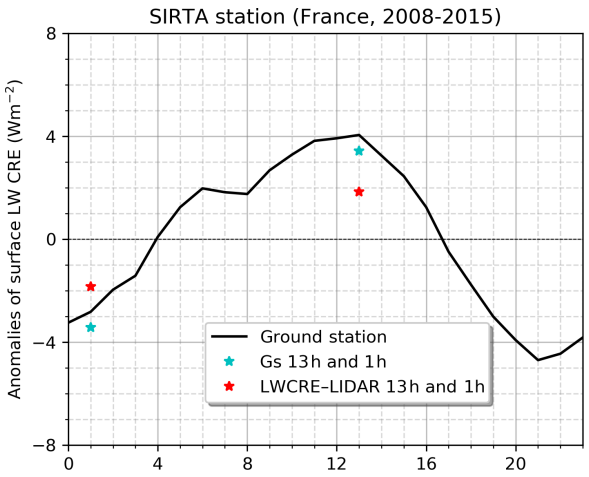

Figure 11. Same as Fig. 9b but in the anomaly of diurnal cycles over 2008–2015.

collected at 01:30 and 13:30 LST is similar to the average of all the profiles collected along the 24 h, with 13:30 LST corresponding to the minimum in cloud profiles along the day and 01:30 LST corresponding to the maximum (Fig. 7 in Noel et al., 2018). However, this statement is valid only between 55° S and 55° N.

Figure 11 shows the diurnal surface LW CRE variation observed at SIRTA in France, together with LWCRE–LIDAR. This comparison suggests that the average of the two CALIPSO overpasses each day is similar to the ground-based observed daily mean over this site. The absence of diurnal cycle correction might not be an important source of error in the LWCRE–LIDAR product.

7 Evaluation of the new surface LW cloud radiative effect against other satellite products

7.1 Comparison along pieces of orbits at footprint scale

CloudSat, CALIPSO, and CERES/Aqua satellites are part of the A-Train constellation (Stephens et al., 2002) and closely matched in time (< 5 min) and hence collocated by default, so we can compare them directly, assuming that the atmospheric changes occurring within 5 min are negligible.

Figure 12 shows a comparison between the surface LW CRE from the three spatial satellite retrievals along four pieces of orbits located over regions with different atmospheres and different surfaces. Figure 12 (top panel) shows the vertical CALIPSO–GOCCP cloud mask (Guzman et al., 2017), while Fig. 12 (bottom panel) represents the comparison between the surface LW CREs.

Orbit A passes over the eastern Pacific Ocean and observes a deep convective tower, a mid-level opaque cloud at an altitude of 7 km, and a low opaque cloud. The differences in surface LW CRE between the three spatial restitutions do not exceed $\sim 5\,\mathrm{W\,m^{-2}}$. Nevertheless, within a small part of the orbit between 11.3 and 11.8° N (Fig. B1), we observe that the LWCRE–LIDAR retrieval is lower than the other two products, because the lidar does not detect a low cloud below Z_{FA}, which is detected by CloudSat (shown in Fig. B1b).

Orbit B passes over the western Pacific Ocean and observes variable yet shallow clouds in the boundary layer (< 2 km). CALIPSO–GOCCP (90 m cross track, 330 m along orbit track) detects well shallow clouds in the boundary layer. $\mathrm{CRE_{LIDAR}}$ compares favorably to $\mathrm{CRE_{2BFLX}}$ over the full scene in presence of shalow clouds but underestimate locally the surface LW CRE in the presence of the deep convective cloud for the same reason as in orbit A (Fig. B1).

Orbit C passes over ocean stratocumulus regions and observes a low opaque cloud. Between 12 and 19° S, the $\mathrm{CRE_{LIDAR}}$ ($\sim 60\,\mathrm{W\,m^{-2}}$) is smaller than $\mathrm{CRE_{2BFLX}}$ by $\sim 5\,\mathrm{W\,m^{-2}}$ and smaller than $\mathrm{CRE_{CERES}}$ by $15\,\mathrm{W\,m^{-2}}$.

Orbit D passes over Antarctica and observes opaque clouds at high (10 km) and mid-level (4–5 km) altitudes. In the presence of high opaque clouds (between 68 and 71° S or between 73 and 77° S), $\mathrm{CRE_{LIDAR}}$ is lower than $\mathrm{CRE_{CERES}}$ by up to $\sim 20\,\mathrm{W\,m^{-2}}$ and $\mathrm{CRE_{2BFLX}}$ by up to $\sim 40\,\mathrm{W\,m^{-2}}$ but typically compares most favorably to $\mathrm{CRE_{CERES}}$ over the full scene.

These orbits show that by not including CloudSat, surface LWCRE–LIDAR is biased low by typically $\sim 10\,\mathrm{W\,m^{-2}}$ compared to 2BFLX and by $\sim 15\,\mathrm{W\,m^{-2}}$ compared to CERES-CCCM in regions of deep convection. In stratocumulus, surface LWCRE–LIDAR is biased low by typically $\sim 5\,\mathrm{W\,m^{-2}}$ compared to 2BFLX and $\sim 15\,\mathrm{W\,m^{-2}}$ compared to CERES-CCCM.

7.2 Global statistic at footprint scale over the ocean

Figure 13a shows a comparison between the surface LW CRE derived from the CALIPSO–GOCCP product (90 m cross track, 330 m along orbit track) collocated with CERES–CCCM that uses full-resolution CALIPSO and CloudSat data and reports the results over 20 km CERES footprints. We consider only the CERES–CCCM footprints where all the CALIPSO–GOCCP profiles falling within this footprint are opaque and where there are more than 40 profiles. To retrieve the surface LWCRE–LIDAR at the CERES–CCCM footprint resolutions, we average all $Z_{T_{\mathrm{Opaque}}}$ falling within CERES–CCCM's footprint and compute the surface LWCRE–LIDAR using the relationships found in Sect. 4.

We see a strong correlation between $\mathrm{CRE_{CERES}}$ and $\mathrm{CRE_{LIDAR}}$ ($R = 0.84$). Two significant departures from the one-to-one comparison line are observed: one for high values of the surface LW CRE and the second for low values. In the first pattern, for surface LW CRE greater than $\sim 70\,\mathrm{W\,m^{-2}}$, $\mathrm{CRE_{LIDAR}}$ is larger than $\mathrm{CRE_{CERES}}$. This pattern corresponds to some low marine opaque clouds in mid-latitude regions (not shown). To reconcile the two products, $\mathrm{CRE_{LIDAR}}$ should be smaller by almost $\sim 5\,\mathrm{W\,m^{-2}}$. One way

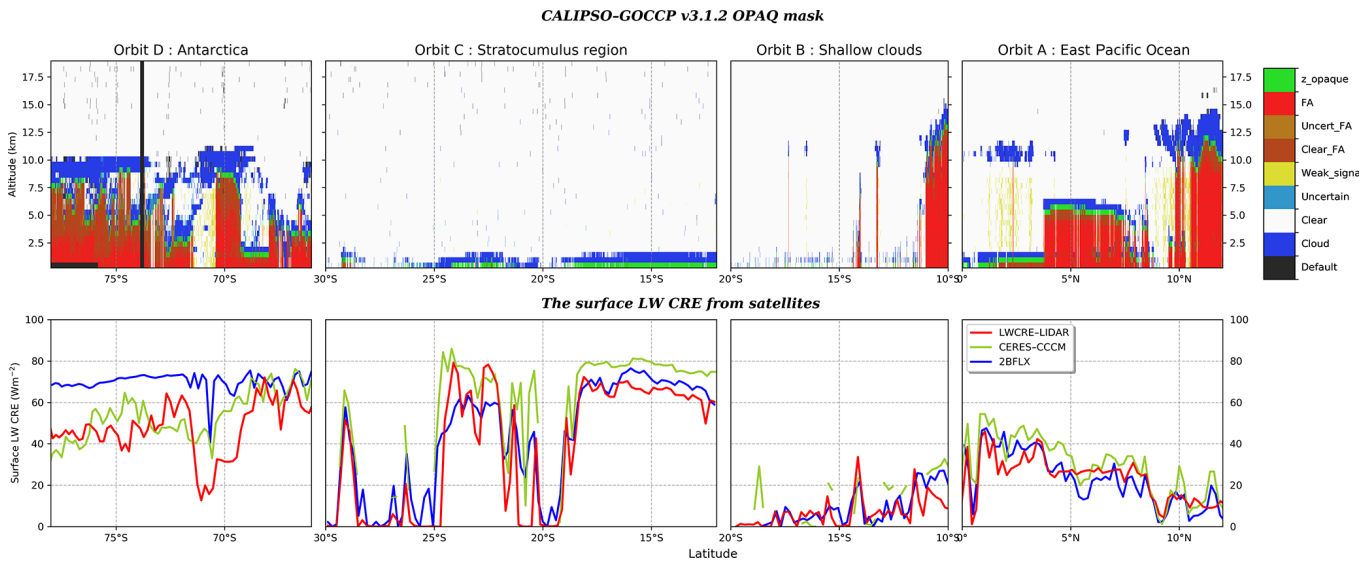

Figure 12. Pieces of CALIPSO orbits passing over **(a)** the eastern Pacific Ocean on 17 October at 08:21:48 LST, **(b)** the shallow cloud region in the Pacific Ocean on 5 April at 12:55:34 LST, **(c)** the stratocumulus region on 13 July at 06:48:37 LST, and **(d)** Antarctica on 21 September at 03:09:46 LST. The four orbit pieces are extracted during the year 2008. Top line: vertical feature mask from the CALIPSO–GOCCP–OPAQ product (Guzman et al., 20017); the black areas below 4 km correspond to land. Bottom line: surface LW CRE of the three satellite products. The locations of the pieces of orbit **(a, b, c, d)** are reported in Fig. 14.

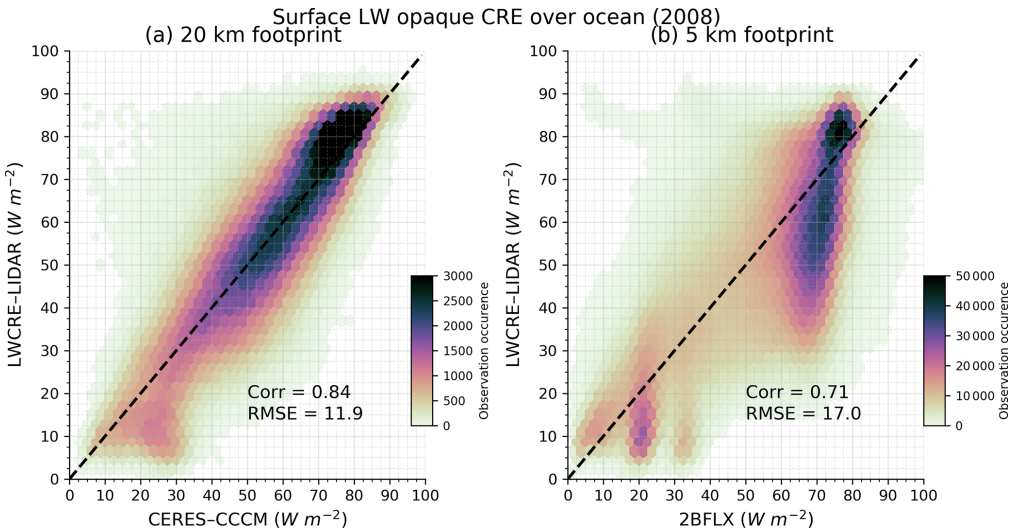

Figure 13. Instantaneous collocated surface LW opaque CRE at footprint scale: **(a)** LWCRE–LIDAR as a function of CERES–CCCM; **(b)** LWCRE–LIDAR as a function of 2BFLX. We only consider CERES (CloudSat) footprints where all CALIPSO footprints falling within the CERES (CloudSat) footprints are opaque and which contain at least 40 (10) profiles. Based on collocated observations over the ocean in 2008.

to reduce this difference would be to increase the altitudes of clouds but, due to attenuation of the signal in opaque clouds, the space-based lidar would already potentially overestimate the overall height of the clouds. Thus, the cloud height is likely not the source of this difference. Another way to reduce the surface LW CRE is by decreasing the cloud cover or the cloud opacity. However, thanks to its high spatial resolution, the space-based lidar measures the cloud cover with precision, and it should not overestimate the cloud opacity. Thus, the source of this apparent bias is more likely an underestimation of the humidity profiles used to retrieve the surface LW CRE in the presence of clouds. An increase in the humidity at these times would increase the $F^{\text{net}}_{\text{Cloudy}-\text{freesky}}$ and therefore decrease the surface LW CRE. A final possibility for the difference is that each product has a unique estimate of the cloud cover due to vastly different fields of view. CALIOP footprints are only a small fraction of the CERES footprint, so part of the CERES footprint could be cloud-

free even if the 40 CALIOP profiles are opaque. A study by Kato et al. (2010) demonstrated that the differences between CERES and CloudSat/CALIPSO cloud fractions decrease when averaged over area and time. Hence, this difference is likely not the primary source of bias when comparing large statistical datasets.

The second regime of differences among the products is for surface LW CRE less than $\sim 30\,\mathrm{W\,m^{-2}}$ (Fig. 13a), which corresponds to high opaque clouds over the warm pool region (not shown). Here, $\mathrm{CRE_{LIDAR}}$ is smaller than $\mathrm{CRE_{CERES}}$. The underestimation of surface LWCRE–LIDAR compared to CERES–CCCM could be caused by the full attenuation of the laser beam in deep convective clouds such that CALIPSO–GOCCP overestimates the mean altitude of opaque clouds.

Figure 13b represents the comparison between the surface LW CRE derived from the CALIPSO–GOCCP product (90 m cross track, 330 m along orbit track) collocated with the CloudSat 2BFLX product at a resolution of the CloudSat footprint (5 km). We also consider only the CloudSat footprints where all the CALIPSO–GOCCP profiles falling within this footprint are opaque and where there are more than 10 profiles, and we compute $\mathrm{CRE_{LIDAR}}$ by averaging all $Z_{T_{\mathrm{Opaque}}}$ falling within the CloudSat footprint.

Three significant departures from the one-to-one comparison line are observed: one for low values where $\mathrm{CRE_{LIDAR}} < \mathrm{CRE_{2BFLX}}$, one for high values of the surface LW CRE where $\mathrm{CRE_{LIDAR}} > \mathrm{CRE_{2BFLX}}$, and one for high values where $\mathrm{CRE_{LIDAR}} < \mathrm{CRE_{2BFLX}}$. The first two patterns appear to be similar to Fig. 13a and show up for the same reasons as described above. The last pattern of differences among the products is for large values of surface LW CRE where $\mathrm{CRE_{2BFLX}}$ is larger than $\mathrm{CRE_{LIDAR}}$. This pattern corresponds to a subsample of marine opaque clouds (25 % of the opaque cloud collocated) in mid-latitude regions (not shown) where CloudSat is able to detect lower clouds than CALIPSO. Using Z_{FA} instead of $Z_{T_{\mathrm{Opaque}}}$ in LWCRE–LIDAR retrieval would shift this pattern upward and reduce the sample (17 % vs. 25 %).

The differences shown in Fig. 13 are expected when comparing satellite products at footprint scales that use different remote sensing techniques. However, when looking at the gridded product distributions (Fig. B3) instead of instantaneous collocated data, the 2BFLX and LWCRE–LIDAR agree well.

7.3 Global mean comparison at gridded scale

To compare 2BFLX and LWCRE–LIDAR at gridded scale, we averaged 2BFLX initially at $1^\circ \times 1^\circ$ resolution to $2^\circ \times 2^\circ$ like the CALIPSO–GOCCP product.

Figure 14a shows global maps of differences between LWCRE–LIDAR and 2BFLX. This comparison gives an overview of the differences between the two surface LW CRE spatial products, but it may mask some differences given the fact that the two spatial products are averaged in time (monthly) and space ($2^\circ \times 2^\circ$ latitude–longitude gridded).

In the global annual mean, $\mathrm{CRE_{LIDAR}}$ is slightly higher compared to $\mathrm{CRE_{2BFLX}}$ ($0.7\,\mathrm{W\,m^{-2}}$).

Compared to 2BFLX (Fig. 14a), $\mathrm{CRE_{LIDAR}}$ is slightly larger than $\mathrm{CRE_{2BFLX}}$ over tropical oceans. Over lands, $\mathrm{CRE_{LIDAR}}$ is slightly lower than $\mathrm{CRE_{2BFLX}}$. The maximum difference occurs over land along the western coasts of the North and South American continents and the Himalayan mountains, where the surface elevation is above 2.5 km. This difference might be due to the CloudSat CPR's long powerful pulse (Fig. B2), which generates a surface clutter echo that tends to partially mask signals from clouds forming below ~ 1 km (Marchand et al., 2008). Over icy polar areas, the two products are very similar.

Zonal averages of the surface LW CRE for 2008–2010 (Fig. 14c) show that the surface LW CRE is generally low in tropical regions and increases towards the mid-latitudes as the atmospheric moisture decreases. Values do not vary much northward of about 50° N. To the south, a maximum occurs at about 60° S, with a decline towards the far south due to less cloudiness. Over the broad domain, reaching from 60° N to 60° S, the two satellite techniques show similar zonal means, with differences among the two typically not exceeding $\sim 3\,\mathrm{W\,m^{-2}}$.

7.4 Variations of 13 years (2008–2020)

Figure 15a shows the temporal evolution of the surface LW CRE anomaly from the two satellite-derived products. A decomposition, separating continents from oceans and Northern Hemisphere (NH) from Southern Hemisphere (SH), is presented in Fig. 17b–g.

The phasing of the annual cycle of $\mathrm{CRE_{LIDAR}}$ and $\mathrm{CRE_{2BFLX}}$ anomalies is roughly similar over the 2008–2010 time period. The phasing of the annual cycle of the two products is actually quite consistent for both the NH and SH over both land and ocean. For the NH land (Fig. 17d), the $\mathrm{CRE_{2BFLX}}$ is slightly larger than $\mathrm{CRE_{LIDAR}}$. However, it is interesting that even over NH land the annual minima match pretty well.

The interannual variability is pretty interesting. For example, the NH winter maximum in LWCRE–LIDAR products appears to vary by up to about $\sim 3\,\mathrm{W\,m^{-2}}$ from year to year. That is the kind of variability that might have significant impacts on climate-relevant processes like melting of the cryosphere.

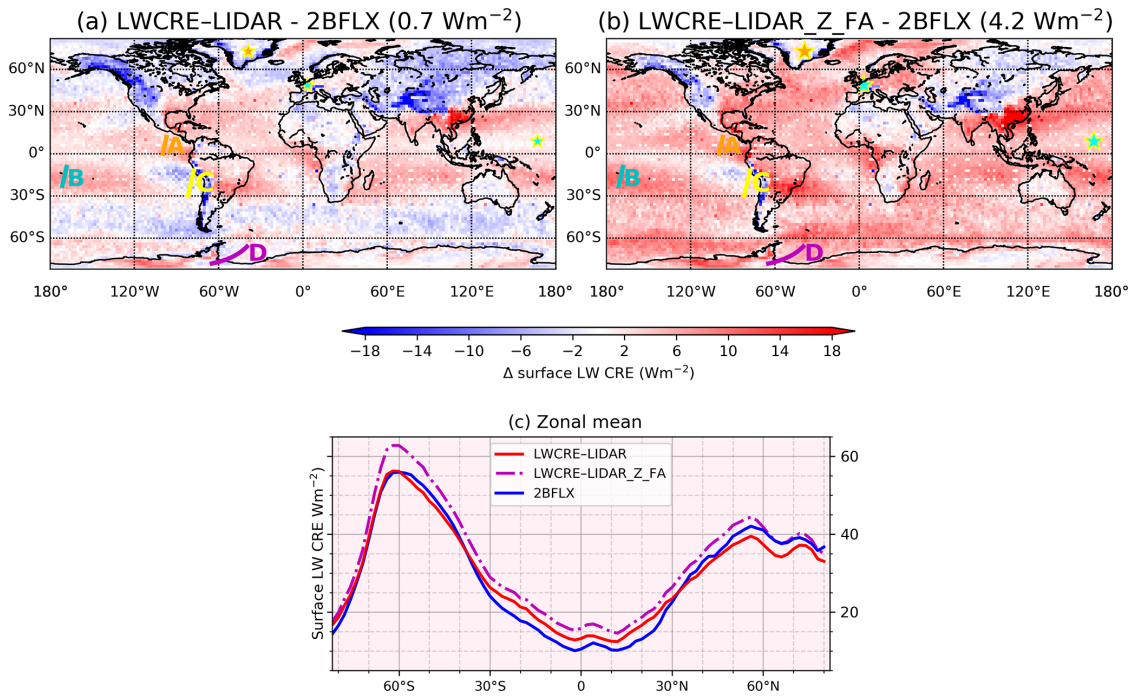

Figure 14. Maps of differences in the surface LW CRE **(a)** LWCRE–LIDAR minus 2BFLX, **(b)** LWCRE–LIDAR_Z_FA minus 2BFLX, and **(c)** zonal means of the two satellite products. Data are averaged over 2008–2010. Locations of the three ground-based sites and pieces of orbits are reported on the maps.

8 Discussion

8.1 About the space lidar missing the opaque cloud base

Based on the comparison of orbits (Fig. B1), we observe that when the space lidar does not see the cloud base, LWCRE–LIDAR underestimates the local surface LW CRE compared to 2BFLX. However, the deep convective opaque clouds cover a small part of the overall tropics compared to other clouds. Therefore, this effect does not dominate the global comparison (Fig. 14a), where surface LWCRE–LIDAR is contrarily slightly larger than the other satellite product. Figure 13b (where 2BFLX is about $\sim 70\,\mathrm{W\,m^{-2}}$) and Fig. 14a (Southern Ocean) consistently suggest that CALIPSO not seeing the cloud base leads to LWCRE–LIDAR underestimating the surface LW CRE more frequently in the extratropical oceanic storm tracks than elsewhere.

To test whether the differences between LWCRE–LIDAR and other satellite products come from the space lidar not seeing the cloud base, we used two different approaches.

First, we used Z_{FA} instead of $Z_{T_{\mathrm{Opaque}}}$ in the LWCRE–LIDAR retrieval. By definition, Z_{FA} is always lower in altitude than $Z_{T_{\mathrm{Opaque}}}$. Therefore, this change should reduce the difference between the surface LWCRE–LIDAR and other surface LW CREs if the differences were due to CALIPSO missing the cloud base. Figure 14b shows that the difference between surface LWCRE–LIDAR and the other satellite product increases instead of decreases when using Z_{FA} instead of $Z_{T_{\mathrm{Opaque}}}$. This suggests that the differences in surface LW CRE are likely not often due to CALIPSO misrepresenting the cloud base and that, in the majority of the cases, the cloud base might not be far from Z_{FA}. Nevertheless, contrary to the satellite retrieval intercomparison, using Z_{FA} instead of $Z_{T_{\mathrm{Opaque}}}$ leads to slightly better agreement between LWCRE–LIDAR and ground-based retrievals (e.g., Figs. 9, 10, Table 1). Ground-based measurements derive directly the surface LW CRE. While there are certainly challenges in comparing ground-based and satellite estimates, we should consider the ground-based estimates to be of pretty high quality.

Second, we used the cloud-base height (called the CBASE dataset) described in Mülmenstädt et al. (2018) instead of Z_{FA} to compute $Z_{T_{\mathrm{Opaque}}}$. In the CBASE dataset, the cloud-base-height value is given at a horizontal resolution of 40 km along the CALIPSO orbit track in the portion of the orbit where clouds are opaque. Along each CALIPSO orbit, we collocated the cloud-base-height dataset with the CALIPSO–GOCCP dataset and replaced Z_{FA} with the cloud-base-height value given in the CBASE dataset. Then we computed $Z_{T_{\mathrm{Opaque}}}$ and the surface LW CRE. CBASE values are distributed at all latitudes and are available in 33.2 % of all the CALIPSO opaque profiles because CBASE can be retrieved only when thin clouds are detected within the 40 km orbit piece that also contains opaque cloud profiles. Comparing Fig. 16a and b indicates that the subsample of opaque

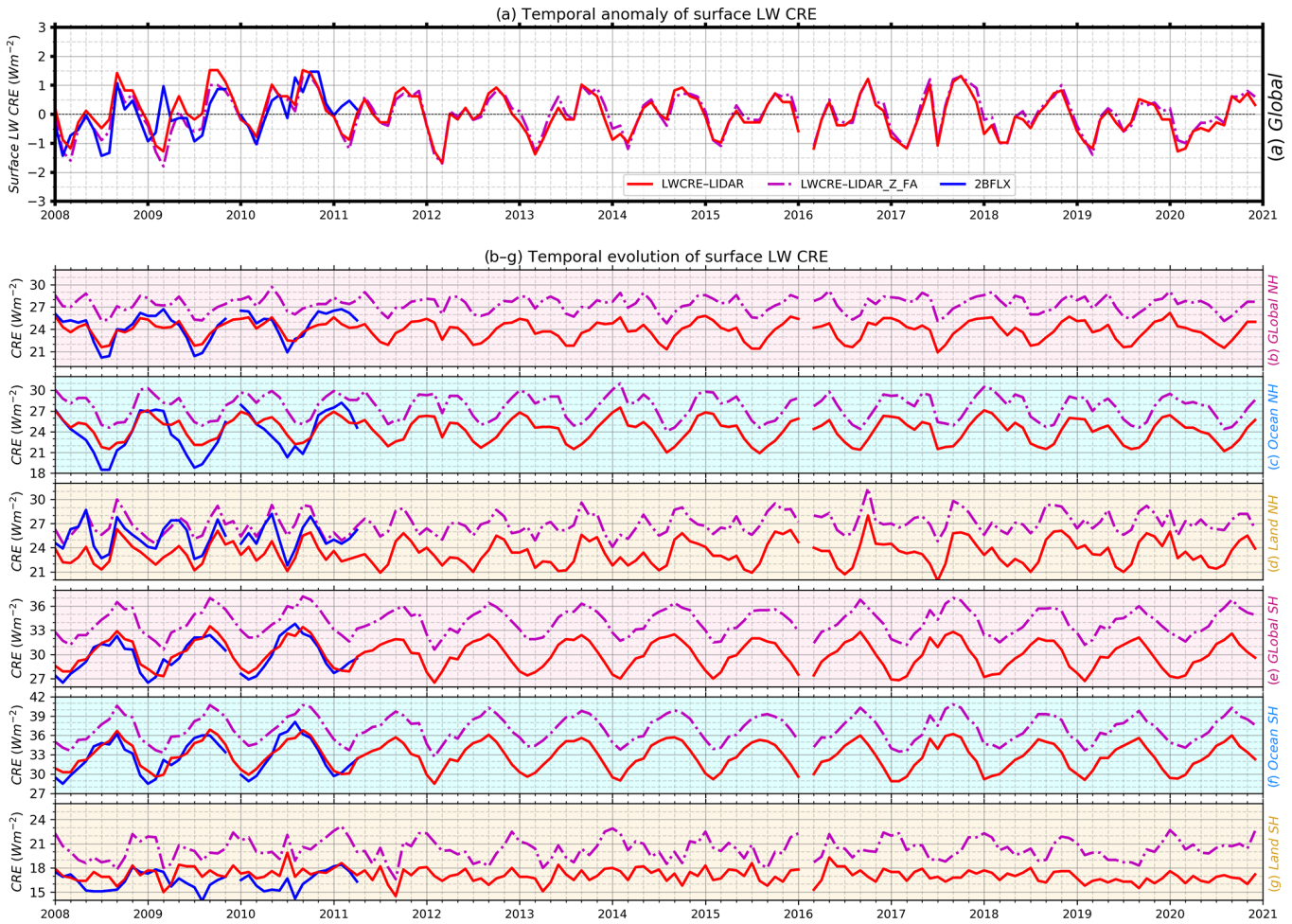

Figure 15. **(a)** Time series of global surface LW CRE anomalies. **(b–f)** Time series of surface LW CREs over all NH, ocean NH, land NH, all SH, ocean SH, and land SH. In panel **(a)** the anomaly is defined as the global average for each month of each product minus its own average over the whole time series. Note that the y-axis scale is different in each subplot.

CALIPSO–GOCCP profiles where CBASE is documented contains both large values of surface LW CRE associated with mid- and low-level clouds located at mid-latitudes (upper right data in panel b) and small values of surface LW CRE (lower left), but it does not include the data where 2BFLX is much larger than LWCRE–LIDAR which correspond to mid-latitude oceanic opaque clouds. When replacing Z_{FA} (Fig. 16b) with CBASE (Fig. 16c) in the LWCRE–LIDAR algorithm, the surface LWCRE–LIDAR rises slightly almost everywhere because CBASE is lower in altitude than Z_{FA}, and surface LWCRE–LIDAR values lower than $\sim 18\,\mathrm{W\,m^{-2}}$ are no longer present. The latter correspond to both deep convective clouds and shallow boundary layer clouds. The correlation between 2BFLX and LWCRE–LIDAR is similar whether we use Z_{FA} (0.79) or CBASE (0.78) in the LWCRE–LIDAR algorithm.

This sensitivity study suggests that using a more advanced cloud base height (here CBASE) derived from lidar measurements than Z_{FA} in the LWCRE–LIDAR algorithm will increase the surface LW CRE value retrieved in some opaque cloud profiles slightly, but it does not fundamentally change the results.

Thus, what these results mean collectively is that (1) the inability of CALIPSO to observe the cloud base likely does have some effect (with respect to ground-based measurements). (2) This effect actually makes the comparison to other satellite products worse, which means that there are other issues (possibly also with the other satellite product), leading to further differences.

8.2 About the sub-daily variability of the humidity and temperature profiles

Looking for other issues that could explain the differences between satellite products, we examined humidity and temperature profiles.

Contrary to the surface LWCRE–LIDAR retrieval method, CERES-CCCM and 2BFLX retrievals of surface flux account for sub-daily variations in temperature/humidity and

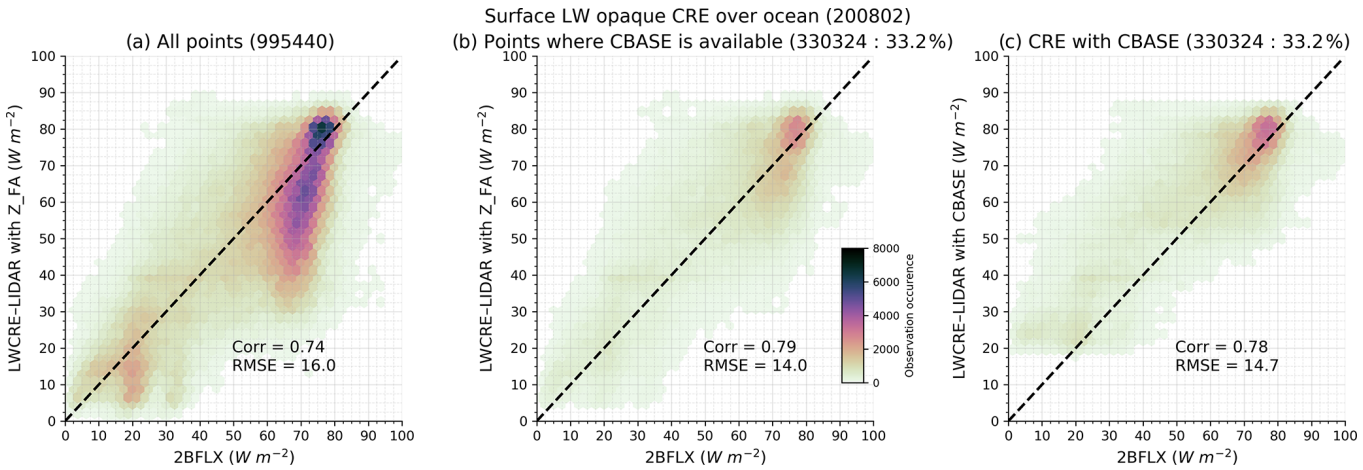

Figure 16. Surface LW CRE derived from LWCRE–LIDAR as a function of the one derived from 2BFLX. **(a)** Surface LWCRE–LIDAR (y axis) computed using the altitude of full lidar attenuation **(b)**, same as **(a)** but containing only the subsample of CALIPSO profiles where cloud-base-height values are available from Mülmenstädt et al. (2018). **(c)** Same as **(b)**, but the surface LWCRE–LIDAR is computed using the cloud-base-height values from Mülmenstädt et al. (2018) instead of the altitude of lidar full attenuation. The color scale indicates the number of occurrences at 5 km resolution (footprint scale of CloudSat) over ocean in February 2008.

capture regional variations (e.g., eastern vs. western tropical Pacific), climate events (e.g., ENSO), and extreme changes over polar regions. 2BFLX uses 3-hourly atmospheric state variable data on a half-degree Cartesian latitude and longitude grid from AN-ECMWF.

As shown in Fig. 14, monthly mean gridded surface LWCRE–LIDAR is consistent with 2BFLX, even though 2BFLX uses sub-daily spatiotemporal resolutions of temperature/humidity profiles, while LWCRE–LIDAR uses monthly mean temperature/humidity profiles. Nevertheless, instantaneous surface LWCRE–LIDAR retrievals are likely more biased than the monthly mean gridded surface LWCRE–LIDAR due to the use of monthly mean temperature/humidity profiles, because monthly means miss extreme humidity and temperature profiles. To estimate the error in the instantaneous surface LWCRE–LIDAR values, we compared the instantaneous surface LWCRE–LIDAR values obtained using 6-hourly temperature/humidity profiles from ERA-I to one obtained using monthly means and 2BFLX, for 1 d at footprint scales.

Figure 17 shows that using sub-daily profiles in LWCRE–LIDAR retrieval makes the comparison to other satellite products worse at footprint scale. More analysis (not shown) indicates that, for thin clouds, surface LWCRE–LIDAR retrieved using sub-daily temperature/humidity profiles agrees better with 2BFLX (at 5 km resolution) than surface LWCRE–LIDAR retrieved using monthly mean profiles. In contrast, the agreement between LWCRE–LIDAR and other products is lower when using sub-daily temperature/humidity profiles in all other cases: opaque clouds and also thin clouds when compared to CERES-CCCM (at 20 km). Overall, this suggests that the differences between the three daily products are likely due to other causes than LWCRE–LIDAR using monthly mean temperature/humidity profiles.

9 Conclusions

In this paper, we build a new surface LWCRE–LIDAR dataset from five cloud properties observed with space-based lidar (CALIPSO–GOCCP product). The robustness of the new surface LWCRE–LIDAR dataset at global scales is evaluated by comparing it to existing independent space-based surface LW CRE retrievals from CERES and CloudSat (Kato et al., 2010; L'Ecuyer et al., 2019) at the instantaneous footprint scale as well as at the $2° \times 2°$ gridded global scale. It is also evaluated locally by comparison to observations collected at three ground stations in polar (Shupe et al., 2013), mid-latitude (Haeffelin et al., 2005; Chiriaco et al., 2018), and tropical (Roesch et al., 2011) locations. The (admittedly limited) ground station comparisons actually showed that the LWCRE–LIDAR product agreed best with the ground measurements compared to the other satellite product. It appears that it captures the interannual variability well. Additionally, there are other specific aspects where the LWCRE–LIDAR product appears to be an improvement over others in providing a longer time series, including over bright polar surfaces.

This might be surprising given the simplicity of the surface radiation retrieval method used to produce the LWCRE–LIDAR product, but this is understandable because of the following two physical elements.

i. The LWCRE–LIDAR method directly retrieves the surface LW CRE without retrieving the surface radiative fluxes first. This approach minimizes the impact of the uncertainties due to surface characteristics (sur-

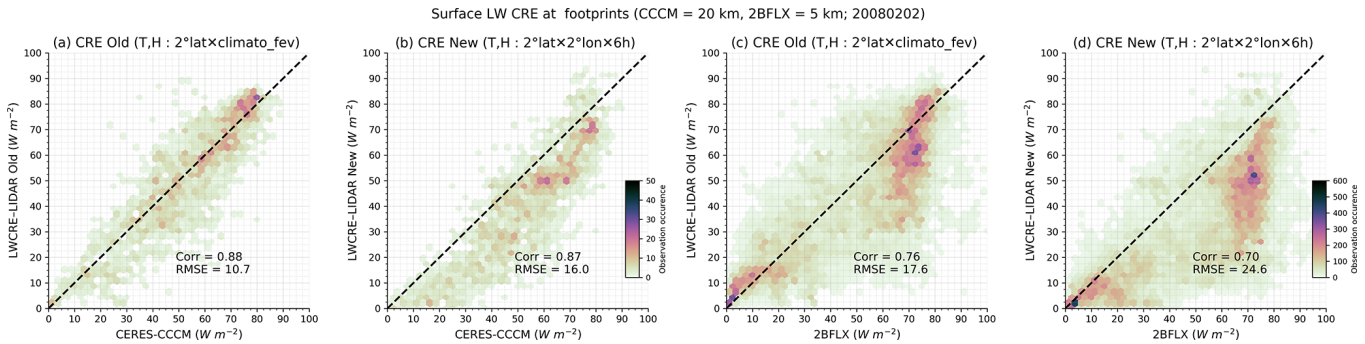

Figure 17. Distribution of the surface LW CRE: **(a)** LWCRE–LIDAR retrieved using monthly mean temperature/humidity profiles as a function of CERES-CCCM with data at 20 km resolution (CERES SSF footprint); **(b)** same as **(a)** but LWCRE–LIDAR retrieved using sub-daily temperature/humidity profiles; **(c, d)** same as **(a, b)** but for 2BFLX instead of CERES-CCCM and using data at 5 km resolution (CloudSat resolution).

face emissivity, roughness, deserts and frozen surfaces), which strongly influence the fluxes but not the surface LW CRE.

ii. The surface LW CRE is primarily driven by the cloud cover, the cloud opacity, and the cloud altitude, which are documented by space-based lidar over all types of surfaces. Moreover, the lidar approach distinguishes quite well the opaque clouds from the optically thin clouds. Lastly, it documents the detailed vertical cloud profile, except below the altitude where the laser is fully attenuated, where we overestimate the mean altitude of opaque clouds. This last limitation only weakly influences the surface LW CRE retrieval because the lidar is fully attenuated at an altitude lower than 3 km above the surface most of the time (Guzman et al., 2017), except in deep convection and some mid-latitude clouds, indeed, in deep convective tropical regions where the attenuation of the lidar beam might not see the whole bottom part of the cloud and can underestimate the surface LW CRE by almost $\sim 5\,\mathrm{W\,m^{-2}}$. All three satellite datasets exhibit some differences relative to ground-based measurements and can go up to $\sim 15\,\mathrm{W\,m^{-2}}$ bias in the surface LW CRE over polar regions. The $\sim 15\,\mathrm{W\,m^{-2}}$ bias in LWCRE–LIDAR over Summit in winter is partly due to CALIPSO–GOCCP missing thin cloud below 2 km above ground level in winter, as shown in Lacour et al. (2017).

The evaluation of this new surface LWCRE–LIDAR against other datasets also showed that (overall) this new retrieval agrees well with CloudSat-based estimates (L'Ecuyer et al., 2019) and CERES–CCCM, but the latter are limited in time until only 2011 due to a battery anomaly.

This new global dataset extends over more than a decade thanks to the long CALIPSO mission. The global mean temporal evolution over 13 years (2008–2020) shows that the maximum anomaly of the surface LWCRE–LIDAR in the NH winter varies by up to about $\sim 3\,\mathrm{W\,m^{-2}}$ from year to year. This new dataset will be extended in time by including future data acquired by CALIPSO as well as data collected by forthcoming space lidars on board the European Earth Cloud, Aerosol and Radiation Explorer mission (EarthCARE; Illingworth et al., 2015) and the next generation of US cloud/aerosol lidar space missions if we are able to reconcile data from successive space lidar missions. The monthly gridded dataset is available for the 2008–2020 time period at https://doi.org/10.14768/70d5f4b5-e740-4d4c-b1ec-f6459f7e5563 (Arouf et al., 2022).

The dataset presented in this paper will be used in a future study to better understand the mechanisms of cloud radiative feedbacks at the Earth's surface, i.e., how a change in surface temperature modifies the cloud properties that change the surface LW CRE, which in turn influences the temperature. An essential first step is to understand which cloud variables have driven the surface LW CRE variations over the last decade in regions that are most sensitive to global warming, such as the polar regions, as well as on a global scale. Several recent studies (e.g., Taylor et al., 2007; Zelinka et al., 2012a, b; Vaillant de Guélis et al., 2017a, b, 2018) have shown that it is possible to attribute changes in CRE to variations in cloud properties when (1) the CRE is related to a limited number of cloud properties by sufficiently simple relationships that they can be derived analytically, (2) the CRE retrieved by these analytical relationships is sufficiently reliable, i.e., within the uncertainty domain of the existing datasets, and (3) the CRE is retrieved using reliable observations over all surface types and on a long global timescale. The surface LWCRE–LIDAR dataset developed in this study satisfies these three conditions. The next step of this work will therefore be to analyze this 13-year dataset to understand these mechanisms. The goal of this research is to improve our understanding of the response of clouds to the warming induced by anthropogenic activities, which is a major source of uncertainty in climate change predictions.

Appendix A: Sensitivity of the surface LW CRE to humidity and temperature

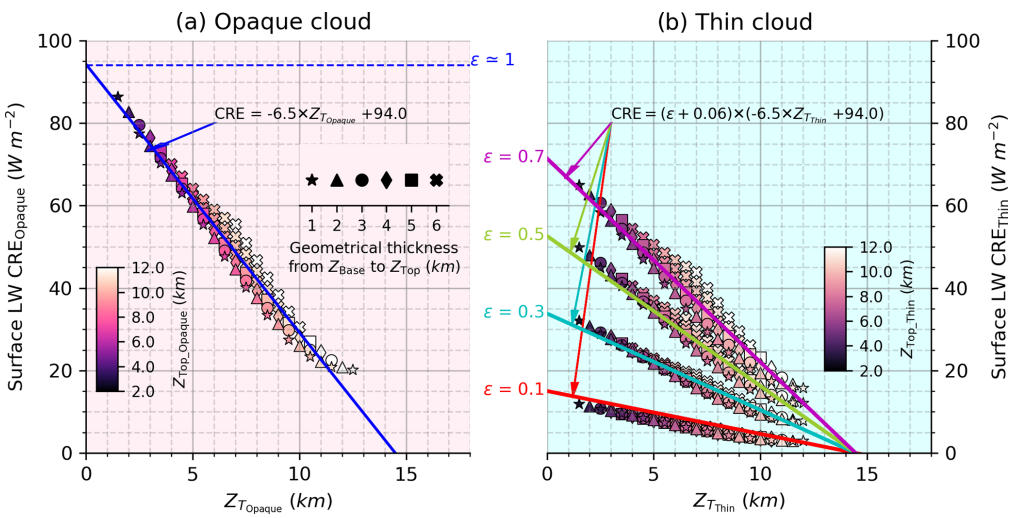

Figure A1. Same as Fig. 3 but over land.

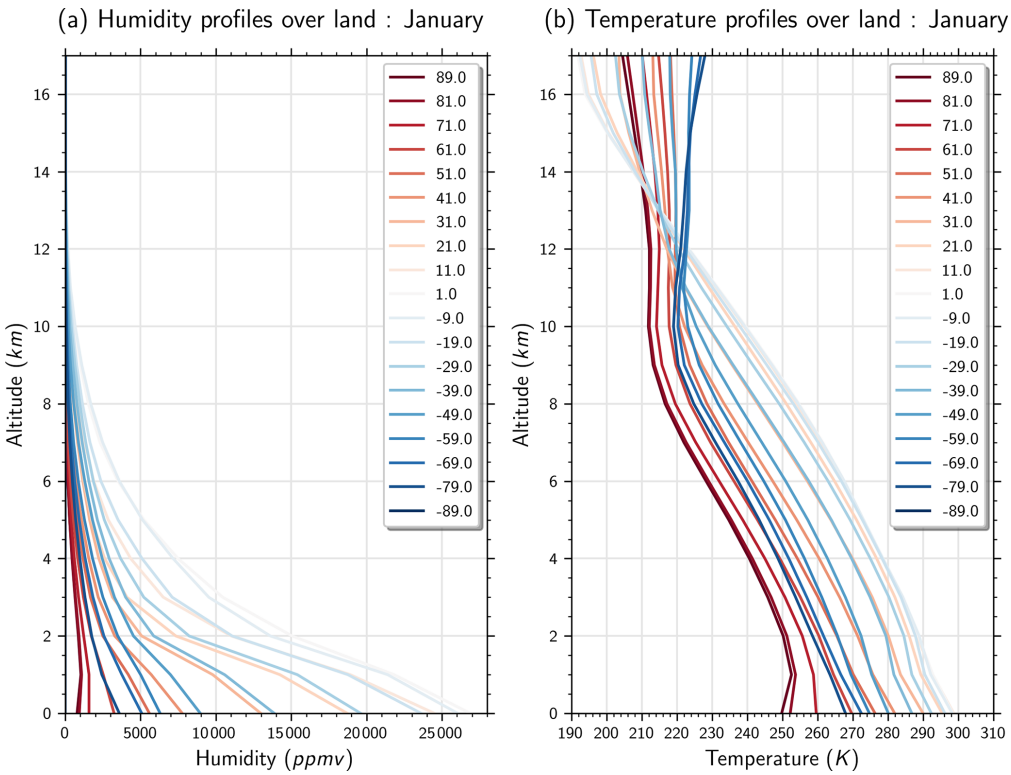

Figure A2. Example of ERA-Interim atmospheric profiles taken over land in January and averaged over 10° latitude bands.

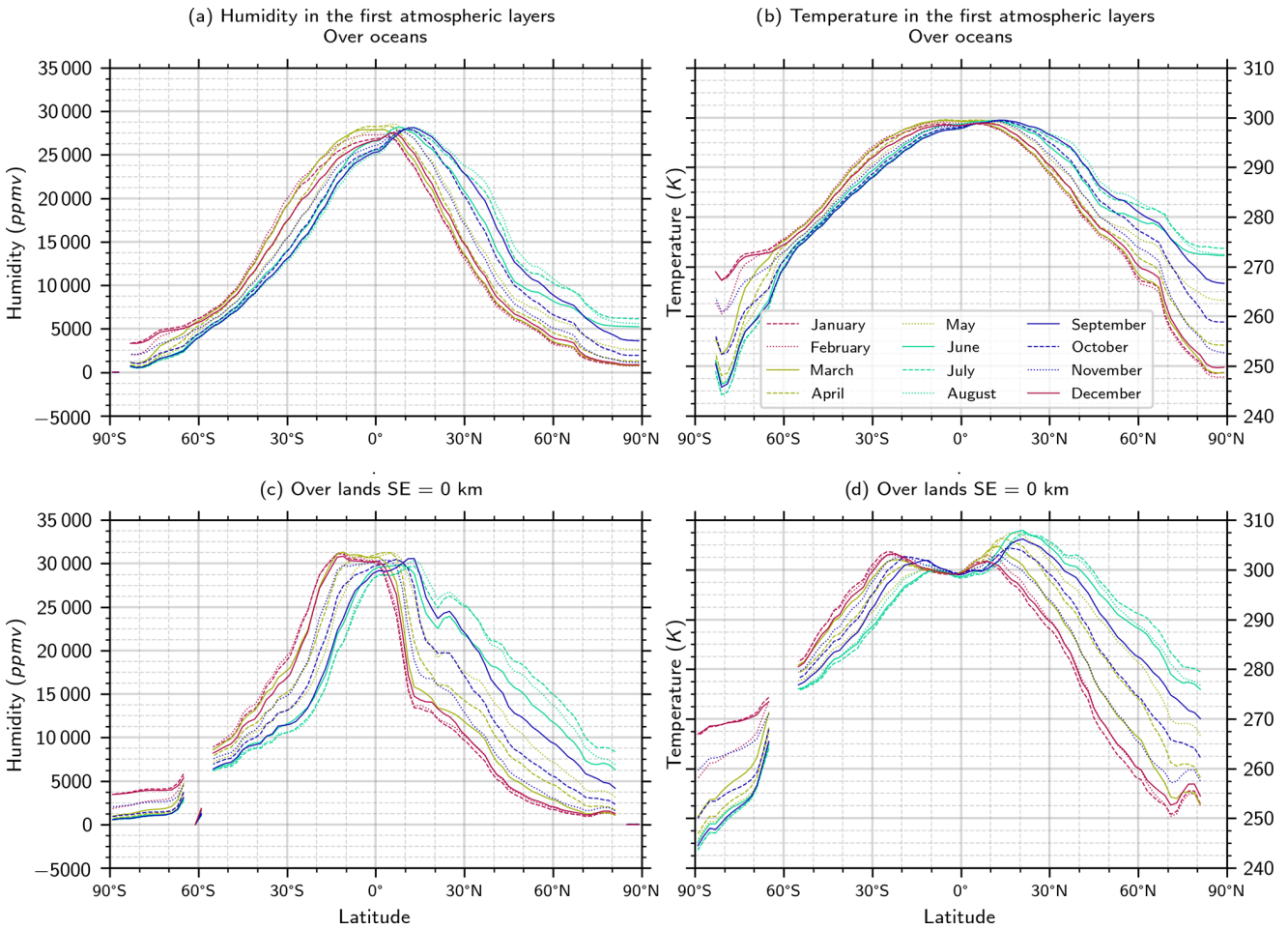

Figure A3. Seasonal and zonal variations of the temperature and humidity in the near-surface atmospheric layer ($Z < 1$ km) from ERA-Interim.

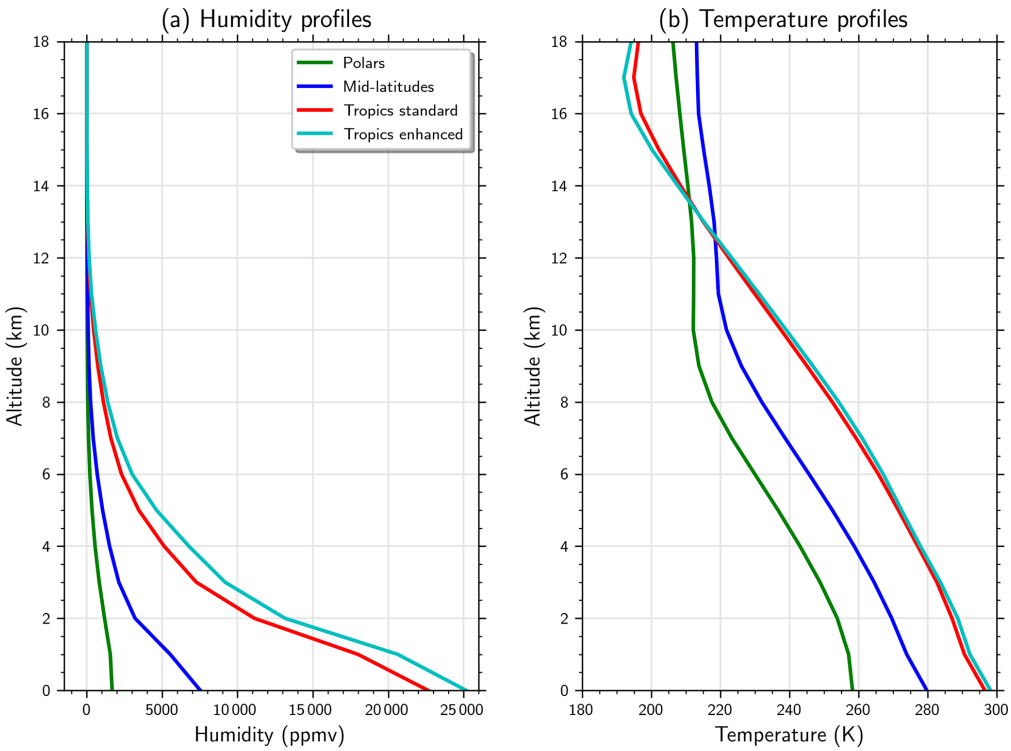

Figure A4. Annual mean profiles of temperature and humidity from ERA-Interim.

Appendix B: Sensitivity of the surface LW CRE to cloud base height

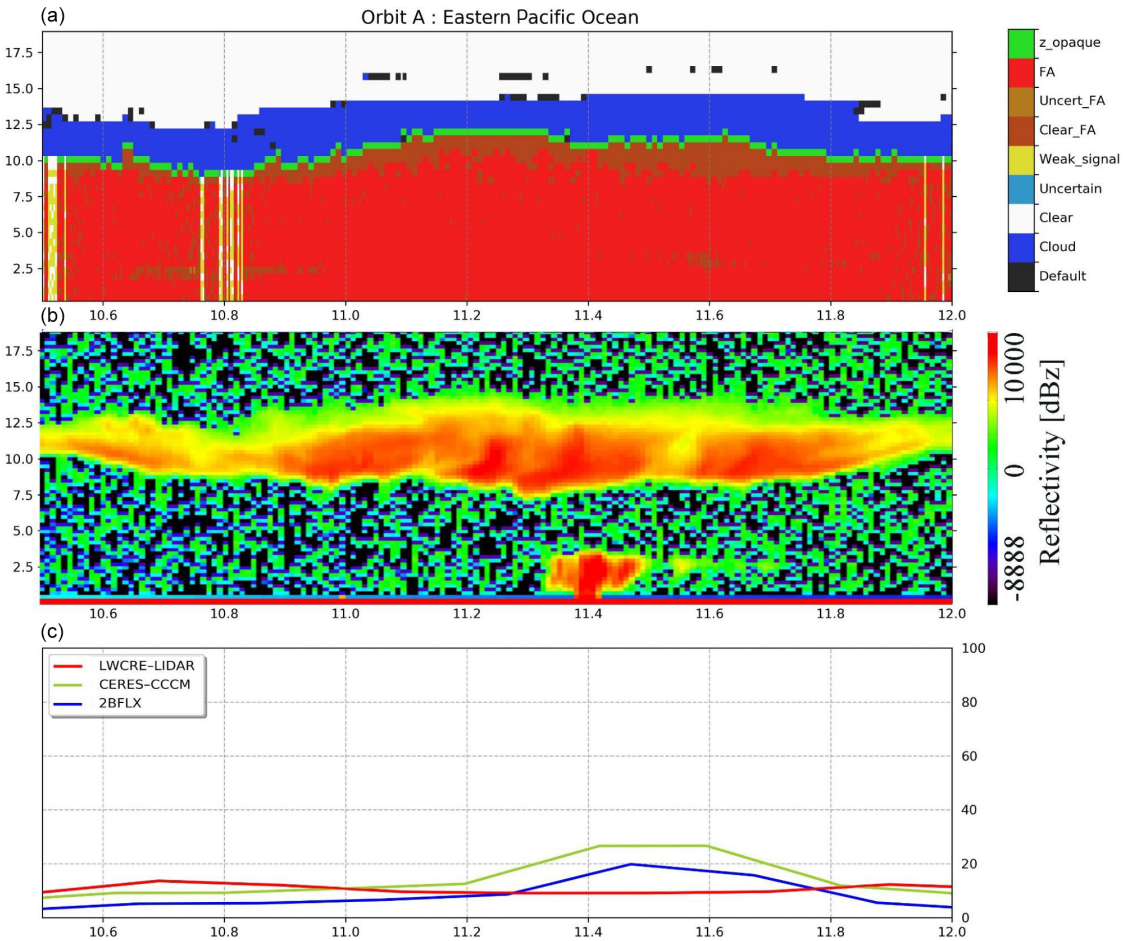

Figure B1. Same as Fig. 12 orbit A between 10.5 and 12° N: **(a)** CALIPSO–GOCCP–OPAQ mask, **(b)** CloudSat reflectivity, and **(c)** surface LW CREs.

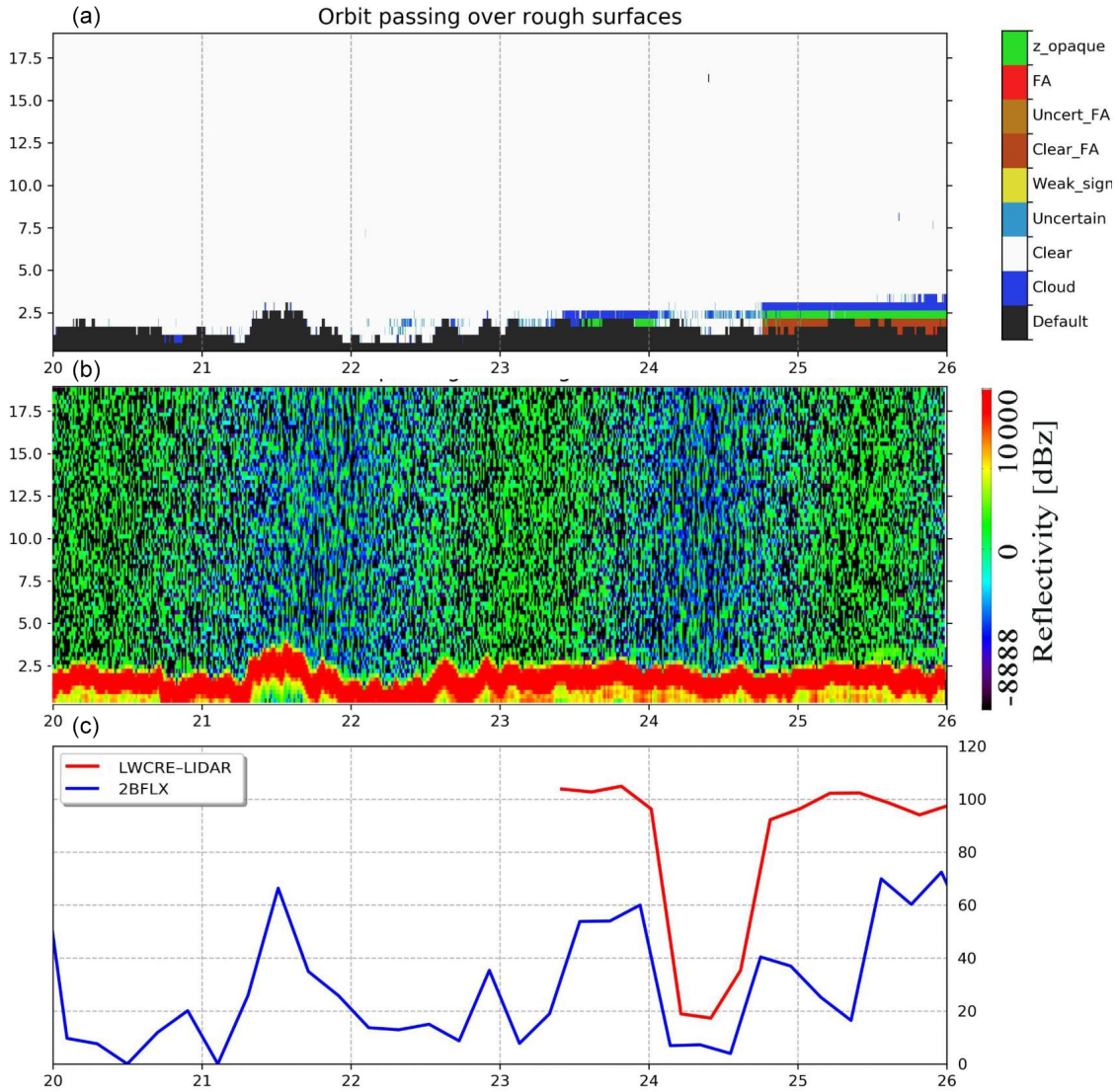

Figure B2. Same as Fig. B1 but for a piece of orbit passing over China on 10 November 2008 at 18:58:39 LST.

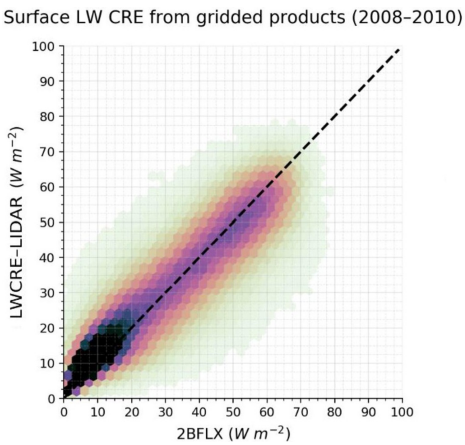

Figure B3. Comparison of monthly 2° × 2° gridded surface LW CRE from LWCRE–LIDAR and 2BFLX.

Appendix C

Table C1. LWCRE–LIDAR–Ed1 monthly gridded products: definitions and variable names.

Geophysical quantity	Variable name in the nc file	Unit	Dim
Time	time	Month	time
Longitude	lon	° E	long
Latitude	lat	° N	lat
Surface cloud radiative effects net longwave flux monthly means (surface LW CRE)	sfc_cre_net_lw_mon	$W\,m^{-2}$	(Time, lat, long)
Surface opaque cloud radiative effects net longwave flux monthly means (surface LW opaque CRE)	sfc_cre_net_lw_mon_opaque	$W\,m^{-2}$	(Time, lat, long)
Surface thin cloud radiative effects net longwave flux monthly means (surface LW thin CRE)	sfc_cre_net_lw_mon_thin	$W\,m^{-2}$	(Time, lat, long)
Surface cloud radiative effects net longwave flux monthly means derived using fully attenuated altitude in opaque scenes (surface LW CRE_Z_FA)	sfc_cre_net_lw_mon_Z_FA	$W\,m^{-2}$	(Time, lat, long)
Top of the atmosphere cloud radiative effects longwave flux monthly means (TOA LW CRE)	toa_cre_lw_mon	$W\,m^{-2}$	(Time, lat, long)
Top of the atmosphere opaque cloud radiative effects longwave flux monthly means (TOA LW opaque CRE)	toa_cre_lw_mon_opaque	$W\,m^{-2}$	(Time, lat, long)
Top of the atmosphere thin cloud radiative effects longwave flux monthly means (TOA LW thin CRE)	toa_cre_lw_mon_thin	$W\,m^{-2}$	(Time, lat, long)
CALIPSO opaque cloud cover (C_Opaque)	cltcalipso_opaque	%	(Time, lat, long)
CALIPSO opaque cloud altitude (Z_T_Opaque)	cltcalipso_opaque_z	km	(Time, lat, long)
CALIPSO fully attenuated altitude (Z_FA)	zopaque	km	(Time, lat, long)
CALIPSO thin cloud cover (C_Thin)	cltcalipso_thin	%	(Time, lat, long)
CALIPSO thin cloud altitude (Z_T_Thin)	cltcalipso_thin_z	km	(Time, lat, long)
CALIPSO thin cloud emissivity (E_Thin)	cltcalipso_thin_emis	1	(Time, lat, long)
Surface elevation	SE	km	(Time, lat, long)

Data availability. The monthly gridded dataset of LWCRE–LIDAR–Ed1 is available for the 2008–2020 time period at https://doi.org/10.14768/70d5f4b5-e740-4d4c-b1ec-f6459f7e5563 (Arouf et al., 2022). The data included in the dataset are presented in Table C1.

Author contributions. Conceptualization, investigation, and methodology were done by HC, AA, and TVdG. Development was done by AA with TVdG with technical support from AF, RG, and PR. Writing the original draft was done by AA and HC. MDS, MC, TSL'E, SK, and MRG brought contributions to the validation of the product and analysis of the results. MDS and TSL'E helped edit the text. The review was done by HC and AA.

Competing interests. The contact author has declared that neither they nor their co-authors have any competing interests.

Disclaimer. Publisher's note: Copernicus Publications remains neutral with regard to jurisdictional claims in published maps and institutional affiliations.

Acknowledgements. We thank Jean Lac for technical support and Erik Hojgard-Olsen for editing the text. We thank NASA/CNES for the CALIPSO level-1 data and the Mesocentre ESPRI/IPSL for the computational resources. We recognize the support of CNES, who supported the development of the CALIPSO–GOCCP product. The

authors thank the anonymous reviewers for their useful comments and help in improving the paper.

Financial support. This research has been supported by EADS (part of a PhD grant for Assia Arouf) and the National Science Foundation (grant nos. PLR-1314156 and OPP-1801477 for Matthew D. Shupe and Michael R. Gallagher).

Review statement. This paper was edited by Manfred Wendisch and reviewed by Hartwig Deneke and two anonymous referees.

References

Acquaotta, F. and Fratianni, S.: The Importance Of The Quality And Reliability Of The Historical Time Series For The Study Of Climate Change, ABClima, 14, 20–38, https://doi.org/10.5380/abclima.v14i1.38168, 2014.

Allan, R. P.: Combining satellite data and models to estimate cloud radiative effect at the surface and in the atmosphere: Cloud radiative effect at the surface and in the atmosphere, Met. Apps, 18, 324–333, https://doi.org/10.1002/met.285, 2011.

Arouf, A., Chepfer, H., Vaillant de Guélis, T., Guzman, R., Feofilov, A., and Raberanto, P.: Longwave Cloud Radiative Effect derived from Space Lidar Observations at the Surface and TOA – Edition 1: Monthly Gridded Product, IPSL [data set], https://doi.org/10.14768/70d5f4b5-e740-4d4c-b1ec-f6459f7e5563, 2022.

Austin, R. T., Heymsfield, A. J., and Stephens, G. L.: Retrieval of ice cloud microphysical parameters using the CloudSat millimeter-wave radar and temperature, J. Geophys. Res., 114, D00A23, https://doi.org/10.1029/2008JD010049, 2009.

Cesana, G., Kay, J. E., Chepfer, H., English, J. M., and Boer, G.: Ubiquitous low-level liquid-containing Arctic clouds: New observations and climate model constraints from CALIPSO-GOCCP, Geophys. Res. Lett., 39, 2012GL053385, https://doi.org/10.1029/2012GL053385, 2012.

Chepfer, H., Bony, S., Winker, D., Cesana, G., Dufresne, J. L., Minnis, P., Stubenrauch, C. J., and Zeng, S.: The GCM-Oriented CALIPSO Cloud Product (CALIPSO–GOCCP), J. Geophys. Res., 115, D00H16, https://doi.org/10.1029/2009JD012251, 2010.

Chepfer, H., Brogniez, H., and Noel, V.: Diurnal variations of cloud and relative humidity profiles across the tropics, Sci. Rep., 9, 16045, https://doi.org/10.1038/s41598-019-52437-6, 2019.

Chiriaco, M., Dupont, J.-C., Bastin, S., Badosa, J., Lopez, J., Haeffelin, M., Chepfer, H., and Guzman, R.: ReOBS: a new approach to synthesize long-term multi-variable dataset and application to the SIRTA supersite, Earth Syst. Sci. Data, 10, 919–940, https://doi.org/10.5194/essd-10-919-2018, 2018.

Chylek, P., Lohmann, U., Dubey, M., Mishchenko, M., Kahn, R., and Ohmura, A.: Limits on climate sensitivity derived from recent satellite and surface observations, J. Geophys. Res., 112, D24S04, https://doi.org/10.1029/2007JD008740, 2007.

Corti, T. and Peter, T.: A simple model for cloud radiative forcing, Atmos. Chem. Phys., 9, 5751–5758, https://doi.org/10.5194/acp-9-5751-2009, 2009.

Curry, J. A., Schramm, J. L., Rossow, W. B., and Randall, D.: Overview of Arctic cloud and radiation characteristics, J. Climate, 9, 1731–1764, https://doi.org/10.1175/1520-0442(1996)009<1731:OOACAR>2.0.CO;2, 1996.

Dee, D. P., Uppala, S. M., Simmons, A. J., Berrisford, P., Poli, P., Kobayashi, S., Andrae, U., Balmaseda, M. A., Balsamo, G., Bauer, P., Bechtold, P., Beljaars, A. C. M., van de Berg, L., Bidlot, J., Bormann, N., Delsol, C., Dragani, R., Fuentes, M., Geer, A. J., Haimberger, L., Healy, S. B., Hersbach, H., Hólm, E. V., Isaksen, L., Kållberg, P., Köhler, M., Matricardi, M., McNally, A. P., Monge-Sanz, B. M., Morcrette, J.-J., Park, B.-K., Peubey, C., de Rosnay, P., Tavolato, C., Thépaut, J.-N., and Vitart, F.: The ERA-Interim reanalysis: configuration and performance of the data assimilation system, Q. J. Roy. Meteorol. Soc., 137, 553–597, https://doi.org/10.1002/qj.828, 2011.

Driemel, A., Augustine, J., Behrens, K., Colle, S., Cox, C., Cuevas-Agulló, E., Denn, F. M., Duprat, T., Fukuda, M., Grobe, H., Haeffelin, M., Hodges, G., Hyett, N., Ijima, O., Kallis, A., Knap, W., Kustov, V., Long, C. N., Longenecker, D., Lupi, A., Maturilli, M., Mimouni, M., Ntsangwane, L., Ogihara, H., Olano, X., Olefs, M., Omori, M., Passamani, L., Pereira, E. B., Schmithüsen, H., Schumacher, S., Sieger, R., Tamlyn, J., Vogt, R., Vuilleumier, L., Xia, X., Ohmura, A., and König-Langlo, G.: Baseline Surface Radiation Network (BSRN): structure and data description (1992–2017), Earth Syst. Sci. Data, 10, 1491–1501, https://doi.org/10.5194/essd-10-1491-2018, 2018.

Dubuisson, P., Dessailly, D., Vesperini, M., and Frouin, R.: Water vapor retrieval over ocean using near-infrared radiometry, J. Geophys. Res., 109, D19106, https://doi.org/10.1029/2004JD004516, 2004.

Dupont, J.-C. and Haeffelin, M.: Observed instantaneous cirrus radiative effect on surface-level shortwave and longwave irradiances, J. Geophys. Res., 113, D21202, https://doi.org/10.1029/2008JD009838, 2008.

Gallagher, M. R., Shupe, M. D., and Miller, N. B.: Impact of Atmospheric Circulation on Temperature, Clouds, and Radiation at Summit Station, Greenland, with Self-Organizing Maps, J. Climate, 31, 8895–8915, https://doi.org/10.1175/JCLI-D-17-0893.1, 2018.

Garnier, A., Pelon, J., Vaughan, M. A., Winker, D. M., Trepte, C. R., and Dubuisson, P.: Lidar multiple scattering factors inferred from CALIPSO lidar and IIR retrievals of semi-transparent cirrus cloud optical depths over oceans, Atmos. Meas. Tech., 8, 2759–2774, https://doi.org/10.5194/amt-8-2759-2015, 2015.

Guzman, R., Chepfer, H., Noel, V., Vaillant de Guélis, T., Kay, J. E., Raberanto, P., Cesana, G., Vaughan, M. A., and Winker, D. M.: Direct atmosphere opacity observations from CALIPSO provide new constraints on cloud-radiation interactions: GOCCP v3.0 OPAQ Algorithm, J. Geophys. Res.-Atmos., 122, 1066–1085, https://doi.org/10.1002/2016JD025946, 2017.

Haeffelin, M., Barthès, L., Bock, O., Boitel, C., Bony, S., Bouniol, D., Chepfer, H., Chiriaco, M., Cuesta, J., Delanoë, J., Drobinski, P., Dufresne, J.-L., Flamant, C., Grall, M., Hodzic, A., Hourdin, F., Lapouge, F., Lemaître, Y., Mathieu, A., Morille, Y., Naud, C., Noël, V., O'Hirok, W., Pelon, J., Pietras, C., Protat, A., Romand, B., Scialom, G., and Vautard, R.: SIRTA, a ground-based atmospheric observatory for cloud and aerosol research, Ann. Geophys., 23, 253–275, https://doi.org/10.5194/angeo-23-253-2005, 2005.

Ham, S.-H., Kato, S., Rose, F. G., Winker, D., L'Ecuyer, T., Mace, G. G., Painemal, D., Sun-Mack, S., Chen, Y., and Miller, W. F.: Cloud occurrences and cloud radiative effects (CREs) from CERES-CALIPSO-CloudSat-MODIS (CCCM) and CloudSat radar-lidar (RL) products: CCCM Versus CloudSat RL Products, J. Geophys. Res.-Atmos., 122, 8852–8884, https://doi.org/10.1002/2017JD026725, 2017.

Hang, Y., L'Ecuyer, T. S., Henderson, D. S., Matus, A. V., and Wang, Z.: Reassessing the Effect of Cloud Type on Earth's Energy Balance in the Age of Active Spaceborne Observations. Part II: Atmospheric Heating, J. Climate, 32, 6219–6236, https://doi.org/10.1175/JCLI-D-18-0754.1, 2019.

He, Y., Risi, C., Gao, J., Masson-Delmotte, V., Yao, T., Lai, C.-T., Ding, Y., Worden, J., Frankenberg, C., Chepfer, H., and Cesana, G.: Impact of atmospheric convection on south Tibet summer precipitation isotopologue composition using a combination of in situ measurements, satellite data, and atmospheric general circulation modeling: IMPACT OF CONVECTION ON TP ISOTOPIC, J. Geophys. Res.-Atmos., 120, 3852–3871, https://doi.org/10.1002/2014JD022180, 2015.

Henderson, D. S., L'Ecuyer, T., Stephens, G., Partain, P., and Sekiguchi, M.: A Multisensor Perspective on the Radiative Impacts of Clouds and Aerosols, 52, 853–871, https://doi.org/10.1175/JAMC-D-12-025.1, 2013.

Hofer, S., Tedstone, A. J., Fettweis, X., and Bamber, J. L.: Decreasing cloud cover drives the recent mass loss on the Greenland Ice Sheet, Sci. Adv., 3, e1700584, https://doi.org/10.1126/sciadv.1700584, 2017.

Illingworth, A. J., Barker, H. W., Beljaars, A., Ceccaldi, M., Chepfer, H., Clerbaux, N., Cole, J., Delanoë, J., Domenech, C., Donovan, D. P., Fukuda, S., Hirakata, M., Hogan, R. J., Huenerbein, A., Kollias, P., Kubota, T., Nakajima, T., Nakajima, T. Y., Nishizawa, T., Ohno, Y., Okamoto, H., Oki, R., Sato, K., Satoh, M., Shephard, M. W., Velázquez-Blázquez, A., Wandinger, U., Wehr, T., and Zadelhoff, G.-J. van: The EarthCARE Satellite: The Next Step Forward in Global Measurements of Clouds, Aerosols, Precipitation, and Radiation, B. Am. Meteorol. Soc., 96, 1311–1332, https://doi.org/10.1175/BAMS-D-12-00227.1, 2015.

Intrieri, J. M., Fairall, C. F., Shupe, M. D., Persson, P. O. G., Andreas, E. L., Guest, P., and Moritz, R. M.: An annual cycle of Arctic surface cloud forcing at SHEBA, J. Geophys. Res., 107, 8039, https://doi.org/10.1029/2000JC000439, 2002.

IPCC: Climate Change 2021: The Physical Science Basis. Contribution of Working Group I to the Sixth Assessment Report of the Intergovernmental Panel on Climate Change, edited by: Masson-Delmotte, V., Zhai, P., Pirani, A., Connors, S., L, Péan, C., Berger, S., Caud, N., Chen, Y., Goldfarb, L., Gomis, M., I, Huang, M., Leitzell, K., Lonnoy, E., Matthews, J., B, R, Maycock, T., K, Waterfield, T., Yelekçi, O., Yu, R., and Zhou, B., Cambridge University Press, in press, 2022.

Kato, S., Sun-Mack, S., Miller, W. F., Rose, F. G., Chen, Y., Minnis, P., and Wielicki, B. A.: Relationships among cloud occurrence frequency, overlap, and effective thickness derived from CALIPSO and CloudSat merged cloud vertical profiles, J. Geophys. Res., 115, D00H28, https://doi.org/10.1029/2009JD012277, 2010.

Kato, S., Rose, F. G., Sun-Mack, S., Miller, W. F., Chen, Y., Rutan, D. A., Stephens, G. L., Loeb, N. G., Minnis, P., Wielicki, B. A., Winker, D. M., Charlock, T. P., Stackhouse, P. W., Xu, K.-M., and Collins, W. D.: Improvements of top-of-atmosphere and surface irradiance computations with CALIPSO-, CloudSat-, and MODIS-derived cloud and aerosol properties, J. Geophys. Res., 116, D19209, https://doi.org/10.1029/2011JD016050, 2011.

Kato, S., Rose, F. G., Rutan, D. A., Thorsen, T. J., Loeb, N. G., Doelling, D. R., Huang, X., Smith, W. L., Su, W., and Ham, S.-H.: Surface Irradiances of Edition 4.0 Clouds and the Earth's Radiant Energy System (CERES) Energy Balanced and Filled (EBAF) Data Product, J. Climate, 31, 4501–4527, https://doi.org/10.1175/JCLI-D-17-0523.1, 2018.

Kato, S., Rose, F. G., Ham, S. H., Rutan, D. A., Radkevich, A., Caldwell, T. E., Sun-Mack, S., Miller, W. F., and Chen, Y.: Radiative Heating Rates Computed With Clouds Derived From Satellite-Based Passive and Active Sensors and their Effects on Generation of Available Potential Energy, J. Geophys. Res.-Atmos., 124, 1720–1740, https://doi.org/10.1029/2018JD028878, 2019.

Kay, J. E., Hillman, B. R., Klein, S. A., Zhang, Y., Medeiros, B., Pincus, R., Gettelman, A., Eaton, B., Boyle, J., Marchand, R., and Ackerman, T. P.: Exposing Global Cloud Biases in the Community Atmosphere Model (CAM) Using Satellite Observations and Their Corresponding Instrument Simulators, J. Climate, 25, 5190–5207, https://doi.org/10.1175/JCLI-D-11-00469.1, 2012.

Kay, J. E., Deser, C., Phillips, A., Mai, A., Hannay, C., Strand, G., Arblaster, J. M., Bates, S. C., Danabasoglu, G., Edwards, J., Holland, M., Kushner, P., Lamarque, J.-F., Lawrence, D., Lindsay, K., Middleton, A., Munoz, E., Neale, R., Oleson, K., Polvani, L., and Vertenstein, M.: The Community Earth System Model (CESM) Large Ensemble Project: A Community Resource for Studying Climate Change in the Presence of Internal Climate Variability, B. Am. Meteorol. Soc., 96, 1333–1349, https://doi.org/10.1175/BAMS-D-13-00255.1, 2015.

King, J. C., Gadian, A., Kirchgaessner, A., Kuipers Munneke, P., Lachlan-Cope, T. A., Orr, A., Reijmer, C., van den Broeke, M. R., van Wessem, J. M., and Weeks, M.: Validation of the summertime surface energy budget of Larsen C Ice Shelf (Antarctica) as represented in three high-resolution atmospheric models: Surface energy budget of Larsen C, J. Geophys. Res.-Atmos., 120, 1335–1347, https://doi.org/10.1002/2014JD022604, 2015.

Kopp, R. E., Kemp, A. C., Bittermann, K., Horton, B. P., Donnelly, J. P., Gehrels, W. R., Hay, C. C., Mitrovica, J. X., Morrow, E. D., and Rahmstorf, S.: Temperature-driven global sea-level variability in the Common Era, P. Natl. Acad. Sci. USA, 113, E1434–E1441, https://doi.org/10.1073/pnas.1517056113, 2016.

Kwok, R. and Untersteiner, N.: The thinning of Arctic sea ice, Physics Today, 64, 36–41, https://doi.org/10.1063/1.3580491, 2011.

Lacour, A., Chepfer, H., Shupe, M. D., Miller, N. B., Noel, V., Kay, J., Turner, D. D., and Guzman, R.: Greenland Clouds Observed in *CALIPSO* -GOCCP: Comparison with Ground-Based Summit Observations, J. Climate, 30, 6065–6083, https://doi.org/10.1175/JCLI-D-16-0552.1, 2017.

Lacour, A., Chepfer, H., Miller, N. B., Shupe, M. D., Noel, V., Fettweis, X., Gallee, H., Kay, J. E., Guzman, R., and Cole, J.: How Well Are Clouds Simulated over Greenland in Climate Models? Consequences for the Surface Cloud Radiative Effect over the Ice Sheet, J. Climate, 31, 9293–9312, https://doi.org/10.1175/JCLI-D-18-0023.1, 2018.

L'Ecuyer, T. S., Wood, N. B., Haladay, T., Stephens, G. L., and Stackhouse, P. W.: Impact of clouds on atmospheric heating based on the R04 CloudSat fluxes and heating rates data set, J. Geophys. Res., 113, D00A15, https://doi.org/10.1029/2008JD009951, 2008.

L'Ecuyer, T. S., Hang, Y., Matus, A. V., and Wang, Z.: Reassessing the Effect of Cloud Type on Earth's Energy Balance in the Age of Active Spaceborne Observations. Part I: Top of Atmosphere and Surface, J. Climate, 32, 6197–6217, https://doi.org/10.1175/JCLI-D-18-0753.1, 2019.

Lindzen, R. S. and Choi, Y.-S.: The Iris Effect: A Review, Asia-Pacific J. Atmos. Sci., 58, 159–168, https://doi.org/10.1007/s13143-021-00238-1, 2021.

Loeb, N. G., Kato, S., Loukachine, K., and Manalo-Smith, N.: Angular Distribution Models for Top-of-Atmosphere Radiative Flux Estimation from the Clouds and the Earth's Radiant Energy System Instrument on the Terra Satellite. Part I: Methodology, J. Atmos. Ocean. Tech., 22, 338–351, https://doi.org/10.1175/JTECH1712.1, 2005.

Loeb, N. G., Kato, S., Loukachine, K., Manalo-Smith, N., and Doelling, D. R.: Angular Distribution Models for Top-of-Atmosphere Radiative Flux Estimation from the Clouds and the Earth's Radiant Energy System Instrument on the Terra Satellite. Part II: Validation, J. Atmos. Ocean. Tech., 24, 564–584, https://doi.org/10.1175/JTECH1983.1, 2007.

Loeb, N. G., Wang, H., Cheng, A., Kato, S., Fasullo, J. T., Xu, K.-M., and Allan, R. P.: Observational constraints on atmospheric and oceanic cross-equatorial heat transports: revisiting the precipitation asymmetry problem in climate models, Clim. Dynam., 46, 3239–3257, https://doi.org/10.1007/s00382-015-2766-z, 2016.

Marchand, R., Mace, G. G., Ackerman, T., and Stephens, G.: Hydrometeor Detection Using Cloudsat – An Earth-Orbiting 94-GHz Cloud Radar, J. Atmos. Ocean. Tech., 25, 519–533, https://doi.org/10.1175/2007JTECHA1006.1, 2008.

Matus, A. V. and L'Ecuyer, T. S.: The role of cloud phase in Earth's radiation budget, J. Geophys. Res.-Atmos., 122, 2559–2578, https://doi.org/10.1002/2016JD025951, 2017.

Minnis, P., Sun-Mack, S., Trepte, Q. Z., Chang, F.-L., Heck, P. W., Chen, Y., Yi, Y., Arduini, R. F., Ayers, K., Bedka, K., Bedka, S., Brown, R., Gibson, S., Heckert, E., Hong, G., Jin, Z., Palikonda, R., Smith, R., Smith, W. L., Spangenberg, D. A., Yang, P., Yost, C. R., and Xie, Y.: CERES Edition 3 Cloud Retrievals, 13th Conf. on Atmospheric Radiation, 28 June–2 July 2010, Portland, OR, Am. Meteorol. Soc., 5.4, https://ams.confex.com/ams/pdfpapers/171366.pdf (last access: 23 June 2022), 2010.

Mülmenstädt, J., Sourdeval, O., Henderson, D. S., L'Ecuyer, T. S., Unglaub, C., Jungandreas, L., Böhm, C., Russell, L. M., and Quaas, J.: Using CALIOP to estimate cloud-field base height and its uncertainty: the Cloud Base Altitude Spatial Extrapolator (CBASE) algorithm and dataset, Earth Syst. Sci. Data, 10, 2279–2293, https://doi.org/10.5194/essd-10-2279-2018, 2018.

Noel, V., Chepfer, H., Chiriaco, M., and Yorks, J.: The diurnal cycle of cloud profiles over land and ocean between 51° S and 51° N, seen by the CATS spaceborne lidar from the International Space Station, Atmos. Chem. Phys., 18, 9457–9473, https://doi.org/10.5194/acp-18-9457-2018, 2018.

Norris, J. R., Allen, R. J., Evan, A. T., Zelinka, M. D., O'Dell, C. W., and Klein, S. A.: Evidence for climate change in the satellite cloud record, Nature, 536, 72–75, https://doi.org/10.1038/nature18273, 2016.

Ohmura, A., Dutton, E. G., Forgan, B., Fröhlich, C., Gilgen, H., Hegner, H., Heimo, A., König-Langlo, G., McArthur, B., and Müller, G.: Baseline Surface Radiation Network (BSRN/WCRP): New precision radiometry for climate research, B. Am. Meteorol. Soc., 79, 2115–2136, https://doi.org/10.1175/1520-0477(1998)079<2115:BSRNBW>2.0.CO;2, 1998.

Prata, A. J.: A new long-wave formula for estimating downward clear-sky radiation at the surface, Q. J. Roy. Meteorol. Soc., 122, 1127–1151, https://doi.org/10.1002/qj.49712253306, 1996.

Ramanathan, V.: Interactions between ice-albedo, lapse-rate and cloud-top feedbacks: An analysis of the nonlinear response of a GCM climate model, J. Atmos. Sci., 34, 1885–1897, https://doi.org/10.1175/1520-0469(1977)034<1885:IBIALR>2.0.CO;2, 1977.

Ramanathan, V., Cess, R. D., Harrison, E. F., Minnis, P., and Barkstrom, B. R.: Cloud-Radiative Forcing and Climate: Results from te Earth Radiation Budget Experiment, Science, 243, 57–63, https://doi.org/10.1126/science.243.4887.57, 1989.

Roesch, A., Wild, M., Ohmura, A., Dutton, E. G., Long, C. N., and Zhang, T.: Assessment of BSRN radiation records for the computation of monthly means, Atmos. Meas. Tech., 4, 339–354, https://doi.org/10.5194/amt-4-339-2011, 2011.

Rienecker, M. M., Suarez, M. J., Todling, R., Bacmeister, J., Takacs, L., Liu, H. C., Gu, W., Sienkiewicz, M., Koster, R. D., Gelaro, R., Stajner, I., and Nielsen, J. E.: The GEOS-5 data assimilation system: Documentation of versions 5.0.1, 5.1.0, and 5.2.0., NASATechnical Report Series on Global Modeling and Data Assimilation, Vol. 27, NASA/TM-2008-105606, 97 pp., https://ntrs.nasa.gov/api/citations/20120011955/downloads/20120011955.pdf (last access: 23 June 2022), 2008.

Rojas Muñoz, O. J., Chiriaco, M., Bastin, S., and Ringard, J.: Estimation of the terms acting on local 1 h surface temperature variations in Paris region: the specific contribution of clouds, Atmos. Chem. Phys., 21, 15699–15723, https://doi.org/10.5194/acp-21-15699-2021, 2021.

Rutan, D. A., Kato, S., Doelling, D. R., Rose, F. G., Nguyen, L. T., Caldwell, T. E., and Loeb, N. G.: CERES Synoptic Product: Methodology and Validation of Surface Radiant Flux, J. Atmos. Ocean. Tech., 32, 1121–1143, https://doi.org/10.1175/JTECH-D-14-00165.1, 2015.

Sassen, K. and Wang, Z.: Classifying clouds around the globe with the CloudSat radar: 1-year of results, Geophys. Res. Lett., 35, L04805, https://doi.org/10.1029/2007GL032591, 2008.

Scott, R. C., Lubin, D., Vogelmann, A. M., and Kato, S.: West Antarctic Ice Sheet Cloud Cover and Surface Radiation Budget from NASA A-Train Satellites, J. Climate, 30, 6151–6170, https://doi.org/10.1175/JCLI-D-16-0644.1, 2017.

Shepherd, A., Ivins, E. R., A, G., Barletta, V. R., Bentley, M. J., Bettadpur, S., Briggs, K. H., Bromwich, D. H., Forsberg, R., Galin, N., Horwath, M., Jacobs, S., Joughin, I., King, M. A., Lenaerts, J. T. M., Li, J., Ligtenberg, S. R. M., Luckman, A., Luthcke, S. B., McMillan, M., Meister, R., Milne, G., Mouginot, J., Muir, A., Nicolas, J. P., Paden, J., Payne, A. J., Pritchard, H., Rignot, E., Rott, H., Sørensen, L. S., Scambos, T. A., Scheuchl, B., Schrama, E. J. O., Smith, B., Sundal, A. V., van Angelen, J. H., van de Berg, W. J., van den Broeke, M. R., Vaughan,

D. G., Velicogna, I., Wahr, J., Whitehouse, P. L., Wingham, D. J., Yi, D., Young, D., and Zwally, H. J.: A Reconciled Estimate of Ice-Sheet Mass Balance, Science, 338, 1183–1189, https://doi.org/10.1126/science.1228102, 2012.

Shupe, M. D. and Intrieri, J. M.: Cloud Radiative Forcing of the Arctic Surface: The Influence of Cloud Properties, Surface Albedo, and Solar Zenith Angle, J. Climate, 17, 13, https://doi.org/10.1175/1520-0442(2004)017<0616:CRFOTA>2.0.CO;2, 2004.

Shupe, M. D., Turner, D. D., Walden, V. P., Bennartz, R., Cadeddu, M. P., Castellani, B. B., Cox, C. J., Hudak, D. R., Kulie, M. S., Miller, N. B., Neely, R. R., Neff, W. D., and Rowe, P. M.: High and Dry: New Observations of Tropospheric and Cloud Properties above the Greenland Ice Sheet, B. Am. Meteorol. Soc., 94, 169–186, https://doi.org/10.1175/BAMS-D-11-00249.1, 2013.

Stephens, G. L., Vane, D. G., Boain, R. J., Mace, G. G., Sassen, K., Wang, Z., Illingworth, A. J., O'connor, E. J., Rossow, W. B., Durden, S. L., Miller, S. D., Austin, R. T., Benedetti, A., Mitrescu, C., and the CloudSat Science Team: THE CLOUDSAT MISSION AND THE A-TRAIN: A New Dimension of Space-Based Observations of Clouds and Precipitation, B. Am. Meteorol. Soc., 83, 1771–1790, https://doi.org/10.1175/BAMS-83-12-1771, 2002.

Stephens, G. L., Vane, D. G., Tanelli, S., Im, E., Durden, S., Rokey, M., Reinke, D., Partain, P., Mace, G. G., Austin, R., L'Ecuyer, T., Haynes, J., Lebsock, M., Suzuki, K., Waliser, D., Wu, D., Kay, J., Gettelman, A., Wang, Z., and Marchand, R.: CloudSat mission: Performance and early science after the first year of operation, J. Geophys. Res.-Atmos., 113, D00A18, https://doi.org/10.1029/2008JD009982, 2008.

Stroeve, J. C., Serreze, M. C., Holland, M. M., Kay, J. E., Maslanik, J., and Barrett, A. P.: The Arctic's rapidly shrinking sea ice cover: a research synthesis, Clim. Change, 110, 1005–1027, https://doi.org/10.1007/s10584-011-0101-1, 2012.

Taylor, K. E., Crucifix, M., Braconnot, P., Hewitt, C. D., Doutriaux, C., Broccoli, A. J., Mitchell, J. F. B., and Webb, M. J.: Estimating Shortwave Radiative Forcing and Response in Climate Models, J. Climate, 20, 2530–2543, https://doi.org/10.1175/JCLI4143.1, 2007.

Vaillant de Guélis, T., Chepfer, H., Noel, V., Guzman, R., Dubuisson, P., Winker, D. M., and Kato, S.: The link between outgoing longwave radiation and the altitude at which a spaceborne lidar beam is fully attenuated, Atmos. Meas. Tech., 10, 4659–4685, https://doi.org/10.5194/amt-10-4659-2017, 2017a.

Vaillant de Guélis, T., Chepfer, H., Noel, V., Guzman, R., Winker, D. M., and Plougonven, R.: Using Space Lidar Observations to Decompose Longwave Cloud Radiative Effect Variations Over the Last Decade: Space lidar decomposes LWCRE variations, Geophys. Res. Lett., 44, 11994–12003, https://doi.org/10.1002/2017GL074628, 2017b.

Vaillant de Guélis, T., Chepfer, H., Guzman, R., Bonazzola, M., Winker, D. M., and Noel, V.: Space lidar observations constrain longwave cloud feedback, Sci. Rep., 8, 16570, https://doi.org/10.1038/s41598-018-34943-1, 2018.

van den Broeke, M., Bamber, J., Ettema, J., Rignot, E., Schrama, E., van de Berg, W. J., van Meijgaard, E., Velicogna, I., and Wouters, B.: Partitioning Recent Greenland Mass Loss, Science, 326, 984–986, https://doi.org/10.1126/science.1178176, 2009.

Van Tricht, K., Lhermitte, S., Lenaerts, J. T. M., Gorodetskaya, I. V., L'Ecuyer, T. S., Noël, B., van den Broeke, M. R., Turner, D. D., and van Lipzig, N. P. M.: Clouds enhance Greenland ice sheet meltwater runoff, Nat. Commun., 7, 10266, https://doi.org/10.1038/ncomms10266, 2016.

Vaughan, M., Pitts, M., Trepte, C., Winker, D., Detweiler, P., Garnier, A., Getzewich, B., Hunt, W., Lambeth, J., Lee, K.-P., Lucker, P., Murray, T., Rodier, S., Tremas, T., Bazureau, A., and Pelon, J.: Cloud-Aerosol LIDAR Infrared Pathfinder Satellite Observations (CALIPSO) data management system data products catalog, Release 4.30, NASA Langley Research Center Document PC-SCI-503, https://www-calipso.larc.nasa.gov/products/CALIPSO_DPC_Rev4x30.pdf (last access: 23 June 2022), 2018.

Wang, W., Zender, C. S., As, D., and Miller, N. B.: Spatial Distribution of Melt Season Cloud Radiative Effects Over Greenland: Evaluating Satellite Observations, Reanalyses, and Model Simulations Against In Situ Measurements, J. Geophys. Res.-Atmos., 124, 57–71, https://doi.org/10.1029/2018JD028919, 2019.

Winker, D. M., Pelon, J., Jr, J. A. C., Ackerman, S. A., Charlson, R. J., Colarco, P. R., Flamant, P., Fu, Q., Hoff, R. M., Kittaka, C., Kubar, T. L., Treut, H. L., Mccormick, M. P., Mégie, G., Poole, L., Powell, K., Trepte, C., Vaughan, M. A., and Wielicki, B. A.: A Global 3D View of Aerosols and Clouds, B. Am. Meteorol. Soc., 91, 1211–1230, https://doi.org/10.1175/2010BAMS3009.1, 2010.

Zelinka, M. D., Klein, S. A., and Hartmann, D. L.: Computing and Partitioning Cloud Feedbacks Using Cloud Property Histograms. Part I: Cloud Radiative Kernels, J. Climate, 25, 3715–3735, https://doi.org/10.1175/JCLI-D-11-00248.1, 2012a.

Zelinka, M. D., Klein, S. A., and Hartmann, D. L.: Computing and Partitioning Cloud Feedbacks Using Cloud Property Histograms. Part II: Attribution to Changes in Cloud Amount, Altitude, and Optical Depth, J. Climate, 25, 3736–3754, https://doi.org/10.1175/JCLI-D-11-00249.1, 2012b.

Chapter 4

Publication II: *Quantifying surface cloud warming increase as Fall Arctic sea ice cover decreases*

Manuscript to be submitted in March, 2023 to *Geophysical Research Letters*.

How to cite: **Arouf, A.**, Chepfer, H., Kay, J. E., L'Ecuyer, T. S., and Lac, J., "Quantifying surface cloud warming increase as Fall Arctic sea ice cover decreases". Submitted to *Geophysical Research Letters* in April, 2023.

Introduction of Publication II

As sea ice and snow melt, optically darker surfaces are exposed, favoring **S**hort**W**ave (SW) absorption by the surface and increasing the initial warming. If the Arctic temperature continues to rise at an extraordinary rate, it will have significant consequences on future climate. For example, the zonal temperature gradient between the Arctic and southern latitudes would decrease, which can impact global circulation and cloud distribution. Also, the sea ice melt have a local effect on low-level cloud formation over newly open water that would have significant impacts on the surface energy budget. During the Summer season, any increase in low-level clouds would have a cooling effect since they would increase the Arctic's albedo: sea ice's bright surface being replaced by cloud's bright surface (Kay and Gettelman, 2009). During non-summer seasons, any increase in low-level clouds would have a warming effect on the surface. Indeed, the increase in low-level cloud occurrence would trap more **L**ong**W**ave (LW) radiation toward the surface that would otherwise escape to space, increasing surface warming (Kay and Gettelman, 2009; Morrison et al., 2018; Huang et al., 2019). This effect would be more consequent during Fall since any increase in surface warming would delay the sea ice refreezing because the sea ice has been thinned during the Summer season.

The lack of high-resolution observations at a global long-time scale, especially in polar regions, has been a limitation for our understanding of the cloud vertical structure, and therefore, of their radiative effects at the surface. This has led to limitations in assessing the representation of clouds and their radiative effect at the surface. Indeed, ground stations, that make direct observations of the surface fluxes on a long time scale, are mostly located in low latitudes and over land. Over polar regions, ground stations are "rare" and hard to maintain (*e.g.* instruments freeze up because of the cold temperature). Satellite observations are the only way to get an Arctic-wide view of clouds and retrieve the surface cloud radiative fluxes and study their interannual variability.

Given the importance of low-level clouds on surface energy budget over the Arctic during Fall, the second study addressed in this thesis seeks to answer the following questions: ***i) By how much Fall Arctic clouds can change surface LW warming in response to sea ice cover changes? ii) How do they evolve through Fall?***. The answers to these questions are given in chapter 4. The new retrieval of the surface LW **C**loud **R**adiative **E**ffect (CRE) developed in chapter 3 is used to answer the questions addressed here. The local instantaneous product provides a high temporal and geographical resolution that is especially needed when one wants to quantify surface cloud warming and sea ice cover co-variability (Kay and L'Ecuyer, 2013) and is used in this study. We found that October large surface cloud warming values (Surface LW CRE $>80\,\mathrm{Wm^{-2}}$) occur much more frequently ($\sim +50\,\%$) over open water than over sea ice and is caused by low-level opaque clouds ($Z_{T_{Opaque}}<2\,\mathrm{km}$). We

found that this increase is even more pronounced during November months, where large surface cloud warming (Surface LW CRE $>80\,\mathrm{Wm^{-2}}$) occur $\sim +200\,\%$ more frequently over open water than over sea ice. Future November may look more like present-day October and future December may look like present-day November with more surface cloud warming over open water than over sea ice. These results suggest that as the Arctic continues to warm up due to human-induced activities and climate feedback, clouds would help to enhance Arctic warming and sea ice loss by increasing downwelling LW fluxes and warming the surface.

The new retrieval of the surface LW CRE developed in chapter 3 is also used to study the interannual variability of the surface LW CRE at a global scale and in polar regions and has been presented in several conferences such as AMS (2022, USA remotely), ESA/LPS (2022 Germany) and IRS (2022, Greece) but the results are not mature enough to be published or to be a chapter of a thesis. It is addressed as a perspective and some preliminary results are presented in Appendix C.

Surface cloud warming increases as late Fall Arctic sea ice cover decreases

Assia Arouf[1], Hélène Chepfer[1], Jennifer E. Kay[2,3], Tristan S. L'Ecuyer[4], Jean Lac[1]

[1]LMD/IPSL, Sorbonne Université, École Polytechnique, Institut Polytechnique de Paris, ENS, PSL Université, CNRS, Palaiseau, France
[2]CIRES, University of Colorado Boulder, Boulder, USA
[3]ATOC, University of Colorado Boulder, Boulder, USA
[4]Department of Atmospheric and Oceanic Sciences, University of Wisconsin-Madison, Madison, USA

Key Points:

- During October, large surface cloud warming with values higher than 80 W m^{-2} occurs ∼+50% more often over open water than over sea ice.
- Compared to October, November large surface cloud warming (> 80 W m^{-2}) occurs even more frequently (∼+200%) over open water than over sea ice
- More frequent large surface warming caused by low-level opaque clouds occurs as open water persists later into the fall.

Corresponding author: Assia Arouf, assia.arouf@lmd.ipsl.fr

Abstract

During the Arctic night, clouds regulate surface energy budgets through longwave warming alone. During fall, any increase in low-level opaque clouds will increase surface cloud warming and could potentially delay sea ice formation. While an increase in clouds due to fall sea ice loss has been observed, quantifying the surface warming is observationally challenging. Here, we use a new observational dataset of surface cloud warming at 330 m × 90 m spatial resolution and instantaneous time scale. By instantaneously co-locating surface cloud warming and sea ice observations in regions where sea ice varies, we find October large surface cloud warming values ($> 80\,\mathrm{W\ m^{-2}}$) are much more frequent ($\sim$+50%) over open water than over sea ice. Notably, in November large surface cloud warming values ($> 80\,\mathrm{W\ m^{-2}}$) occur more frequently ($\sim$+200%) over open water than over sea ice. These results suggest more surface warming caused by low-level opaque clouds in the future as open water persists later into the fall.

Plain Language Summary

Over the past 40 years, Arctic sea ice has experienced an extreme decline, leaving a large surface of open water and an increased surface temperature. Through their impact on energy budgets, clouds have the potential to increase or decrease sea ice decline. More low-level clouds over open water than over sea ice during non-summer seasons have already been observed. But quantifying their radiative effect remains challenging. Therefore, this study seeks to answer the following question: By how much late fall Arctic clouds can change surface warming in response to sea ice loss? Using cloud surface warming data at high temporal and spatial resolution, we found that large surface cloud warming, higher than $80\,\mathrm{W\ m^{-2}}$, occurs much more frequently over open water than over sea ice during October and November months. This suggests that Arctic clouds favor sea ice loss by delaying sea ice recovery. As the Arctic continues to warm up due to human activities, cloud surface warming will delay sea ice freeze-up later into the fall and may amplify Arctic sea ice loss.

1 Introduction

Over the past 40 years, the Arctic has experienced the largest warming on Earth (Serreze & Barry, 2011). Specifically, the Arctic has warmed nearly four times faster than the global average (Rantanen et al., 2022) and also lost sea ice, especially in late summer and early fall since the satellite record began (Stroeve et al., 2012). More summer melt and a longer melt season lead to more shortwave (SW) absorption in the Arctic ocean and greater ocean warming (Manabe & Stouffer, 1980). Warmer and larger areas of open water during longer duration can influence the adjacent ice cover, contributing to further thinning and delaying sea ice freeze-up (Stroeve et al., 2012, 2014).

On the other hand, enhanced surface longwave (LW) warming due to increased water vapor and cloudiness may accelerate sea ice melt in early spring (Huang et al., 2019) and would delay sea ice freeze-up in fall (Morrison et al., 2018), resulting in a longer melt season. Air-sea coupling during non-summer season promotes the formation of low-level liquid clouds above open water in response to sea ice loss (Kay & Gettelman, 2009). These low-level clouds affect surface radiative fluxes and may affect sea ice formation. Indeed, clouds radiatively warm the surface in the LW by trapping upward LW earth surface radiation that would otherwise escape the earth system. Conversely, they radiatively cool the surface in the SW by reflecting solar radiation back to space. During Arctic summer over the ocean, the SW effect dominates over the LW effect and clouds cool the surface. In all other seasons, clouds warm the surface and may enhance sea ice loss. On average overall, Arctic clouds warm the ocean surface (Kay & L'Ecuyer, 2013).

In fall, Morrison et al. (2018) using 8 years of high-resolution instantaneous spaceborne lidar observations, found more low-level clouds over open water than over sea ice. But, quantifying the surface radiative impact of these low-level clouds formed over newly open water is challenging. Therefore, this study investigates to answer the following questions: i) By how much late fall Arctic clouds can change surface LW warming in response to sea ice cover changes? ii) How do they evolve through late fall? Due to the limited availability of ground-based observations in the Arctic, satellite observations are unquestionably needed for investigating changes in the Arctic climate system. As low-level clouds exert a large surface warming effect (Arouf, Chepfer, Vaillant de Guélis, Chiriaco, et al., 2022; Matus & L'Ecuyer, 2017; Shupe & Intrieri, 2004), we need to accurately observe them above sea ice and open water to detect surface cloud warming changes in response to Arctic sea ice variability. Spaceborne active sensors are good candidates as they sample vertically the atmosphere above all surface types, including sea ice and open water, providing consistent cloud observations at relatively long time periods with near-global spatial coverage (Stubenrauch et al., 2013). We use 13 years of Cloud–Aerosol Lidar and Infrared Pathfinder Satellite Observations (CALIPSO; Winker et al., 2010) observations between 2008 and 2020, a period with a large sea ice loss and a large sea ice concentration interannual variability (Serreze & Meier, 2019) to document clouds. We also use a new dataset of surface LW cloud warming at high spatial resolution (330 m $\times$ 90 m) and instantaneous time scale (Arouf, Chepfer, Vaillant de Guélis, Chiriaco, et al., 2022) to quantify the warming effect induced by low-level liquid clouds formed over newly open water during late fall.

2 Data

Cloud data used in this study are based on CALIPSO spaceborne lidar observations with a high spatiotemporal resolution (90 m cross track, 330 m along orbit track). CALIPSO data are surface type independent, *i.e.* accurate observations over sea ice and over open water, unlike spaceborne radiometers that are dependent on the background surface type to detect clouds and are limited over icy bright surfaces. Moreover, space lidar samples the atmosphere and observes clouds at all atmosphere levels, except the ones under the altitude where the space lidar is fully attenuated. We use 13 years (2008–2020) of CALIPSO observations which allows having a large area where Arctic sea ice cover varies during fall, with almost half of CALIPSO's profiles over sea ice and the other half over open water. We use cloud data from GCM Oriented CALIPSO Cloud Product (CALIPSO–GOCCP v3.1.2; Chepfer et al., 2010; Cesana et al., 2012; Guzman et al., 2017; Vaillant de Guélis et al., 2017). Space lidar differentiates well cloud types and each profile is classified (*Profile-flag*) as *Clear sky* when no cloud is detected; *Thin cloud* when clouds and surface echo are detected; *Opaque cloud* when clouds, with visible optical depth $> 3-5$ depending on the cloud's microphysical properties (Chepfer et al., 2014), are detected but no surface echo is detected (Guzman et al., 2017); *Uncertain* in all other cases (*e.g.* surface echo not detected and no fully attenuated altitude detected). When a cloud is detected, we can retrieve its *cloud altitude*. $Z_{T_{Opaque}}$ is an altitude computed for each opaque cloud profile as follows: $Z_{T_{Opaque}} = \frac{Z_{Top}+Z_{FA}}{2}$ where Z_{Top} is the cloud top altitude and Z_{FA} the altitude where the space lidar gets completely attenuated in opaque clouds. $Z_{T_{Thin}}$ is an altitude computed for each thin cloud profile as follows: $Z_{T_{Thin}} = \frac{Z_{Top}+Z_{Base}}{2}$ where Z_{Top} is the cloud top altitude and Z_{Base} cloud base altitude.

Surface longwave cloud radiative effect (LW CRE) quantifies the impact of clouds on the surface energy budget. It corresponds to the surface net radiative fluxes over all types of scenes minus the corresponding fluxes where the influence of clouds has been removed. We use satellite-based surface CRE data at two different resolutions: the instantaneous 330 m $\times$ 90 m data (hereafter high-resolution data) and the monthly gridded data.

The monthly gridded Surface SW CRE data are from the and CloudSat 2B–FLXHR–LIDAR P1–R04 (hereafter, 2BFLX; L'Ecuyer et al., 2019) product and the monthly gridded Surface LW CREs comes from both 2BFLX and the LWCRE–LIDAR Edition 1 product (Arouf, Chepfer, Vaillant de Guélis, Chiriaco, et al., 2022). These monthly gridded datasets over the time period 2008−2011 are used to put the context of the current study (Fig. 1) The 2BFLX product at a monthly 2.5°×2.5° resolution is currently available between August 2006 through April 2011 before CloudSat experienced a battery anomaly that limited observations to daylight only. The dataset does not provide data during late fall after 2011. Uncertainties in monthly-mean surface LW fluxes from 2BFLX are ∼11 W m^{-2}, owing primarily to errors in lower tropospheric temperature and humidity and uncertainty in cloud base height (Henderson et al., 2013).

The high resolution (instantaneous 330 m × 90 m) surface LW CRE are from LWCRE-LIDAR Edition 1 product (Arouf, Chepfer, Vaillant de Guélis, Chiriaco, et al., 2022). It extends for over a decade (13 years, 2008−2020) which allows us to have a lot of surface LW CRE values over open water in October months (10447547) and in November months (4677922) and also a lot of surface LW CRE values over sea ice in October months (12846572) and in November months (17939079). These high-resolution data are used to study how daily sea-ice cover and surface LW CRE co-variability which provide the new and main results of this paper (Fig. 3 and Fig. 4).

Each lidar footprint (90 m) each 330 m contains either zero, for clear sky footprint, a value of surface LW Thin CRE or a value of surface LW Opaque CRE. The surface LW Opaque CRE is computed from $Z_{T_{Opaque}}$. Since the space lidar cannot observe under the altitude where the lidar is fully attenuated, it might potentially miss low-level clouds laying under this altitude. One would think that this limitation would create a large bias in the surface LW CRE retrieval and may underestimate the surface LW CRE. However, Arctic liquid clouds that are optically opaque are usually at low levels and the space lidar attenuates most of the time in the boundary layer at altitudes lower than 3 km above the surface (Guzman et al., 2017). Uncertainties reaching ∼13 W m^{-2} can be induced by the lower tropospheric temperature and humidity representations and cloud base height but would not change the overall results shown in this paper.

Sea ice concentrations are from the National Snow and Ice Data Center's Near Real-Time SSM/I EASE-Grid Daily Global Sea Ice Concentration and Snow Extent data product (NSIDC; Nolin et al., 1998). Sea ice observations, at a daily 25 km horizontal resolution, are from passive microwave imagers and have uncertainties ranging from ±5% in winter to ±15% in summer (Agnew & Howell, 2003). Each CALIPSO footprint contains a sea ice concentration value, which is assigned from the latitude/longitude closest to that satellite footprint. We also use sea ice extent at a monthly resolution between 1979 and 2021 (Fetterer et al., 2017).

3 Methods

We built surface masks following a method developed by Morrison et al. (2018) to isolate the influence of Arctic sea ice cover variability on clouds from other cloud-controlling factors. We split the Arctic, defined as the area poleward 70 °N, into two regions delimited by two masks: the perennial mask and the intermittent mask. The perennial mask isolates regions of the Arctic where the daily sea ice concentration has not changed between 2008–2020 during October months. Explicitly, this mask contains grid boxes over land including coastlines, grid boxes that remain always ice-free (< 15% every day between 2008–2020), and grid boxes that remain always ice-covered (> 80% every day between 2008–2020). The data over the perennial mask are excluded from our study. The intermittent mask isolates regions of the Arctic Ocean where the 1° × 1° daily sea ice concentration has varied between 2008–2020 during October months. Specifically, the intermittent mask contains grid boxes that never remain always ice-free (< 15%) nor

always ice-covered ($> 80\%$). Said differently, in the intermittent mask, the daily mean sea ice concentration within a $1° \times 1°$ grid box is not either $< 15\%$ nor $> 80\%$ every single day between 2008–2020 during October months. We built another intermittent mask for November months in the same way as for October months.

Within the intermittent mask, we split the clouds into low/high, opaque/thin, over open water/over sea ice using high spatiotemporal resolution (90 m cross track, 330 m along orbit track) cloud properties for October and November months. We built low-level opaque (thin) cloud cover by dividing the number of opaque (thin) cloud profiles with mean altitudes $Z_{T_{Opaque}}$ ($Z_{T_{Thin}}$) < 2 km by the total number of profiles within a $1°\times 1°$ grid box for a given month. Then we built low-level opaque cloud cover over open water only by dividing the number of opaque profiles with $Z_{T_{Opaque}} < 2$ km over open water (footprint sea ice cover $< 15\%$) by the total number of profiles over open water within a $1°\times1°$ grid box for a given month. Similarly, we built the low-level opaque cloud cover over sea ice only considering the profiles with footprints of sea ice cover $> 80\%$. This classification excludes profiles containing both open water and sea ice (footprint sea ice cover $> 15\%$ and $< 80\%$). In the same way, we split the surface LW CRE high-resolution data (90 m cross track, 330 m along orbit track) into over open water and over sea ice and look at its distribution for opaque and thin clouds over each surface type. Similarly, we delimit the surface LW Opaque CRE high-resolution data caused by low-level opaque clouds (when $Z_{T_{Opaque}} < 2$ km) and by high-level opaque clouds (when $Z_{T_{Opaque}} > 2$ km) over each surface type.

This approach assumes that local processes affect more low-level clouds than large-scale patterns since clouds over open water and over sea ice are subject to the same large-scale atmospheric circulation regimes.

4 Results

October is a particularly interesting month for investigating the observed co-variability of sea ice and cloud radiative effects (Figure 1). At this time of year, the sun is setting and cloud influence on radiative fluxes is increasingly explained by the longwave cloud warming alone. In fact, from October through February, the shortwave cloud cooling is close to zero and the total cloud radiative effect is the same as the longwave cloud warming (Figure 1a). Of the months when the longwave cloud warming is the total cloud radiative effect, October has the largest Arctic sea ice loss (Figure 1b). When one compares the solid blue line (average over $2011-2021$) and the dashed pink line (average over $1979-1990$), October lost $\sim$2.8 millions of km^2 of sea ice extent during this last 40 years.

To understand cloud-sea ice relationships in this interesting month, we map October high-resolution cloud properties within the intermittent mask which isolates regions where sea ice varies (Figure 2). October is very cloudy throughout the entire intermittent mask. Averaged over intermittent mask (Figure 2b), clear sky is only present $\sim$13% of the time (Figure 2a) while clouds occur $\sim$81% of the time ($\sim$ 6% of CALIPSO's profiles within the intermittent mask are classified as uncertain). We can divide this cloud cover ($\sim$81%) into opaque and thin clouds. Furthermore, more than half of October clouds are opaque ($\sim$52%), especially at lower latitudes (Figure 2c) and half of these opaque clouds have mean altitudes under 2 km (Figure 2d) resulting in low-level opaque cloud cover of $\sim$27%. Thin clouds dominate at higher latitudes (> 75 °N), especially in the Pacific sector of the Arctic above the Canadian Archipelago (Figure 2e) which is the coldest region of the Arctic. Most thin clouds ($\sim$19% out of $\sim$29%) also have mean altitudes under 2 km.

Low-level opaque clouds are the dominant cloud type during October months within the intermittent mask (Figure 2d; $\sim$27% of CALIPSO's profiles) and warm the surface

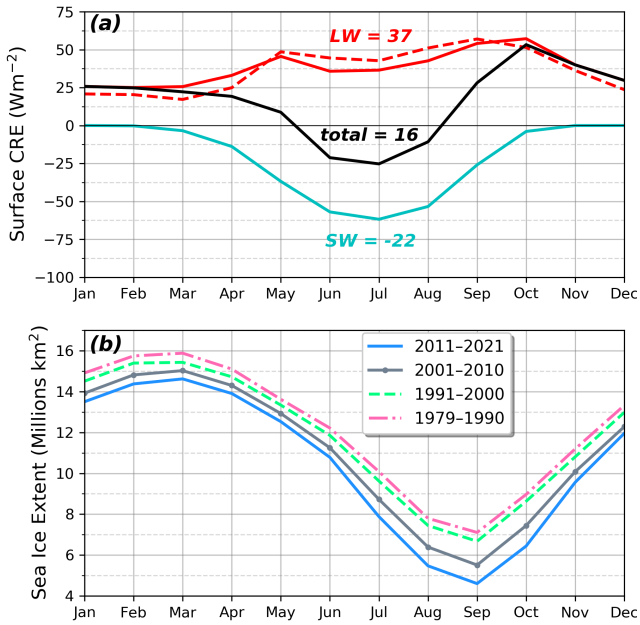

Figure 1. (a) Seasonal cycle of the surface cloud radiative effect (CRE) over Arctic oceans without northern Atlantic: longwave (LW), shortwave (SW) and total. The solid lines are from monthly gridded 2.5°×2.5° 2BFLX product (L'Ecuyer et al., 2019) between 2007–2010. The dashed line is from monthly gridded 2°×2° LWCRE–LIDAR product (Arouf, Chepfer, Vaillant de Guélis, Chiriaco, et al., 2022) between 2008–2020. (b) Seasonal cycles of sea ice extent.

more than the other clouds. Therefore, we focus on these clouds. We split these clouds into over open water and over sea ice (Figure 3). Maps show there are more low-level opaque clouds over open water than over sea ice in almost all locations. When averaged over the intermittent mask, there are ∼12% more low-level opaque clouds over open water than over sea ice. Analyzing PDFs of high-resolution surface longwave cloud warming (330 m × 90 m) over open water and over sea ice are consistent (Figure 3c) with these low-level opaque cloud cover differences (Figure 3a–b). The largest high-resolution surface longwave cloud warming values occur more over open water than they do over sea ice. Specifically, large high-resolution surface longwave cloud warming values (*i.e.* high-resolution surface LW CRE values $> 80\,\mathrm{W\ m^{-2}}$) are much more frequent (∼+50%) over open water than over sea ice and are caused by low-level opaque clouds. For thin clouds, even though they are numerous at averaged altitudes lower than 2 km, they warm less the surface with high-resolution surface longwave cloud warming ranging from 0 to $40\,\mathrm{W\ m^{-2}}$.

Comparing October with November, a month with less open water in the observational record (Figure 4b-d), shows that like October, November also has more low-level opaque clouds over open water than over sea ice within the November intermittent mask (Figures A-B in the supplementary material). The low-level opaque cloud cover differences over sea ice and over open water are 12% in October and 24% in November. Therefore, even though November has a lot more sea ice within the intermittent mask (59% in November Vs 31% in October), the low-level opaque cloud cover differences seen in October persist into November. Consistent with these low-level opaque cloud cover differences, there are also more very large high-resolution surface longwave cloud warming (*i.e.* high-resolution surface LW CRE values $> 80\,\mathrm{W\ m^{-2}}$) over open water than over sea ice. But, unlike October, the occurrence frequency difference is even larger in November. In November, large high-resolution surface longwave cloud warming (*i.e.* high-resolution

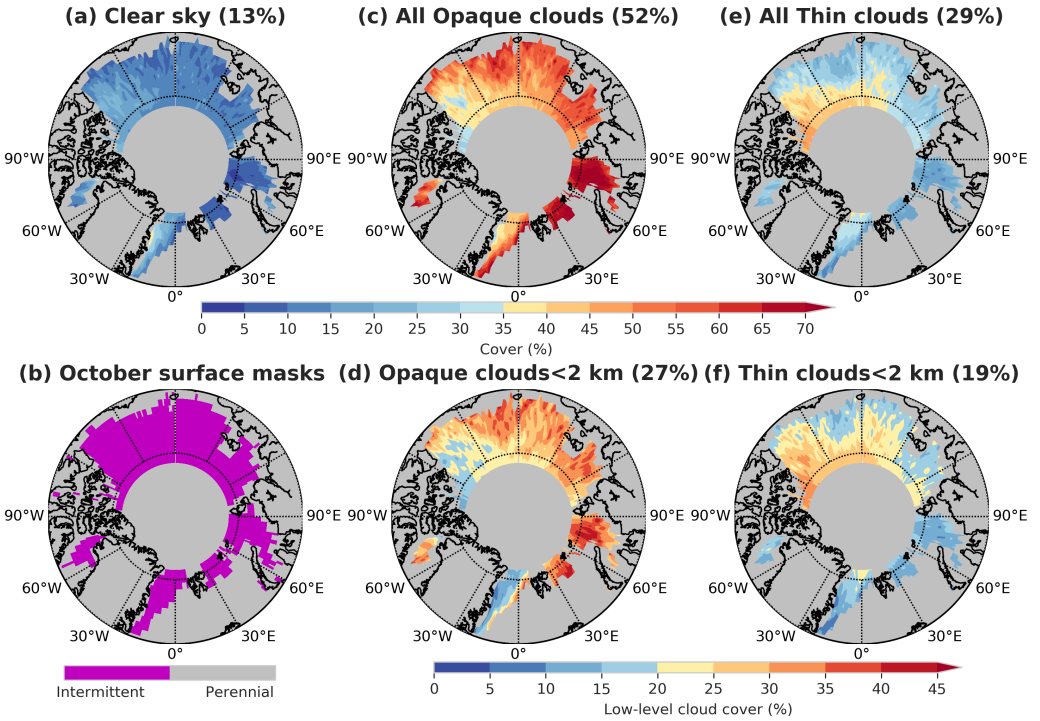

Figure 2. (a) Clear sky cover, (b) October surface masks established between 2008–2020, (c) Opaque cloud cover, (d) Low-level opaque cloud cover, (e) Thin cloud cover, (f) Low-level thin cloud cover. The covers sown in the figure are built from high-resolution CALIPSO–GOCCP profiles (90 m cross track, 330 m along orbit track) (Guzman et al., 2017) as described in the method section. Data are collected during October months between 2008–2020 period within the intermittent mask. The grid boxes with less than 100 profiles in each grid box for each October month are masked on these plots. The gray area represents the perennial mask that isolates regions of the Arctic where the $1^\circ \times 1^\circ$ daily sea ice concentration has not changed between 2008–2020 during October months and latitudes $> 82^\circ$ N where CALIPSO do not collect observations. The data over the perennial mask are excluded from our study. Every other color represents the intermittent mask that isolates regions of the Arctic Ocean where the $1^\circ \times 1^\circ$ daily sea ice concentration has varied between 2008–2020 during October months. Covers averaged over the intermittent mask are reported in parentheses. $\sim$ 6% of CALIPSO–GOCCP profiles within the intermittent mask are classified as uncertain and are excluded from our study.

surface LW CRE values $> 80\,\mathrm{W\,m^{-2}}$) occur $\sim$+200% more frequently over open water than over sea ice.

5 Discussion and conclusions

Our results suggest that cloud surface warming could lengthen the melt season by delaying sea ice freeze-up. We show that low-level opaque clouds formed over newly open water warm the surface during late fall. These low-level opaque clouds are dominant in regions where sea ice varies (intermittent mask) and are more numerous over open water than over sea ice. Using high-resolution surface warming data, we found that large values of surface longwave cloud warming occurs $\sim$+50% more often over open water than over sea ice during October months. During November compared to October, we found

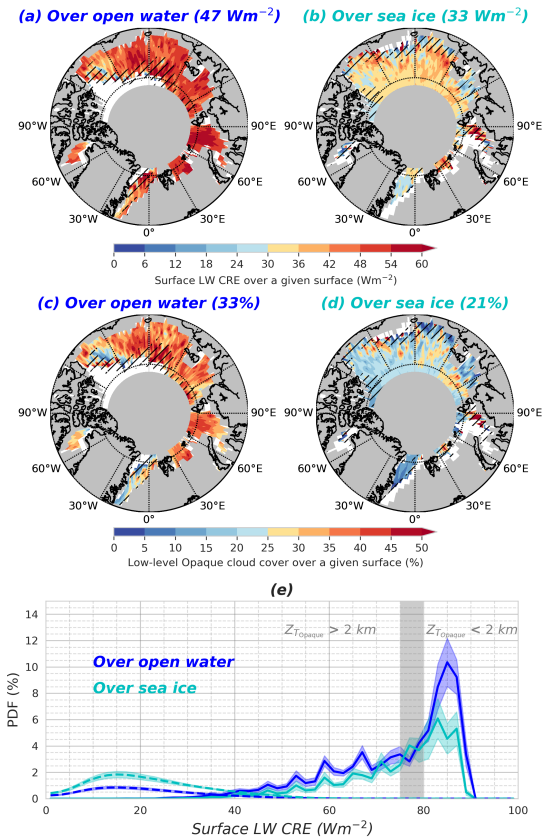

Figure 3. 1^{st} line: Maps of surface longwave cloud warming: (a) Over open water, (b) Over sea ice. 2^{nd} line: Maps of Low-level opaque cloud cover: (c) Over open water, (d) Over sea ice. The grid boxes with less than 100 profiles for each October month are masked and the grid boxes with less than 5 years of data over a given surface type are dashed in the interannual means. The gray area represents the perennial mask and is excluded from our study. These maps are built from high-resolution cloud profiles within the intermittent mask over open water (footprint sea ice concentration $< 15\%$) and over sea ice (footprint sea ice concentration $> 80\%$). The white area represents the intermittent mask where the surface is mixed with open water and sea ice (footprint sea ice concentration $> 15\%$ and $< 80\%$) and is excluded from our study hereafter. Surface cloud warming and covers averaged over the intermittent mask, including the dashed area, are reported in parentheses. (e) PDF of high-resolution surface LW cloud radiative effect (CRE) (90 m cross track, 330 m along orbit track) collected during October months between 2008–2020 period within the intermittent mask over open water (blue; when the footprint sea ice concentration $< 15\%$) and over sea ice (cyan; when the footprint sea ice concentration $> 80\%$). The solid line represents the surface LW Opaque CRE and the dashed line represents the surface LW Thin CRE. The CRE PDFs are built from high-resolution instantaneous surface LW CRE data from LWCRE–LIDAR (Arouf, Chepfer, Vaillant de Guélis, Chiriaco, et al., 2022) and are normalized by the number of profiles over each surface type for each year. The color-shaded regions are the interannual variance around the interannual mean of surface LW CRE distributions over each surface type and for each cloud type. The gray-shaded vertical bar delimits low-level and high-level opaque clouds.

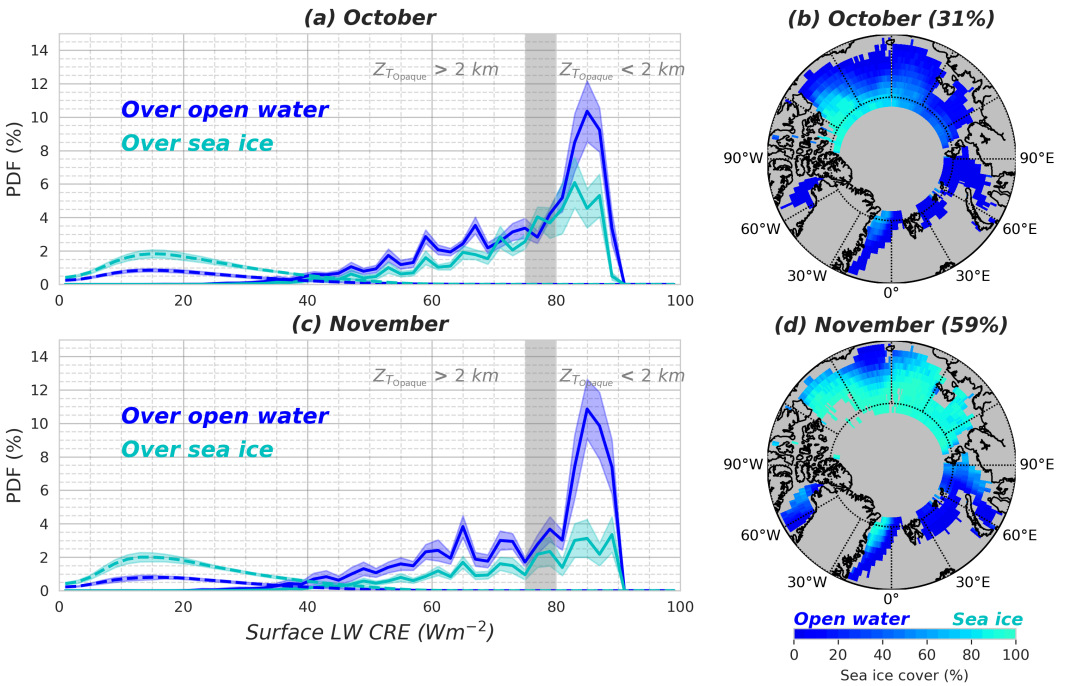

Figure 4. (a) same as Figure 3c, (c) same as Figure (a) but for November months over the November intermittent mask. (b,d) maps of the sea ice cover within the intermittent masks for October and November months respectively. The gray area represents the perennial mask and is excluded from our study. Averages established over the intermittent masks are reported in parentheses. High resolution (330 m × 90 m) surface LW CRE data used to build these PDFs are collected between 2008–2020 period for October months (1^{st} line) and November months (2^{nd} line).

an even higher increase of occurrence of large surface longwave cloud warming over open water than over sea ice. Thus, low-level opaque clouds warm the surface ∼+200% more often over open water than over sea ice during November.

Uncertainties in the high-resolution surface longwave cloud warming values would not change the overall results drawn in this study. Specifically, uncertainties in the high-resolution surface longwave cloud warming dataset might be induced by the space lidar not seeing the opaque cloud base as discussed in the method section. The altitude of low opaque clouds ($Z_{T_{Opaque}}$) would be even lower if the cloud base is documented better. Therefore, the values of the high-resolution surface longwave cloud warming would be larger. The space lidar missing the cloud base height results in less occurrence of large values of surface longwave cloud warming. Said differently, large surface longwave cloud warming would occur even more frequently than +50% over open water compared to over sea ice during October months if the space lidar documents better cloud base height and would emphasize more the fact that large surface longwave cloud warming occurs more frequently over open water than over sea ice. ∼6% of CALIPSO profiles are classified as uncertain and are excluded from our study but their percentage remains small to change drastically our results. Adding to this, ∼25% of all CALIPSO profiles occur over mixed surface types during October months and are excluded from our study when we split CALIPSO's profiles into over open water and over sea ice.

Our results suggest even more large surface longwave cloud warming as the Arctic goes ice-free. Indeed, during the last two decades, sea ice has been subject to more melt and longer melt seasons with quite a lot of variability (Serreze & Meier, 2019), *i.e.* early melt season onset and a delay in the freeze-up season leaving more open water later into the fall. As the Arctic warms, the melt season is expected to lengthen further (Stroeve et al., 2014) leading to more open water in late fall. Future November may look more like actual October and future December may look like actual November with a huge increase in the occurrence of large surface longwave cloud warming over open water than over sea ice. Said in other words, more open water extent as the Arctic goes sea ice-free in the future (Pistone et al., 2019) combined with ocean-atmosphere coupling during non-summer seasons, will promote low-level cloud formation (Kay & Gettelman, 2009; Palm et al., 2010; Sato et al., 2012) leading to more frequent large surface cloud warming values ($> 80\,\mathrm{W\ m^{-2}}$; fig. 4).

To sum up, our study helps to improve our understanding of cloud influence on surface energy budget during late fall as Arctic sea ice retreats. Thanks to a new high-resolution (330 m $\times$ 90 m) surface longwave cloud warming dataset, it quantifies the surface longwave warming induced by low-level clouds as sea ice retreats in late fall and suggests that surface longwave cloud warming would help to lengthen the melt season by potentially delaying sea ice freeze-up.

Acknowledgments

We are grateful to Airbus for contributing to the funding of the first author PhD grant. We thank NASA/CNES for the CALIPSO level-1 data and the Mesocentre ESPRI/IPSL for the computational resources. We recognize the support of CNES for the development of the CALIPSO–GOCCP product. Contributions of JEK and TSL were funded by NASA CloudSat/CALIPSO Science Team grant 80NSSC20K0135.

Open Research

The LWCRE–LIDAR–Ed1 is available for the 2008–2020 time period at doi.org/10.14768/70d5f4b5-e740-4d4c-b1ec-f6459f7e5563 for the monthly $2°\times2°$ gridded dataset (Arouf, Chepfer, Vaillant de Guélis, Guzman, et al., 2022), and at doi.org/10.14768/d4de28c3-0912-4244-8c2b-6fe259eb863c for the dataset along orbit track. The 2BFLX monthly $2.5° \times 2.5°$ dataset for the 2007−2010 time period is described at https://www.cloudsat.cira.colostate.edu/data-products/2b-flxhr-lidar and users can create a free account to order the data at this link https://www.cloudsat.cira.colostate.edu/accounts/login/?next=/order/ . The NSIDC sea ice extent dataset is available on doi.org/10.7265/N5K072F8 (Fetterer et al., 2017).

References

Agnew, T., & Howell, S. (2003). The use of operational ice charts for evaluating passive microwave ice concentration data. *Atmosphere-ocean*, *41*(4), 317–331. doi: 10.3137/ao.410405

Arouf, A., Chepfer, H., Vaillant de Guélis, T., Chiriaco, M., Shupe, M. D., Guzman, R., ... Gallagher, M. R. (2022). The surface longwave cloud radiative effect derived from space lidar observations. *Atmospheric Measurement Techniques*, *15*, 3893–3923. doi: 10.5194/amt-15-3893-2022

Arouf, A., Chepfer, H., Vaillant de Guélis, T., Guzman, R., Feofilov, A., & Raberanto, P. (2022). *Longwave cloud radiative effect derived from space lidar observations at the surface and toa – edition 1: Monthly gridded product* [dataset]. IPSL. doi: 10.14768/70d5f4b5-e740-4d4c-b1ec-f6459f7e5563

Cesana, G., Kay, J. E., Chepfer, H., English, J. M., & de Boer, G. (2012). Ubiquitous low-level liquid-containing Arctic clouds: New observations and climate

model constraints from CALIPSO-GOCCP. *Geophysical Research Letters*, *39*(20). doi: 10.1029/2012GL053385

Chepfer, H., Bony, S., Winker, D., Cesana, G., Dufresne, J. L., Minnis, P., ... Zeng, S. (2010). The GCM-Oriented CALIPSO Cloud Product (CALIPSO-GOCCP). *Journal of Geophysical Research*, *115*, D00H16. doi: 10.1029/2009JD012251

Chepfer, H., Noel, V., Winker, D., & Chiriaco, M. (2014). Where and when will we observe cloud changes due to climate warming? *Geophysical Research Letters*, *41*(23), 8387–8395. doi: 10.1002/2014GL061792

Fetterer, F., Knowles, K., Meier, W. N., Savoie, M., & Windnagel., A. K. (2017). *Sea ice index, version 3.* National Snow and Ice Data Center. doi: 10.7265/N5K072F8

Guzman, R., Chepfer, H., Noel, V., Vaillant de Guélis, T., Kay, J. E., Raberanto, P., ... Winker, D. M. (2017). Direct atmosphere opacity observations from CALIPSO provide new constraints on cloud-radiation interactions. *Journal of Geophysical Research: Atmospheres*, *122*, 1066–1085. doi: 10.1002/2016JD025946

Henderson, D. S., L'Ecuyer, T., Stephens, G., Partain, P., & Sekiguchi, M. (2013). A Multisensor Perspective on the Radiative Impacts of Clouds and Aerosols. *Journal of Applied Meteorology and Climatology*, *52*, 853–871. doi: 10.1175/JAMC-D-12-025.1

Huang, Y., Dong, X., Bailey, D. A., Holland, M. M., Xi, B., DuVivier, A. K., ... Deng, Y. (2019). Thicker Clouds and Accelerated Arctic Sea Ice Decline: The Atmosphere-Sea Ice Interactions in Spring. *Geophysical Research Letters*, *46*(12), 6980–6989. doi: 10.1029/2019GL082791

Kay, J. E., & Gettelman, A. (2009). Cloud influence on and response to seasonal Arctic sea ice loss. *Journal of Geophysical Research*, *114*, D18204. doi: 10.1029/2009JD011773

Kay, J. E., & L'Ecuyer, T. (2013). Observational constraints on Arctic Ocean clouds and radiative fluxes during the early 21st century. *Journal of Geophysical Research: Atmospheres*, *118*, 7219–7236. doi: 10.1002/jgrd.50489

L'Ecuyer, T. S., Hang, Y., Matus, A. V., & Wang, Z. (2019). Reassessing the Effect of Cloud Type on Earth's Energy Balance in the Age of Active Spaceborne Observations. Part I: Top of Atmosphere and Surface. *Journal of Climate*, *32*(19), 6197–6217. doi: 10.1175/JCLI-D-18-0753.1

Manabe, S., & Stouffer, R. J. (1980). Sensitivity of a global climate model to an increase of CO2 concentration in the atmosphere. *Journal of Geophysical Research: Oceans*, *85*(C10), 5529–5554. doi: 10.1029/JC085iC10p05529

Matus, A. V., & L'Ecuyer, T. S. (2017). The role of cloud phase in Earth's radiation budget: CLOUD PHASE IN EARTH'S RADIATION BUDGET. *Journal of Geophysical Research: Atmospheres*, *122*, 2559–2578. doi: 10.1002/2016JD025951

Morrison, A. L., Kay, J. E., Chepfer, H., Guzman, R., & Yettella, V. (2018). Isolating the Liquid Cloud Response to Recent Arctic Sea Ice Variability Using Spaceborne Lidar Observations. *Journal of Geophysical Research: Atmospheres*, *123*, 473–490. doi: 10.1002/2017JD027248

Nolin, A., Armstrong, R., & Maslanik, J. (1998). Near-real-time SSM/I-SSMIS EASE-Grid daily global ice concentration and snow extent, version 4. *NASA National Snow and Ice Data Center Distributed Active Archive Center*, *10*. doi: 10.5067/VF7QO90IHZ99

Palm, S. P., Strey, S. T., Spinhirne, J., & Markus, T. (2010). Influence of arctic sea ice extent on polar cloud fraction and vertical structure and implications for regional climate. *Journal of Geophysical Research: Atmospheres*, *115*(D21). doi: 10.1029/2010JD013900

Pistone, K., Eisenman, I., & Ramanathan, V. (2019). Radiative heating of an ice-free arctic ocean. *Geophysical Research Letters*, *46*, 7474–7480. doi: 10.1029/

2019GL082914

Rantanen, M., Karpechko, A. Y., Lipponen, A., Nordling, K., Hyvärinen, O., Ruosteenoja, K., ... Laaksonen, A. (2022). The Arctic has warmed nearly four times faster than the globe since 1979. *Communications Earth & Environment*, *3*(1), 1–10. doi: 10.1038/s43247-022-00498-3

Sato, K., Inoue, J., Kodama, Y.-M., & Overland, J. E. (2012). Impact of arctic sea-ice retreat on the recent change in cloud-base height during autumn. *Geophysical Research Letters*, *39*(10). doi: 10.1029/2012GL051850

Serreze, M. C., & Barry, R. G. (2011). Processes and impacts of Arctic amplification: A research synthesis. *Global and Planetary Change*, *77*, 85–96. doi: 10.1016/j.gloplacha.2011.03.004

Serreze, M. C., & Meier, W. N. (2019). The Arctic's sea ice cover: trends, variability, predictability, and comparisons to the Antarctic. *Annals of the New York Academy of Sciences*, *1436*(1), 36–53. doi: 10.1111/nyas.13856

Shupe, M. D., & Intrieri, J. M. (2004). Cloud Radiative Forcing of the Arctic Surface: The Influence of Cloud Properties, Surface Albedo, and Solar Zenith Angle. *Journal of Climate*, *17*, 616–628. doi: 10.1175/1520-0442(2004)017⟨0616:CRFOTA⟩2.0.CO;2

Stroeve, J. C., Markus, T., Boisvert, L., Miller, J., & Barrett, A. (2014). Changes in Arctic melt season and implications for sea ice loss. *Geophysical Research Letters*, *41*, 1216–1225. doi: 10.1002/2013GL058951

Stroeve, J. C., Serreze, M. C., Holland, M. M., Kay, J. E., Malanik, J., & Barrett, A. P. (2012). The Arctic's rapidly shrinking sea ice cover: a research synthesis. *Climatic Change*, *110*, 1005–1027. doi: 10.1007/s10584-011-0101-1

Stubenrauch, C. J., Rossow, W. B., Kinne, S., Ackerman, S., Cesana, G., Chepfer, H., ... Zhao, G. (2013). Assessment of global cloud datasets from satellites: Project and database initiated by the GEWEX radiation panel. *Bulletin of the American Meteorological Society*, *94*, 1031–1049. doi: 10.1175/BAMS-D-12-00117.1

Vaillant de Guélis, T., Chepfer, H., Noel, V., Guzman, R., Dubuisson, P., Winker, D. M., & Kato, S. (2017). The link between outgoing longwave radiation and the altitude at which a spaceborne lidar beam is fully attenuated. *Atmospheric Measurement Techniques*, *10*, 4659–4685. doi: 10.5194/amt-10-4659-2017

Winker, D. M., Pelon, J., Coakley, J. A., Ackerman, S. A., Charlson, R. J., Colarco, P. R., ... Wielicki, B. A. (2010). The CALIPSO mission: A global 3d view of aerosols and clouds. *Bulletin of the American Meteorological Society*, *91*, 1211–1229. doi: 10.1175/2010BAMS3009.1

Conclusions, discussions and perspectives

My thesis aims at better understanding Earth's surface cloud warming over a global long-time scale using cloud properties derived from CALIPSO observations. We focus further on the Arctic region, a region highly sensitive to global warming and where clouds may influence future Arctic trajectory (Kay et al., 2016). Indeed, clouds may enhance or offset Arctic sea ice loss. We asked three questions in the introduction and we answered those three questions in the previous chapters. Here, I give an overview of the three main results in a summarized form.

- *Can we retrieve the surface cloud warming from spaceborne lidar observations over more than a decade?*

  The surface **L**ong**W**ave (LW) **C**loud **R**adiative **E**ffect (CRE) depends on three "major" cloud properties: *cloud cover*, increase cloud cover would increase the surface of interaction between the upwelling LW radiation with the cloud. Therefore, clouds would absorb and emit more radiation and warm more the surface; *cloud emissivity*, in the infrared, radiation is proportional to the cloud emissivity and cloud temperature power 4 (Eq.A.7), clouds with larger emissivities emit more LW radiation; and *cloud altitude*, clouds at lower altitudes would be at warmer temperatures most of the time and would emit more LW radiation toward the surface. These three cloud properties can be well documented from a spaceborne lidar since it documents the cloud's vertical structure. Thus, lidar cloud detection is based on the round-trip time of photons between the transmitter and the receiver (Eq 2.1). In the first part of this thesis, I derived theorical parameterizations from a large number of $1D$ radiative transfer simulations. These parameterizations linearly link the surface LW CRE to the three fundamental cloud properties that it depends on. To account for changes in humidity and temperature profiles in the lower troposphere, radiative transfer simulations are done for various humidity and temperature profiles. Specifically, each 2° latitude band, each $100\,\mathrm{m}$ surface elevation, and each month is assigned with a theorical parametrization. Then, we retrieve the surface LW CRE by combining the theorical parametrizations and the cloud properties derived from CALIPSO–GOCCP product. Two surface LW CRE

datasets are derived (LWCRE–LIDAR), the first one at *monthly*–$2° \times 2°$ gridded scale[1], and the second one at full CALIPSO horizontal resolution ($90\,\mathrm{m}$ cross-track; $330\,\mathrm{m}$ along orbit-track), both datasets are derived over the $2008 - 2020$ time period. We found that in the LW, clouds warm the surface at a global scale over $2008 - 2020$ time period by $27.0\,\mathrm{Wm^{-2}}$ and mostly due to opaque clouds ($23.0\,\mathrm{Wm^{-2}}$).

- *How accurately can we retrieve the surface cloud warming from space?*

  To evaluate the surface LW CRE new retrieval (LWCRE–LIDAR), I compared it against independent retrievals from both ground and spaceborne perspectives. Ground stations are the only way to get direct observations of surface radiations as stated many times before, therefore, they are the reference for surface fluxes. However, the comparison of satellite retrievals to ground stations can be limited because of the time and space scale differences. Indeed, the ground station represents a few meters in the grid box of the satellite product surrounding the ground station. Satellites with active remote sensing instruments do not overpass the ground station each day. For this reason, the ground station and the satellite do not observe exactly the same scenes. For instance, the ground station can be $100\,\%$ cloudy and the satellite grid box can be $50\,\%$ cloudy. Therefore, the exact amplitude of surface fluxes would be different when comparing satellite retrievals to ground station measurements. However, the surface fluxes' interannual variability should be similar from both ground and spaceborne perspectives. For example, if Summer is cloudier than Winter, both the ground station and satellite should capture this seasonal variability. The comparison at *monthly*–$2° \times 2°$ gridded scale to three ground stations showed that the surface LWCRE–LIDAR captures the interannual variability well (correlation of 0.69, 0.77, 0.08) but is somehow biased low (bias of $-13.6\,\mathrm{Wm^{-2}}$, $-6.6\,\mathrm{Wm^{-2}}$, $-3.4\,\mathrm{Wm^{-2}}$). The surface LW CRE from the 2BFLX product shows the same behavior as the LWCRE–LIDAR product when compared to ground stations (Chap. 3). The surface LW CRE from CERES–EBAF product shows that it has limited representation of the seasonal cycle over icy surfaces when compared to the ground station and to 2BFLX and LWCRE–LIDAR products (Appendix B).
  Comparison of the LWCRE–LIDAR to the 2BFLX product at *monthly*–$2° \times 2°$ gridded scale over the $2008 - 2011$ period showed that these two products agree well, especially over polar regions. The global average over this period showed a difference of $0.7\,\mathrm{Wm^{-2}}$ between these two products. However, some differences can be locally observed ($\sim \pm 13\,\mathrm{Wm^{-2}}$), especially over rough

[1]The LWCRE–LIDAR *monthly*–$2° \times 2°$ gridded product is available at doi/10.14768/70d5f4b5-e740-4d4c-b1ec-f6459f7e5563 (Arouf et al., 2022a), the $90\,\mathrm{m}$ cross-track; $330\,\mathrm{m}$ along orbit-track resolution will be soon available online.

surfaces of continents. Comparison to CERES-CCCM and 2BFLX products at footprint scales ($20\,\mathrm{km}$ and $5\,\mathrm{km}$ respectively) showed that the LWCRE–LIDAR is strongly correlated to that two retrievals. However, in some specific regions such as deep convective regions, the surface LWCRE–LIDAR can be biased low. Indeed, the surface LW CRE from LWCRE–LIDAR is retrieved from the mean altitude of clouds. In presence of deep convective opaque clouds, the space lidar can be attenuated quickly without seeing much of the bottom part of clouds. Here, the surface LWCRE–LIDAR at full horizontal resolution ($90\,\mathrm{m}$ cross-track; $330\,\mathrm{m}$ along orbit-track) can be biased low by $\sim 10\,\mathrm{Wm}^{-2}$ to $\sim 15\,\mathrm{Wm}^{-2}$. The combination of CALIPSO observation with CloudSat would document better the cloud base height and reduce this bias, but would also limit LWCRE–LIDAR's time period to $2008-2011$ only like for 2BFLX and CERES-CCCM products, while using CALIPSO alone provide a time series over the $2008-2020$ period and can be extended until 2022. We prefer to have 13 years time period long to document the surface LW CRE interannual variability (knowing that it can be biased low) than to improve the cloud base height with CloudSat observations and limit our time period to ~ 4 years. Moreover, using a better cloud base representation from CALIPSO (Mülmenstädt et al., 2018) did not improve considerably the retrieval of surface LWCRE–LIDAR because CALIPSO attenuates most of the time in the boundary layer (Guzman et al., 2017).
Overall, the largest uncertainties in LWCRE–LIDAR retrieval are caused by the specification of cloud base height and atmospheric humidity and temperature profiles in the low troposphere, which can introduce a bias of $\sim 10\,\mathrm{Wm}^{-2}$ to $\sim 15\,\mathrm{Wm}^{-2}$ at $90\,\mathrm{m}$ cross-track and $330\,\mathrm{m}$ along orbit-track resolution and a bias of $\sim \pm 13\,\mathrm{Wm}^{-2}$ at *monthly*–$2^\circ \times 2^\circ$ gridded scale. These limitations are found in the 2BFLX product too (Henderson et al., 2013). Unlike CERES-CCCM and 2BFLX products, the LWCRE–LIDAR is available over the $2008-2020$ time period (13 years). This product may be extended further with CALIPSO observations and with future spaceborne lidars if possible (*e.g.* EarthCARE (Illingworth et al., 2014) that will be launched soon).

- *How the surface cloud warming varies in response to Arctic sea ice cover variability during Fall?*

  It is useful to study the covariability of the sea ice cover and surface LW CRE as they have direct effects on one another. The sea ice cover determines the surface of exposed open water and the amount of water vapor in the boundary layer. This affects the formation of low-level clouds during non-summer seasons (Kay and Gettelman, 2009; Morrison et al., 2018). The low-level clouds enhance the downwelling LW fluxes toward the surface and may amplify the

sea ice loss. Previous studies showed a clear increase in low-level clouds occurrence of $\sim 30\,\%$ over open water compared to over sea ice during Fall, suggesting the potential increase of LW surface cloud warming (Morrison et al., 2018). But the lack of reliable surface cloud warming retrieval over polar regions on a long time scale limited quantifying in $\mathrm{W m^{-2}}$ surface cloud warming increase in response to this low-level cloud occurrence increase. Here, we dispose of new retrieval of surface LW cloud warming over 13 years time period allowing us to have a robust study of this covariability.
To isolate the effect of sea ice cover variability on surface LW CRE, we rely on an interesting method that isolates a region in the Arctic where the *daily* sea ice cover has varied between $2008-2020$ during October months. Specifically, this region (delimited by the Intermittent mask) includes all $1^\circ \times 1^\circ$ grid boxes that never remain always ice-free ($< \ 15\%$) nor always ice-covered ($> \ 80\%$) during October months. We relied on Morrison et al. (2018) previous study that developed a similar approach. By instantaneously collocating surface cloud warming and sea ice observations in regions where sea ice varies, we found that low-level clouds ($Z_{T_{Opaque}}$<2 km) formed over newly open water warm the surface by values higher than $80\,\mathrm{W\,m^{-2}}$. We found that these high values of surface cloud warming occur much more frequently over open water than over sea ice. Quantitatively, high values of surface cloud warming (surface LW CRE $>80\,\mathrm{W\,m^{-2}}$) occur $\sim \ +50\%$ more often over open water than over sea ice during October months. Compared to October, November large surface cloud warming values (surface LW CRE $>80\,\mathrm{W\,m^{-2}}$) occur even more frequently ($\sim \ +200\%$) over open water than over sea ice. Future November may look more like actual October and future December may look like actual November with a large increase in the occurrence of high values of surface cloud warming over open water than over sea ice. This suggests that as the Arctic continues to warm up due to human-induced activities, cloud surface warming will delay sea ice freeze-up later into the Fall and may amplify Arctic sea ice loss.

Perspectives

At the end of this thesis, several interesting ideas came to light, but due to a lack of time, they could not be explored more deeply or have relevant results. Therefore, I present here a few ideas that can be logical follow-ups to this thesis with some preliminary results for some of them.

- *Do clouds help to set up the sea ice melt onset during Spring?*

  The third part of this thesis (Chap. 4) is about quantifying surface cloud warming increase in response to sea ice loss during Fall. What about Spring? I think

that it would be interesting to investigate the sea ice cover and surface cloud warming covariability during Spring with this new surface LW CRE retrieval (LWCRE–LIDAR). In Spring, any increase in low-level clouds would increase surface warming and weaken the sea ice. Thin sea ice would be more sensitive to warming and would melt more easily and quickly during Summer. Space-borne lidar observations showed more low-level clouds over open water than over sea ice during Fall, Spring, and Winter (Kay and Gettelman, 2009; Morrison et al., 2018). Low-level clouds may accelerate the onset of sea ice melt in Spring (Apr., May). An interesting study would be to isolate years of large sea ice loss during the CALIPSO period, such as 2012 and 2020, and investigate the surface cloud warming during Spring over open water and over sea ice, investigate if clouds have an effect on the onset of large sea ice loss. An issue that we can be confronted with, is the small areas of open water during Spring. Indeed, during Spring, the Arctic is largely covered by sea ice. Isolating a new region where the sea ice concentration has varied over the $2008 - 2022$ during Spring (see chapter 4) may allow us to observe the increase of surface cloud warming over open water compared to over sea ice. This study would be a logical follow-up to chapter 4.

- *How low-energy laser shots effect the stability of CALIPSO observations?*

  As stated before, CALIPSO is experiencing low-energy laser shots induced by a slow pressure leak in the laser's canister. These low-energy laser shots occur primarily over the SAA region (Noel et al., 2014). In order to study the variability of cloud properties and surface LW CRE at a global scale, one needs to take precautions when using CALIPSO observations after 2017, especially when attributing changes in surface LW CRE due to cloud properties variations or when studying global trends of cloud properties and surface LW CRE. For those reasons, we need to accurately understand how these low-energy laser shots affect our retrieval and how we can over-pass this issue in order to maintain a certain time series length. Before studying surface cloud warming variations during this last decade, we first analyze the effect of low-energy laser shots on cloud properties over these 13 years ($2008 - 2020$). If the global cloud properties time series are stable, cloud variability and trend studies can be considered in some specific regions that are more sensitive to human-induced climate warming. We will try to lengthen the surface LW CRE derived from CALIPSO–GOCCP cloud properties to 16 years long.

- *What are the cloud properties that drove surface cloud warming variations during this last decade?*

  As the climate warms and the sea ice melts, cloud properties are changing and

would change surface LW CRE. Clouds' vertical structure is more sensitive to climate warming than the horizontal structure and can be better documented with active spaceborne instruments (Chepfer et al., 2014). In the third perspective, I propose to study the temporal and spatial variations of surface LW CRE and variations induced by cloud properties variations. For this end, the surface LW CRE and cloud properties need to be linked with simple relationships. The LWCRE-LIDAR is derived from linear theoretical parameterizations (see chapter 3) allowing us to decompose its variation into contributions from each cloud property that it depends on. Some preliminary results and conclusions are given in Appendix C but need further investigation. We need to understand which cloud property has driven the surface LW CRE variation over the last decade in order to better understand, predict and adapt to future climate change.

Appendices

Appendix A

Radiation physics

The radiation energy that crosses our Earth system is transported by electromagnetic waves between the emitting and receiving sources. The electromagnetic energy can be characterized by its wavelength λ [m], its frequency ν [Hz] or its wavenumber $\widetilde{\nu}$ [m^{-1}] witch the three are linked by the following relations:

$$\nu = c\widetilde{\nu} = \frac{c}{\lambda} \tag{A.1}$$

where c is the velocity of light.

Sun's electromagnetic radiation is centered around the visible domain, 0.4–$0.8\,\mu\mathrm{m}$, because the surface temperature of the Sun is close to $5700\,\mathrm{K}$. This is known as the *Wien Displacement Law*, which states that the wavelength of peak blackbody[1] emission is inversely proportional to its temperature. Same for radiation emitted by Earth and its atmosphere that is largely confined in the infrared domain. The Sun, the Earth, and clouds are not perfect blackbodies, but some physics of blackbodies remain valid. The intensity of emitted radiation B_λ [$\mathrm{W\,m^{-2}\,sr^{-1}\,nm^{-1}}$] for a blackbody at a given temperature T [K] is described by *Planck's Law* :

$$B_\lambda(\lambda, T) = \frac{2hc^2}{\lambda^5} \frac{1}{e^{\frac{hc}{k_B \lambda T}} - 1} \tag{A.2}$$

where λ [nm] is the wavelength, T [K] is the blackbody temperature, c [$\approx 3.00 \times 10^8\,\mathrm{m\,s^{-1}}$] is the velocity of light, h [$\approx 6.63 \times 10^{-34}\,\mathrm{J\,s}$] is the Planck constant and k_B [$\approx 1.38 \times 10^{-23}\,\mathrm{J\,K^{-1}}$] is the Boltzmann constant.

Integrating equation A.2 over the entire wavelength domain, and after some rearranging, gives the flux density of radiative energy emitted by a blackbody (hereafter referred to as radiative flux), which is described by the *Stefan–Boltzmann Law*:

$$F = \sigma T^4 \tag{A.3}$$

[1] A mass of material with a uniform temperature and composition that completely absorbs all incident radiation and reemit it back

where σ [$\approx 5.67 \times 10^{-8}\,\mathrm{W\,m^{-2}\,K^{-4}}$] is the Stefan-Boltzmann constant.

When an electromagnetic wave travels in vacuums, such as space, it remains unchanged. When the electromagnetic wave encounters matter, it is subjected to one of these three processes: *Absorption* (α), *Reflection* (R) and *Transmission* (τ) and are wavelength dependent. The sum of the three coefficients is equal to 1:

$$\alpha + R + \tau = 1 \tag{A.4}$$

Reflection (R) is when the incident flux encounter matter, part of it might be reflected back to the medium from which it comes. The reflection can give a unique incident flux, *specular reflection*, or it can occur after some penetration into the material and then be *scattered* by molecules or particles, *diffuse reflection*, which can occur in clouds for instance. The ratio of the reflected energy to the incident radiation is called albedo and is close to 0.3 for our Earth in the SW domain.

Transmission (τ) describes the radiant energy that travels through a matter without any interaction with the matter or by *scattering*, *diffuse transmission*. The radiant energy scattered is not converted into any other energy and remains in the form of radiation but is redirected.

The *scattering* regime is dependent on the *size parameter*[2] which is defined, for a spherical particle with a radius a, as the ratio of the particle circumference to the incident wavelength λ:

$$x = \frac{2\pi a}{\lambda} \tag{A.5}$$

Particles and molecules of different sizes suspended in the atmosphere interact differently with radiation of different wavelengths. If the particle/molecule size is close to the radiation wavelength ($x \gtrsim 1$), then the Mie scattering regime occurs. If the particle/molecule size is smaller than the radiation wavelength ($x << 1$), then the Rayleigh scattering regime occurs.

The *Absorption* (α) quantifies the radiant energy that is not reflected nor transmitted by the matter but is absorbed. It can be changed into heating for example and that is what happens to the Sun radiation that is not reflected back to space and goes to heat Earth.

The energy absorbed by a matter is emitted back, known as the *emissivity* (ε), defined as the ratio of the radiance emitted by a gray-body[3] to the radiance emitted by a blackbody at the same temperature. The *emissivity* is equal to the *absorption*, as described by *Kirchhoff's Law*, for a given wavelength λ.

[2] The effect of particle size on scattering.
[3] Incomplete absorption and emission of the incident radiation

$$\varepsilon_\lambda = \alpha_\lambda \tag{A.6}$$

Equation A.3 for a gray-body is:

$$F = \varepsilon_\lambda \sigma T^4 \tag{A.7}$$

The text in this Appendix is based primarily on Lenoble (1993) and Liou (2002) handbooks.

Appendix B

Comparison of LWCRE-LIDAR and 2BFLX products to CERES–EBAF product

B.1 Global mean comparison at gridded scale

Figure B.1 represents a comparison of LWCRE–LIDAR to CERES–EBAF. The surface LW CRE from LWCRE–LIDAR is larger than CERES–EBAF one over the oceans (except in stratocumulus regions). LWCRE–LIDAR is smaller than CERES–EBAF over icy surfaces and over ocean stratocumulus regions.

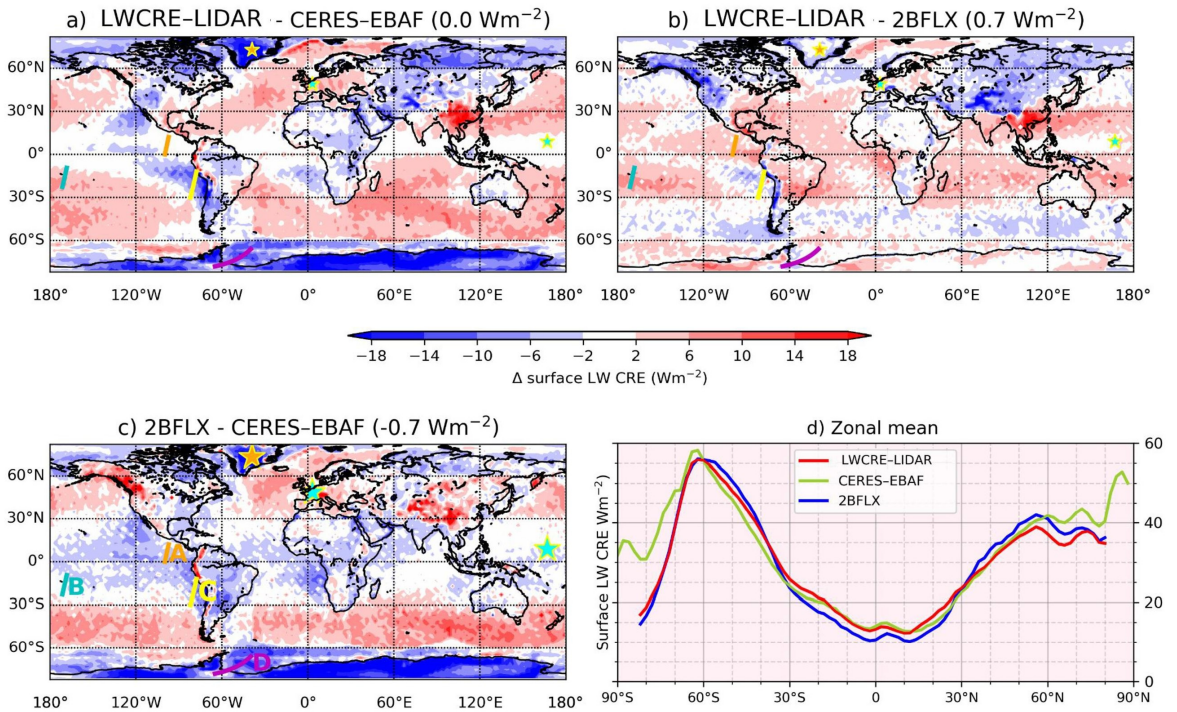

Figure B.1 : Maps of differences in the surface LW CRE (a) LWCRE–LIDAR minus CERES–EBAF, (b) LWCRE–LIDAR minus 2BFLX, and (c) 2BFLX minus CERES–EBAF, (d) zonal means of the satellite products. Data are averaged over 2008 – 2010.

The larger differences (~ -14 to $\sim -18\,\mathrm{Wm^{-2}}$) occur over Greenland, Antarctica, and tropical stratocumulus regions. Over icy surfaces, like Greenland and the Antarctic ice sheets, CERES–EBAF has limited ability to differentiate the radiative fluxes emitted by the surface from those emitted by clouds (Liu et al., 2010; Stubenrauch et al., 2013). The retrieval of surface LW CRE from CERES–EBAF relies on cloud characterization from MODIS–CERES, which detects more clouds than other spaceborne sensors over icy surfaces (GEWEX Cloud Assessment; Stubenrauch et al., 2013). Similarly, since stratocumulus clouds are low warm clouds at temperatures close to the surface temperature, CERES's radiometer can also have some bias when differentiating the LW cloud fluxes from surface fluxes over these regions. However, over stratocumulus regions, CALIPSO may not see the cloud base height and underestimate the surface LW CRE. As this is already seen in the global instantaneous scale comparison with the CERES–CCCM product that combines passive instruments as well as active instruments (Lidar and Radar) to document the vertical cloud structure (Chap. 3, Fig. 12).

Comparison of 2BFLX to CERES–EBAF shows similar behavior as the previous comparison over icy surfaces with large differences (~ -14 to $\sim -18\,\mathrm{Wm^{-2}}$) but the differences over stratocumulus regions don't persist. Indeed, 2BFLX product combines observations from CALIPSO, MODIS, and CloudSat. The latest provides a better representation of cloud base height than CALIPSO. Therefore, 2BFLX product does not underestimate the surface LW CRE is stratocumulus regions. Comparison of LWCRE–LIDAR to 2BFLX is already presented in chapter 3.

Zonal averages of the surface LW CRE for $2008 - 2010$ (Fig. B.1d) show that over the broad domain reaching from $60°$ N to $60°$ S, the three satellites techniques show similar zonal means with differences among the three typically not exceeding $\sim 3\,\mathrm{Wm^{-2}}$. Over polar regions, the surface LW CRE from CERES–EBAF is generally higher than the other two products derived from active sensors.

B.2 Seasonal evolution of the zonal mean

Figure B.2 represents the annual evolution of the zonal mean of the surface LW CRE from CERES–EBAF (Fig. B.2a), LWCRE–LIDAR (Fig. B.2b), and 2BFLX (Fig. B.2c). The two active sensor figures exhibit the same behavior whilst CERES–EBAF has a stronger surface LW CRE in the polar regions during winter months, which corresponds to the minimum of opaque cloud cover and the maximum of sea ice. To see where the largest differences with CERES–EBAF are located, Figures B.2d and B.2e represent the differences between LWCRE–LIDAR and CERES–EBAF and the differences between 2BFLX and CERES–EBAF respectively. The same feature is observed in both figures with CERES–EBAF having larger surface LW CRE than the

other two products in polar regions during their respective winters. CERES–EBAF also has smaller surface LW CRE in the mid-latitude regions.

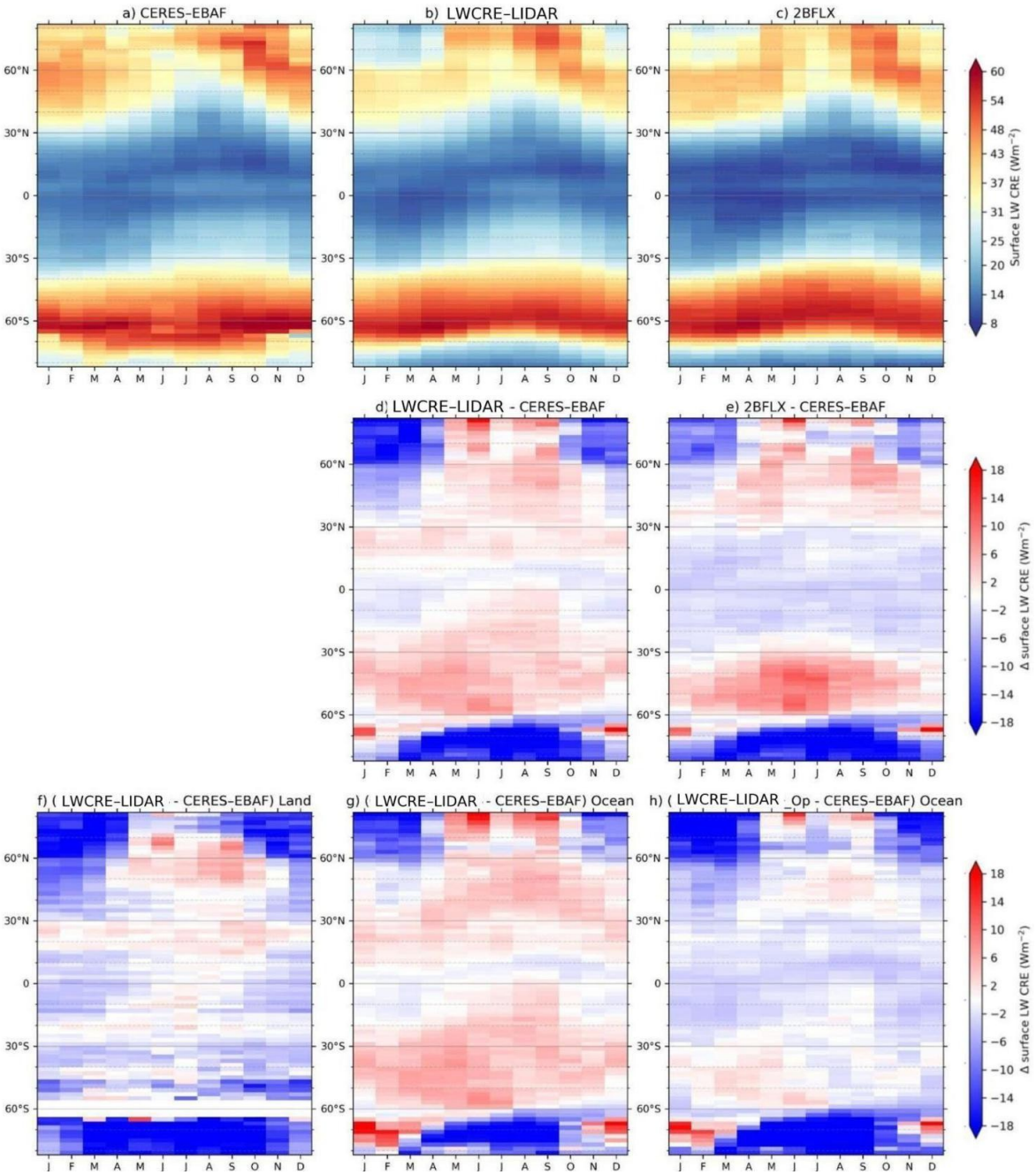

Figure B.2 : Seasonal evolution of the zonal mean of the surface LW CRE: first line) for each satellite product, second line) differences between satellite products, third line) differences between LWCRE–LIDAR and CERES–EBAF decomposed into f) land only, g) ocean only, and h) ocean only but using surface LW CRE-Opaque instead of surface LW CRE for LWCRE–LIDAR product. Data are averaged over $2008 - 2010$.

Decomposing the difference (Fig. B.2d) into land only (Fig. B.2f) and ocean only (Fig. B.2g) shows LWCRE–LIDAR lower than CERES–EBAF over NH land [$50°$ N to $80°$ N] during winter (September to May) and over the icy Antarctic all

year long. The oceans contribute to this difference during months of significant sea ice cover. These results suggest that the differences in surface LW CRE are likely due to CERES–EBAF detecting clouds over icy surfaces when there are no clouds (Stubenrauch et al., 2013).

On the contrary, CERES–EBAF is lower than LWCRE–LIDAR mostly over mid-latitude oceanic regions all year long (Fig. B.2g) and this difference is also observed in the annual mean maps (Fig B.1a). These regions contain low-level altitude thin clouds and few low opaque clouds (1 to $2\,\mathrm{km}$: 2.6b,d). To see if these differences are caused by thin clouds in the boundary layer, we have computed the difference between the surface LW opaque CRE from LWCRE–LIDAR observations and the CERES–EBAF product (Fig. B.2h) over ocean only. The differences over mid-latitude oceans are smaller and close to 0 in this case (Fig. B.2h). Thus, the reason for the CERES–EBAF surface LW CRE being weaker than the LWCRE–LIDAR in these regions is likely because the CERES–EBAF does not see the optically thin broken clouds in the boundary layer over mid-latitude oceans.

B.3 Comparison to ground-based stations

Figure B.3 presents the comparison of seasonal cycles between the satellite retrievals and the ground-based observations. Over the Greenland site (Fig. B.3a,d), LWCRE–LIDAR and 2BFLX find the same seasonal cycle of the surface LW CRE with maxima in July, which corresponds to the maximum of opaque cloud cover, same as the ground station's seasonal cycle. The CERES–EBAF retrieval maximum is shifted by about three months (October, Fig. B.3a,d), to a time of year that shows the minimum of opaque cloud cover based on CALIPSO–GOCCP (not shown). This result suggests that during these months, the CERES–EBAF retrieval does not successfully distinguish LW upward fluxes from clouds and the surface. This is consistent with CERES–EBAF low-mid and high-mid cloud fractions being biased high over the *Summit* site except for summertime (not shown). Consistently, Figure B.3d shows CERES–EBAF's surface LW CRE is overestimated compared to ground-base retrievals in all seasons except in Summer. As a consequence, CERES–EBAF does not capture the surface LW CRE annual cycle, contrarily to LWCRE–LIDAR and 2BFLX retrievals. Over Greenland, on average compared to *Summit* ground-based observations, LWCRE–LIDAR underestimates the surface LW CRE by $-8.5\,\mathrm{Wm}^{-2}$, while 2BFLX underestimates it by $-16.4\,\mathrm{Wm}^{-2}$ and CERES–EBAF overestimates it by $+36.6\,\mathrm{Wm}^{-2}$ (not shown). The comparison of averages is made only when all products are available and for the Greenland site, this is just for three months (JFM 2011). These differences calculated for three months persist when compared to the values over the $2011-2015$ period. CERES–EBAF follows a different annual cycle

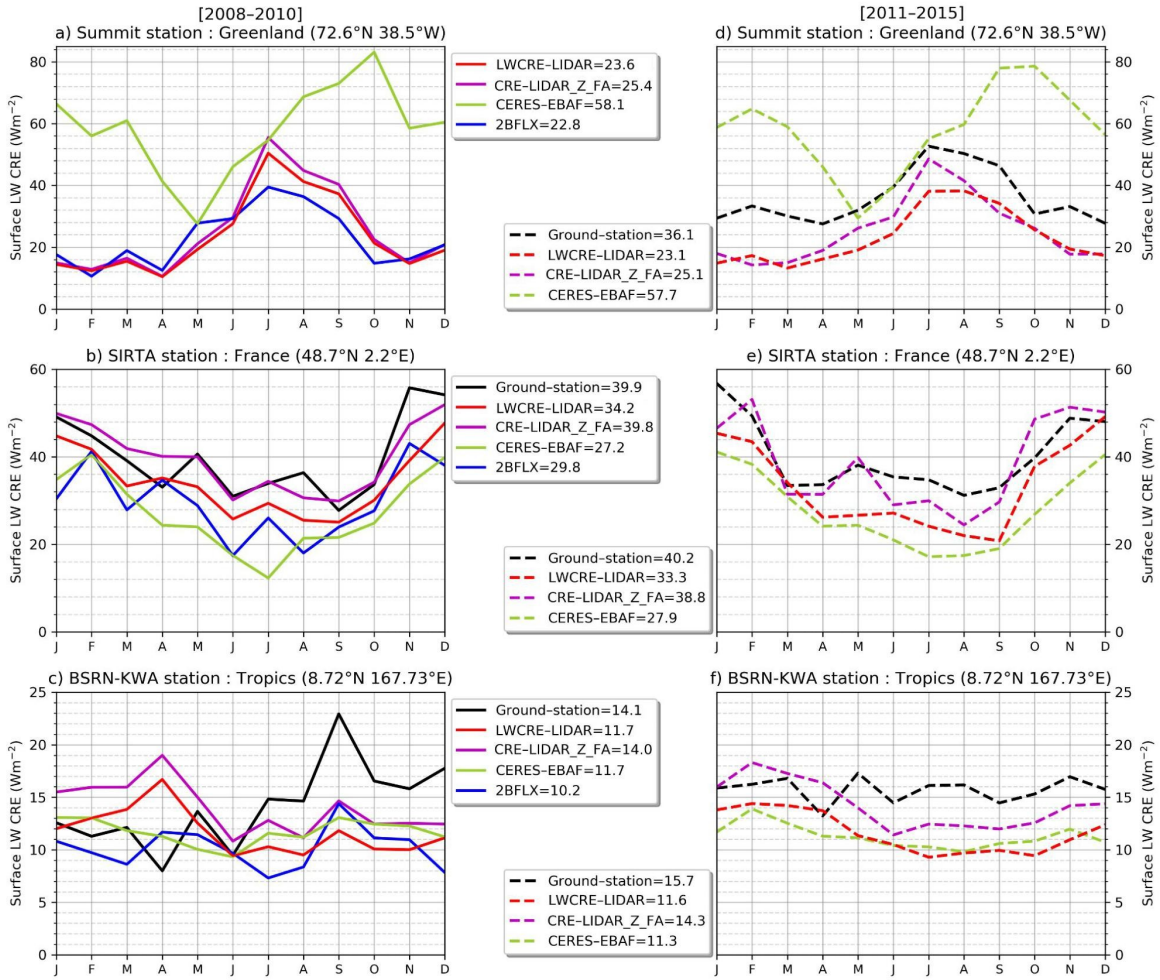

Figure B.3 : Comparisons between the surface LW CRE derived from ground-stations measurements and from satellites over three locations in mean seasonal cycles: first line) polar region at Greenland *Summit* site, second line) mid-latitudes at *SIRTA* site, and third line) tropics at *KWA* site. Mean values are reported in the legend. The left column corresponds to $2008-2010$ and the right column corresponds to $2011-2016$. Note that the y-axis scale is different in each subplot.

with maxima wider and shifted by about two to six months in the temporal time series (not shown).

The same behavior where CERES–EBAF overestimates the surface LW CRE compared to LWCRE–LIDAR and 2BFLX is observed over the map of difference (Fig. B.1a,c) in icy polar regions, for instance over Greenland and Antarctica ice sheets, and CERES–EBAF different seasonal cycle compared to LWCRE–LIDAR and 2BFLX (Fig. B.2d,e). While this comparison suggests that LWCRE–LIDAR could be biased somewhat low compared to the ground-station perspective over Greenland, it is also clear that LWCRE–LIDAR approach does appropriately capture the seasonal cycle and annual variability, while the CERES–EBAF approach appears to be significantly biased high with an unrealistic annual cycle.

Over the mid-latitude continental site (*SIRTA*, Fig. B.3b,e), the surface LW CRE seasonal cycle of LWCRE–LIDAR and 2BFLX are close to each other and the three satellite-derived products show similar seasonal cycles as the ground station. On average over all (not shown), LWCRE–LIDAR underestimates the surface LW CRE by $-5.7\,\mathrm{Wm^{-2}}$ compared to ground-based observations, while 2BFLX underestimates it by $-9.4\,\mathrm{Wm^{-2}}$ and CERES–EBAF underestimates it by $-12.1\,\mathrm{Wm^{-2}}$.

Over the tropical ocean site (Fig. B.3c,f), the surface LW CRE seasonal cycle is relatively flat. On average over all (not shown), LWCRE–LIDAR underestimates the surface LW CRE by $-2.3\,\mathrm{Wm^{-2}}$compared to ground-based observations and 2BFLX underestimates it by $-4.1\,\mathrm{Wm^{-2}}$, and CERES–EBAF underestimates it by $-2.7\,\mathrm{Wm^{-2}}$.

Even though 2BFLX and surface LWCRE-LIDAR don't apply a diurnal cycle correction to their retrieval, they found a realistic seasonal cycle of the surface LW CRE over the Greenland ice sheet. CERES–EBAF apply a diurnal cycle correction to their retrieval. However, they find a seasonal cycle completely biased over polar regions because of limitations in passive instruments technology that highly depends on the surface type (see section 2.4.2).

B.4 Variation of the surface LW CRE over 13 years (2008 – 2020)

Figure B.4a shows the temporal evolution of the surface LW CRE anomaly from the three satellite-derived products over 13 years (2008 – 2020). A decomposition separating continents from oceans and Northern Hemisphere (NH) from Southern Hemisphere (SH) is presented in Figs. B.4b–g.

There is consistent annual variability in the global surface LW CRE anomaly between the three satellite retrievals. This appears to be because of the annual cycle variations in the SH and NH, which are out of sync from each other, and the fact that the SH annual amplitude (and magnitude) are larger. Thus, the annual variation of the global surface LW CRE is most closely aligned with the annual variation of the SH.

The phasing of the annual cycle of LWCRE–LIDAR and 2BFLX anomalies are roughly similar over the 2008 – 2010 time period while, as noted before, CERES–EBAF anomaly shows a shift in the annual cycle of about two months compared to the other two satellite-derived products. This shift remains between CERES–EBAF and LWCRE–LIDAR anomalies over the 13 years.

The phasing of the annual cycle for the CERES–EBAF product is actually quite consistent with the other two products for both NH and SH over oceans, but is

inconsistent over lands especially in the NH (Fig. B.4d,g) because of false cloud detection as already explained and shown in figures B.1, B.2 and B.3. However, it is interesting that even over NH land, the annual minima match pretty well between CERES–EBAF and LWCRE–LIDAR. Thus, the overall two months shift (Fig. B.4a) is in part due to the differences in NH land annual maximum but apparently also somewhat due to the different amplitudes of the annual cycles for different areas and how they combine in unique ways for the different datasets.

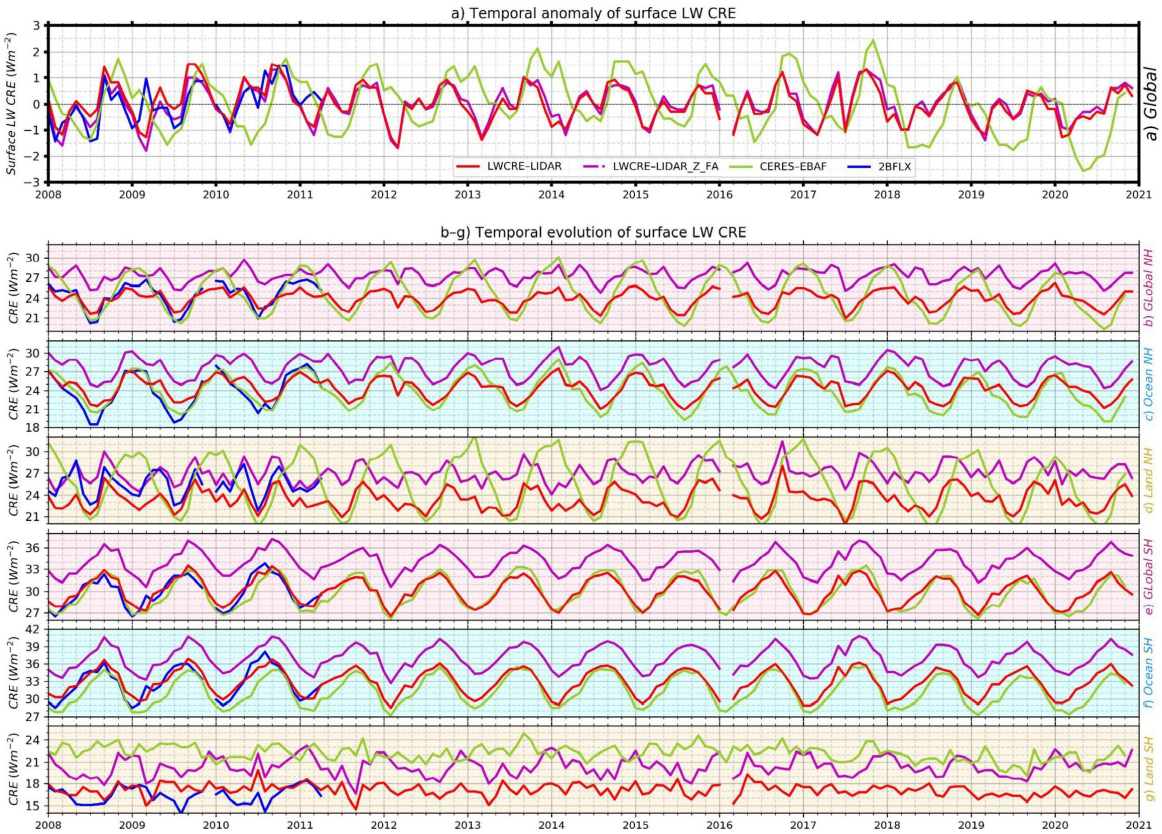

Figure B.4 : a) Time series of global surface LW CRE anomalies. b-f) Time series of surface LW CREs over all NH, ocean NH, land NH, all SH, ocean SH, land SH. In a) the anomaly is defined as the global average for each month of each product minus its own average over the whole time series. Note that the y-axis scale is different in each subplot.

The inter-annual variability is pretty interesting. For example, the NH winter maximum in CERES–EBAF and LWCRE–LIDAR products appears to vary by up to about $3\,\mathrm{Wm}^{-2}$ from year to year. That is the kind of variability that might have significant impacts on climate-relevant processes like the melting of the cryosphere.

B.5 Conclusion

The evaluation of this new CALIPSO-based surface LW CRE against other datasets showed that overall this new retrieval agrees well with CloudSat-based estimate

(2BFLX, L'Ecuyer et al., 2019) but this latter is limited in time until only 2011 due to a battery anomaly. Compared to CERES–EBAF, the new LWCRE–LIDAR retrieval provides new and more reliable information on the surface LW CRE over specific regions such as over icy and continental regions. Over these regions, space-based lidar is successful in distinguishing clouds from the surface. It provides new information over mid-latitude oceans, where space-lidar detects well-optically thin small clouds.

Appendix C

Decomposition of the temporal variations of surface longwave cloud radiative effect during the last decade

C.1 Methodology

C.1.1 Retrieval of surface longwave cloud radiative effect from simple parametrizations

The methodology followed to retrieve the surface **L**ong**W**ave (LW) **C**loud **R**adiative **E**ffect (CRE) is detailed in chapter 3. Here, I will not give a further explanation but only the linear parametrization of the surface LW CRE that would be needed in the following sections. As stated before, the total surface LW CRE (CRE_{Total}) can be decomposed into opaque (CRE_{Opaque}) and thin (CRE_{Thin}) cloud contributions:

$$CRE_{Opaque} = C_{Opaque} \times (a \times Z_{T_{Opaque}} + b) \tag{C.1}$$

$$CRE_{Thin} = C_{Thin} \times (\varepsilon_{Thin} + 0.06) \times (a \times Z_{T_{Thin}} + b) \tag{C.2}$$

$$CRE_{Total} = CRE_{Thin} + CRE_{Opaque} \tag{C.3}$$

where a [$\mathrm{Wm^{-2}k^{-1}}$] and b [$\mathrm{Wm^{-2}}$] are constants whose values depend on humidity and temperature profiles.

C.1.2 Decomposition of the temporal variations of the surface longwave cloud radiative effect into contributions due to cloud properties

A change in the surface LW CRE between two states of the atmosphere can be expressed as contributions due to changes in cloud properties. To decompose these variations into components, the surface LW CRE should be derived from linear parametrizations that link the surface LW CRE to cloud properties. This method is used in Vaillant de Guélis et al. (2017b) to partition the TOA LW CRE change into components due to cloud property variations. The decomposition of the ΔCRE_{Total} is done through these five variables:

$$\Delta CRE_{Total} = \sum_{i=1}^{5} \frac{\partial CRE_{Total}}{\partial V_i} \times \Delta V_i \tag{C.4}$$

where Δ represents a change between two states of the atmosphere and V_i the five cloud properties derived from CALIPSO: C_{Opaque}, $Z_{T_{Opaque}}$, C_{Thin}, $Z_{T_{Thin}}$ et ε_{Thin}.

We can decompose the ΔCRE_{Total} into contributions due to opaque clouds ΔCRE_{Opaque} through the opaque cloud properties C_{Opaque} and $Z_{T_{Opaque}}$ (Eq. C.1) and in contributions due to the thin clouds ΔCRE_{Thin} through the thin cloud properties C_{Thin}, $Z_{T_{Thin}}$ and ε_{Thin} (Eq. C.2). Equation C.4 would be:

$$\Delta CRE_{Opaque} = \frac{\partial CRE_{Opaque}}{\partial C_{Opaque}} \Delta C_{Opaque} + \frac{\partial CRE_{Opaque}}{\partial Z_{T_{Opaque}}} \Delta Z_{T_{Opaque}} \tag{C.5}$$

$$\Delta CRE_{Thin} = \frac{\partial CRE_{Thin}}{\partial C_{Thin}} \Delta C_{Thin} + \frac{\partial CRE_{Thin}}{\partial Z_{T_{Thin}}} \Delta Z_{T_{Thin}} + \frac{\partial CRE_{Thin}}{\partial \varepsilon_{Thin}} \Delta \varepsilon_{Thin} \tag{C.6}$$

$$\Delta CRE_{Total} = \Delta CRE_{Opaque} + \Delta CRE_{Thin} \tag{C.7}$$

where Δ represents the monthly anomaly, *i.e.* the difference between the value of the variable V_i in the current month minus the averaged value of V_i over the whole observation time series.

To obtain the partial derivatives of equations C.5 and C.6, we use the linear equations established in chapter 3 (Equations C.1 and C.2).

C.1.3 Relative contribution of cloud properties to the surface longwave cloud radiative effect variation

We will use the decomposition established earlier to determine the relative contribution X_i of each cloud property V_i to the overall interannual variations of CRE_{Total}. We use the Boer and Yu (2003) equation in time variations which is used in Vaillant de Guélis et al. (2017b) too:

$$X_i = \frac{cov(\Delta CRE_{Total}(t), \Delta CRE_{V_i}(t))}{\sigma^2_{\Delta CRE_{Total}}(t)} \tag{C.8}$$

where $cov(\Delta CRE_{Total}(t), \Delta CRE_{V_i}(t))$ represents the covariance between ΔCRE_{Total} and the contribution of the cloud property V_i to the variations in CRE_{Total}. $\sigma^2_{\Delta CRE_{Total}}(t)$ represents the variance of ΔCRE_{Total}.

The relative contribution X_i of each cloud property cannot exceed $100\,\%$ but can be negative. The sum of all contributions X_i is $100\,\%$. This method was used in Vaillant de Guélis et al. (2017b) to study the temporal variation of TOA LW CRE and to attribute these variations to variations occurring in cloud properties. Here, we use the same approach to study the *surface* LW CRE variations.

C.2 Some preliminary results

Variations of the sea ice cover affect cloud properties (Kay and Gettelman, 2009; Morrison et al., 2018). Therefore, it affect the surface LW CRE (Kay and Gettelman, 2009; Vaillant de Guélis et al., 2017a). Here we document how an extremely low sea ice cover may affect cloud properties and surface LW CRE. I present some preliminary results developed following the methodology explained above. The results that I show here have been presented at three international conferences (AMS, ESA-LPS, and IRS) but need further investigation. What I show is not an attribution of cause and effect but just looking at the overall interannual behavior of sea ice and surface LW CRE and how they may covary together using *monthly*–$2^\circ \times 2^\circ$ gridded data. To attribute cause and effect, one needs to work at an instantaneous local scale as shown in chapter 4 to capture better sea ice and cloud covariability.

C.2.1 Interannual variation of surface LWCRE–LIDAR and sea ice cover

To isolate a region in the Arctic where the sea ice cover varies, we define the Intermittent mask for September moths. The Intermittent mask contains grid boxes

that never remain only ice-free (monthly sea ice concentration $< 15\%$) or only ice-covered (monthly sea ice concentration $> 80\%$) over $2008 - 2020$. We chose September because each year, September has the least sea ice cover. But October would be a better month to look at because the surface SW CRE vanishes away. In future work, I would use October to apply my decomposition of surface LW CRE variations and use *daily* rather than *monthly* temporal resolution to determine the Intermittent mask.

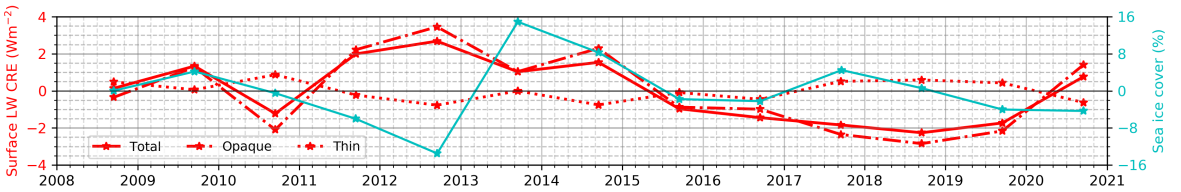

Figure C.1 : Time series of the surface LW CRE (red) and sea ice cover (cyan) anomalies in September over the Intermittent mask. The anomaly is defined as the average over the Intermittent mask for each September minus the average over September of the whole time series. Note that the y-axis scale is different for sea ice cover and surface LW CRE.

Figure C.1 shows that the correlation between surface LW Opaque CRE variation and sea ice cover variation is weakly negative (-0.14) in September over $2008-2020$ period. Over sea ice, the dry cold air promotes thin cloud formation. Therefore, the correlation between the surface LW Thin CRE variation and sea ice variation is weakly positive ($+0.22$). September 2012 corresponds to an extremely low sea ice cover during the CALIPSO period ($2008 - 2020$), we next focus on this year to look at the spatial distribution of sea ice and surface LW CREs.

C.2.2 Spatial distribution of surface LW CRE and sea ice cover anomalies in September 2012

Figure C.2 shows the spatial distribution of the sea ice cover and surface LW CREs for September 2012 (extremely low sea ice cover). A negative anomaly of sea ice cover (-13.6%) is associated with a positive surface LW CRE ($+2.7\,\mathrm{Wm^{-2}}$) that is mainly due to a positive surface LW Opaque CRE anomaly ($+3.5\,\mathrm{Wm^{-2}}$). The averages are made over the Intermittent mask. On the contrary, thin clouds vanish to favor opaque cloud formation over open water and therefore result in a negative surface LW Thin CRE anomaly (-$0.8\,\mathrm{Wm^{-2}}$). The opaque cloud result is consistent with previous works (Morrison et al., 2018) that show more low liquid clouds over open water in fall and here we quantify the warming effect of these clouds (Surface LW CRE in $\mathrm{Wm^{-2}}$). Morrison et al. (2018) used instantaneously data from CALIPSO and here we use monthly data. The results should be taken with a pinch of salt.

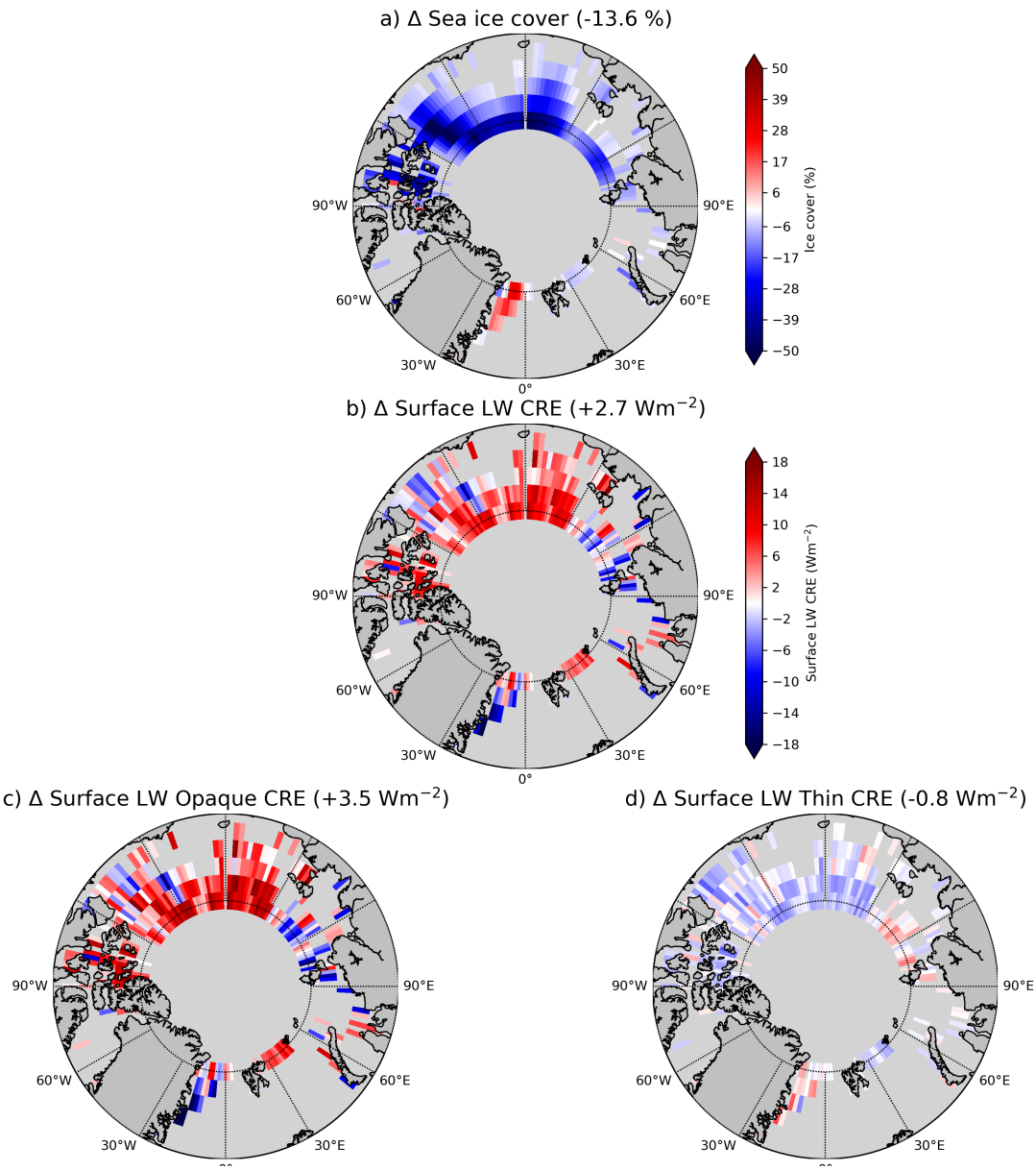

Figure C.2 : Maps of a) sea ice cover anomaly, b) surface LW CRE anomaly, c) surface LW Opaque CRE anomaly, and d) surface LW Thin CRE anomaly in September 2012. The anomaly is computed for September 2012 minus the average of September over the $2008-2020$ period. The anomalies are computed over the Intermittent mask. (Preliminary results).

C.2.3 Where and which cloud property drives the surface LW CRE variation in response to an extremely low sea ice cover in September 2012?

We apply equations C.5 and C.6 to decompose the variation of surface LW CRE into contributions due to cloud properties as shown in section C.1.2 for September 2012 over the Intermittent mask. We found that the augmentation of opaque cloud cover generates a positive surface LW CRE anomaly over the Beaufort and Siberian seas of $+4.9\,\mathrm{Wm}^{-2}$ and $+4.0\,\mathrm{Wm}^{-2}$ respectively. These regions are associated with a large sea ice loss during September 2012. The augmentation of opaque cloud altitude in the Beaufort sea creates a negative surface LW CRE anomaly of $-1.0\,\mathrm{Wm}^{-2}$. In contrast, the diminution of opaque cloud altitude in the Siberian sea creates a positive surface LW CRE anomaly of $+1.6\,\mathrm{Wm}^{-2}$. The difference in sign of the opaque cloud altitude contributions might be due to the surface type (open water Vs sea ice) or to atmospheric circulation and will be investigated in future work. The decrease in sea ice cover is associated with a decrease in thin cloud cover and thus a negative surface LW CRE anomaly of $-0.7\,\mathrm{Wm}^{-2}$.

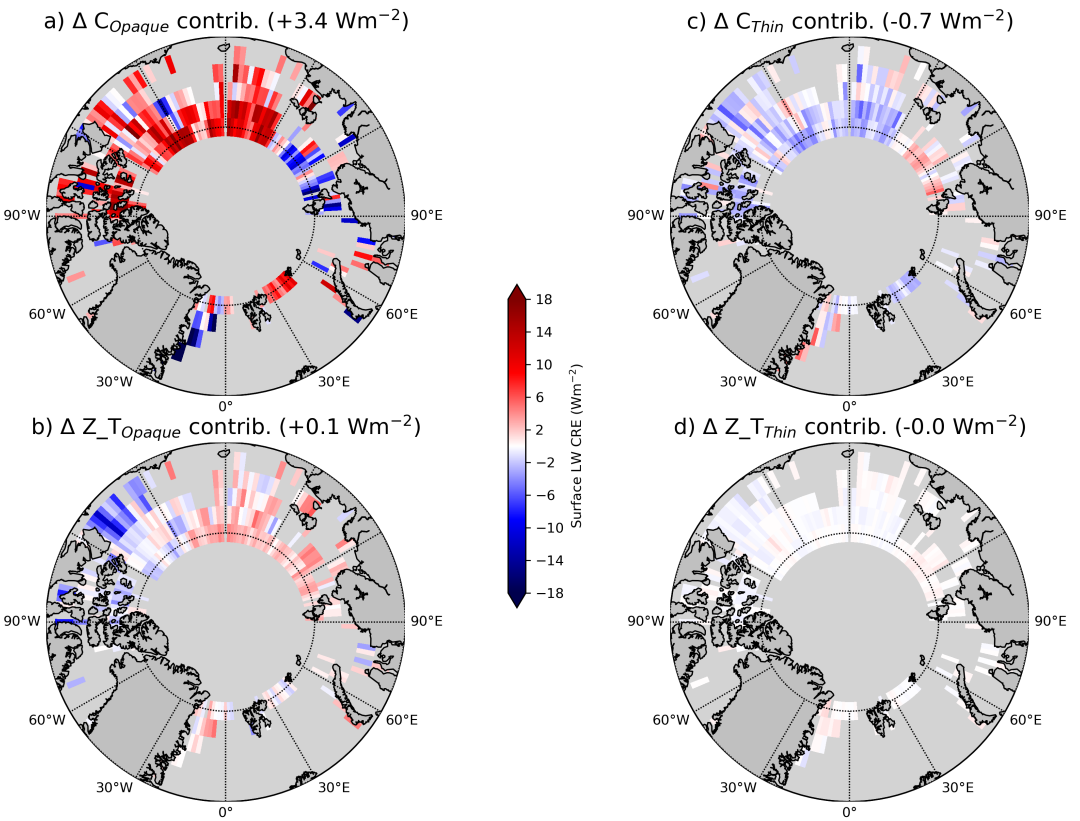

Figure C.3 : Partitioning of the surface LW CRE anomaly during September 2012 into components due to changes in a) opaque cloud cover, b) opaque cloud altitude, c) thin cloud cover, d) thin cloud altitude. (preliminary results).

C.2.4 Interannual variation of surface LWCRE–LIDAR and sea ice cover

We apply equation C.8 to quantify the relative contribution of each cloud property to surface LW CRE temporal variation over the $2008-2020$ period within the Intermittent mask. Opaque cloud cover variations drive the total surface LW CRE temporal variations over the $2008-2020$ period (102%) within the Intermittent mask for September. Interestingly, thin cloud cover variations have a negative relative contribution to the surface LW CRE variations. We showed in chapter 3 that the surface LW CRE is largely defined by opaque clouds. Increasing thin cloud cover would decrease opaque cloud cover. Therefore, it would decrease the total surface LW CRE. Hence, thin cloud cover variations have a negative relative contribution to the surface LW CRE variations.

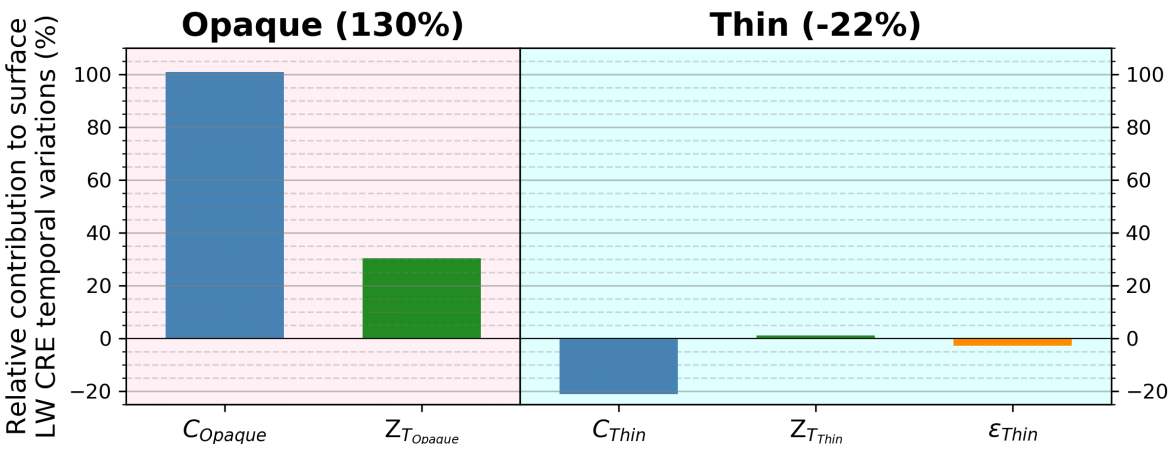

Figure C.4 : Fractional contribution of the five cloud properties to the surface LW CRE variations within the Intermittent mask for September ($2008-2020$).

C.2.5 Conclusion

New estimates of the surface LW **C**loud **R**adiative **E**ffect (CRE) from 13 years of CALIPSO space lidar observations are reliable over polar regions. The CALIPSO surface LW CRE retrieved from simple relationships (LWCRE–LIDAR) allows us to decompose its temporal and spatial variations into components and quantify the relative contribution of each cloud property. For instance, an extremely low sea ice cover (-13.6%) is associated with an increase of surface LW CRE ($+2.7\,\mathrm{Wm^{-2}}$) mainly caused by variations occurring in the opaque cloud cover.

Extending this CALIPSO record with the upcoming spaceborne lidars would lengthen our observational record and help us to capture better variations occurring in clouds.

List of abbreviations

2BFLX level-**2** **FL**u**X**es and **H**eating **R**ates release 04–LIDAR

AFRL **A**ir **F**orce **R**esearch **L**aboratory

AOS **A**tmosphere **O**bserving **S**ystem

ATB **AT**tenuated **B**ackscatter

BSRN **B**aseline **S**urface **R**adiation **N**etwork

CALIOP **C**loud–**A**erosol **LI**dar with **O**rthogonal **P**olarization

CALIPSO **C**loud–**A**erosol **L**idar and **I**nfrared **P**athfinder **S**atellite **O**bservations

CCCM **C**ALIPSO, **C**loudSat, **C**ERES, and **M**ODIS Merged Product

CERES **C**louds and **E**arth's **R**adiant **E**nergy **S**ystems

CFMIP **C**loud **F**eedback **M**odel **I**ntercomparison **P**roject

CMIP **C**oupled **M**odel **I**ntercomparison **P**roject

COSP **C**FMIP **O**bservation **S**imulator **P**ackage

CPR **C**loud **P**rofiling **R**adar

CRE **C**loud **R**adiative **E**ffect

DISORT **DI**screte **O**rdinates **R**adiative **T**ransfer

EBAF **E**nergy **B**alanced and **F**illed

ECMWF **E**uropean **C**entre for **M**edium-**R**ange **W**eather **F**orecasts

ENSO **E**l **N**iño **S**outhern **O**scillation

ERA-I **ERA**–**I**nterim

ERBE **E**arth **R**adiation **B**udget **E**xperiment

GAME **G**lobal **A**tmospheric **Mod**el

GCM **G**eneral **C**irculation **M**odel

GEO geostationary satellites

GEOS **G**oddard **E**arth **O**bserving **S**ystem

GEOS5-DAS **G**oddard **E**arth **O**bserving **S**ystem version **5** **D**ata **A**ssimilation **S**ystem

GOCCP **G**CM-**O**riented **C**ALIPSO **C**loud **P**roduct

IIR **I**maging **I**nfra**R**ed Imager

IPCC–6AR **I**ntergovernmental **P**anel on **C**limate **C**hange–**Sixth** **A**ssessment **R**eport

IPSL **I**nstitut **P**ierre-**S**imon-**L**aplace

ITCZ **I**nter**T**ropical **C**onvergence **Z**one

KWA **Kwa**jalein

Lidar **Li**ght **D**etection **A**nd **R**anging

LMD **L**aboratoire de **M**étéorologie **D**ynamique

LW **L**ong**W**ave

MD **M**olecular **D**ensity

MODIS **MOD**erate-resolution **I**maging **S**pectroradiometer

m.s.l. **m**ean **s**ea **l**evel

NAO **N**orth **A**tlantic **O**scillation

NSIDC **N**ational **S**now and **I**ce **D**ata **C**enter

NSL **N**ear–**S**urface **L**ayer

Radar **Ra**diation **D**etection **A**nd **R**anging

RH **R**elative **H**umidity

RTE **R**adiative **T**ransfer **E**quation

SAA **S**outh **A**tlantic **A**nomaly

SIRTA **S**ite **I**nstrumental de **R**echerche par **T**élédétection **A**tmosphérique

SR **S**cattering **R**atio

SSF **S**ingle **S**canner **F**ootprint

SW **S**hort**W**ave

TOA **T**op **O**f the **A**tmosphere

WFC **W**ide-**F**ield **C**amera

List of notations

Z_{Top} Altitude of the highest cloud layer

Z_{Base} Altitude of the lowest cloud layer

Z_{Opaque} Altitude of lidar beam where it is fully attenuated

Z_{FA} Altitude of lidar beam where it is fully attenuated

$Z_{T_{Opaque}}$ Altitude of the opaque cloud temperature [$\frac{Z_{Top}+Z_{Opaque}}{2}$]

$Z_{T_{Thin}}$ Altitude of the thin cloud temperature [$\frac{Z_{Top}+Z_{Base}}{2}$]

ε_{Thin} Emissivity of thin clouds

C_{Opaque} Cover of opaque clouds

C_{Thin} Cover of thin clouds

C_{Clear} Cover of clear sky

Notation	**Name**	**Unit**
CRE_{Thin}	Thin clouds radiative effect	$\mathrm{W\,m^{-2}}$
CRE_{Opaque}	Opaque clouds radiative effect	$\mathrm{W\,m^{-2}}$
CRE_{Total}	All clouds radiative effect	$\mathrm{W\,m^{-2}}$
Z	Altitude	km
C	Cover	$\%$

Conferences, Workshops, and Symposiums

Poster Presentations

- ***IRS**: International Radiation Symposium*; Jul. 2022; Thessalonique, Greece
  The Surface Longwave Cloud Radiative Effect derived from Space Lidar Observations
- ***LPS**: Living Planet Symposium;* May 2022; Bonn, Germany
  The Surface Longwave Cloud Radiative Effect derived from Space Lidar Observations
- ***AMS**: American Meteorological Society*; Jan 2022; Remote
  Analysis of Decadal Variations of Global Surface Longwave Cloud Radiative Effect derived from Space Lidar Observations
- ***WCRP**: World Climate Research Programme*; Sept. 2021; Remote
  Analysis of Time Series of Global Surface Longwave Cloud Radiative Effect from Space Lidar Observations
- ***EGU**: Eropen Geoscience Union*; May 2021; Remote
  The Surface Longwave Cloud Radiative Effect from Space Lidar Observations, 10.5194/egusphere-egu21-2064

Oral Presentations

- ***EECLAT**: Expecting Earth-Care, Learning from A-train*; Jan. 2023; Banyuls, France
  Quantifying surface cloud warming increase as Fall Arctic sea ice cover decreases
- ***EECLAT***; Jan. 2022; Remote
  Cloud warming effect: A-Train Observations Vs CMIP6 Models
- **EECLAT**; Jan. 2021; Remote
  Effect of clouds on surface temperature from space lidar observations

- ***EECLAT***; Jan. 2020; Avignon, France
  Clouds influence on surface heating in the infrared range on a global scale

Invited Seminars

- *Max-Planck-Institut für Meteorologie*; Jul. 2021; Remote
  The Surface Longwave Cloud Radiative Effect from Space Lidar Observations

Awards

- **Seconde place for a poster presentation at the 102nd American Meteorological Society Annual Meeting,** January 2022.

List of Figures

List of Tables

Bibliography

Agnew, T. and S. Howell (Dec. 2003). "The use of operational ice charts for evaluating passive microwave ice concentration data". en. In: *Atmosphere-Ocean* 41.4, pp. 317–331. DOI: 10.3137/ao.410405.

Arouf, A., H. Chepfer, T. Vaillant de Guélis, R. Guzman, A. Feofilov, and P. Raberanto (2022a). *Longwave Cloud Radiative Effect derived from Space Lidar Observations at the Surface and TOA – Edition 1: Monthly Gridded Product*. dataset. DOI: 10.14768/70d5f4b5-e740-4d4c-b1ec-f6459f7e5563.

Arouf, A., H. Chepfer, T. Vaillant de Guélis, M. Chiriaco, M. D. Shupe, R. Guzman, A. Feofilov, P. Raberanto, T. S. L'Ecuyer, S. Kato, and M. R. Gallagher (July 2022b). "The surface longwave cloud radiative effect derived from space lidar observations". English. In: *Atmospheric Measurement Techniques* 15.12. Publisher: Copernicus GmbH, pp. 3893–3923. DOI: 10.5194/amt-15-3893-2022.

Boer, G. and B. Yu (2003). "Climate sensitivity and response". In: *Climate Dynamics* 20.4, pp. 415–429. DOI: 10.1007/s00382-002-0283-3.

Boisvert, L. N. and J. C. Stroeve (2015). "The Arctic is becoming warmer and wetter as revealed by the Atmospheric Infrared Sounder". en. In: *Geophysical Research Letters* 42, pp. 4439–4446. DOI: 10.1002/2015GL063775.

Boucher, O., D. Randall, P. Artaxo, C. Bretherton, G. Feingold, P. Forster, V.-M. Kerminen, Y. Kondo, H. Liao, U. Lohmann, P. Rasch, S. Satheesh, S. Sherwood, B. Stevens, and X. Zhang (2013). "Clouds and aerosols". In: *Climate Change 2013: The Physical Science Basis. Contribution of Working Group I to the Fifth Assessment Report of the Intergovernmental Panel on Climate Change*. Ed. by T. Stocker, D. Qin, G.-K. Plattner, M. Tignor, S. Allen, J. Boschung, A. Nauels, Y. Xia, V. Bex, and P. Midgley. Cambridge, United Kingdom and New York, NY, USA: Cambridge University Press. Chap. 7, pp. 571–657. DOI: 10.1017/CBO9781107415324.016.

Briffa, K. R., G. van der Schrier, and P. D. Jones (2009). "Wet and dry summers in Europe since 1750: evidence of increasing drought". In: *International Journal of Climatology* 29.13, pp. 1894–1905. DOI: 10.1002/joc.1836.

Budyko, M. I. (1961). "The heat balance of the earth's surface". In: *Soviet Geography* 2.4, pp. 3–13. DOI: https://doi.org/10.1080/00385417.1961.10770761.

Capderou, M. (Jan. 28, 2012). *Satellites : de Kepler au GPS, Springer Science & Business Media*.

Cesana, G. and H. Chepfer (July 27, 2013). "Evaluation of the cloud thermodynamic phase in a climate model using CALIPSO-GOCCP: CALIPSO-GOCCP CLOUD THERMODYNAMIC PHASE". In: *Journal of Geophysical Research: Atmospheres* 118.14, pp. 7922–7937. DOI: 10.1002/jgrd.50376.

Chepfer, H., S. Bony, D. Winker, G. Cesana, J. L. Dufresne, P. Minnis, C. J. Stubenrauch, and S. Zeng (Mar. 4, 2010). "The GCM-Oriented CALIPSO Cloud Product (CALIPSO-GOCCP)". In: *Journal of Geophysical Research* 115. DOI: 10.1029/2009JD012251.

Chepfer, H., V. Noel, D. Winker, and M. Chiriaco (Dec. 16, 2014). "Where and when will we observe cloud changes due to climate warming?" In: *Geophysical Research Letters* 41.23, pp. 8387–8395. DOI: 10.1002/2014GL061792.

Chiriaco, M., J.-C. Dupont, S. Bastin, J. Badosa, J. Lopez, M. Haeffelin, H. Chepfer, and R. Guzman (2018). "ReOBS: a new approach to synthesize long-term multi-variable dataset and application to the SIRTA supersite". In: *Earth System Science Data* 10, pp. 919–940. DOI: 10.5194/essd-10-919-2018.

Curry, J. A., J. L. Schramm, W. B. Rossow, and D. Randall (1996). "Overview of Arctic Cloud and Radiation Characteristics". In: *Journal of Climate* 9.8, pp. 1731–1764. DOI: 10.1175/1520-0442(1996)009<1731:OOACAR>2.0.CO;2.

Dee, D. P., S. M. Uppala, A. J. Simmons, P. Berrisford, P. Poli, S. Kobayashi, U. Andrae, M. A. Balmaseda, G. Balsamo, P. Bauer, and others (2011). "The ERA-Interim reanalysis: Configuration and performance of the data assimilation system". In: *Quarterly Journal of the Royal Meteorological Society* 137.656, pp. 553–597. DOI: 10.1002/qj.828.

Di Michele, S., T. McNally, P. Bauer, and I. Genkova (Apr. 2013). "Quality Assessment of Cloud-Top Height Estimates From Satellite IR Radiances Using the CALIPSO Lidar". In: *IEEE Transactions on Geoscience and Remote Sensing* 51.4, pp. 2454–2464. DOI: 10.1109/TGRS.2012.2210721.

Dines, W. H. (Apr. 1, 1917). "The heat balance of the atmosphere". In: *Quarterly Journal of the Royal Meteorological Society* 43.182, pp. 151–158. DOI: 10.1002/qj.49704318203.

Doelling, D. R., N. G. Loeb, D. F. Keyes, M. L. Nordeen, D. Morstad, C. Nguyen, B. A. Wielicki, D. F. Young, and M. Sun (June 2013). "Geostationary Enhanced Temporal Interpolation for CERES Flux Products". EN. In: *Journal of Atmospheric and Oceanic Technology* 30.6, pp. 1072–1090. DOI: 10.1175/JTECH-D-12-00136.1.

Driemel, A., J. Augustine, K. Behrens, S. Colle, C. Cox, E. Cuevas-Agulló, F. M. Denn, T. Duprat, M. Fukuda, H. Grobe, M. Haeffelin, G. Hodges, N. Hyett, O. Ijima, A. Kallis, W. Knap, V. Kustov, C. N. Long, D. Longenecker, A. Lupi, M. Maturilli, M. Mimouni, L. Ntsangwane, H. Ogihara, X. Olano, M. Olefs, M. Omori, L. Passamani, E. B. Pereira, H. Schmithüsen, S. Schumacher, R. Sieger, J. Tamlyn, R. Vogt, L. Vuilleumier, X. Xia, A. Ohmura, and G. König-Langlo (2018). "Baseline Surface Radiation Network (BSRN): structure and data description (1992–2017)". In: *Earth System Science Data* 10.3, pp. 1491–1501. DOI: 10.5194/essd-10-1491-2018.

Dubuisson, P., D. Dessailly, M. Vesperini, and R. Frouin (Oct. 16, 2004). "Water vapor retrieval over ocean using near-infrared radiometry". In: *Journal of Geophysical Research: Atmospheres* 109.D19, p. D19106. DOI: 10.1029/2004JD004516.

Duffy, P. B. and C. Tebaldi (2012). "Increasing prevalence of extreme summer temperatures in the U.S." In: *Climatic Change* 111.2, pp. 487–495. DOI: 10.1007/s10584-012-0396-6.

Dupont, J.-C. and M. Haeffelin (2008). "Observed instantaneous cirrus radiative effect on surface-level shortwave and longwave irradiances". In: *Journal of Geophysical Research* 113.D21, p. D21202. DOI: 10.1029/2008JD009838.

Döscher, R., T. Vihma, and E. Maksimovich (2014). "Recent advances in understanding the Arctic climate system state and change from a sea ice perspective: a review". en. In: *Atmospheric Chemistry and Physics* 14.24, pp. 13571–13600. DOI: 10.5194/acp-14-13571-2014.

Fetterer, F., K. Knowles, W. N. Meier, M. Savoie, and A. K. Windnagel. (2017). *Sea Ice Index, Version 3*. DOI: 10.7265/N5K072F8.

Frey, R. A., S. A. Ackerman, Y. Liu, K. I. Strabala, H. Zhang, J. R. Key, and X. Wang (2008). "Cloud Detection with MODIS. Part I: Improvements in the MODIS Cloud Mask for Collection 5". In: *Journal of Atmospheric and Oceanic Technology* 25.7, pp. 1057–1072. DOI: 10.1175/2008JTECHA1052.1.

Gallagher, M. R., M. D. Shupe, and N. B. Miller (2018). "Impact of Atmospheric Circulation on Temperature, Clouds, and Radiation at Summit Station, Greenland, with Self-Organizing Maps". In: *Journal of Climate* 31.21, pp. 8895–8915. DOI: 10.1175/JCLI-D-17-0893.1.

Garnier, A., J. Pelon, M. A. Vaughan, D. M. Winker, C. R. Trepte, and P. Dubuisson (July 15, 2015). "Lidar multiple scattering factors inferred from CALIPSO lidar and IIR retrievals of semi-transparent cirrus cloud optical depths over oceans". In: *Atmospheric Measurement Techniques* 8.7, pp. 2759–2774. DOI: 10.5194/amt-8-2759-2015.

Goosse, H., J. E. Kay, K. C. Armour, A. Bodas-Salcedo, H. Chepfer, D. Docquier, A. Jonko, P. J. Kushner, O. Lecomte, F. Massonnet, H.-S. Park, F. Pithan, G. Svensson, and M. Vancoppenolle (May 2018). "Quantifying climate feedbacks in polar regions". en. In: *Nature Communications* 9.1. Number: 1 Publisher: Nature Publishing Group, p. 1919. DOI: 10.1038/s41467-018-04173-0.

Guzman, R., H. Chepfer, V. Noel, T. Vaillant de Guélis, J. E. Kay, P. Raberanto, G. Cesana, M. A. Vaughan, and D. M. Winker (Jan. 27, 2017). "Direct atmosphere opacity observations from CALIPSO provide new constraints on cloud-radiation interactions: GOCCP v3.0 OPAQ Algorithm". In: *Journal of Geophysical Research: Atmospheres* 122.2, pp. 1066–1085. DOI: 10.1002/2016JD025946.

Hadley, G. (1735). "Concerning the cause of the general trade-winds". In: *Philosophical Transactions* 39, pp. 58–62. DOI: https://doi.org/10.1098/rstl.1735.0014.

Haeffelin, M., L. Barthès, O. Bock, C. Boitel, S. Bony, D. Bouniol, H. Chepfer, M. Chiriaco, J. Cuesta, J. Delanoë, P. Drobinski, J.-L. Dufresne, C. Flamant, M. Grall, A. Hodzic, F. Hourdin, F. Lapouge, Y. Lemaître, A. Mathieu, Y. Morille, C. Naud, V. Noël, W. O'Hirok, J. Pelon, C. Pietras, A. Protat, B. Romand, G. Scialom, and R. Vautard (2005). "SIRTA, a ground-based atmospheric observatory for cloud and aerosol research". In: *Annales Geophysicae* 23, pp. 253–275. DOI: 10.5194/angeo-23-253-2005.

Ham, S.-H., S. Kato, F. G. Rose, D. Winker, T. L'Ecuyer, G. G. Mace, D. Painemal, S. Sun-Mack, Y. Chen, and W. F. Miller (2017). "Cloud occurrences and cloud radiative effects (CREs) from CERES-CALIPSO-CloudSat-MODIS (CCCM) and CloudSat radar-lidar (RL) products: CCCM Versus CloudSat RL Products". en. In: *Journal of Geophysical Research: Atmospheres* 122.16, pp. 8852–8884. DOI: 10.1002/2017JD026725.

Hang, Y., T. S. L'Ecuyer, D. S. Henderson, A. V. Matus, and Z. Wang (Oct. 2019). "Reassessing the Effect of Cloud Type on Earth's Energy Balance in the Age of Active Spaceborne Observations. Part II: Atmospheric Heating". en. In: *Journal of Climate* 32.19, pp. 6219–6236. DOI: 10.1175/JCLI-D-18-0754.1.

Hartmann, D. L., V. Ramanathan, A. Berroir, and G. E. Hunt (May 1, 1986). "Earth Radiation Budget data and climate research". In: *Reviews of Geophysics* 24.2, pp. 439–468. DOI: 10.1029/RG024i002p00439.

Hartmann, D. L., H. H. Hendon, and R. A. Houze (1984). "Some Implications of the Mesoscale Circulations in Tropical Cloud Clusters for Large-Scale Dynamics and Climate". In: *Journal of the Atmospheric Sciences* 41.1, pp. 113–121. DOI: 10.1175/1520-0469(1984)041<0113:SIOTMC>2.0.CO;2.

Haynes, J. M., T. H. Vonder Haar, T. L'Ecuyer, and D. Henderson (2013). "Radiative heating characteristics of Earth's cloudy atmosphere from vertically resolved active sensors". en. In: *Geophysical Research Letters* 40.3. _eprint: https://onlinelibrary.wiley.com/doi/pdf/10.1002/grl.50145, pp. 624–630. DOI: 10.1002/grl.50145.

Henderson, D. S., T. L'Ecuyer, G. Stephens, P. Partain, and M. Sekiguchi (Apr. 2013). "A Multisensor Perspective on the Radiative Impacts of Clouds and Aerosols". In: *Journal of Applied Meteorology and Climatology* 52.4, pp. 853–871. DOI: 10.1175/JAMC-D-12-025.1.

Hofer, S., A. J. Tedstone, X. Fettweis, and J. L. Bamber (2017). "Decreasing cloud cover drives the recent mass loss on the Greenland Ice Sheet". In: *Science Advances* 3.6, e1700584. DOI: 10.1126/sciadv.1700584.

Holland, M. M. and C. M. Bitz (2003). "Polar amplification of climate change in coupled models". en. In: *Climate Dynamics* 21, pp. 221–232. DOI: 10.1007/s00382-003-0332-6.

Holz, R. E., S. A. Ackerman, F. W. Nagle, R. Frey, S. Dutcher, R. E. Kuehn, M. A. Vaughan, and B. Baum (Apr. 27, 2008). "Global Moderate Resolution Imaging Spectroradiometer (MODIS) cloud detection and height evaluation using CALIOP". In: *Journal of Geophysical Research: Atmospheres* 113 (D8). DOI: 10.1029/2008JD009837.

Hu, Y., D. Winker, M. Vaughan, B. Lin, A. Omar, C. Trepte, D. Flittner, P. Yang, S. L. Nasiri, B. Baum, R. Holz, W. Sun, Z. Liu, Z. Wang, S. Young, K. Stamnes, J. Huang, and R. Kuehn (Nov. 2009). "CALIPSO/CALIOP Cloud Phase Discrimination Algorithm". In: *Journal of Atmospheric and Oceanic Technology* 26.11, pp. 2293–2309. DOI: 10.1175/2009JTECHA1280.1.

Huang, Y., X. Dong, D. A. Bailey, M. M. Holland, B. Xi, A. K. DuVivier, J. E. Kay, L. L. Landrum, and Y. Deng (2019). "Thicker Clouds and Accelerated Arctic Sea Ice Decline: The Atmosphere-Sea Ice Interactions in Spring". en. In: *Geophysical Research Letters* 46.12, pp. 6980–6989. DOI: 10.1029/2019GL082791.

Hudson, J. G. (1993). "Cloud Condensation Nuclei". In: *Journal of Applied Meteorology and Climatology* 32.4, pp. 596–607. DOI: 10.1175/1520-0450(1993)032<0596:CCN>2.0.CO;2.

Illingworth, A. J., H. W. Barker, A. Beljaars, M. Ceccaldi, H. Chepfer, N. Clerbaux, J. Cole, J. Delanoë, C. Domenech, D. P. Donovan, S. Fukuda, M. Hirakata, R. J. Hogan, A. Huenerbein, P. Kollias, T. Kubota, T. Nakajima, T. Y. Nakajima, T. Nishizawa, Y. Ohno, H. Okamoto, R. Oki, K. Sato, M. Satoh, M. W. Shephard, A. Velázquez-Blázquez, U. Wandinger, T. Wehr, and G.-J. van Zadelhoff (Dec. 18, 2014). "The EarthCARE Satellite: The Next Step Forward in Global Measurements of Clouds, Aerosols, Precipitation,

and Radiation". In: *Bulletin of the American Meteorological Society* 96.8, pp. 1311–1332. DOI: 10.1175/BAMS-D-12-00227.1.

Intrieri, J. M., C. W. Fairall, M. D. Shupe, P. O. G. Persson, E. L. Andreas, P. S. Guest, and R. E. Moritz (2002). "An annual cycle of Arctic surface cloud forcing at SHEBA". In: *Journal of Geophysical Research: Oceans* 107, p. 8039. DOI: 10.1029/2000JC000439.

IPCC (2021). *Climate Change 2021: The Physical Science Basis. Contribution of Working Group I to the Sixth Assessment Report of the Intergovernmental Panel on Climate Change*. Ed. by V. Masson-Delmotte, P. Zhai, A. Pirani, S. Connors, C. Péan, S. Berger, N. Caud, Y. Chen, L. Goldfarb, M. Gomis, M. Huang, K. Leitzell, E. Lonnoy, J. Matthews, T. Maycock, T. Waterfield, O. Yelekçi, R. Yu, and B. Zhou. Vol. In Press. Cambridge, United Kingdom and New York, NY, USA: Cambridge University Press. DOI: 10.1017/9781009157896.

Kato, S., S. Sun-Mack, W. F. Miller, F. G. Rose, Y. Chen, P. Minnis, and B. A. Wielicki (2010). "Relationships among cloud occurrence frequency, overlap, and effective thickness derived from CALIPSO and CloudSat merged cloud vertical profiles". en. In: *Journal of Geophysical Research* 115, D00H28. DOI: 10.1029/2009JD012277.

Kato, S., F. G. Rose, S. Sun-Mack, W. F. Miller, Y. Chen, D. A. Rutan, G. L. Stephens, N. G. Loeb, P. Minnis, B. A. Wielicki, D. M. Winker, T. P. Charlock, P. W. Stackhouse, K.-M. Xu, and W. D. Collins (Oct. 14, 2011). "Improvements of top-of-atmosphere and surface irradiance computations with CALIPSO-, CloudSat-, and MODIS-derived cloud and aerosol properties". In: *Journal of Geophysical Research* 116. DOI: 10.1029/2011JD016050.

Kato, S., N. G. Loeb, F. G. Rose, D. R. Doelling, D. A. Rutan, T. E. Caldwell, L. Yu, and R. A. Weller (2013). "Surface Irradiances Consistent with CERES-Derived Top-of-Atmosphere Shortwave and Longwave Irradiances". en. In: *Journal of Climate* 26.9, pp. 2719–2740. DOI: 10.1175/JCLI-D-12-00436.1.

Kato, S., F. G. Rose, D. A. Rutan, T. J. Thorsen, N. G. Loeb, D. R. Doelling, X. Huang, W. L. Smith, W. Su, and S.-H. Ham (2018). "Surface Irradiances of Edition 4.0 Clouds and the Earth's Radiant Energy System (CERES) Energy Balanced and Filled (EBAF) Data Product". In: *Journal of Climate* 31.11, pp. 4501–4527. DOI: 10.1175/JCLI-D-17-0523.1.

Kato, S., F. G. Rose, S. H. Ham, D. A. Rutan, A. Radkevich, T. E. Caldwell, S. Sun-Mack, W. F. Miller, and Y. Chen (2019). "Radiative Heating Rates Computed With Clouds Derived From Satellite-Based Passive and Active Sensors and their Effects on Generation of Available Potential Energy". In: *Journal of Geophysical Research: Atmospheres* 124.3, pp. 1720–1740. DOI: 10.1029/2018JD028878.

Kay, J. E. and A. Gettelman (Sept. 2009). "Cloud influence on and response to seasonal Arctic sea ice loss". en. In: *Journal of Geophysical Research* 114.D18, p. D18204. DOI: 10.1029/2009JD011773.

Kay, J. E. and T. L'Ecuyer (2013). "Observational constraints on Arctic Ocean clouds and radiative fluxes during the early 21st century". In: *Journal of Geophysical Research: Atmospheres* 118, pp. 7219–7236. DOI: 10.1002/jgrd.50489.

Kay, J. E., T. L'Ecuyer, H. Chepfer, N. Loeb, A. Morrison, and G. Cesana (2016). "Recent Advances in Arctic Cloud and Climate Research". In: *Current Climate Change Reports* 2.4, pp. 159–169. DOI: 10.1007/s40641-016-0051-9.

Kiehl, J. T. and K. E. Trenberth (1997). "Earth's Annual Global Mean Energy Budget". en. In: *Bulletin of the American Meteorological Society* 78.2, pp. 197–208. DOI: 10.1175/1520-0477(1997)078<0197:EAGMEB>2.0.CO;2.

King, M., W. Menzel, Y. Kaufman, D. Tanre, B.-C. Gao, S. Platnick, S. Ackerman, L. Remer, R. Pincus, and P. Hubanks (2003). "Cloud and aerosol properties, precipitable water, and profiles of temperature and water vapor from MODIS". In: *IEEE Transactions on Geoscience and Remote Sensing* 41, pp. 442–458. DOI: 10.1109/TGRS.2002.808226.

Lacour, A., H. Chepfer, N. B. Miller, M. D. Shupe, V. Noel, X. Fettweis, H. Gallee, J. E. Kay, R. Guzman, and J. Cole (2018). "How Well Are Clouds Simulated over Greenland in Climate Models? Consequences for the Surface Cloud Radiative Effect over the Ice Sheet". In: *Journal of Climate* 31.22, pp. 9293–9312. DOI: 10.1175/JCLI-D-18-0023.1.

L'Ecuyer, T. S., N. B. Wood, T. Haladay, G. L. Stephens, and P. W. Stackhouse (2008). "Impact of clouds on atmospheric heating based on the R04 CloudSat fluxes and heating rates data set". en. In: *Journal of Geophysical Research* 113, D00A15. DOI: 10.1029/2008JD009951.

L'Ecuyer, T. S., H. K. Beaudoing, M. Rodell, W. Olson, B. Lin, S. Kato, C. A. Clayson, E. Wood, J. Sheffield, R. Adler, G. Huffman, M. Bosilovich, G. Gu, F. Robertson, P. R. Houser, D. Chambers, J. S. Famiglietti, E. Fetzer, W. T. Liu, X. Gao, C. A. Schlosser, E. Clark, D. P. Lettenmaier, and K. Hilburn (Nov. 2015). "The Observed State of the Energy Budget in the Early Twenty-First Century". In: *Journal of Climate* 28.21, pp. 8319–8346. DOI: 10.1175/JCLI-D-14-00556.1.

L'Ecuyer, T. S., Y. Hang, A. V. Matus, and Z. Wang (2019). "Reassessing the Effect of Cloud Type on Earth's Energy Balance in the Age of Active Spaceborne Observations. Part I: Top of Atmosphere and Surface". In: *Journal of Climate* 32.19, pp. 6197–6217. DOI: 10.1175/JCLI-D-18-0753.1.

Lenoble, J. (1993). *Atmospheric radiative transfer*. A. Deepak Pub.

Lindzen, R. S. and Y.-S. Choi (Feb. 2022). "The Iris Effect: A Review". In: *Asia-Pacific Journal of Atmospheric Sciences* 58.1, pp. 159–168. DOI: 10.1007/s13143-021-00238-1.

Liou, K.-N. (2002). *An introduction to atmospheric radiation*. Vol. 84. Elsevier.

Liu, Y., S. A. Ackerman, B. C. Maddux, J. R. Key, and R. A. Frey (2010). "Errors in Cloud Detection over the Arctic Using a Satellite Imager and Implications for Observing Feedback Mechanisms". In: *Journal of Climate* 23.7, pp. 1894–1907. DOI: 10.1175/2009JCLI3386.1.

Loeb, N. G., K. J. Priestley, D. P. Kratz, E. B. Geier, R. N. Green, B. A. Wielicki, P. O. Hinton, and S. K. Nolan (Apr. 2001). "Determination of Unfiltered Radiances from the Clouds and the Earth's Radiant Energy System Instrument". In: *Journal of Applied Meteorology* 40.4, pp. 822–835. DOI: 10.1175/1520-0450(2001)040<0822:DOURFT>2.0.CO;2.

Loeb, N. G., S. Kato, K. Loukachine, and N. Manalo-Smith (Apr. 2005). "Angular Distribution Models for Top-of-Atmosphere Radiative Flux Estimation from the Clouds and the Earth's Radiant Energy System Instrument on the Terra Satellite. Part I: Methodology". In: *Journal of Atmospheric and Oceanic Technology* 22, pp. 338–351. DOI: 10.1175/JTECH1712.1.

Loeb, N. G., B. A. Wielicki, D. R. Doelling, G. L. Smith, D. F. Keyes, S. Kato, N. Manalo-Smith, and T. Wong (Feb. 2009). "Toward Optimal Closure of the Earth's Top-of-Atmosphere Radiation Budget". In: *Journal of Climate* 22.3, pp. 748–766. DOI: 10.1175/2008JCLI2637.1.

Loeb, N. G., S. Kato, W. Su, T. Wong, F. G. Rose, D. R. Doelling, J. R. Norris, and X. Huang (July 2012). "Advances in Understanding Top-of-Atmosphere Radiation Variability from

Satellite Observations". In: *Surveys in Geophysics* 33.3, pp. 359–385. DOI: 10.1007/s10712-012-9175-1.

Loeb, N. G., H. Wang, A. Cheng, S. Kato, J. T. Fasullo, K.-M. Xu, and R. P. Allan (2016). "Observational constraints on atmospheric and oceanic cross-equatorial heat transports: revisiting the precipitation asymmetry problem in climate models". en. In: *Climate Dynamics* 46.9-10, pp. 3239–3257. DOI: 10.1007/s00382-015-2766-z.

Loeb, N. G., D. R. Doelling, H. Wang, W. Su, C. Nguyen, J. G. Corbett, L. Liang, C. Mitrescu, F. G. Rose, and S. Kato (Jan. 2018). "Clouds and the Earth's Radiant Energy System (CERES) Energy Balanced and Filled (EBAF) Top-of-Atmosphere (TOA) Edition-4.0 Data Product". EN. In: *Journal of Climate* 31.2. Publisher: American Meteorological Society Section: Journal of Climate, pp. 895–918. DOI: 10.1175/JCLI-D-17-0208.1.

Loeb, N. G., M. Mayer, S. Kato, J. T. Fasullo, H. Zuo, R. Senan, J. M. Lyman, G. C. Johnson, and M. Balmaseda (2022). "Evaluating Twenty-Year Trends in Earth's Energy Flows From Observations and Reanalyses". In: *Journal of Geophysical Research: Atmospheres* 127.12, e2022JD036686. DOI: 10.1029/2022JD036686.

London, J. (1957). *A study of the atmospheric heat balance. Final Report, College of Engineering, New York University*. New York.

Mace, G. G. and F. J. Wrenn (Dec. 2013). "Evaluation of the Hydrometeor Layers in the East and West Pacific within ISCCP Cloud-Top Pressure–Optical Depth Bins Using Merged *CloudSat* and CALIPSO Data". In: *Journal of Climate* 26.23, pp. 9429–9444. DOI: 10.1175/JCLI-D-12-00207.1.

Marchand, R., G. G. Mace, T. Ackerman, and G. Stephens (Apr. 2008). "Hydrometeor Detection Using Cloudsatâ"An Earth-Orbiting 94-GHz Cloud Radar". en. In: *Journal of Atmospheric and Oceanic Technology* 25.4, pp. 519–533. DOI: 10.1175/2007JTECHA1006.1.

Masson-Delmotte, V., P. Zhai, A. Pirani, S. L. Connors, C. Péan, S. Berger, N. Caud, Y Chen, L Goldfarb, M. Gomis, et al. (2021). "Climate change 2021: the physical science basis". In: *Contribution of working group I to the sixth assessment report of the intergovernmental panel on climate change* 2.

Matus, A. V. and T. S. L'Ecuyer (Mar. 2017). "The role of cloud phase in Earth's radiation budget: CLOUD PHASE IN EARTH'S RADIATION BUDGET". en. In: *Journal of Geophysical Research: Atmospheres* 122.5, pp. 2559–2578. DOI: 10.1002/2016JD025951.

McClatchey, R. A., R. W. Fenn, J. A. Selby, F. E. Volz, and J. S. Garing (1972). *Optical properties of the atmosphere, 3rd Edition, DTIC Document*.

Meier, W. N., G. K. Hovelsrud, B. E. van Oort, J. R. Key, K. M. Kovacs, C. Michel, C. Haas, M. A. Granskog, S. Gerland, D. K. Perovich, A. Makshtas, and J. D. Reist (2014). "Arctic sea ice in transformation: A review of recent observed changes and impacts on biology and human activity". en. In: *Reviews of Geophysics* 52.3. _eprint: https://onlinelibrary.wiley.com/doi/pdf/10.1002/2013RG000431, pp. 185–217. DOI: 10.1002/2013RG000431.

Minnis, P., S. Sun-Mack, D. F. Young, P. W. Heck, D. P. Garber, Y. Chen, D. A. Spangenberg, R. F. Arduini, Q. Z. Trepte, W. L. Smith, J. K. Ayers, S. C. Gibson, W. F. Miller, G. Hong, V. Chakrapani, Y. Takano, K.-N. Liou, Y. Xie, and P. Yang (2011). "CERES Edition-2 Cloud Property Retrievals Using TRMM VIRS and Terra and Aqua MODIS Dataâ"Part I: Algorithms". In: *IEEE Transactions on Geoscience and Remote Sensing* 49.11, pp. 4374–4400. DOI: 10.1109/TGRS.2011.2144601.

Morrison, A. L., J. E. Kay, H. Chepfer, R. Guzman, and V. Yettella (2018). "Isolating the Liquid Cloud Response to Recent Arctic Sea Ice Variability Using Spaceborne Lidar Observations". en. In: *Journal of Geophysical Research: Atmospheres* 123.1, pp. 473–490. DOI: 10.1002/2017JD027248.

Mülmenstädt, J., O. Sourdeval, D. S. Henderson, T. S. L'Ecuyer, C. Unglaub, L. Jungandreas, C. Böhm, L. M. Russell, and J. Quaas (2018). "Using CALIOP to estimate cloud-field base height and its uncertainty: the Cloud Base Altitude Spatial Extrapolator (CBASE) algorithm and dataset". In: *Earth System Science Data* 10.4, pp. 2279–2293. DOI: 10.5194/essd-10-2279-2018.

Nakajima, T. and M. Tanaka (1988). "Algorithms for radiative intensity calculations in moderately thick atmospheres using a truncation approximation". In: *Journal of Quantitative Spectroscopy and Radiative Transfer* 40, pp. 51–69. DOI: https://doi.org/10.1016/0022-4073(88)90031-3.

National Research Council (1979). *Carbon Dioxide and Climate: A Scientific Assessment*. Washington, DC: The National Academies Press. DOI: 10.17226/12181.

Noel, V., H. Chepfer, C. Hoareau, M. Reverdy, and G. Cesana (2014). "Effects of solar activity on noise in CALIOP profiles above the South Atlantic Anomaly". In: *Atmospheric Measurement Techniques* 7.6, pp. 1597–1603. DOI: 10.5194/amt-7-1597-2014.

Nolin, A., R Armstrong, and J Maslanik (1998). "Near-real-time SSM/I-SSMIS EASE-Grid daily global ice concentration and snow extent, version 4". In: *NASA National Snow and Ice Data Center Distributed Active Archive Center* 10. DOI: 10.5067/VF7QO90IHZ99.

Notz, D. and J. Stroeve (2018). "The Trajectory Towards a Seasonally Ice-Free Arctic Ocean". In: *Current Climate Change Reports* 4, pp. 407–416. DOI: 10.1007/s40641-018-0113-2.

Ohmura, A., E. G. Dutton, B. Forgan, C. Fröhlich, H. Gilgen, H. Hegner, A. Heimo, G. König-Langlo, B. McArthur, and G. Müller (1998). "Baseline Surface Radiation Network (BSRN/WCRP): New precision radiometry for climate research". In: *Bulletin of the American Meteorological Society* 79.10, pp. 2115–2136. DOI: https://doi.org/10.1175/1520-0477(1998)079<2115:BSRNBW>2.0.CO;2.

Poitou, J. (2013). "Composition atmosphérique et bilan radiatif". fr. In: *Reflets de la physique* 33, pp. 28–33. DOI: 10.1051/refdp/201333028.

Prata, A. J. (1996). "A new long-wave formula for estimating downward clear-sky radiation at the surface". In: *Quarterly Journal of the Royal Meteorological Society* 122, pp. 1127–1151. DOI: 10.1002/qj.49712253306.

Ramanathan, V. (1987). "The role of earth radiation budget studies in climate and general circulation research". In: *Journal of Geophysical Research: Atmospheres* 92, pp. 4075–4095. DOI: https://doi.org/10.1029/JD092iD04p04075.

Ramanathan, V., R. D. Cess, E. F. Harrison, P. Minnis, B. R. Barkstrom, E. Ahmad, and D. Hartmann (Jan. 6, 1989). "Cloud-Radiative Forcing and Climate: Results from the Earth Radiation Budget Experiment". In: *Science* 243.4887, pp. 57–63. DOI: 10.1126/science.243.4887.57.

Rienecker, M. M., M. J. Suarez, R. Todling, J. Bacmeister, L. Takacs, H.-C. Liu, W. Gu, M. Sienkiewicz, R. D. Koster, R. Gelaro, I. Stajner, and J. E. Nielsen (2008). *The GEOS-5 Data Assimilation System – Documentation of Versions 5.0.1, 5.1.0, and 5.2.0*.

Roesch, A., M. Wild, A. Ohmura, E. G. Dutton, C. N. Long, and T. Zhang (2011). "Assessment of BSRN radiation records for the computation of monthly means". In: *Atmospheric Measurement Techniques* 4, pp. 339–354. DOI: 10.5194/amt-4-339-2011.

Rutan, D. A., S. Kato, D. R. Doelling, F. G. Rose, L. T. Nguyen, T. E. Caldwell, and N. G. Loeb (June 2015). "CERES Synoptic Product: Methodology and Validation of Surface Radiant Flux". In: *Journal of Atmospheric and Oceanic Technology* 32.6, pp. 1121–1143. DOI: 10.1175/JTECH-D-14-00165.1.

Serreze, M. C. and R. G. Barry (May 2011). "Processes and impacts of Arctic amplification: A research synthesis". en. In: *Global and Planetary Change* 77.1, pp. 85–96. DOI: 10.1016/j.gloplacha.2011.03.004.

Serreze, M. C. and J. Stroeve (2015). "Arctic sea ice trends, variability and implications for seasonal ice forecasting". In: *Philosophical transactions. Series A, Mathematical, physical, and engineering sciences* 373, p. 20140159. DOI: 10.1098/rsta.2014.0159.

Shea, Y. L., B. A. Wielicki, S. Sun-Mack, and P. Minnis (Mar. 21, 2017). "Quantifying the Dependence of Satellite Cloud Retrievals on Instrument Uncertainty". In: *Journal of Climate*. DOI: 10.1175/JCLI-D-16-0429.1.

Sherwood, S. C., M. J. Webb, J. D. Annan, K. C. Armour, P. M. Forster, J. C. Hargreaves, G. Hegerl, S. A. Klein, K. D. Marvel, E. J. Rohling, M. Watanabe, T. Andrews, P. Braconnot, C. S. Bretherton, G. L. Foster, Z. Hausfather, A. S. von der Heydt, R. Knutti, T. Mauritsen, J. R. Norris, C. Proistosescu, M. Rugenstein, G. A. Schmidt, K. B. Tokarska, and M. D. Zelinka (2020). "An Assessment of Earth's Climate Sensitivity Using Multiple Lines of Evidence". en. In: *Reviews of Geophysics* 58.4, e2019RG000678. DOI: 10.1029/2019RG000678.

Sherwood, S. C., J.-H. Chae, P. Minnis, and M. McGill (June 2004). "Underestimation of deep convective cloud tops by thermal imagery: CLOUD TOP HEIGHTS". In: *Geophysical Research Letters* 31.11. DOI: 10.1029/2004GL019699.

Shupe, M. D. and J. M. Intrieri (Feb. 2004). "Cloud Radiative Forcing of the Arctic Surface: The Influence of Cloud Properties, Surface Albedo, and Solar Zenith Angle". In: *Journal of Climate* 17.3, pp. 616–628. DOI: 10.1175/1520-0442(2004)017<0616:CRFOTA>2.0.CO;2.

Shupe, M. D., D. D. Turner, V. P. Walden, R. Bennartz, M. P. Cadeddu, B. B. Castellani, C. J. Cox, D. R. Hudak, M. S. Kulie, N. B. Miller, R. R. Neely, W. D. Neff, and P. M. Rowe (Feb. 2013). "High and Dry: New Observations of Tropospheric and Cloud Properties above the Greenland Ice Sheet". In: *Bulletin of the American Meteorological Society* 94.2, pp. 169–186. DOI: 10.1175/BAMS-D-11-00249.1.

Stamnes, K., S.-C. Tsay, W. Wiscombe, and K. Jayaweera (June 15, 1988). "Numerically stable algorithm for discrete-ordinate-method radiative transfer in multiple scattering and emitting layered media". In: *Applied Optics* 27.12, p. 2502. DOI: 10.1364/AO.27.002502.

Stephens, G. L. (2005). "Cloud feedbacks in the climate system: A critical review". In: *Journal of climate* 18.2, pp. 237–273.

Stephens, G. L., D. G. Vane, R. J. Boain, G. G. Mace, K. Sassen, Z. Wang, A. J. Illingworth, E. J. O'Connor, W. B. Rossow, S. L. Durden, S. D. Miller, R. T. Austin, A. Benedetti, C. Mitrescu, and T. CloudSat Science Team (Dec. 2002). "THE CLOUDSAT MISSION AND THE A-TRAIN: A New Dimension of Space-Based Observations of Clouds and Precipitation". In:

Bulletin of the American Meteorological Society 83.12, pp. 1771–1790. DOI: 10.1175/BAMS-83-12-1771.

Stocker, T. F., D. Qin, G.-K. Plattner, M. Tignor, S. K. Allen, J. Boschung, A. Nauels, Y. Xia, V. Bex, and P. M. Midgley, eds. (2013). *IPCC, 2013: Climate Change 2013: The Physical Science Basis. Contribution of Working Group I to the Fifth Assessment Report of the Intergovernmental Panel on Climate Change*. Cambridge, United Kingdom and New York, NY, USA: Cambridge University Press.

Stroeve, J. C., M. C. Serreze, M. M. Holland, J. E. Kay, J. Malanik, and A. P. Barrett (2012). "The Arctic's rapidly shrinking sea ice cover: a research synthesis". In: *Climatic Change* 110, pp. 1005–1027. DOI: 10.1007/s10584-011-0101-1.

Stroeve, J. C., T. Markus, L. Boisvert, J. Miller, and A. Barrett (2014). "Changes in Arctic melt season and implications for sea ice loss". en. In: *Geophysical Research Letters* 41, pp. 1216–1225. DOI: 10.1002/2013GL058951.

Stubenrauch, C. J., W. B. Rossow, S. Kinne, S. Ackerman, G. Cesana, H. Chepfer, L. Di Girolamo, B. Getzewich, A. Guignard, A. Heidinger, B. C. Maddux, W. P. Menzel, P. Minnis, C. Pearl, S. Platnick, C. Poulsen, J. Riedi, S. Sun-Mack, A. Walther, D. Winker, S. Zeng, and G. Zhao (Jan. 17, 2013). "Assessment of Global Cloud Datasets from Satellites: Project and Database Initiated by the GEWEX Radiation Panel". In: *Bulletin of the American Meteorological Society* 94.7, pp. 1031–1049. DOI: 10.1175/BAMS-D-12-00117.1.

Sun-Mack, S., P. Minnis, Y. Chen, D. R. Doelling, B. R. Scarino, C. O. Haney, and W. L. Smith (Oct. 2018). "Calibration Changes to Terra MODIS Collection-5 Radiances for CERES Edition 4 Cloud Retrievals". In: *IEEE Transactions on Geoscience and Remote Sensing* 56.10, pp. 6016–6032. DOI: 10.1109/TGRS.2018.2829902.

Thomson, W. (1871). "On the Equilibrium of Vapour at a Curved Surface of Liquid". In: *Philosophical Magazine* 7.448. DOI: 10.1017/S0370164600041729.

Trenberth, K. E. (Oct. 1, 1991). "Storm Tracks in the Southern Hemisphere". In: *Journal of the Atmospheric Sciences* 48.19, pp. 2159–2178. DOI: 10.1175/1520-0469(1991)048<2159:STITSH>2.0.CO;2.

Trenberth, K. E. and J. T. Fasullo (2012). "Tracking Earth's Energy: From El Niño to Global Warming". en. In: *Surveys in Geophysics* 33.3-4, pp. 413–426. DOI: 10.1007/s10712-011-9150-2.

Trenberth, K. E., J. T. Fasullo, and J. Kiehl (2009). "Earth's Global Energy Budget". In: *Bulletin of the American Meteorological Society* 90.3, pp. 311–324. DOI: 10.1175/2008BAMS2634.1.

Vaillant de Guélis, T., H. Chepfer, V. Noel, R. Guzman, P. Dubuisson, D. M. Winker, and S. Kato (2017a). "The link between outgoing longwave radiation and the altitude at which a spaceborne lidar beam is fully attenuated". In: *Atmospheric Measurement Techniques* 10.12, pp. 4659–4685. DOI: 10.5194/amt-10-4659-2017.

Vaillant de Guélis, T., H. Chepfer, R. Guzman, M. Bonazzola, D. M. Winker, and V. Noel (Dec. 2018). "Space lidar observations constrain longwave cloud feedback". In: *Scientific Reports* 8.1, p. 16570. DOI: 10.1038/s41598-018-34943-1.

Vaillant de Guélis, T. (2017). "Apport des observations par lidar spatial pour comprendre l'effet radiatif des nuages dans l'infrarouge". PhD thesis.

Vaillant de Guélis, T., H. Chepfer, V. Noel, R. Guzman, D. M. Winker, and R. Plougonven (Dec. 2017b). "Using Space Lidar Observations to Decompose Longwave Cloud Radiative

Effect Variations Over the Last Decade: Space lidar decomposes LWCRE variations". In: *Geophysical Research Letters* 44.23, pp. 11,994–12,003. DOI: 10.1002/2017GL074628.

van den Broeke, M., J. Bamber, J. Ettema, E. Rignot, E. Schrama, W. J. van de Berg, E. van Meijgaard, I. Velicogna, and B. Wouters (2009). "Partitioning Recent Greenland Mass Loss". en. In: *Science* 326.5955, pp. 984–986. DOI: 10.1126/science.1178176.

van Tricht, K., S. Lhermitte, J. T. M. Lenaerts, I. V. Gorodetskaya, T. S. L'Ecuyer, B. Noël, M. R. van den Broeke, D. D. Turner, and N. P. M. van Lipzig (Apr. 2016). "Clouds enhance Greenland ice sheet meltwater runoff". en. In: *Nature Communications* 7.1, p. 10266. DOI: 10.1038/ncomms10266.

von Schuckmann, K., L. Cheng, M. D. Palmer, J. Hansen, C. Tassone, V. Aich, S. Adusumilli, H. Beltrami, T. Boyer, F. J. Cuesta-Valero, D. Desbruyères, C. Domingues, A. García-García, P. Gentine, J. Gilson, M. Gorfer, L. Haimberger, M. Ishii, G. C. Johnson, R. Killick, B. A. King, G. Kirchengast, N. Kolodziejczyk, J. Lyman, B. Marzeion, M. Mayer, M. Monier, D. P. Monselesan, S. Purkey, D. Roemmich, A. Schweiger, S. I. Seneviratne, A. Shepherd, D. A. Slater, A. K. Steiner, F. Straneo, M.-L. Timmermans, and S. E. Wijffels (Sept. 2020). "Heat stored in the Earth system: where does the energy go?" English. In: *Earth System Science Data* 12.3. Publisher: Copernicus GmbH, pp. 2013–2041. DOI: 10.5194/essd-12-2013-2020.

Wendisch, M., M. Brückner, J. Burrows, S Crewell, K. Dethloff, K Ebell, C. Lüpkes, A. Macke, J. Notholt, J Quaas, et al. (2017). "Understanding causes and effects of rapid warming in the Arctic". In: *Eos* 98. DOI: 10.1029/2017EO064803.

Wielicki, B. A., B. R. Barkstrom, E. F. Harrison, R. B. Lee, G. Louis Smith, and J. E. Cooper (May 1996). "Clouds and the Earth's Radiant Energy System (CERES): An Earth Observing System Experiment". In: *Bulletin of the American Meteorological Society* 77.5, pp. 853–868. DOI: 10.1175/1520-0477(1996)077<0853:CATERE>2.0.CO;2.

Wild, M., D. Folini, C. Schär, N. Loeb, E. G. Dutton, and G. König-Langlo (2013). "The global energy balance from a surface perspective". In: *Climate Dynamics* 40.11, pp. 3107–3134. DOI: 10.1007/s00382-012-1569-8.

Wild, M., D. Folini, M. Z. Hakuba, C. Schär, S. I. Seneviratne, S. Kato, D. Rutan, C. Ammann, E. F. Wood, and G. König-Langlo (2015). "The energy balance over land and oceans: an assessment based on direct observations and CMIP5 climate models". In: *Climate Dynamics* 44.11-12, pp. 3393–3429. DOI: 10.1007/s00382-014-2430-z.

Wild, M., A. Ohmura, C. Schär, G. Müller, D. Folini, M. Schwarz, M. Z. Hakuba, and A. Sanchez-Lorenzo (2017). "The Global Energy Balance Archive (GEBA) version 2017: A database for worldwide measured surface energy fluxes". In: *Earth System Science Data* 9.2, pp. 601–613. DOI: 10.5194/essd-9-601-2017.

Wild, M., M. Z. Hakuba, D. Folini, P. Dörig-Ott, C. Schär, S. Kato, and C. N. Long (2019). "The cloud-free global energy balance and inferred cloud radiative effects: an assessment based on direct observations and climate models". In: *Climate Dynamics* 52.7-8, pp. 4787–4812. DOI: 10.1007/s00382-018-4413-y.

Winker, D. M., J. Pelon, J. A. Coakley, S. A. Ackerman, R. J. Charlson, P. R. Colarco, P. Flamant, Q. Fu, R. M. Hoff, C. Kittaka, T. L. Kubar, H. Le Treut, M. P. McCormick, G. Mégie, L. Poole, K. Powell, C. Trepte, M. A. Vaughan, and B. A. Wielicki (Sept. 2010). "The CALIPSO Mission: A Global 3D View of Aerosols and Clouds". In: *Bulletin of the American Meteorological Society* 91.9, pp. 1211–1229. DOI: 10.1175/2010BAMS3009.1.

Winker, D. M., W. H. Hunt, and C. A. Hostetler (Nov. 4, 2004). *Status and performance of the CALIOP lidar*. DOI: 10.1117/12.571955.

Zelinka, M. D. and D. L. Hartmann (Aug. 27, 2010). "Why is longwave cloud feedback positive?" In: *Journal of Geophysical Research: Atmospheres* 115 (D16), p. D16117. DOI: 10.1029/2010JD013817.

Zelinka, M. D., S. A. Klein, and D. L. Hartmann (Jan. 18, 2012a). "Computing and Partitioning Cloud Feedbacks Using Cloud Property Histograms. Part I: Cloud Radiative Kernels". In: *Journal of Climate* 25.11, pp. 3715–3735. DOI: 10.1175/JCLI-D-11-00248.1.

– (2012b). "Computing and partitioning cloud feedbacks using cloud property histograms. Part II: Attribution to changes in cloud amount, altitude, and optical depth". In: *Journal of Climate* 25.11, pp. 3736–3754. DOI: 10.1175/JCLI-D-11-00249.1.

Zelinka, M. D., C. Zhou, and S. A. Klein (Sept. 16, 2016). "Insights from a refined decomposition of cloud feedbacks". In: *Geophysical Research Letters* 43.17. DOI: 10.1002/2016GL069917.

Effet radiatif des nuages à la surface dans le domaine des grandes longueurs d'onde à partir des observations lidar spatial

Résumé — Les nuages jouent un rôle important dans la régulation du bilan énergétique à la surface de la Terre. Par exemple, ils absorbent le rayonnement tellurique émis par la surface de la Terre et le réémettent vers la surface, réchauffant ainsi cette dernière. Ce réchauffement peut être quantifié au travers de l'effet radiatif des nuages (CRE) infrarouge (LW) à la surface. Cependant, il n'est pas bien connu en tout point du globe et sa variabilité instantané et interdécennale est mal connue. En effet, il dépend fortement de la distribution verticale des nuages qui n'est pas bien restitué à l'échelle globale. Dans cette thèse, nous proposons de restituer le CRE LW à la surface sur 13 ans ($2008-2020$) sur tout le globe en utilisant les observations du lidar **C**loud–**A**erosol **L**idar and **I**nfrared **P**athfinder **S**atellite **O**bservations (CALIPSO). A partir de calculs de transfert radiatif $1D$, nous établissons des paramétrisations linéaires entre le CRE LW à la surface et des propriétés nuageuses dont l'altitude des nuages. En combinant les paramétrisations avec les observations nuages, nous restituons le CRE LW à la surface, à l'échelle *mensuelle* ($2^\circ \times 2^\circ$) et instantané à la pleine résolution horizontale de CALIPSO ($90\,\mathrm{m}/330\,\mathrm{m}$). Nous avons trouvé que les nuages réchauffent la surface de $27.0\,\mathrm{Wm}^{-2}$ sur la période $2008-2020$ à l'échelle globale. Le CRE LW à la surface est particulièrement important dans les régions polaires, où les nuages peuvent avoir un effet sur la fonte des glaces. En colocalisant instantanément le CRE LW à la surface et les observations de la banquise dans les régions où la concentration de la banquise Arctique varie, nous avons montré que les grandes valeurs du CRE LW à la surface ($> 80\,\mathrm{W\,m}^{-2}$) sont beaucoup plus fréquentes au-dessus des océans ouverts que de la banquise en fin d'automne. Nos résultats suggèrent que les nuages peuvent retarder la reconstruction de la banquise plus tard dans la saison.

Mots clés : Lidar spatial, Effet radiatif des nuages, Infrarouge, Transfert radiatif, Surface de la Terre, Arctique

Surface longwave cloud radiative effect derived from space lidar observations: application in the Arctic

Abstract — Clouds play an important role in regulating Earth's energy budget at the surface. For example, clouds absorb thermal radiation emitted by Earth's surface and reemit it toward the surface and warming the surface. This can be quantified through surface **L**ong**W**ave (LW) **C**loud **R**adiative **E**ffect (CRE). However, surface LW CRE on a global scale is not well retrieved and its instantaneous and interdecadal variability is poorly known. Indeed, it depends highly on vertical cloud distribution, which is poorly documented globally. In this thesis, we propose to retrieve the surface LW CRE over 13 years ($2008-2020$) at a global scale using **C**loud–**A**erosol **L**idar and **I**nfrared **P**athfinder **S**atellite **O**bservations (CALIPSO) spaceborne lidar observations. From $1D$ radiative transfer computations, we establish linear parametrizations between surface LW CRE and cloud properties including cloud altitude. Combining the parametrizations with the cloud observations, we derive two datasets of surface LW CRE, at *monthly*–$2^\circ \times 2^\circ$ gridded scale and instantaneously at full CALIPSO horizontal resolution ($90\,\mathrm{m}$ cross-track; $330\,\mathrm{m}$ along orbit-track). We found that clouds warm the surface by $27.0\,\mathrm{Wm}^{-2}$ over the $2008-2020$ time period at a global scale. Surface LW CRE is particularly important in polar regions such that clouds may have an effect on ice melting. By instantaneously co-locating surface cloud warming and sea ice observations in regions where sea ice varies, we showed that large surface cloud warming values ($> 80\,\mathrm{W\,m}^{-2}$) are much more frequent over open water than over sea ice during late Fall. Our results suggest that clouds may delay sea ice freeze-up later into the Fall.

Keywords: Space-lidar, Surface cloud radiative effect, Longwave, Radiative transfer, Arctic